Rationalising reactivity: a Combined DFT and Hyperpolarisation Approach

Richard Owain John

PhD

University of York

Chemistry

October 2014

Abstract

The complexes $Ru(CO)_3(dpae)$ and $Ru(CO)_2(dpae)(PPh_3)$ have been found experimentally to undergo various reactions with *para*-hydrogen and substrates. Reactions with *para*-hydrogen and diphenylacetylene led to the detection of hydrogenation products, confirming the complexes as hydrogenation catalysts. The catalytic behaviour was identified to be different to that of the equivalent phosphine containing complex.

High level DFT investigations have revealed significant insight into the mechanism of reaction. The experimentally detected dihydride complex $Ru(H)_2(CO)(dpae)$ was calculated to be a viable reaction product, with various pathways modelled for rearrangement. In contrast, the rearrangements for the complex $Ru(H)_2(CO)dpae)(PPh_3)$ were found to compete with the reductive elimination of dihydrogen. The routes of reaction by initiation method was examined, with the high energy 14-electron intermediates only accessible photochemically. Routes for the hydrogenation of diphenylacetylene were identified, alongside the mechanism of *cis-trans* scrambling of stilbene and formation of 1,2-diphenylethane. The formation of 1,2,3,4-tetraphenylbutadiene was also rationalised.

The reaction of hydrogen with $W(N_2)_2(dppe\text{-}\kappa^2P)_2$ was shown theoretically to involve an intra-molecular *ortho*-metallation reaction from the reactive 14-electron intermediate $W(dppe\text{-}\kappa^2P)_2$. Low barriers were obtained from the 16-electron intermediate $W(H)_2(dppe\text{-}\kappa^2P)_2$. This rationalised the formation of the experimentally proposed complex $W(H)_3(dppe\text{-}\kappa^2P)(PPh(C_6H_4CH_2CH_2Ph_2P)\text{-}\kappa^2P)$. The 14-electron intermediate $W(dppe\text{-}\kappa^2P)_2$ was calculated to adopt a butterfly geometry in a singlet state, which than rearranges upon reaction to form 16-electron intermediates. The observation of PHIP in the end products confirms the involvement of an electronic singlet state. Limited solvation was predicted from THF despite its ability to coordinate to metal centres.

In summary, the combination of high level DFT models and the use of *para*-hydrogen reactions is demonstrated to be a powerful tool for probing chemical processes and pathways, and contributes to achieving a greater understanding of reactivity in these metal complex systems.

Table of Contents

Table of Figures

Acknowledgements

I would like to thank my supervisors Martin Cockett and Simon Duckett for their support, time and patience. I would also like to thank John Slattery for additional suggestions and for guidance with setting up hardware and discussions regarding calculations. The whole of the Duckett group is also acknowledged as it is their experimental work which provides information for me to model theoretically.

Finally, special acknowledgements go to Dr. Glyn John, Dr. Ryan Mewis, Dr. Louise Highton, Dr. Peter Richardson, Laura Sharp and Amy Gibson for assistance in the editing of this thesis.

Declaration

This thesis has not previously been accepted in substance for any degree and is not being concurrently submitted in candidature for any degree other than Doctor of Philosophy of the University of York. This thesis is the result of my own investigations, except where otherwise stated. Other sources are acknowledged by explicit references. The work presented in Chapter 4 has previously been published in the Journal of the American Chemical Society with the reference article included in Appendix 1. It should be noted that this work has been repeated here with more accurate computational models.

Chapter 1: Introduction

1.1 Nuclear Magnetic Resonance

Nuclear Magnetic Resonance (NMR) spectroscopy is a technique in which the magnetic states of nuclei are investigated. It was first discovered by Rabi in 1938[1] and later extended by Bloch and Purcell in 1946.[2] The technique has been refined over the years and is now a standard analytical tool in the modern laboratory. NMR has a multitude of uses, ranging from kinetic measurements during reactions, structure elucidation and can determine the chirality of enantiomers. A detailed discussion into the workings of the technique is not given here, with many sources detailing the fundamentals such as that by Levitt.[3] The technique has also been extended for use in medical imaging, known as Magnetic Resonance Imaging (MRI). However, NMR is regarded as an insensitive technique, requiring typically 2 - 50 mg of sample to be dissolved in the deuterated solvent for analysis. The reason for the inherent insensitivity arises from the nuclear phenomenon it is based upon.

1.1.1 Nuclear energy splittings in a magnetic field

The resonance of nuclei arises from their spin aligning with the applied magnetic field or against it, as illustrated in Figure 1.1.

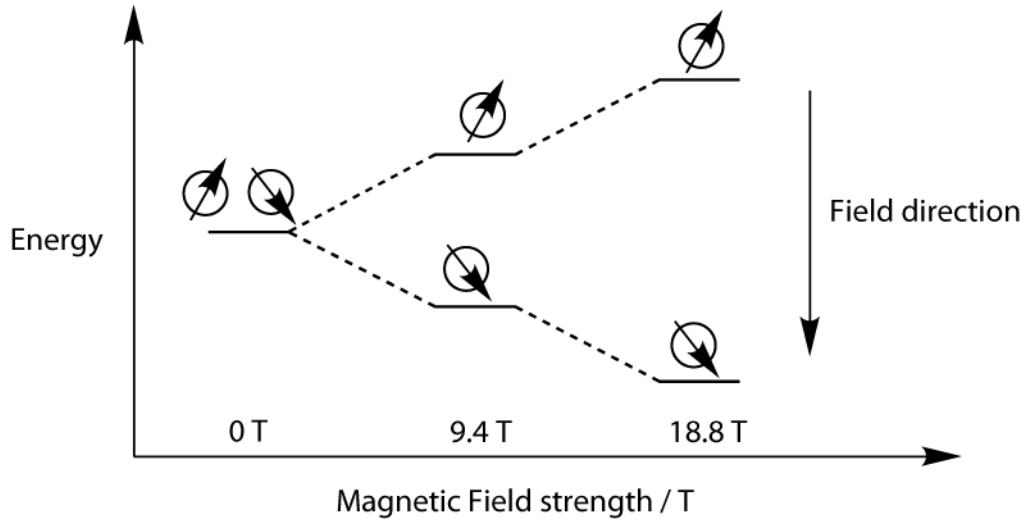

Figure 1.1: Energy level splitting of fermions when present in a magnetic field

The energy difference between states is dependent upon the magnetic field and the gyromagnetic ratio. The gyromagnetic ratio is the ratio between the observed angular frequency and the magnetic field strength. The relationship between the nucleus, field strength and energy difference is given by the Larmor equation shown in Equation 1.1:

$$\nu_0 = \gamma B_0 / 2\pi \qquad \text{Equation 1.1}$$

where B_0 is the magnetic field strength, γ is the gyromagnetic ratio of the nucleus and ν is the frequency the energy difference gives rise to. For example, for a proton nucleus with γ = 42.58 MHz T^{-1}, in a 9.4 Tesla magnet, frequency of the nucleus will precess at 400 MHz. This frequency is the resonant frequency of the nucleus, which can be probed by NMR spectroscopy. The resonant frequency can then be combined with the Boltzmann equation to obtain the relative proportion of the two energy states, as shown in Equation 1.2;

$$\frac{N_{upper}}{N_{lower}} = e^{\frac{-h\nu}{kT}} \qquad \text{Equation 1.2}$$

with h as Plank's constant, ν being energy difference in Hz, k being the Boltzmann constant and T being the temperature of the system. For a proton at room temperature in a 9.4 T magnetic field, the ratio of the populations of the two levels is 0.99994. This means that for every 30000 nuclei, only one nucleus occupies the lower level more than the upper level. This results in only one nucleus being able to make the transition between energy levels (or resonate) in every 30000 nuclei, which gives rise to the low sensitivity of the technique.

To overcome this, the magnetic field strength can be adjusted to increase the separation of the energy states and so increase the number of nuclei occupying the lower energy state relative to the higher energy state. However, an increase in magnet strength presents significant challenges, and there is a limit to the size of magnet available. Currently, the largest commercial magnets used for spectrometers have a magnetic field strength of 23.5 T (corresponding to a proton resonant frequency of 1GHz). An alternative approach to increasing the sensitivity is to artificially perturb the Boltzmann distribution of the spin states given by Equation 1.2. This technique is known as hyperpolarisation or simply polarisation, for which several techniques can be employed.

1.2 Hydrogen and its reactions with transition metals

Hydrogen exists as a stable diatomic molecule and is the most abundant element in the universe. It has a multitude of uses, such as for the processing of fossil fuels (cracking), production of ammonia, production of energy in fuel cells and is used in heterogeneous and homogeneous catalysis. Homogeneous catalysis generally involves the use of a transition metal complex in solution with the substrate under reaction. However, the study of these reactions has proved challenging; a recent review by Kubas outlines such challenges, whilst also presenting a brief historic overview of the reactions of dihydrogen.[4]

An important discovery into the reactions of hydrogen was made by Vaska and DiLuzio in 1962; the complex $Ir(CO)(PPh_3)_2Cl$ can react reversibly with hydrogen to form an Iridium(III) dihydride complex.[5] Today, the precursor of this dihydride complex is known as Vaska's complex. This complex was important in the mechanistic understanding homogenous catalysis. This reaction is illustrated in Figure 1.2.

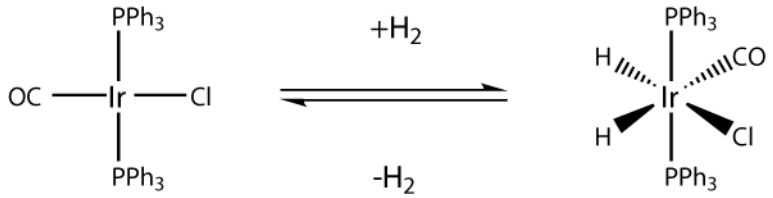

Figure 1.2: Reaction of hydrogen with Vaska's complex

Studies into the reaction mechanism of hydrogen with transition metals revealed that the Dewar-Chatt-Duncanson model developed in the 1950s for the coordination of alkenes to metals could be used to rationalise the reactions of hydrogen with a metal centre. These two models for understanding the coordination of alkenes and hydrogen to metals are illustrated in Figure 1.3.

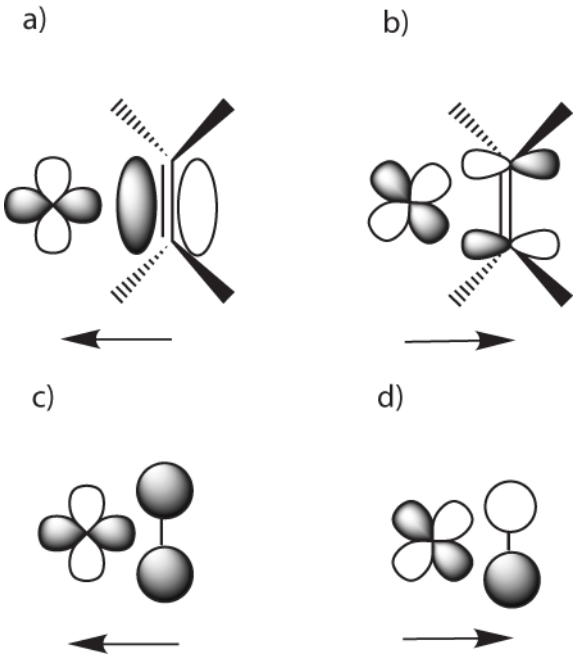

Figure 1.3: Electron donation involving alkenes, hydrogen and metals: a) σ-donation to the metal from an alkene, b) π-donation from the metal to the alkene. c) σ-donation from the hydrogen molecule to the metal, d) π-donation from the metal to the σ*-orbital of the hydrogen molecule

For alkene coordination, the electron density from an occupied π-molecular orbital in the alkene is donated to an unoccupied d-orbital on the metal centre via a σ-type interaction. At the same time, electron density from an occupied d-orbital on the metal can back-donate to an unoccupied π*-molecular orbital on the alkene, via a π-type donation. With hydrogen coordination, a similar situation is present. Electron density from the occupied σ-molecular orbital is donated to an unoccupied d-orbital on the metal via a σ- type donation. Back-donation also occurs from an occupied d-orbital on the metal to the unoccupied σ*-orbital of the hydrogen molecule. Importantly, this back-donation into the anti-bonding molecular orbital typically results in the cleavage of the hydrogen-hydrogen bond and the formation of two hydride ligands on the metal.

This reaction is referred to as oxidative addition; the two electrons from the hydrogen bond combine with two electrons from the metal and form two new metal hydride bonds. This means that the metal oxidation number increases by two. However, work by Kubas in the 1980s revealed that this back-donation to hydrogen could be changed by the metal and the coordinated ligands so that the bond cleavage no longer occurred. This resulted in the discovery of the first dihydrogen complex.[6, 7] This is discussed in more detail in Chapter 4.

The formation of hydride ligands at a metal centre allows catalytic hydrogenation of substrates to occur, such as hydrogenation of alkenes (olefins) and hydroformylation, where alkenes are converted to aldehydes. One of the earliest hydrogenation catalysts studied in detail was Wilkinson's catalyst $Rh(PPh_3)_3Cl$[8] and the mechanism was by Halpern in 1981.[9] The core of the cycle is illustrated in Figure 1.4.

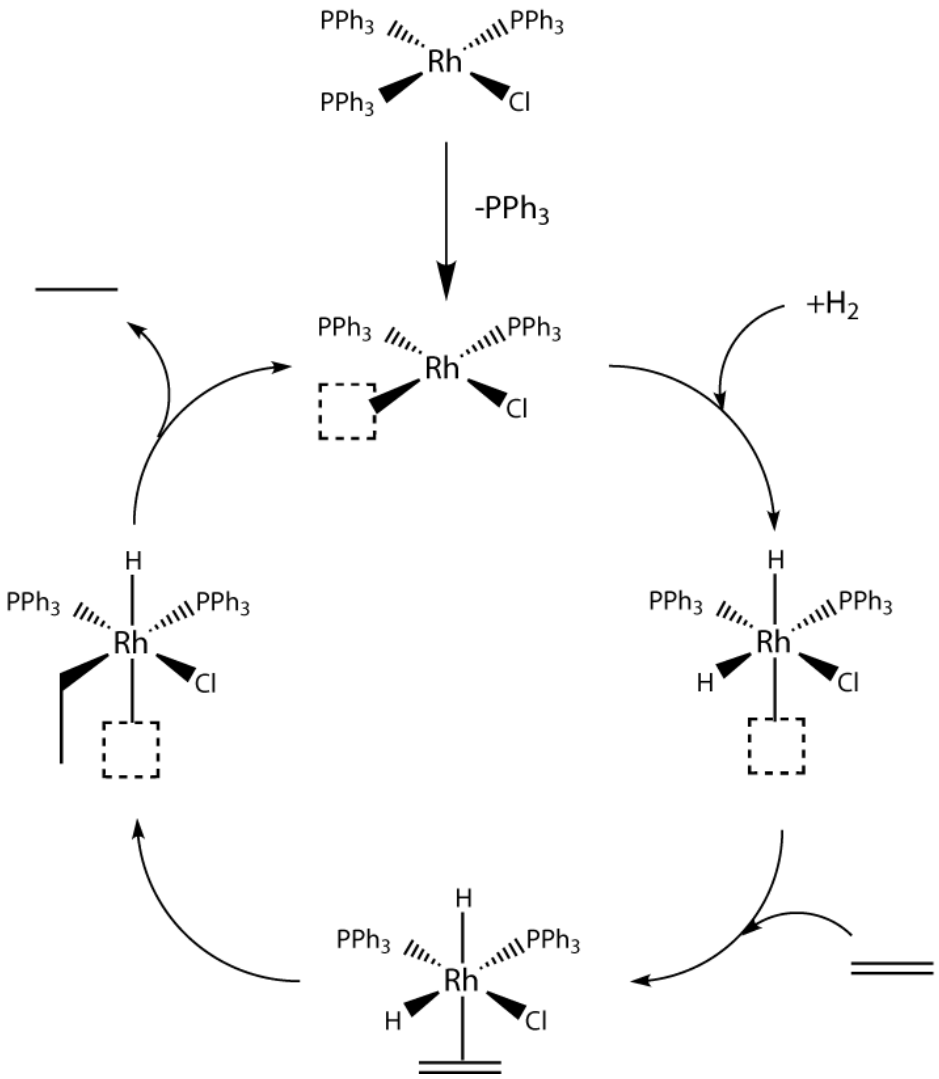

Figure 1.4: Catalytic hydrogenation cycle for Wilkinson's catalyst with ethane

In this cycle, the active species for the catalysis is formed by the dissociation of one of the phosphine ligands which then allows the coordination of hydrogen. This results in the oxidative reaction forming a 5-coordinate complex which can then coordinate a molecule of substrate, in this case ethene. A hydride transfer reaction then occurs, with the transfer of the hydride *cis* to the olefin. The olefin then becomes coordinated to the metal via a σ-

bond, which allows the second hydride transfer reaction to occur. Importantly, a rearrangement occurs to position the olefin *cis* to the remaining hydride ligand. This rearrangement is favourable, as it results in the remaining hydride ligand being *trans* to a vacant site. The second transfer reaction results in the olefin becoming an alkane, which is then released into solution and unable to coordinate to the metal centre. This loss of substrate results in the reformation of the active 3-coordinate species and the cycle is repeated with more hydrogen and substrate. However, the work by Halpern determined that this core cycle was accompanied by many side reactions such as the coordination of the olefin prior to the coordination of hydrogen, the recoordination of the lost phosphine or even dimerisation of the metal complexes.[9] It also revealed that the study of mechanistic cycles was complicated by the fact that the individual steps in the cycle proceed at different rates.

The role of the transition metals in such catalytic cycles is to bring together the substrate and hydrogen atoms to a distance where bonding can occur and also reduce the high barriers for reaction. These high barriers arise from the stability of carbon-carbon bonds and carbon–hydrogen bonds; carbon-carbon bonds can range from around 350 kJ mol^{-1} to over 800 kJ mol^{-1} and carbon-hydrogen bonds are around 400 kJ mol^{-1}.[10] The reduction in the reaction barriers occurs as the metal is able to use occupied and unoccupied d-orbitals to stabilise the geometries of the transition states that are involved in the hydride transfer reactions. The ability of the metal to change oxidation state is also key to the cycles; the metal centre in this cycle starts as rhodium(I) which becomes rhodium(III) after the oxidative addition of hydrogen. It is then reduced back to rhodium(I) in the second hydride transfer reaction. Rhodium, a Group 9 metal is stable in the +1 oxidation state has a d^8-configuration. This allows stable 4-coordinate complexes which have square-planar geometries. Upon oxidative addition of hydrogen, the rhodium is oxidised to a d^6-configuration which allows a stable octahedral geometry. The change in oxidation state linked with the second hydride transfer reaction then leads to the stable square-planar geometry with a d^8-configuration.

Transition-metal homogeneous catalysts can also be used in asymmetric synthesis of compounds. This was demonstrated by Noyori in 1987 for the asymmetric hydrogenation of ketones and aldehydes which involved the complex $Ru(BINAP)(L)_2(Cl)_2$, where L is the

solvent and BINAP is 2,2'-Bis(diphenylphosphino)-1,1'-binaphthyl.[11] The mechanism was determined in 1993 by Noyori[12] and is illustrated in Figure 1.5.

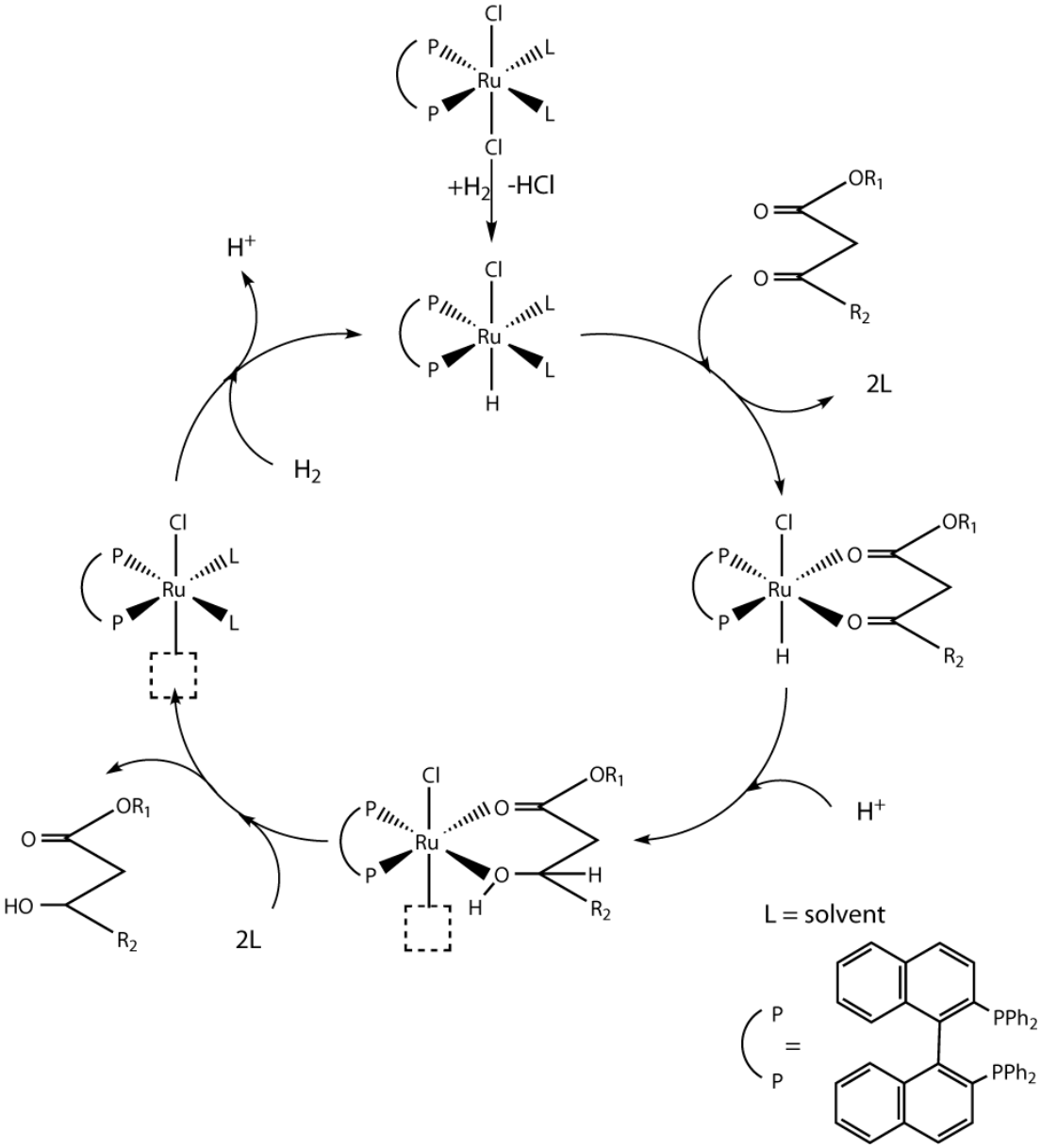

Figure 1.5: Catalytic asymmetric hydrogenation cycle for Ru-BINAP with esters

This mechanism was included in a general review of the ruthenium hydride catalysis in 2004.[13] In this system, the precursor $Ru(BINAP)(L)_2(Cl)_2$ forms the active complex via the reaction with hydrogen, followed by the loss of HCl. The active complex contains a single hydride ligand and the replacement of both solvent molecules (L) with the ester molecule results in the complex $Ru(BINAP)HCl(R_2CO(CH_2)COR_1)$. This complex can then undergo protonation, where the proton attaches to the ketone oxygen, after which the hydride

ligand is transferred to the carbon of the ketone group. The subsequent loss of the ester molecule and solvation of the complex forms a 5-coordinate complex which can react with hydrogen, reforming the active complex and catalysis can occur again. This overall process leads to the formation of either the R or S enantiomer of the hydrogenation product in high enantiomeric excess, which relies upon the chirality of the BINAP ligand used in the complex.

1.3 Polarisation in NMR by the use of *para*-hydrogen

The polarisation of nuclei for use in NMR experiments can be achieved in several different ways, with commercial systems from manufacturers (e.g. Oxford Instruments, General Electric and Bruker) widely available. Polarisation can result in the signal enhancement of many orders of magnitude for suitable cases.

Examples of polarisation methods are:

1. *Para*-Hydrogen Induced Polarisation (PHIP)[14-18]
2. Dynamic Nuclear Polarisation (DNP)[18-22]
3. Nuclear Overhauser Effect (NOE)[18, 19, 23]
4. Chemically-Induced DNP (CIDNP)[24-27]
5. Optical pumping of polarized noble gases[28-30]
6. Optical Nuclear Polarisation (ONP)[23, 31]
7. Hartmann-Hahn cross-polarisation[32, 33]
8. Brute-force Nuclear Orientation[34]

The focus of the research in this thesis involves the use of *para*-hydrogen, and so only the origins of PHIP are presented. The polarisation effect in PHIP relies on the disruption of the Boltzmann distribution previously described (Equation 1.2). This is achieved by the quantum mechanical properties of *para*-hydrogen. Molecular hydrogen is composed of two atoms of hydrogen coordinated together by a single σ-bond. Both of these nuclei possess a nuclear property called total angular momentum (*I*) and this is referred to as nuclear spin. It is this property which is exploited in the NMR experiment. The hydrogen nucleus possesses a nuclear spin of $I=^1/_2$ which means that it is a fermion. This value of $I=^1/_2$ results in the formation of two possible alignments described previously, as the number of possible

alignments is given by 2*I* + 1. As hydrogen atoms are fermions, the overall wavefunction for the molecule must change sign upon particle interchange to obey the Pauli Exclusion Principle. This can also be described as the wavefunction being antisymmetric with respect to particle interchange. However, the situation for the dihydrogen molecule is further complicated by the fact that the interchange alters the nuclear spins if they are paired, but not if they are parallel. The overall wavefunction of a molecule, Ψ, is composed of multiple contributions as defined in Equation 1.3:

$$\Psi = \Psi_{nuclear} \cdot \Psi_{electronic} \cdot \Psi_{translational} \cdot \Psi_{rotational} \cdot \Psi_{vibrational} \qquad \text{Equation 1.3}$$

When the spins are parallel, the rotational wavefunction must change sign upon interchange in order for the overall wavefunction to change sign. Similarly, when the spins are paired, the rotational wavefunction must not change sign in order for a change in sign of the overall wavefunction. This means that the parallel nuclear spins must have odd values for *J* (the rotational quantum number) and paired spins must have even values. The nomenclature for describing the spin states of nuclei follows the convention that spin states are assigned to be α when parallel and β when antiparallel with an external magnetic field. This results in four possible combinations for H_2 which are αα, αβ, βα and ββ. The first and last have the spins parallel and so are symmetric with respect to interchange, whereas αβ and βα are neither symmetric nor asymmetric. However, the use of linear combinations for these functions results in the formation of the states αβ+βα and αβ-βα. Interchange for the spin state of αβ+βα results in the state βα+αβ which is equivalent to αβ+βα. This means that the interchange for the αβ+βα state must also require an odd value of *J* to ensure the overall wavefunction becomes antisymmetric. However, the interchange of the αβ-βα state results in the state βα-αβ which can be rewritten as -1(αβ- βα) and only even numbers for the rotational quantum number are allowed. This means that there are three possible spin states of dihydrogen where odd numbers of the rotational quantum numbers are required and one spin state where even numbers are required. The three parallel spin states (αα, ββ and αβ+βα) are also known as the triplet states or *ortho*-hydrogen and the single paired spin state (βα-αβ) is known as singlet hydrogen, or *para*-hydrogen.

1.3.1 Conversion of *ortho*-hydrogen to *para*-hydrogen

At room temperature, the three *ortho* spin states and single *para* spin state will be equally populated. However, the *ortho* spin states must have odd rotational quantum numbers (*J*),

which means that the molecule of dihydrogen cannot have the *J*=0 rotational state. This results in rotation still occurring even at very low temperatures, with the non-rotating *para*-state being more stable. The conversion of hydrogen from the gas to the liquid phase at 20.3 K results in the slow conversion of the *ortho*-isomer to the *para*-isomer, which results in the release of 532 J/g of energy.[35] This is higher than that required for the liquid to gas phase conversion (453 J/g) and so the spin state conversion results in part of the liquid hydrogen condensed returning back to the gas phase (at approximately 1% per hour).[35] Techniques were identified to allow efficient conversion of *ortho*-hydrogen to *para*-hydrogen, as the conversion is symmetry forbidden. One solution identified was with the use of a paramagnetic catalyst, such as activated-carbon or iron oxide. The relationship between the purity of *para*- hydrogen and the conversion temperature is also known; this is illustrated in Table 1.1 which has been duplicated from previously reported work.[36]

Table 1.1: Relative proportion of *para*-hydrogen at various temperatures

Temperature / K	**Purity of *para*-hydrogen / %**
20	99.86
65	62.24
77	52.09
190	26.43
200	26.10
230	25.51
250	25.30
273	25.16
298	25.09

The result of this relationship means that *para*-hydrogen can be purified from hydrogen gas by cooling to around 20 K in the presence of a paramagnetic catalyst with a resulting value of around 100% purity. However, the cooling of hydrogen gas to 30 K leads to an efficient conversion of over 90% purity. A commercial system is currently available which utilises a conversion temperature of between 36 K and 40 K and gives a purity of the *para*-hydrogen spin state of over 85%. Importantly, because the conversion of *para*-hydrogen to *ortho*-hydrogen is symmetry forbidden, the *para*-hydrogen spin isomer produced after conversion

has a long lifetime, providing it does not come into contact with any paramagnetic material, allowing its use in chemical reactions and investigations.

1.3.2 Utilisation of *para*-hydrogen in NMR

The existence of two spin isomers of hydrogen has been known since the 1930s[37-39] but it was only when Bowers and Weitekamp predicted in 1986 that spin polarisation would occur in NMR experiments that its potential was realised.[15] This utilisation of *para*-hydrogen required the chemical reaction via hydrogenation reactions, and would result in spin polarisation of the order of 10000 at thermal equilibrium. Additional factors were considered, such as the reaction of *para*-hydrogen would have to occur faster than any exchange reactions and that the symmetry of the hydrogen molecule would have to be broken upon reaction. To provide this break in symmetry, the two hydrogen atoms have to be in different environments to cause the nuclei to adopt different chemical shifts. In 1987 Bowers and Weitekamp demonstrated the use of *para*-hydrogen in NMR experiments, where spin polarisation was observed for the conversion of acrylonitrile to propionitrile using Wilkinson's catalyst.[17] In this work, the term *Para*-hydrogen and Synthesis Allow Dramatically Enhanced Nuclear Alignment (PASADENA) was introduced to describe the method of polarisation. Separate work was published in the same year by Eisenschmid *et al.*, which detailed the experimental polarisation of signals arising from the hydrogenation of phenyl acetylene.[14] This work introduced a different term for the method; *Para*-Hydrogen Induced Polarisation (PHIP) and this term will be used within this thesis to describe the method of polarisation.

The work by Eisenschmid *et al.* included experiments on deuterated substrates which found that in the case of the 1,1,2,2,-tetradeuteroethane hydrogenation product, polarisation was observed, despite the chemical equivalence of the hydrogen nuclei. The reason for the observation of polarisation was due to the two nuclei being magnetically inequivalent from the different scalar couplings to the deuterium atoms. This broke the symmetry of the *para*-hydrogen molecule and showed that PHIP could be used in a variety of reactions.

Work reported by Weitekamp and Pravica in 1988 described a new variant to the PASADENA experiment which was called Adiabatic Longitudinal Transport After Dissociation Engenders Net Alignment (ALTADENA).[16] This method of polarisation was different to

previous methods because the hydrogenation reaction was carried out at low magnetic field (9.4 mT) and was then transferred to high field in the spectrometer. This resulted in the alignment of the signals for each multiplet compared to the out-of-phase signals that occurred with the PASADENA method in cases where fast coherence decay (small T_2 values) was present with long scalar coupling evolution times (small J values).

1.3.3 Hyperpolarisation from *para*-hydrogen

The signal enhancement observed in spectra obtained using PHIP can be significant, which assists in the detection of minor species and even reaction intermediates. Additionally, the signals obtained from hydrogen nuclei derived from *para*-hydrogen show a distinct profile, where one part of the signal appears in absorption and the other part appears in emission. This means that the location of *para*-hydrogen derived nuclei can be determined and this can aid mechanistic assignments. The distinct profile arises from the specific transitions that arise from the use of *para*-hydrogen.

When hydrogen reacts with a metal complex and undergoes oxidative addition, a dihydride complex is obtained, as previously described. The spins in this system form an AX system when the chemical shifts are distinct, (represented by the A and the X terms) which arises from the chemical environment difference for each hydride. As the two nuclei couple to each other, they have to be considered together and they can be represented by the labels αα, αβ, βα and ββ as previously defined. These four states lie at different energies when present in a magnetic field, with the αα state lowest in energy and the ββ state highest in energy. When the source of hydrogen is the non-polarised mix of 75% *ortho* and 25% *para*-hydrogen spin states, all four of the spin states are occupied. However, if the source of hydrogen contains purely the *para*-hydrogen spin state, only the αβ and βα spin states of AX system are populated. This means that the possible transitions are limited to those from these spin states. As only one nucleus can change spin at a time, four transitions are possible and result in the formation of the αα and ββ spin states; this is illustrated in Figure 1.6.

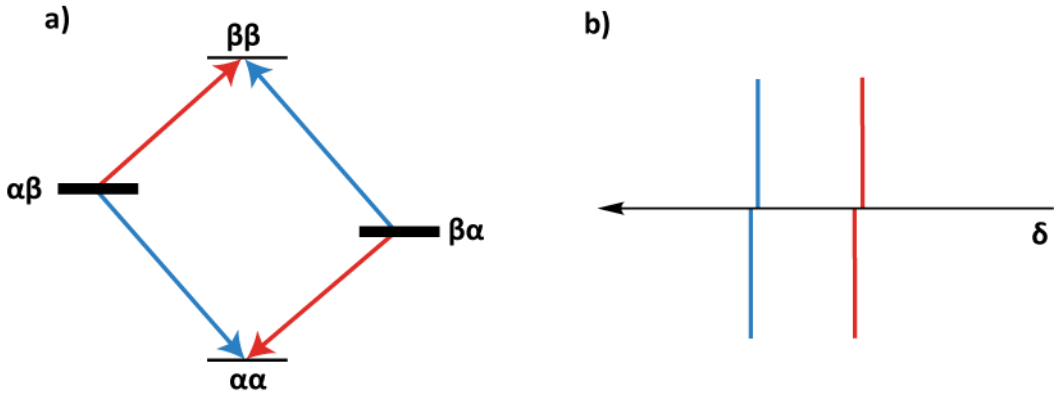

Figure 1.6: a) Spin transitions of an AX system where the hydrides are derived from *para*-hydrogen. b) Resulting ^{1}H NMR signals

The transitions to the αα spin state result in peaks in the experimental spectra which appear in emission whereas the transitions to the ββ spin state appear in absorption. Crucially, as only these transitions can occur, combined with the presence of all starting spin states being in either the αβ and βα configuration, the signals obtained with *para*-hydrogen are significantly enhanced and are said to be hyperpolarised. An example of the signals obtained for the detection of a minor complex is illustrated in Figure 1.7 which was taken from work reported by Duckett, Eisenberg and Newell in 1994.[40] In this work, Wilkinson's catalyst ($RhCl(PPh_3)_3$) was used to hydrogenate both *cis* and *trans* isomers of 2-hexene along with *para*-hydrogen. The use of PHIP allowed the detection of minor isomers of the binuclear complex $H_2Rh(PPh_3)_2(\mu\text{-}Cl)_2RhPPh_3$(olefin), previously unobserved.

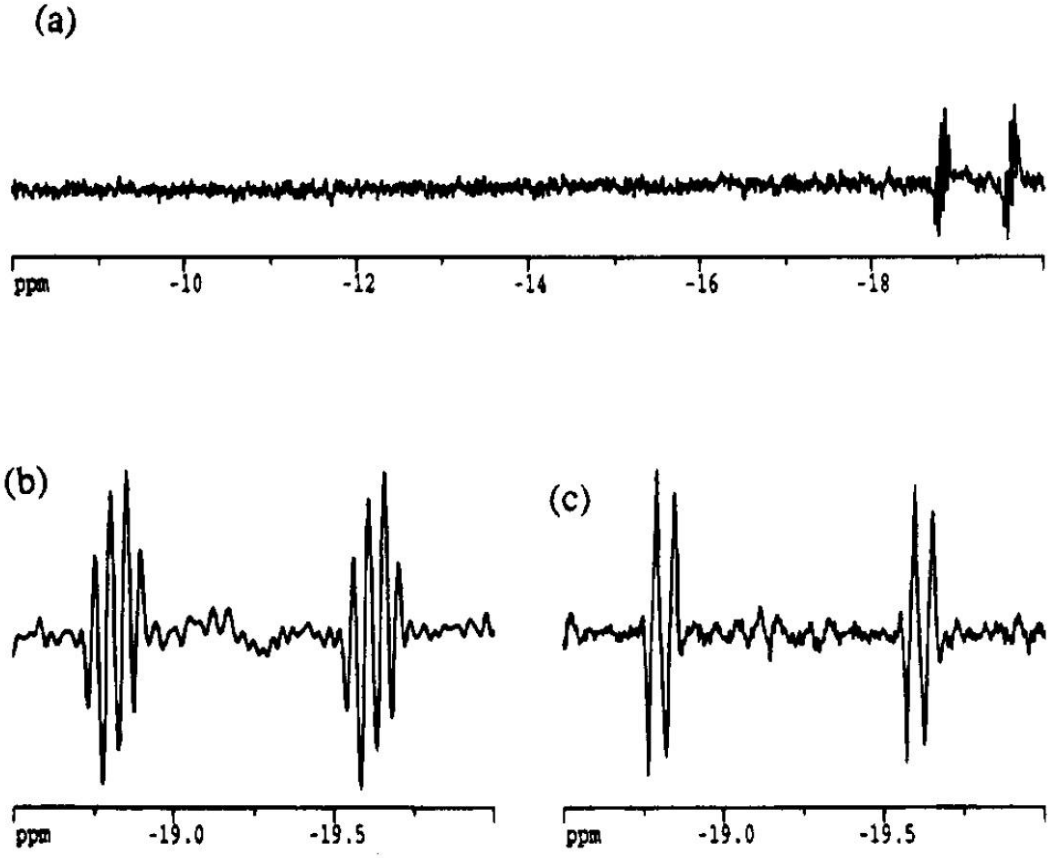

Figure 1.7: Enhanced signals for species detected during the hydrogenation of 2-hexene with Wilkinson's catalyst. a) Hydride region of spectra. b) expansion of the hydride signals, c) ^{1}H spectrum (^{31}P decoupled) – taken from reference [40]

The requirement for the nuclei from *para*-hydrogen to break their symmetry upon reaction to allow observation has previously been described, where the nuclei have to exist as chemically or magnetically inequivalent. This latter situation allowed the detection of the minor isomer of the hydrogenation product for Vaska's complex. Theoretical investigations have previously been undertaken into the mode of dihydrogen addition, as two possible complexes are possible but only one observed.[41, 42] These investigations found that the change in the complex from four-coordinate to six-coordinate involves concentration of charge density around the metal centre. It is the effect that this concentration has on the ligands in the plane of addition that controls the direction of addition. The presence of weak electron donating ligands stabilises the 5-coordinate transition state, whereas stronger electron donors destabilise it. This means that the addition of hydrogen to Vaska's complex results in the reaction across the Cl-Ir-CO plane, forming the isomer shown in

Figure 1.2. Work by Hasnip *et al.* on this addition using *para*-hydrogen revealed that detection of the minor isomer is possible,[43] illustrated in Figure 1.8.

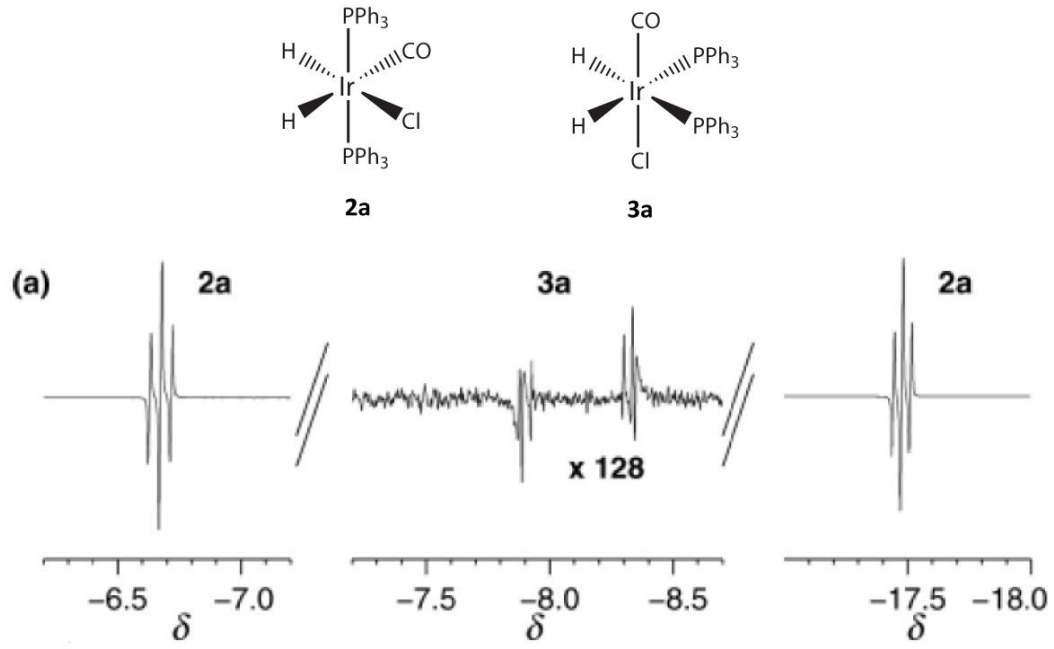

Figure 1.8: Enhanced signals for species detected after the hydrogenation with Vaska's catalyst. The minor signals arise from *cis*,*cis*-$IrH_2(CO)(PPh_3)_2Cl$ (from Reference 48)

Side reactions also have the potential to be mapped; if a hydrogen atom from *para*-hydrogen is transferred from a metal centre by the formation of a new bond, it is possible that the signal for this nucleus will maintain the polarisation from the original *para*-hydrogen molecule. This enables the location of a hydrogen atom that has been transferred from the metal centre by a hydride transfer reaction to be determined. Additionally, any substrate that simultaneously coordinates to the metal centre with polarised hydride ligands has the potential to interact with the polarisation through the scalar-coupling framework. This is the mechanism involved in Signal Enhancement by Reversible Exchange (SABRE), discovered in 2008 by Duckett and co-workers.[44] Additional information is also gained by the use of *para*-hydrogen in the mapping of mechanistic pathways; there are certain conditions which relax the polarisation of the nuclei back to the Boltzmann distribution. If the coordination of a molecule of *para*-hydrogen to a metal centre does not lead to oxidative addition and a dihydrogen ligand is formed, the polarisation of the rapidly rotating dihydrogen ligand, combined with the short T_1 values of the dihydrogen ligand means that the polarisation is quenched.[45] Therefore, if polarisation is seen in a substrate

or complex, a relatively long lived-dihydrogen intermediate cannot be present in the pathway to its formation. The quenching of the polarisation of hydrogen nuclei from *para*-hydrogen can also occur when a metal in an electronic triplet state reacts with these nuclei, as the metal centre becomes paramagnetic. This effect was demonstrated by Perutz *et al.* in 2004 where the two complexes of $M(CO)_3$(dppe) (M = Fe or Ru) were investigated.[46] The iron complex is generally accepted to adopt an electronic triplet state for the 16-electron intermediate formed after CO loss, whereas that of ruthenium is expected to be an electronic singlet.[47, 48] The reactions of these two intermediates with *para*-hydrogen revealed substantially different spectra; the spectrum obtained with $Fe(CO)_3$(dppe) showed no anti-phase character of the hydride signals whereas the spectrum for $Ru(CO)_3$(dppe) did show anti-phase character. These spectra are illustrated in Figure 1.9.

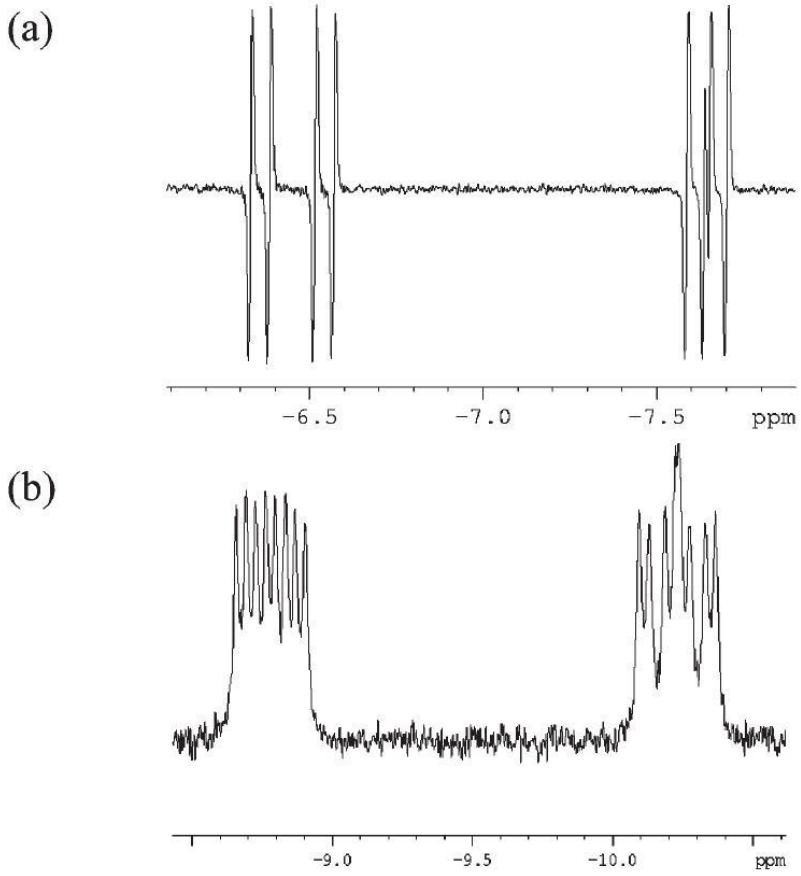

Figure 1.9: Proton spectra obtained for the reaction of *para*-hydrogen with $M(CO)_3$(dppe); a) M = Ru, b) M = Fe (from Reference 51)

The use of *para*-hydrogen to allow detailed information to be obtained about reaction pathways is not just limited to the spectra obtained for the protons in a sample. The polarisation of the protons derived from *para*-hydrogen are able to couple to other NMR active nuclei such as ^{13}C and ^{15}N through the scalar coupling network.[36] It has also been demonstrated that more complex NMR experiments than 1D proton experiments are possible. Such examples are illustrated in Reference 42; Heteronuclear Single Quantum Coherence (HSQC), Heteronuclear Multiple Bond Coherence (HMBC), and 2D Nuclear Overhauser Effect (NOE) experiments can all benefit from the use of *para*-hydrogen. A recent NMR pulse sequence developed by Adams *et al.*[49] (OPSY; Only *Para*-hydrogen Spectroscopy) allows the exclusion of signals from nuclei which are not derived from *para*-hydrogen from the spectrum; the exclusion of these signals can simplify spectra, along with the additional cost benefit associated with the potential to use protonated solvents.

1.4 Computational Chemistry via Density Functional Theory (DFT)

Theoretical methods have been used to aid the understanding of chemical systems since early calculations by Heitler and London in 1927.[50] These calculations involved valence bond theory applied to model the exchange forces in the hydrogen molecule. The field of computational chemistry has expanded dramatically in the following years, with modern computers allowing complex calculations to be performed. The work presented in this thesis relies primarily on the use of theoretical calculations. These calculations primarily use DFT but some calculations utilise Hartree-Fock theory. A brief introduction into these methods is now described, along with advantages and limitation of the methods.

1.4.1 Quantum mechanics

Theoretical quantum chemistry relies upon simplification of the Schrödinger equation, formed by Erwin Schrödinger and was published in 1927.[51] It describes how the quantum state of a physical system changes with time. A good background to the field of quantum mechanics can be found in the textbook by Atkins, elements of this are presented here.[52] The Schrödinger equation can be written in a simple form which is shown in Equation 1.4:

$$\hat{H}\Psi = E\Psi \qquad \text{Equation 1.4}$$

where $\hat{H}$ represents the Hamiltonian operator, Ψ is a wavefunction and E is the energy of the system in one dimension, the Hamiltonian operator adopts the form shown in Equation 1.5:

$$\hat{H} = -\frac{\hbar}{2m}\frac{d^2}{dx^2} + \nabla(x) \qquad \text{Equation 1.5}$$

where m is the mass of the particle, $\hbar$ is Planks constant h divided by 2π and ∇ is the potential energy of the particle at point x. Solutions for Equation 1.4 can readily be determined for single particles but not however for systems with multiple particles, as a further complication arises from the presence of electron-electron interaction terms. The potential energy of the electrons in a multi particle system is shown in Equation 1.6:

$$\nabla = -\sum_i \frac{Ze^2}{4\pi\epsilon_0 r_i} + \frac{1}{2}\sum_{ij}{}' \frac{e^2}{4\pi\epsilon_0 r_{ij}} \qquad \text{Equation 1.6}$$

where the first term accounts for the total attractive interaction between the electrons and the nucleus, Z is the atomic number, ϵ_0 is the vacuum permittivity and r_i is the nucleus-electron distance. The total repulsive interaction is accounted for by the second term, where r_{ij} is the distance between electrons i and j and the prime on the second term indicates that $i \neq j$. This complex potential energy term means that solving the Schrödinger equation for systems with multiple particles and electrons is not possible. Nevertheless, approximations exist that allow solutions for the wavefunctions and energies to be determined. One key approximation was proposed by Hartree in 1927,[53-55] which was modified by Fock in 1930 to form the Hartree-Fock (HF) method.[56] In this method, the wavefunction is approximated by a single Slater determinant made up of one spin orbital per electron. Importantly, the electron correlation is neglected and this leads to significant differences between calculated and experimental parameters. Several corrections exist, where the corrections are made after the main Self Consistent Field (SCF) step of the HF method (SCF; the iterative method that allows the HF equations to be solved); these are known as post-Hartree-Fock methods. Such methods include the configuration interaction,[57, 58] coupled cluster[59-61] and Möller-Plesset theories.[62] The use of second order Möller-Plesset theory has been applied to transition metal chemistry and shown to produce good results;[63] although it is computationally expensive. However, the Density

Functional Theory computational method has been found to yield reasonably accurate results without being too computationally expensive.

1.4.2 Density Functional Theory background

The method proposed by Hohenberg, Kohn and Sham in 1964-65 entitled Density Functional Theory (DFT)[64, 65] has gained popularity over the past 50 years.[66] Indeed, the review by Becke in 2014 found that citations for notable DFT papers were in the order of tens of thousands.[66] The DFT methodology can also offer a decrease in computational cost compared to the lower HF theory; this potential decrease in computational cost can be achieved by the theorems DFT is based upon, proposed by Hohenberg and Kohn in 1964.[64] The first of these theorems shows that the ground state properties of a many electron system rely on the electron density which can be derived from three coordinates. The second theorem describes an energy functional for the system and that this functional is at a minimum for the ground state. Essentially, the electron density is found to be a function of spatial position, with a second function acting on this electron density to allow the calculation of an energy (hence density functional theory). The calculation of the functions of electron density in terms of spatial position is undertaken with the Kohn-Sham equations. The advantage of DFT over more rigorous methods arises from these two approximations; a system of *n* electrons has 4*n* coordinates in its wavefunction (when spin is considered along with the three spacial coordinates). However, the electron density depends solely upon the three coordinates involved in the density, independent of the number of electrons.[67] This simplification decreases computational cost as the number of electrons increases with larger systems. A review article by Ramos *et al.* in 2007 provides an introduction into the fundamentals of DFT; main points of which are presented here.[68] The general form of the functional used in DFT is shown in Equation 1.7 for a system of N nuclei and *n* electrons:

$$E[\rho] = -\frac{1}{2}\sum_{i=1}^{n}\int \psi_i^*(r_i)\nabla_i^2\psi_i(r_i)dr_1 - \sum_{X=1}^{N}\int \frac{Z_X}{rX_i}\rho(r_1)dr_1 + \frac{1}{2}\int\int \frac{\rho(r_1)\rho(r_2)}{r_{12}}dr_1dr_2 + E_{xc}[\rho] \qquad \text{Equation 1.7}$$

where ψ_i (with i = 1, 2 to *n*) represents the Kohn-Sham orbitals and the first term describes the non-interacting kinetic energy. The second term represents the nuclear-electron

interaction and the third term describes the total Coulombic interaction between the total charge distributions between the centres at r_1 and r_2. This equation is actually similar to that used in HF theory, except that the final E_{xc}[ρ] term is not included; this final term (E_{xc}) accounts for the interaction between the electrons which was excluded from Kohn-Sham orbitals. This term also corrects for the non-classical corrections to the electron-electron repulsion energy and the term is known as exchange-correlation. The Kohn-Sham orbitals (one-electron orbitals) for a ground state electron density $\rho(r)$ can be expressed as:

$$\rho(r) = \sum_{i=1}^{n} |\psi_i(r)|^2 \qquad \text{Equation 1.8}$$

The Kohn-Sham orbitals can be determined by solving the Kohn-Sham equations, which is achieved by combining the charge density obtained from Equation 1.8 with the application of the variational principle to the electronic energy $E[\rho]$:

$$\hat{h}_i \Psi_i(r_1) = \epsilon_i \Psi_i(r_1) \qquad \text{Equation 1.9}$$

where ϵ_i is the Kohn-Sham orbital energy and $\hat{h}_i$ is the Kohn-Sham Hamiltonian. This Hamiltonian can adopt that shown by:

$$\hat{h} = -\frac{1}{2}\nabla_1^2 - \sum_{X=1}^{N} \frac{Z_X}{r_{X_1}} + \int \frac{\rho(r_2)}{r_{12}} dr_2 + V_{xc}(r_1) \qquad \text{Equation 1.10}$$

where $\nabla_1^2$is the potential energy and V_{xc} is given by:

$$V_{xc}[\rho] = \frac{\delta E_{xc}[\rho]}{\delta \rho} \qquad \text{Equation 1.11}$$

and V_{xc} in Equation 1.11 is the functional derivative of the exchange-correlation energy. The E_{xc} term also appears in Equation 1.7 and it is this term which causes issues with DFT, as this term is not exactly known, but approximations for it exist. This exchange-correlation energy is usually spilt into two component parts:

$$E_{xc}[\rho] = E_x[\rho] + E_c[\rho] \qquad \text{Equation 1.12}$$

Once the E_{xc} term in Equation 1.12 is known, the V_{xc} term can be calculated. The calculation of the electron density in Equation 1.8 relies on the existence of the Kohn-Sham orbitals defined in Equation 1.9 and Equation 1.10. The calculation of these orbitals requires the use of the Self Consistent Field (SCF) method that the HF method employs. An initial guess for the charge density ρ can be obtained from the combination of the

individual electron densities for the individual atoms. The initial Kohn-Sham orbitals can then be obtained using an approximate form of the functional. These orbitals are then used to solve Equation 1.8 to obtain an improved electron density. Once the density and exchange-correlation energies are consistent between iterations (different convergence criteria are possible), the overall electronic energy is calculated from Equation 1.7.

1.4.3 Classes of DFT functional

1.4.3.1 Local Density Approximation

The simplest approximation to represent the exchange term E_x is by the Local Density Approximation (LDA), which treats the local density as a uniform electron gas. This allows the Dirac formula[69] shown in Equation 1.13 to be used to obtain the exchange energy:

$$E_x^{LDA}[\rho] = -C_x \int \rho^{4/3}(r)dr \qquad \text{Equation 1.13}$$

$$C_x = -\frac{3}{4}\left(\frac{3}{\pi}\right)^{1/3}$$

This approximation is for a uniform electron gas and ignores the spin properties of electrons and so the Local Spin Density Approximation (LSDA) was formulated by Slater in 1951[70] and resulted in the exchange functional, shown in Equation 1.14:

$$E_x^{LSDA}[\rho] = -2^{1/3}C_x \int \left(\rho_\alpha^{4/3} + \rho_\beta^{4/3}\right) \qquad \text{Equation 1.14}$$

where α and β represent the spin up and spin down densities. The LDA and LSDA terms are typically used interchangeably, as for closed shell systems the two methods are essentially equal. The correlation energy E_c of these models proved difficult to obtain separately from the exchange energy, but has been achieved by the use of Monte Carlo methods with several different electron densities of a homogeneous electron gas.[71, 72] A popular formulation for this functional was developed by S. Vosko, L. Wilk and M. Nusair,[73] which is known as the VWN functional. Other popular functionals include that formulated by J. Perdew and A. Zunger in 1981 (PL functional)[74] and that of Perdew and Wang in 1992 (PW functional).[75] It has been found that these approximations (LDA and LSDA) allow the calculation of values similar to those obtained via the use of HF, which is based on wave mechanics. However, it has also been found that these types of functionals do not correlate well with experimental data.

1.4.3.2 Generalised Gradient Approximation

The main limitation of the LDA method is that the electron density is a non-uniform electron gas. One approach developed to improve this inconsistency was to consider not just the electron density at any point but to include the gradient of the density i.e. $\Delta\rho(r)$. It has been found that this type of approximation can yield accurate results using various calculations.[76] Two routes for its development were taken by separate research groups run by Becke and Perdew. Becke took a route which was partially empirical, with large molecular training set used to allow numerical fitting procedures.[77-82] Examples of popular functionals which were developed in this way are the Perdew-Wang (PW)[83] and Becke88 (B)[84] functionals. The second route was undertaken by Perdew and involved a more rational-based approach.[75, 85-90] Perdew's route was linked more closely to quantum mechanics than that of Becke, with common functionals in this class as Becke86 (B86),[78] Perdew 86 (P)[87] and Perdew-Burke-Ernzerhof (PBE).[89] The first class of functionals was found to perform well at predicting atomisation energies and reaction barriers for molecular reactions, whereas the second class of functionals was better at predicting solid-state properties.[80, 90] Several different correlation functionals have been developed, with popular GGA correlation functionals being Perdew 86 (P86),[87] and Perdew-Wang (PW91).[91] The Lee-Yang-Parr functional (LYP)[92] which is based on the Colle-Salvetti correlation energy formula[93] is also in this class of functionals and has been extremely popular with researchers, with over 45000 citations. Combinations of the exchange and correlation functionals have been proposed, which form standard functionals. Such combinations are the PBE functional, which uses both the PBE exchange and PBE correlation functionals,[75, 89] BLYP which combines the B88 exchange with the LYP correlation functional and BP86 which combines the B88 exchange with the VWN and P86 correlation functionals. This last functional combination is also recommended by the authors of the Turbomole package[94] for the whole of the periodic table.[76] Whilst the inclusion of gradients to form GGA functionals improves the match between experimental values with calculated values compared to those obtained from LSDA functionals, GGA functionals are still not accurate enough for several chemical systems. For this reason hybrid density functionals have been developed.

1.4.3.3 Hybrid functionals

Hybrid functionals utilise the same methodology as that used in GGA functionals, but include a percentage of HF exchange. The percentage of HF energy which is needed cannot be obtained from first principles and so is generally obtained empirically. The most widely used scheme to represent the form of hybrid functionals is that proposed by Becke in 1993,[95] as shown in Equation 1.15:

$$E_{xc} = E_{xc}^{LSDA} + a_1(E_x^{HF} - E_x^{LSDA}) + a_2 E_x^{GGA} + a_3 E_c^{GGA} \qquad \text{Equation 1.15}$$

where the local and gradient functionals can be varied, along with the constants a_1 to a_3. It is these three constants which are determined by fitting to experimental data (generally). The E_{xc} term uses GGA functionals previously described. The popular B3LYP functional from Becke[95] adopts the form shown in Equation 1.16:

$$E_{xc} = E_{xc}^{LSDA} + 0.2(E_x^{HF} - E_x^{LSDA}) + 0.72\Delta E_x^{B88} + 0.81\Delta E_c^{LYP} \qquad \text{Equation 1.16}$$

The B3LYP name originates from the use of the B exchange functional with the LYP correlation functional, combined with 3 empirical parameters. These parameters were determined by optimising the results obtained with the G1 database of molecules.[96, 97] A contribution from the VWN correlation function is also included (with a coefficient of 0.19). Another hybrid functional of note is the PBE0 functional from Adamo in 1999 which does not include adjustable parameters; this functional takes the form shown in Equation 1.17:

$$E_{xc} = E_{xc}^{LSDA} + 0.25(E_x^{HF} - E_x^{LSDA}) + \Delta E_x^{PBE} + \Delta E_c^{PBE} \qquad \text{Equation 1.17}$$

where the correlation description has contributions from both the PBE and PW functionals described in Section 1.4.3.1. The value of the single parameter (0.25) was derived from work by Perdew in 1996 which showed that the parameter value of 0.25 taken from fourth-order perturbation theory (MP) leads to sufficiently accurate results.[98]

The B3LYP functional is popular and is often used in theoretical investigations, although investigations into its performance have revealed that it does not perform as well as other functionals for models involving transition metals.[99-101] However, good results are obtained when used for main group elements as recommended by the authors of Turbomole.[94]

1.4.3.4 Dispersion corrected functionals

The classes of DFT functionals described so far all suffer from the same failing; modelling long-range electron correlations such as dispersive effects or van der Waals forces.[102] This arises from the form of these functionals; long-range interactions of the London form $-C_6/R^6$ are needed (where C_6 represents a coefficient for a given atom and R is the distance), whereas the functionals result in the long-range interaction decreasing exponentially.[66] A significant piece of work by Grimme reported in 2006,[102] added an empirical dispersion correction to several functionals, with improved results obtained from the B-97D functional. Further corrections were reported in 2010 under the term GD3 and this work detailed corrections for many more functionals.[103] At the time of writing, the latest version of the Gaussian software (Gaussian 09 Rev D.01) has 19 functionals with the correction applied available with simple keywords.

1.4.3.5 Double hybrid functionals

An alternative method was also presented by Grimme in 2006, where the long-range correlation energy from second order Möller-Plesset perturbation theory (MP2) was also included.[104] The first functional of this type reported in the work was named B2PLYP; this family is referred to as double-hybrid functionals. A significant efficiency was determined with the calculation of the MP2 term; the Kohn-Sham orbitals and eigenvalues calculated in the GGA part of the functional are used for the MP2 calculation. This saving decreases the computational cost of the overall functional as new orbitals are not needed for the MP2 term. The double hybrid functionals adopt the general form for the exchange-correlation energy E_{xc} shown in Equation 1.18 (note, the correlation term E_c^{MP2} is referred to by Grimme as E_c^{PT}):

$$E_{xc} = (1-a)E_x^{GGA} + a_x E_x^{HF} + bE_c^{GGA} + cE_c^{MP2} \qquad \text{Equation 1.18}$$

where the cE_c^{MP2} term is calculated via:

$$E_c^{MP2} = \frac{1}{4}\sum_{ia}\sum_{jb}\frac{[(ia|jb) - (ib|ja)]^2}{\epsilon_i + \epsilon_j - \epsilon_a - \epsilon_b} \qquad \text{Equation 1.19}$$

with Equation 1.19 expressed in spin-orbital form and is the standard second-order Möller-Plesset correlation term. The difference to the standard term is that the Kohn-Sham orbitals

and corresponding eigenvalues ϵ are used, the indices ia and ib represent the single occupied-virtual replacements and the regular two-electron integrals over the KS orbitals are represented by the term in brackets. The work of Grimme assessed the performance of the B2PLYP functional with the G2 standard benchmark set and very good results were obtained.[104] The development of this type of functional is currently an active research area and several functionals exist, such as mPW2PLYP[105] and PBE0-DH from Adamo.[106]

1.4.3.6 Jacob's Ladder and DFT

The performance of the different classes of functionals was summarised by Perdew in 2001,[107] with the concept of a DFT functional "Jacob's Ladder". In this, the lowest accuracy is defined as the HF method, with the highest being a level of theory that describes chemical properties very accurately. A series of five rungs then represent the different classes of functional described previously. The ladder proposed by Adamo in 2012 is illustrated in Figure 1.10, with examples of each functional type included alongside.[108]

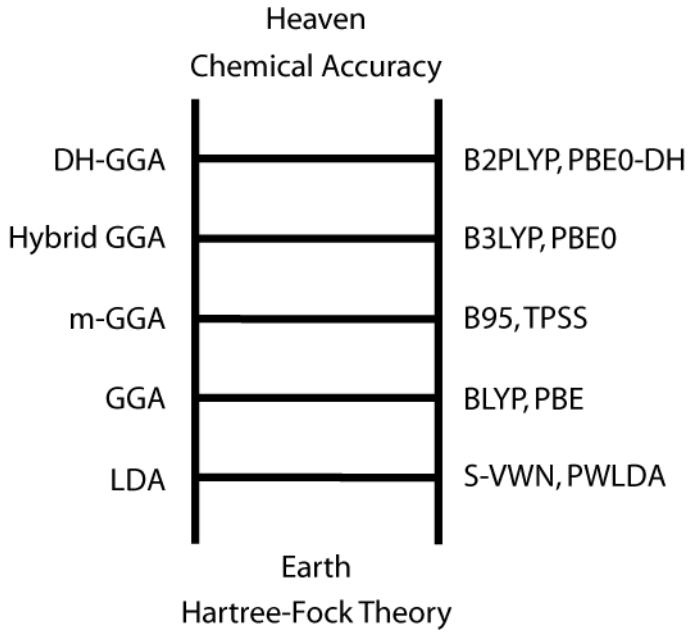

Figure 1.10: Jacob's Ladder for DFT functionals proposed by Adamo in 2012[108]

In its original concept, the final rung of the ladder involved the modelling of the nonlocal correlation to give accurate results. Recent work by Adamo has proposed that this rung has been achieved.[108] However, other researchers are not convinced, as stated by Becke in 2014[66] who pointed out that double hybrid functionals have formal scaling as an order higher than HF or traditional DFT functionals (when no approximations are used).

1.4.4 Basis sets

Two distinct types of basis sets are used to obtain the electron density used for the initial guess in the SCF procedure. These are the Slater-type orbital (STO), mentioned for Hartree-Fock theory and the more common Gaussian-type orbital (GTO). STOs, introduced in 1930 by Slater[109] are formed from functions which take the form shown in Equation 1.20:

$$S_\upsilon(r) = e^{-\zeta\upsilon|r|} = e^{-\zeta\upsilon\sqrt{x^2+y^2+z^2}} \qquad \text{Equation 1.20}$$

where r relates to a given point in space and ζ is the orbital exponent constant. However, these orbitals are computationally expensive and so a set of GTOs are generally used to approximate the STOs, which decreases the computational load. These orbitals are formed from functions which take the form shown in Equation 1.21:

$$g_\upsilon(r) = e^{-\zeta\upsilon r^2} = e^{-\zeta\upsilon(x^2+y^2+z^2)} \qquad \text{Equation 1.21}$$

However, multiple gaussian functions are required to obtain electron density profiles that match those from STOs. Even so, the computational efficiency advantage of calculations using multiple Gaussian functions is still greater than calculations with STOs. Many different basis sets exist, with different exponents used to change the profile of the function. Basis sets such as those from Dunning (e.g. cc-pVDZ)[110] were additionally optimised for use with the MP2 method, other basis sets were optimised for the HF method, such as the lanl2dz basis sets.[111] The basis sets from Ahlrichs denoted as the "def2" family are recommended for calculations in Turbomole.[94] These types of basis sets are available with or without polarisation functions for hydrogen; however, the computational cost saving by omitting the hydrogen polarisation functions is low, even with multiple atoms. These sets have been found to provide good results, especially for arsenic.[112] This "def2" family of basis sets is used extensively in this thesis; it is worth noting however that the all-electron basis set from this family for arsenic was used in this work, rather than the set which includes a pseudo core-potential. Additionally, the use of these basis sets was recommended by Truhlar for use with calculations with ruthenium.[101] No diffuse functions were included, due to the recommendation of the authors of Turbomole.[94]

1.4.5 Calculation of NMR parameters

The calculation of the nuclear magnetic shielding constant allows the chemical shift of nuclei to be obtained via the use of an appropriate shift reference. This calculation significantly aids the interpretation of NMR spectra. The first calculation of the magnetic shielding constant was undertaken by Ramsey in 1950[113, 114] who proposed a method using Perturbation theory. Additional methods were developed, such as those from Hirschfelder and Hornig,[115] Tillieu and Guy,[116] Das and Bersohn,[117] and McGarvey.[118] Recent methods rely on the use of DFT methods to calculate the chemical shielding values, with a good summary reported by Ziegler and Autschbach in 2005.[119] The chemical shielding constants can be calculated via the use of second-order properties of a system. The classical interaction for a nuclear magnetic moment (μ_N)) with an external magnetic field (B) can be described by Equation 1.22:

$$E = -\mu_N . B \qquad \text{Equation 1.22}$$

but the interaction of the field with the nuclei is also dependent upon the shielding of the nuclei by the electrons, and so the equation can be rewritten as Equation 1.23:

$$E = -\mu_N . (1 - \sigma) B \qquad \text{Equation 1.23}$$

where the term σ represents the shielding tensor for a nucleus *A* in a given environment. This shielding constant is derived from the mixed second derivative of the energy with respect to the external magnetic field (*B*) and the magnetic moment of nucleus N (μ_N) as shown in Equation 1.24:

$$\sigma_{ij}^{N} = \frac{\delta^2 E}{\delta B_i \delta \mu_{N_j}} \qquad \text{Equation 1.24}$$

where i is the component of the external magnetic field and j is the induced magnetic moment.[120] Once the shielding constant has been obtained, the chemical shift can be referenced via the use of a reference shielding constant. However, difficulties are encountered when calculating shielding constants due to gauge problems, where the dependence of the coordinate system's origin is important.

Two popular methods exist to account for this dependence; Gauge Including Atomic Orbitals (GIAO)[120] and Individual Gauge for Local Orbitals (IGLO).[121] The IGLO method is

not available in all computational software and is not always implemented alongside the methodology to calculate spin-spin coupling constants.[122]

The calculation of shielding constants for heavier nuclei such as transition metals is hindered by an additional factor. The use of effective core potentials (ECP) to account for the relativistic effects of the inner core electrons in these nuclei can lead to problems, as the electron density around the nuclei is critical for the calculation of the electron density and the subsequent shielding constant. However, there are very few basis sets for transition metals which do not use ECPs and so this problem can be difficult to avoid. Additionally, relativistic corrections such as the 0th Order Regular Approximation (ZORA) which account for relativistic effects[123] are not implemented in all computational packages.

Calculation of the spin-spin coupling constant J is more complex than that of the shielding constant due to the reliance on four separate terms. These are the Fermi Contact (FC), spin-dipolar (SD), paramagnetic spin-orbit (PSO) and diamagnetic spin-orbit (DSO) terms.[124] Work reported by Helgaker in 2000[125] allowed the use of hybrid-GGA functionals to calculate spin-spin coupling constants, with the equations which allow the calculation of J presented here. The magnetic moment μ_A relates to the nuclear spin I_A as shown in Equation 1.25:

$$\mu_A = \gamma_A \hbar I_A \qquad \text{Equation 1.25}$$

where the gyromagnetic ratio is defined by γ_A. The normal nuclear indirect spin-spin coupling constant J_{AB} is calculated by Equation 1.26:

$$J_{AB} = \frac{h}{4\pi^2} \cdot \gamma_A \gamma_B K_{AB} \qquad \text{Equation 1.26}$$

where K_{AB} is the reduced indirect nuclear spin-spin constant, and is calculated by Equation 1.27:

$$K_{AB} = \frac{\delta^2 E}{\delta_{\gamma_A} \delta_{\gamma_B}} \qquad \text{Equation 1.27}$$

and so the *J* coupling constant is proportional to the reduced coupling constant K and the gyromagnetic ratios γ. A significant dependence of the coupling constants on the basis sets and functionals used in the calculations results from this equation. Additionally, work carried out by Rablen *et al.* in 1999[126] recommends the use of at least double zeta basis

sets (such as the 6-31G*) and that the basis sets used should be all-electron sets. Specific basis set families exist for the use of NMR parameter calculations, such as the IGLO-II and IGLO-III families.[127] However, these families are only available for several nuclei in rows 1-3 of the periodic table and so are of not applicable for transition metal chemistry calculations. Gaussian offers an improved method for the calculation of the spin-spin coupling values for various nuclei via the use of the *mixed* keyword. With this keyword, the specified basis set is uncontracted and tight polarisation functions are added to allow accurate calculation of the FC term. The second part of the calculation is then performed using unmodified basis sets specified to allow the calculation of the remaining three terms (SD, PSO and DSO); however this option utilises basis sets developed for the first two rows only and so cannot be used for calculations involving transition metals[124]

1.4.6 Solvation

Typically the default behaviour of quantum mechanical packages is to model the geometry given as an input in the gas phase, usually at 0 K in a vacuum. However, reactions of chemical systems are commonly carried out in solution, where the solvent can have a dramatic effect such as stabilising intermediates, changing the electronic excited states of molecules (and changing UV-Visible spectra). However, the use of explicit models where a solvent cavity surrounds the molecule can be computationally very expensive. This is especially important for solvents such as water where several "shells" of solvent molecules would be required to account for the hydrogen bonding of the solvent. In contrast, the use of implicit solvation to account for solvation effects is computationally feasible, where the solvent is approximated to a polarisable continuum with a dielectric constant ϵ. One of the first polarisable continuum models was reported in 1981 and this model has been found to model solvation effects well and has formed the basis of additional models.[128] A summary of continuum models was reported by Mennucci in 2012,[129] selected parts which illustrate general solvation models are reproduced here. The solution to a classical electrostatic problem (the Poisson problem) forms the basis of the continuum models, illustrated in Equation 1.28:

$$-\nabla[\varepsilon(r)\nabla V(r)] = 4\pi\rho_M(r) \qquad \text{Equation 1.28}$$

where $\rho_M(r)$ is the solute charge distribution, $\nabla V(r)$ is the voltage potential function and $\varepsilon(r)$ is the general position-dependent permittivity. The assumption that the charge

distribution $\rho_M(r)$ is contained within a molecular cavity C of proper shape and dimension, built within a homogeneous and isotropic solvent, allows $\varepsilon(r)$ to take the simple form shown in Equation 1.29:

$$\varepsilon(r) = \begin{cases} 1 \; r \epsilon C \\ \varepsilon \; r \epsilon C' \end{cases} \qquad \text{Equation 1.29}$$

where ε is the dielectric constant of the solvent. The use of appropriate boundary conditions with Equation 1.29 allows Equation 1.28 to be solved in terms of a potential *V*. This term is the sum of the solute potential along with the contribution due to a fictitious charge distribution $\sigma(s)$ on the boundary between the solvent and the solute, as shown in Equation 1.30 and Equation 1.31:

$$V(r) = V_M(r) + V_\sigma(r) \qquad \text{Equation 1.30}$$

$$V_\sigma(r) = \int_\Gamma \frac{\sigma(s)}{|r-s|} d^2 s \qquad \text{Equation 1.31}$$

Once $\sigma(s)$ is known, the whole problem is solved and the electrostatic component of the solvation free energy is described by Equation 1.32:

$$G^{el} = \frac{1}{2} \int_\Gamma \sigma(s) \left[\int_\Gamma \frac{\rho_M(r)}{|r-s|} d^3 r \right] d^2 s \qquad \text{Equation 1.32}$$

Within the PCM framework, different formulations for $\sigma(s)$ have been developed over the years, such as the CPCM model[130, 131] and the IEFPCM model.[132] An alternative method to the PCM method was introduced by Klamt and Schürmann in 1993[133] entitled the COnductor like Screening MOdel (COSMO). In this method, the dielectric constant of the medium is changed from the specific finite value ϵ (which varies with each solvent), to $\epsilon = \infty$. This value means that the medium is a conductor, with this alteration strongly modifying the boundary conditions of the electrostatic issue, the most significant effect of which is to cancel out the *V (r)* term in Equation 1.30. To account for the fact that the dielectric constant is finite, the unscreened density operator σ^* is scaled by a proper function of ϵ, as shown in Equation 1.33:

$$\sigma(s) = f(\epsilon)\sigma^*(s) \qquad \text{Equation 1.33}$$

where the scaling function $f(\epsilon)$ has been empirically determined. The availability of the different solvation models varies across different quantum calculation packages available

for this work. The Gaussian package allows calculations with the PCM model and variants,[122] whereas only the COSMO model is available in Turbomole[94] and ORCA.[134-137]

1.4.7 Computational cost considerations

A significant problem faced by computational chemists relates to the computational cost of methods, functionals and basis sets. The larger basis sets provide more complete representation of the atomic orbitals for the nuclei being modelled, but the computational time required increases with the number of basis functions and nuclei. As the scaling for DFT methods with the size of the model behaves as N^4, for significantly large systems triple-zeta basis sets are not viable. The increase from rung 1 to 5 on Jacob's Ladder also increases computational cost due to the additional terms which are present, for example the calculation of the HF energy in hybrid-GGA functionals. More accurate methods such as MP2 theory give better results than typical DFT calculations, but the computational cost scales more significantly than DFT, as N^5 is common. This means that the use of such methods for real systems is not feasible.

Several approximations exist to reduce the computational cost of various methods. One common approach is the Resolution-of-Identity (RI), which can provide speed increases of 10-fold in Turbomole.[138] This is achieved by the use of an approximation for the Coulomb interaction (RI-J), where the third term in Equation 1.7 (shown here in Equation 1.34):

$$\frac{1}{2}\int\int\frac{\rho(r_1)\rho(r_2)}{r_{12}}dr_1dr_2 \qquad \text{Equation 1.34}$$

is changed for the more efficient expression as in Equation 1.35:

$$\rho(r) \approx \sum_{\alpha} C_\alpha \alpha(r) = \tilde{\rho}(r) \qquad \text{Equation 1.35}$$

where α describes an atom-centred auxiliary basis set. This substitution allows the evaluation of four centre two-electron integrals to be avoided[139] and is equivalent to two-electron integral approximations.[140] The ORCA program has an additional approximation in addition to the RI approximation, called the Chain of Spheres approximation (COSX).[141] In this approximation, the calculation of the two electron integrals is done first by integration numerically on a grid and secondly done analytically (involving the Coulomb singularity).

This approximation can be combined with the RI approximation to give the RIJCOSX approximation which allows shorter running times of 60-fold.

1.5 Mechanistic investigations with *para*-hydrogen and DFT in tandem

Few examples of investigations combine the power of *para*-hydrogen along with DFT calculations.[46, 142-145] The two methods are complementary, as spectra obtained with the use of *para*-hydrogen can allow intermediates to be detected which would otherwise be invisible. Additionally, the end location of a nucleus from *para*-hydrogen can sometimes be determined providing significant insight that can lead DFT investigations, which enhance experimental understanding. An example of this is illustrated here, with figures taken from the work by Duckett *et al.* in 2008.[144] In this study, the hydrogenation of alkynes by a palladium-biphosphine catalyst of the type $Pd(P_2)(OTf)_2$ (where P_2 represents $2PEt_3$ or the bidentate ligands $(C_8H_{14})PCH_2CH_2P(C_8H_{14})$ and $(C_8H_{14})PC_6H_4CH_2P(^tBu)_2$) was investigated. The hydrogenation of diphenylacetylene was found to lead to the formation of *cis*-stilbene; this was determined by the signals that arise from the hydrogenation product of mono-^{13}C diphenylacetylene. These signals are illustrated as the trace in Figure 1.11.

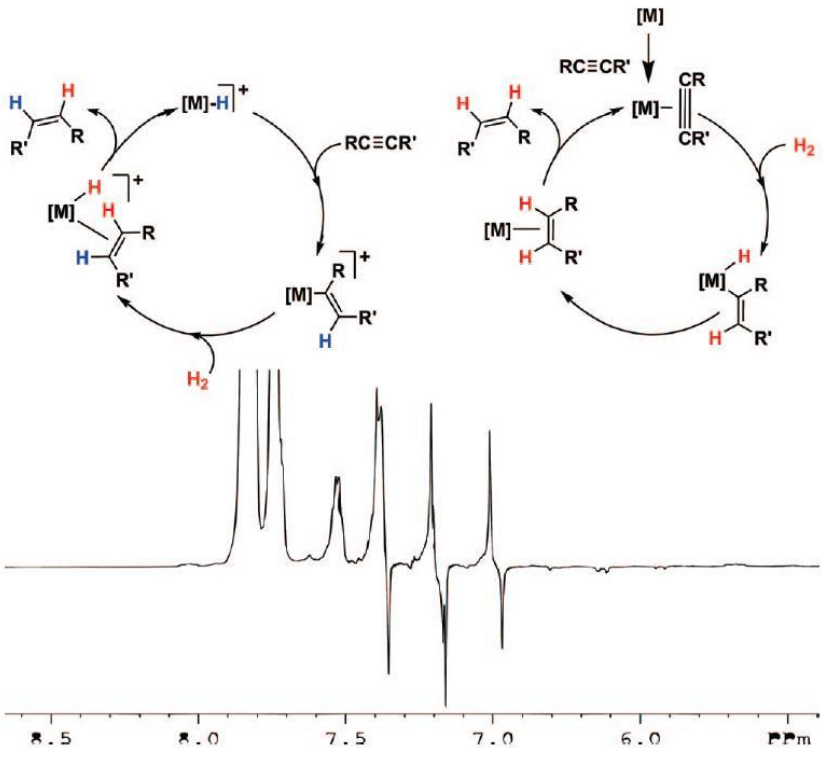

Figure 1.11: Experimentally proposed catalytic cycles for the cationic cycle (left) and neutral cycle (right); the trace underneath is from the experimental spectra

From the associated investigations, two catalytic cycles were proposed; one involving neutral species and the other involving cationic species. In Figure 1.11 the colour red was used to indicate nuclei of hydrogen which originated from *para*-hydrogen, assigned from signals arising from the PHIP mechanism. A detailed DFT investigation then allowed the mapping of these two cycles to be undertaken which allowed the evaluation of the double hydrogenation product of diphenylethane.

In the neutral cycle, the palladium catalyst starts as the complex Pd(alkyne)$(PR_3)_2$ which reacts by the loss of a phosphine ligand. The coordination of *para*-hydrogen to the vacant site can then occur, followed by the first hydride transfer reaction. The second transfer reaction can then take place resulting in the alkene, with the complex then able to coordinate another phosphine ligand to form Pd(η^2-alkene)$(PR_3)_2$. However, a phosphine ligand can coordinate before the second hydride transfer reaction. The second hydride transfer reaction can then occur to form the same complex via the former route. The loss of the newly formed alkene can then occur and is replaced by a new alkyne molecule, which reforms the starting complex. This cycle is illustrated in Figure 1.12.

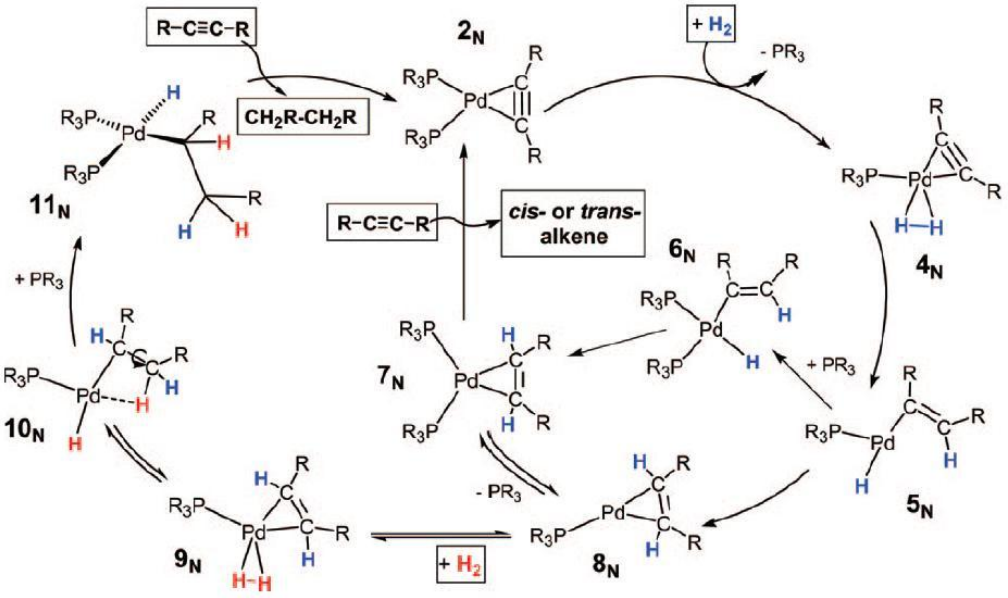

Figure 1.12: Neutral cycle for the hydrogenation of the alkyne by Pd$(P_2)(OTf)_2$. The alkyne considered was acetylene and the phosphines either $2PH_3$ or $PH_2CH_2CH_2PH_2$

The cationic cycle is illustrated in Figure 1.13. This cycle is subtly different to that of the neutral cycle, as the starting complex is $[Pd(H)(alkyne)(PR_3)_2]^+$ which already contains a hydride ligand. The first hydride transfer reaction can then occur, which creates a vacant site for the coordination of *para*-hydrogen. The second hydride transfer reaction forms the alkene complex $[Pd(H)(\eta^2\text{-alkene})(PR_3)_2]^+$. This complex can then undergo the loss of the alkene and coordinate a new alkyne ligand to reform the starting complex. Another difference with this cationic cycle compared to that of the neutral cycle is that the second hydride transfer reaction is the only step that can occur after the first hydride transfer reaction; this is due to the complex being coordinatively saturated.

The dominant catalytic cycle was revealed by the computed reaction thermodynamics. The barrier resulting from the transition state in the first hydride transfer reaction in the neutral cycle was found to be significant, having a barrier height of 135.7 kJ mol^{-1}. In contrast, the cationic mechanism was computed to have a barrier for the same reaction of just 48.5 kJ mol^{-1}. This was found to be more consistent with the experimental evidence, as the solvent adducts of complexes where only the first hydride transfer reaction had occurred were detected. These thermodynamics are fully illustrated in Figure 1.14.

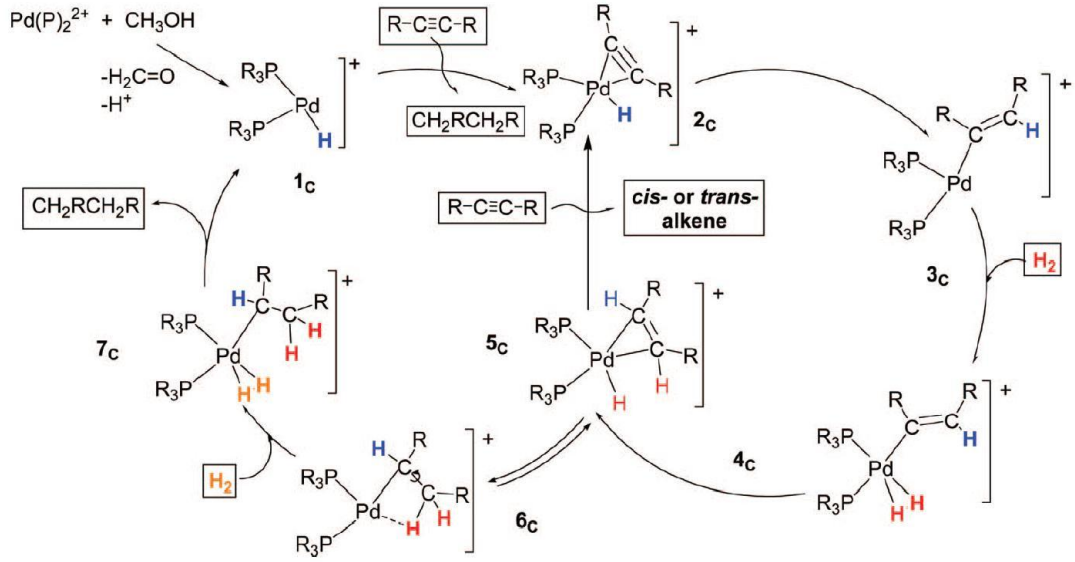

Figure 1.13: Cationic cycle for the hydrogenation of the alkyne by $Pd(P_2)(OTf)_2$. The alkyne considered was acetylene and the phosphines either $2PH_3$ or $PH_2CH_2CH_2PH_2$

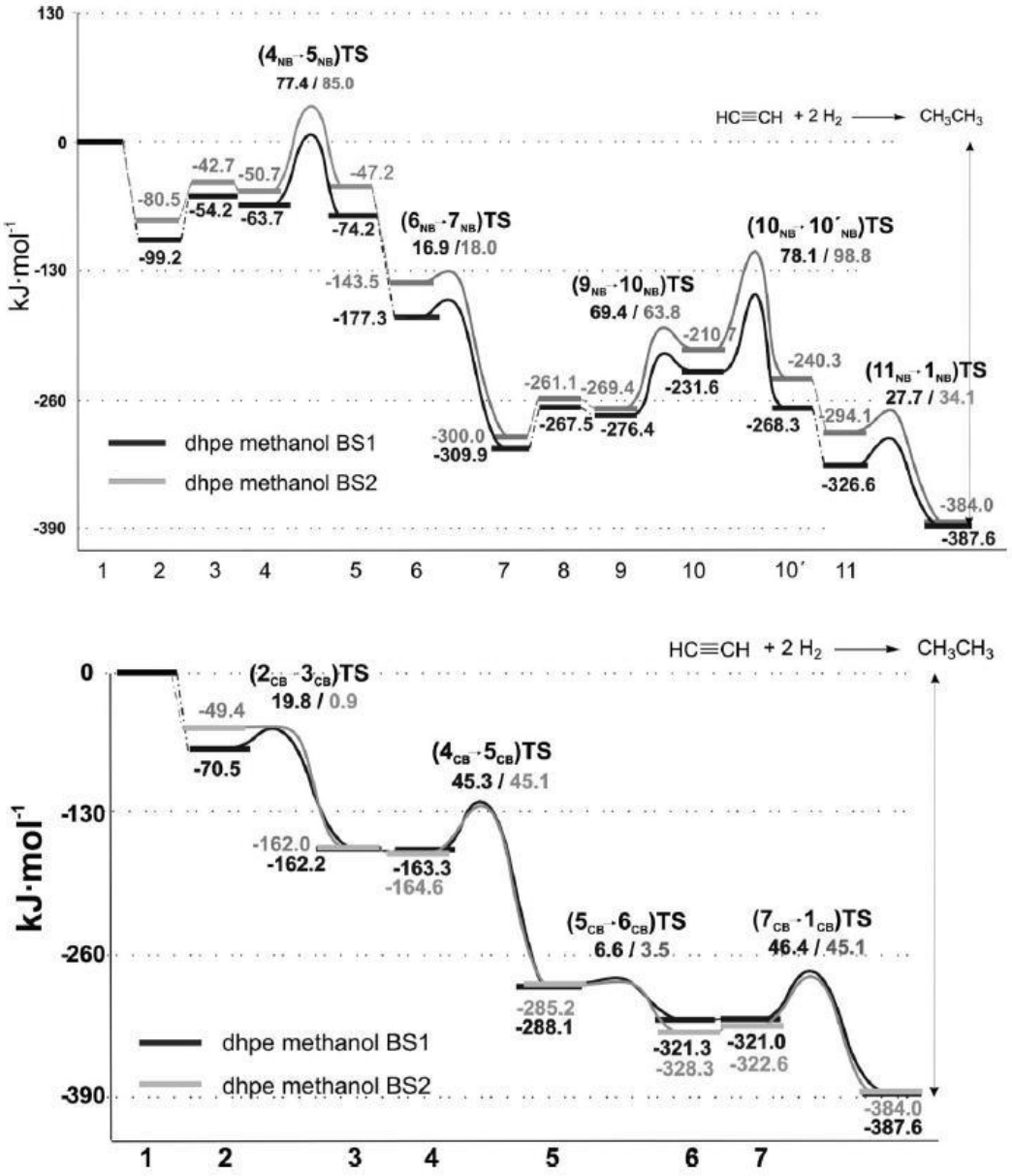

Figure 1.14: Potential energy profiles for the neutral cycle (top) and cationic cycle (bottom)

In this thesis, high level DFT calculations are described to account for experimental observations. Multiple reaction pathways are considered, together with the conversion of distinct isomeric complexes involving reaction intermediates and/or coordinatively saturated complexes.

Chapter 2: Ruthenium-Arsenic complexes and *para*-hydrogen

2.1 Introduction to phosphine-ruthenium complexes

Since the discovery by Wilkinson and co-workers in 1965 that $Ru(CO)_3(PPh_3)_2$ catalyses the hydroformylation of alkenes,[146, 147] ruthenium catalysis has been an active area of research. Studies have been conducted into the scope[148] and mechanism[149] of catalysis. The increase in the use of computational chemistry has aided such investigations, whilst the use of *p*-H_2 has also allowed detailed mechanistic information to be gained.[14] Studies by Perutz and Eisenstein in 1998[150] identified that the addition of CO or the oxidative addition of H_2 to $[M(dmpe)_2]$ (M = Fe or Ru, dmpe = dimethylphosphinoethane) both proceed with zero activation energy and are diffusion controlled. It was also found that the approach of the incoming H_2 molecule was via an end-on geometry, until a 'swing' occurred near the metal centre (at around 1.7 Å for ruthenium); the molecule then approached in a side-on η^2-geometry. Later studies by Harvey *et al.* focused on the electronic structure of the related iron d^8 intermediate.[151, 152] The identification of a triplet state for $Fe(L)_4$ in theoretical calculations agreed with experimental results. The extension of that work to include the ruthenium system in 2004 revealed that the electronic singlet state based $Ru(L)_4$ intermediate was more stable than its triplet counterpart. This finding supported the observation of polarisation from *p*-H_2 in the resulting product $[M(H)_2(CO)_2(dppe)]$ when M is Ru but not Fe.[46] The lack of PHIP with the iron system was attributed to the reaction of *p*-H_2 with the triplet state, which quenched the associated nuclear polarisation.

2.1.1 Investigations with *para*-hydrogen

Previous studies have looked at the reactions of *p*-H_2 with various ruthenium-based complexes and phosphines.[153, 154] The work of Dunne *et al.* investigated the product isomers formed from $Ru(CO)_3(L)_2$ and *p*-H_2 upon *in-situ laser* photolysis at 325 nm and found that two competing processes occurred; the first involved the loss of CO to create the *cis-cis-trans*-L isomer of $Ru(CO)_2(L)_2(H)_2$, whereas the second involved the loss of L and

CO.[142] In the case of *cct*-L $Ru(CO)_2(L)_2(H)_2$, the nomenclature *cis-cis-trans*-L was introduced to define the geometries of the different isomers; *trans*-L defines that the L ligands are *trans* position relative to themselves, with the remaining two types of ligands arranged as mutually *cis*. The simultaneous loss of CO and L following one photon excitation, leads to the formation of *cis-cis-cis*-$Ru(CO)_2(L)_2(H)_2$, *fac*-$Ru(H)_2(CO)_3(L)$ and $Ru(H)_2(CO)_2(L)$(solvent). Figure 2.1 shows the mechanisms associated with these results.

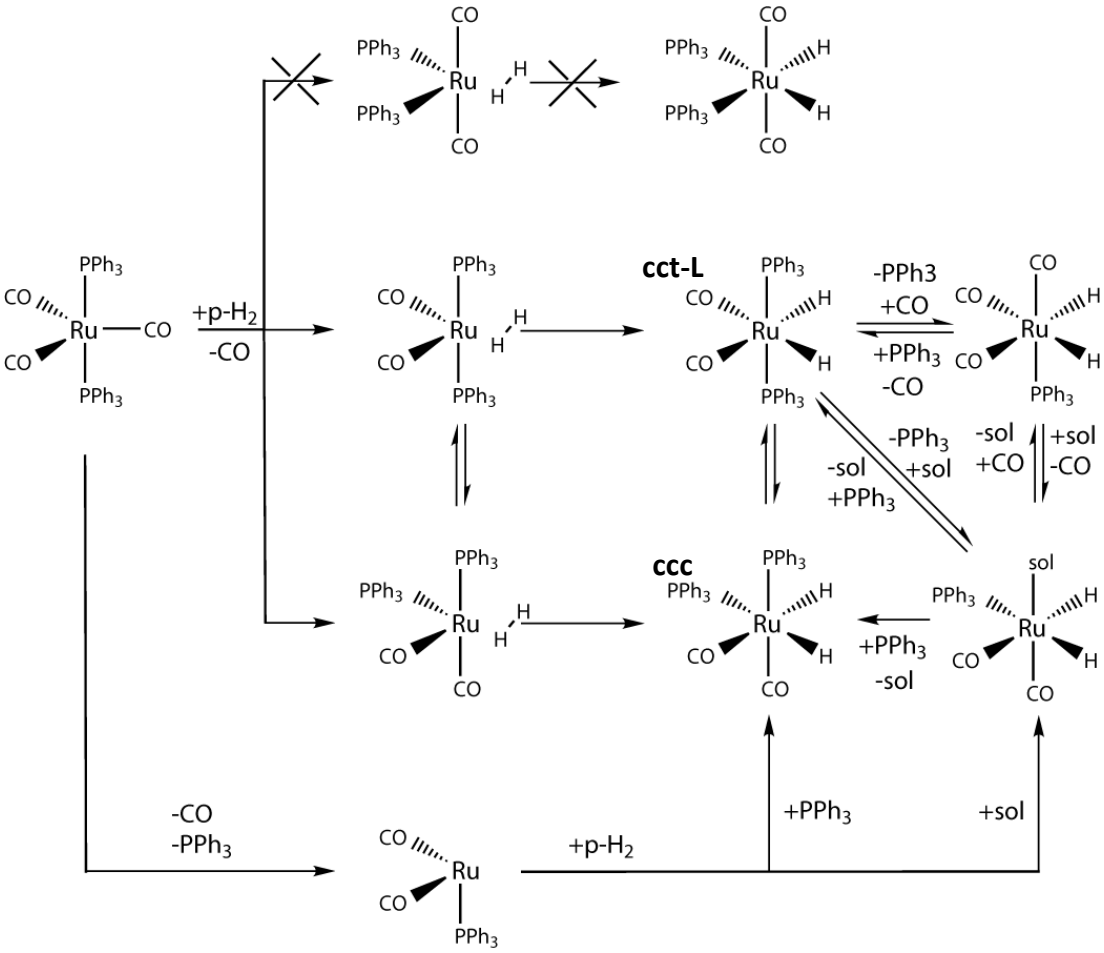

Figure 2.1: Proposed mechanism for the formation of the detected photoproducts from the reaction of $Ru(CO)_3(PPh_3)_2$ with *p*-H_2

When pyridine was utilised as the solvent, a complex was also detected where both phosphines had been replaced by pyridine. This complex was assigned to $Ru(H)_2(CO)_2(pyridine)_2$, where one hydride was *trans* to CO and the other *trans* to pyridine.

This complex was only observed under thermal initiation and not under photochemical initiation. The introduction of a bidentate phosphine changed the detected product isomer.

The ligand 1,2-bis(diphenylphosphino)ethane (dppe) prefers to occupy a *cis* configuration, with the ligand occupying one axial and one equatorial site on a metal centre where these positions are at 90° to each other. This coordination requirement means that the *cct*-L isomer is not accessible and so the *ccc* isomer dominates. Additionally, the propensity for de-chelation of one end of this ligand by phosphine dissociation is also reduced due to the chelate effect. This process was however shown to occur when a sample of $Ru(CO)_3(dppe)$ (**P1**) was photolysed in the presence of H_2 in toluene-d_8. The loss of CO was followed by the formation of the *ccc* isomer of the dihydride $Ru(H)_2(CO)_2(dppe)$ (**P2**). Photolysis of the sample in pyridine-d_5 allowed the detection of two more products at 1% of the **P2** isomer level; one where the bidentate phosphine had become de-chelated as $Ru(H)_2(CO)_2(\eta^1$-dppe)(pyridine) (**P2a**) and one where two CO ligands had been lost, $Ru(H)_2(CO)$(dppe) pyridine) (**P2c**). These structures are illustrated in Figure 2.2.

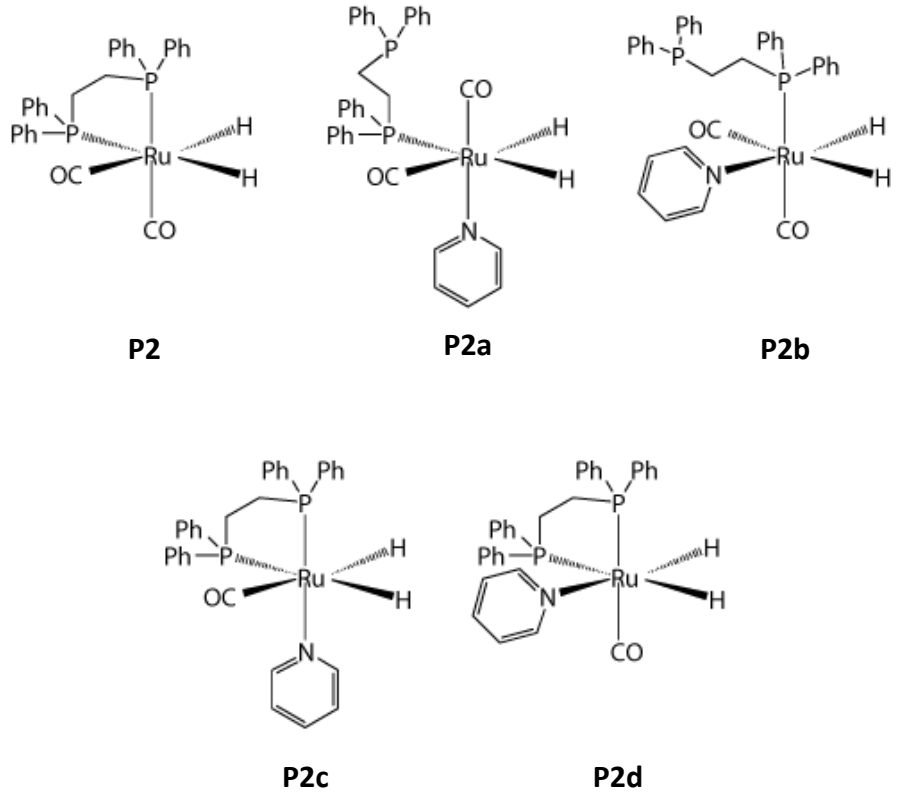

Figure 2.2: Complexes detected in the reaction of *p*-H_2 with $Ru(CO)_3(dppe)$ (**P1**), under photolysis in pyridine solvent

The same species were observed when a pyridine-d_5 containing solution of **P1** was heated to 315 K without photolysis. However, the ratio of the species with thermal initiation was 1:1:1 (assuming identical extents of polarisation). When the temperature was raised to 335

K, the most intense proton NMR signal was from **P2a** and low levels of a new species were observed. This species was also observed with PPh_3 and assigned as $Ru(H)_2(CO)_2(pyridine)_2$. These observations led to the conclusion that de-chelation and total ligand loss was possible at elevated temperatures. Further signals were also observed for **P2b** and **P2d**, isomeric forms of **P2a** and **P2c** respectively. However, the low intensity of these signals, at 3% of those of **P2a**, precluded further characterisation.

This work revealed that any catalytic behaviour of complex **P1** would depend upon the method of activation, and that if thermal activation was used, the creation of a vacant site could occur via more than one route. When the catalytic hydrogenation of diphenylacetylene was investigated, polarised resonances for *cis*-stilbene were seen. This allowed the catalytic activity of the precursors to be ordered as PPh_3 > $P(p\text{-tolyl})_3$ > PMe_3 > PCy_3 > dppe and parallels the ease of phosphine loss. A similar trend was also suggested by Kim who studied the catalytic cycle of aldehyde hydrogenation using $Ru(H)_2(CO)(AsPh_3)_3$ and $Ru(H)_2(CO)(AsPh_3)(L–L)$ (where L-L = 1,2-Bis(diphenylphosphino)ethane (dppe), 1-diphenylphosphino-2-diphenylarsinoethane (arphos) or 1,2-Bis(diphenylarsino)ethane (dpae)).[155] Theoretical work was undertaken to rationalise the observations of isomer stability and it was confirmed that the *ccc*-isomer was less stable than the *cct*-isomer.[142] When the phosphines modelled were PH_3, the experimentally inaccessible *ccc* isomer was predicted to be 12.7 kJ mol^{-1} more stable than the *cct* isomer. In contrast, for PMe_3, the *cct* isomer is favoured by 19.6 kJ mol^{-1} whilst for $AsMe_3$ the difference was only 9.4 kJ mol^{-1}. The 16-electron precursors of the form $Ru(CO)_2(L)_2$ were also found to follow a similar trend, with PH_3 resulting in a difference in energy between the complex with *trans* phosphines and the complex with *trans* CO ligands of +10.0 kJ mol^{-1}, PF_3 resulting in a difference of -1.2 kJ mol^{-1} and $AsMe_3$ resulting in a difference of +21.1 kJ mol^{-1}. This difference in stability for PF_3 was assigned to its highly π-acidic nature and the investigations revealed that the strongest π-acceptor prefers an equatorial position. It should be noted that for the bidentate dppe ligand, the *cct*-L isomer of $Ru(H)_2(CO)_2(dppe)$ is not accessible and was not modelled theoretically.

In addition to the theoretical work, it was proposed that to account for the solvent effects, these reactions are assisted by solvent participation in the breakage of the Ru-PPh_3 bonds. This participation is illustrated for the hydrogenation of diphenylacetylene in Figure 2.3.

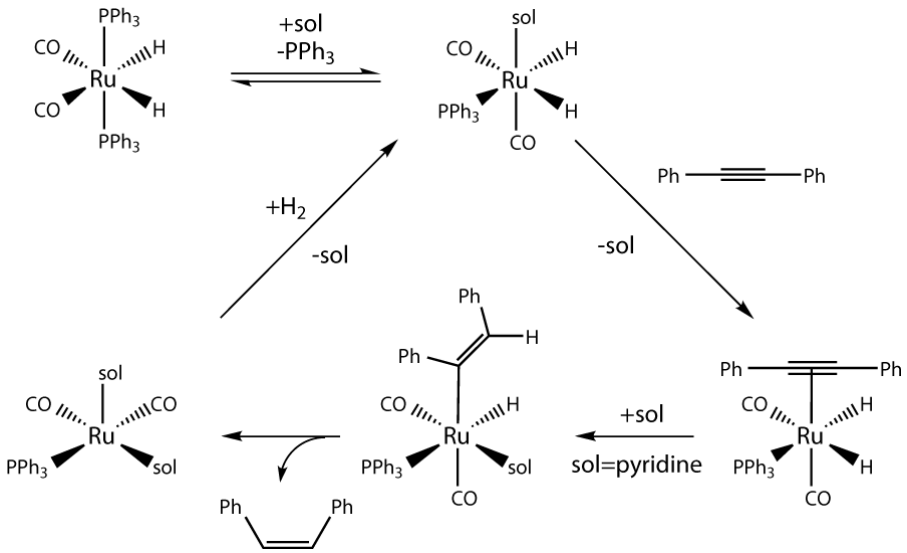

Figure 2.3: Catalytic cycle proposed for the hydrogenation of diphenylacetylene by *cct*-$Ru(H)_2(CO)(PPh_3)_2$ in pyridine

A more recent study into the reaction of *p*-H_2 with the related ruthenium complex $Ru(CO)_2(dppe)(PPh_3)$ (**P3**) combined detailed experimental investigations with higher level theoretical calculations.[143] As this complex is known to adopt a trigonal bipyramidal (TBP) structure, the steric demands imposed by the bidentate ligand means it has to occupy axial and equatorial sites, thus allowing a 90° bite angle. If the ligand occupied two equatorial sites, an unfavourable 120° bite angle would result. However, the monodendate triphenylphosphine ligand could occupy either an axial site or an equatorial site. Experimental analysis yielded NMR and IR data that indicated the presence of both isomers in solution. DFT calculations (detailed further later on) located two local minima for the complex and it was found that the isomer with the phosphine in an equatorial position was marginally favoured by 1.5 kJ mol^{-1}.

The reactivity of **P3** towards *p*-H_2 was studied by thermal and photochemical methods. Thermal reaction yielded the dihydride **P2** previously described and its formation was unaffected by the presence of 2 atm. of CO. However, the addition of a ten-fold excess of PPh_3 quenched the signals from the hydrides in the ^1H NMR experiment. It was concluded that initial PPh_3 loss allowed reaction with *p*-H_2 to occur. When photochemical methods were employed (*in-situ* via a laser operating at 325 nm), the same dihydride (**P2**) was seen in the proton NMR experiments, along with another dihydride which gave signals of a

similar intensity. This latter dihydride was identified as Ru(CO) $(H)_2$(dppe)(PPh_3) (**P4a**), a complex which has previously been reported.[156, 157] Further products were identified using *in-situ* photolysis and included a complex where the bidentate ligand was found to de-chelate. These products are illustrated in Figure 2.4.

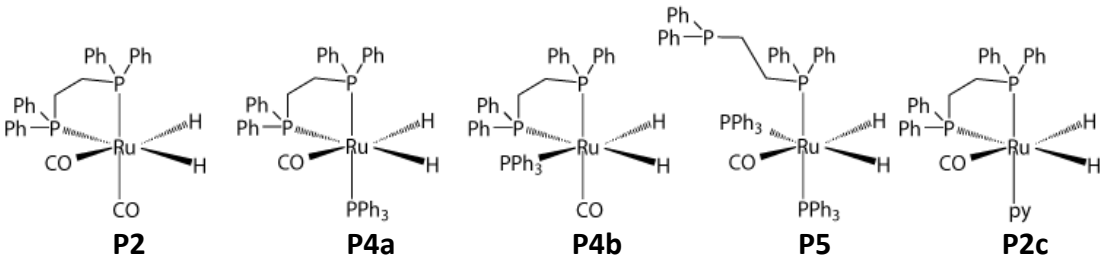

Figure 2.4: Complexes detected under *in-situ* photolysis of $Ru(H)_2(CO)_2$(dppe)(PPh_3) in the presence of *p*-H_2

The background work discussed so far provides evidence for the possible existence of a 14-electron intermediate when photolysis is used in the reaction of **P3** and similar complexes with *p*-H_2. This was illustrated by the detection of complex **P2c**, which can only be formed by PPh_3 and CO loss from **P3**. The 14-electron intermediate will be unlikely to be involved in thermal reactions as its formation is highly unfavourable and is only likely to be formed via photochemical initiation. Additional work also indicated that a common intermediate is likely to be involved in the single ligand and double ligand loss pathway.[143]

High level DFT calculations were undertaken by McGrady *et al.*[143] using a modified form of the hybrid functional B3PW91[84, 91] (B3PW91*) along with a mixture of double and triple-zeta basis sets on the model complexes where all phenyl rings had been replaced by hydrogens. These calculations investigated the thermodynamics of ligand loss (PH_3 or CO) from Ru$(CO)_2$(dhpe)(PH_3). For PH_3 loss, two local minima were identified; one where the bidentate ligand and both carbonyl ligands are *cis* to one another in a distorted square-planar geometry (one CO-Ru-dhpe bond angle was approximately linear and the other was significantly bent) and the other where dhpe was *cis* and the two carbonyls were *trans* in a highly distorted tetrahedral like geometry. The former geometry was found to be significantly more stable and would be formed after phosphine loss as the dominant intermediate. For the loss of a carbonyl ligand three local minima were found; two with similar energies and geometries to the distorted square-planar intermediate (one geometry

with the PH_3-Ru-dhpe bond angle as approximately linear, the other with the bond angle significantly bent) and one similar to the highly distorted tetrahedral geometry. Again, the distorted tetrahedral geometry was the highest in energy and so reaction would be likely to proceed through the two lower geometries. The lower intermediate geometry would lead to **P4a** and the other would lead to **P4b**, both consistent with experimental observations. Hydride interchange was also observed for the dihydride **P2** and was investigated with EXSY measurements, in a similar way to that previously reported.[153, 154, 158] The experimental enthalpy of activation was calculated from the resulting Eyring plot to be $\Delta H^{\ddagger} = 85.5 \pm 2$ kJ mol^{-1}, in close agreement with the DFT calculated values of 78.6 and 82.0 kJ mol^{-1}. The mechanism for interchange was consistent with pseudorotation where the dihydrides formed a η^2-dihydrogen unit which could then rotate in a clockwise or anticlockwise direction, relative to the other ligands.[46, 154]

Various studies have been conducted on similar compounds, with a high level investigation undertaken on the related complex $Ru(H)_2(CO)_2(PMe_3)_2$.[159] The presence of an isomer where the phosphine ligands could be *trans* to each other also limits the relevance of this work for the present study. A previous investigation[46] on $Ru(H)_2(CO)_2$(dppe) found two pathways involving the trigonal twist[160] and pseudo-rotation mechanisms.[161] An older study on $Ru(PH_3)_4$ and $Fe(CO)_4$ outlined six different possible mechanism types and sixteen possible transition states.[162] However, only six transition states were found for the ruthenium complex and five states for the iron complex. The work of Albright *et al.* in 2001 provides a useful summary of key possible exchange processes.[162] The six types proposed are:

1. Trigonal Twist Mechanism
2. Tetrahedral jump mechanism
3. Ray-Dutt mechanism
4. Bicapped tetrahedral mechanism
5. A variant of the Ray-Dutt mechanism involving a square-based pyramid (SBP) geometry with rotation of an η^2-dihydrogen unit (also known as Berry pseudo-rotation)
6. A second variant of the Ray-Dutt mechanism involving a trigonal bipyramidal (TBP) geometry an η^2-dihydrogen unit

Ruthenium dihydride complexes are known to undergo hydride site interchange via trigonal twist and η^2-H_2/SBP mechanisms. However, Albright's computational studies found that the Ray-Dutt mechanism and the η^2-H_2/TBP were also possible.

2.2 Reactions of analogous arsenic-ligand containing ruthenium complexes to with *para*-hydrogen

2.2.1 Previous experimental findings

The reactions of the analogous arsenic complexes $Ru(CO)_3$(dpae) (**A1**) and $Ru(CO)_2$(dpae)(PPh_3) (**A2**) with *p*-H_2 to **P1** and **P3** were studied experimentally by Adams and Eguillor *et al*. Both thermal and *in-situ* photochemical initiation techniques were used, and differences were observed between the reactivity of complexes **A1** and **A2**. These investigations were undertaken prior to the start of the work reported herein. Some of these early observations are recounted herein, with additional information included where appropriate before starting to address how this DFT investigation links to the experimental observations.

Compound **A1** proved to react thermally to form a single dihydride product $Ru(H)_2(CO)_2$(dpae) (**A3**) when heated to 308 K in a solution of C_6D_6 under a head-space of *p*-H_2. As a consequence, anti-phase doublets were observed at -7.21 ppm and -7.61 ppm that exhibited a coupling of J_{HH} = -5 Hz, where the signal at -7.21 ppm arose from a hydride ligand *trans* to As and the signal at -7.61 ppm from a hydride ligand *trans* to CO. No signals other than those for **A3** were seen with heating to 348 K. The addition of CO to the reaction mixture was found to reduce the hydride ligand signal intensities of **A3** thereby indicating it is formed from **A1** by loss of CO rather than by unhooking the bidentate dpae ligand. *In-situ* photolysis of **A1** led to the same dihydride (**A3**) but this reaction was possible at 263 K.

Compound **A2** reacted differently to **A1** in both its thermal and photochemical reactions. With thermal initiation, the dominant product is **A3** but additional signals were observed. These were attributed to be $Ru(H)_2(CO)_2(PPh_3)$(sol) (**A4**), *cis-cis*-$Ru(H)_2(CO)_2(\kappa^1$-dpae)(PPh_3) (**A5**) and $Ru(H)_2(CO)(\kappa^1$-dpae)$_2(PPh_3)$ (**A6**). The addition of PPh_3 prior to H_2 was shown to allow the detection of $Ru(H)_2(CO)_2(PPh_3)_2$ in addition to **A3** whilst suppressing the formation

of **A4**, **A5** and **A6**. This finding showed a de-chelation mechanism and total displacement of dpae were possible.

The lack of useful coupling from the arsenic centres in dpae or from the CO ligands into the hydride ligands in these products limits the structural information that is available in these NMR spectra. This lack of detail means that these data can be interpreted in more than one way, and lead to incorrect assignments as illustrated by work on related ruthenium clusters.[163] This contrasts that of the earlier work, where the coupling of the hydride ligands to phosphorus centres allowed detailed structural information to be gleaned.

The photochemical reaction of complex **A2** led to the detection of two further dihydride complexes; both with a proposed of structure $Ru(H)_2(CO)(dpae)(PPh_3)$. One dihydride complex was determined to contain a hydride ligand that was *trans* to CO and the other *trans* to As (**A7a**), while the other complex has one hydride ligand *trans* to As and the other *trans* to PPh_3 (**A7b**). All of these proposed products are shown in Figure 2.5, alongside their designating number.

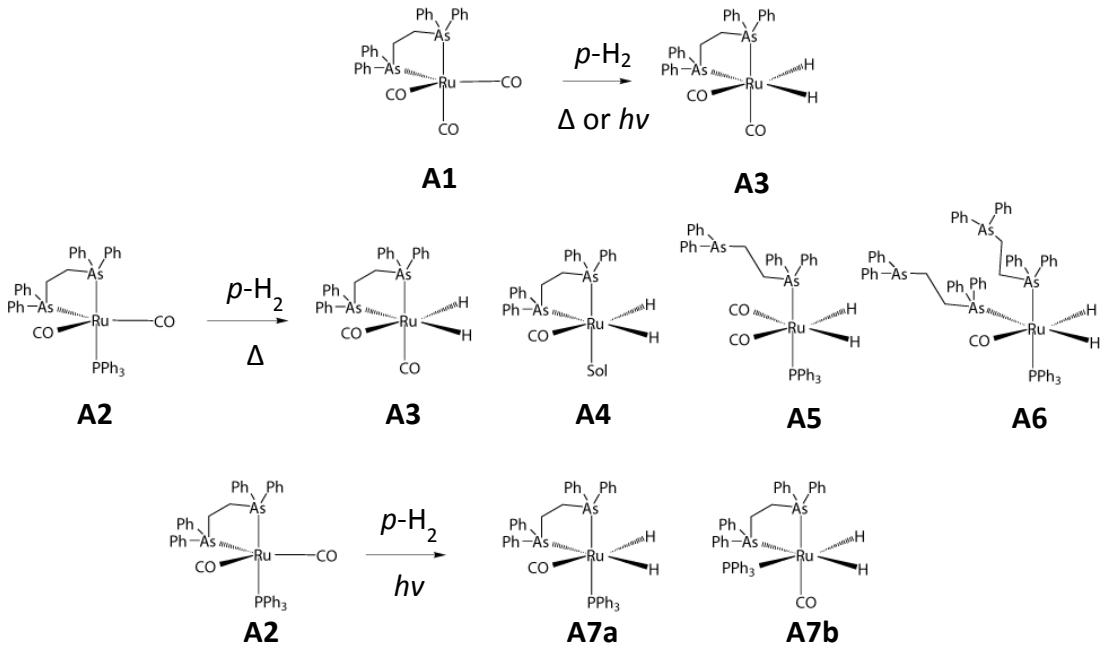

Figure 2.5: Proposed complexes from the reaction of **A1** or **A2** with *p*-H_2

2.3 Theoretical modelling of the reactions of arsenic containing ruthenium complexes with *p*-H_2

The following sections describe how DFT has been used to rationalise the reactions of **A1** and **A2**. The model systems $Ru(CO)_3$(dhae) (**1**) and $Ru(CO)_2$(dhae)(PH_3) (**2**) (where dhae is defined as 1,2-bis(dihydridoarsino)ethane) were used to model the reactions of **A1** and **A2**. Additional calculations were also performed with the full ligand system, with the inclusion of phenyl rings on the bidentate ligand and the phosphine ligand. This was undertaken to allow the efficient mapping of possible reactions, with the subsequent higher level studies then being introduced.

2.3.1 Computational Details

Phenyl substituents on the arsine and phosphine ligands were replaced by hydrogen atoms in the same way as previous studies describe.[143] All calculations were performed using the Gaussian 03[164] or Gaussian 09[122] software packages. Structures were optimised using the BP86 DFT functional[84, 87] and a custom basis set. Ruthenium, arsenic and phosphorus were assigned the lanl2dz basis sets with associated ECPs.[165-167] The arsenic and phosphorus basis sets were also augmented by single *d* polarisation functions (α = 0.286 and 0.364 respectively).[168] All other elements were assigned the 6-311(d,p) basis sets.[169, 170] Frequency calculations were undertaken to determine the nature of structures located and also obtain the corrections for enthalpy and free energy at 1 atm. and 298.15 K. Transition states were located using STQN methods[171, 172] and confirmed as first order saddle points (transition states) by examination of the associated frequency calculations. Single point energy calculations were performed on the optimised structures using the PBE0 functional[173] and the def2-TZVP basis sets from Ahlrichs[174, 175] to get more accurate energies. The combination of the PBE0 functional with the def2-SVP and def2-TZVP was recommended by Truhlar in 2011.[101] An investigation into the performance of various functionals for group 8 transition metal carbonyl complexes found that the best general performance (considering geometries and energetics) was achieved with the PBE0 and B3PW91 hybrid functionals.[176] The approach where a higher level of theory is used after optimisation (using a lower level of theory) has precedent and has been discussed in the literature.[177] Additionally, the use of the def2-TZVP basis set family for all atoms will help to avoid any potential basis set imbalance arising from the use of different basis sets classes

to describe the chemical bonds present. The Basis Set Superposition Error (BSSE) was also investigated for the CO ligand in **1**, using the counterpoise correction function of Gaussian 09.[178, 179] The BSSE of a CO ligand in the equatorial position was calculated to be 2.4 kJ mol^{-1} for the single point calculations with the TZVP basis sets. As this error is relatively low, counterpoise corrections were not deemed necessary in the theoretical investigations due to their additional computational cost. The main number assigned represents the complex, with suffixes indicating another isomer of a particular geometry e.g. **3a** and **3b** are the same are different isomers of the same complex.

The character " ' " represents transition states, which are numbered by the complex which leads to them i.e. **3c** would then result in **3c'**. A superscript 3 represents a triplet state i.e. **$4a^3$**.

2.3.2 Theoretical modelling of the ground state of $Ru(CO)_3$(dhae)

The structure of $Ru(CO)_3$(dhae) (**1**) was optimised using an initial guess based on the structure of the related phosphorus analogue **P1**. A local minimum was located and confirmed by frequency analysis. The computed geometry for the model complex **1** is compared to that of the analogous phosphine complex **P1m** as well as the experimental geometry for **P1**, shown in Figure 2.6. The bond distances and angles for **P1** are from x-ray crystallographic data, taken from work by Bunten *et al.,*[180] whereas those of the model complex $Ru(CO)_3$(dhpe) (**P1m**) were calculated here using the same model used in the original work (no Cartesian coordinates were provided in the supporting information in Reference [46]). It is noted that the use of Gaussian09 rather than the original Gaussian98 could lead to a variation in geometry from the original work.[181]

The structure of **1** is trigonal bipyramidal where the bidentate dhae ligand occupies an equatorial and an axial site to minimise strain, resulting in a bite angle of 82.5°. This angle compares to that experimentally determined as 82.66(4)° for $Ru(CO)_3$(dppe).[180] The bond lengths for the ruthenium-arsenic bonds in **1** are longer than those of ruthenium-phosphorus bonds in **P1m** and **P1** in keeping with the reduced electron donation from arsenic compared to phosphorus, along with the increase in size of the atom. The Ru-CO bond distances in **P1m** and **1** are of a similar length and this indicates a similar electron

density on ruthenium. The complex has two distinct carbonyl ligands; one equatorial and one axial. The two equatorial carbonyl ligands lie in a plane with one arsenic centre and lie approximately 120° to each other and at approximately 90° to the other two ligands. The axial carbonyl occupies a site which is *trans* to the other arsenic centre with an angle of 177°. This suggests two possible routes for carbonyl loss from the complex.

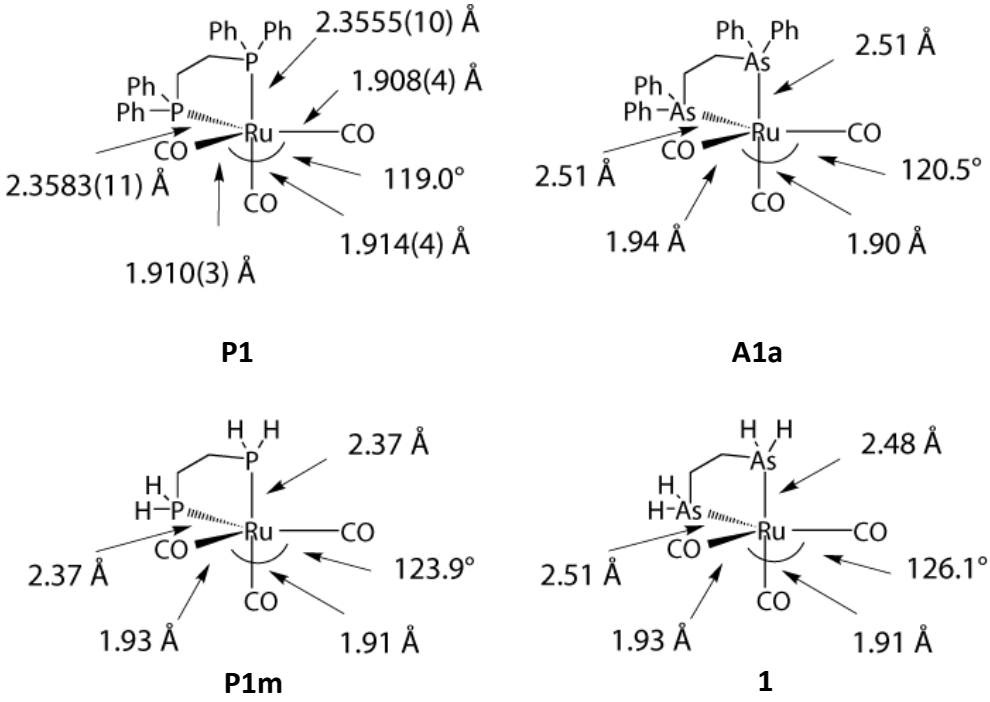

Figure 2.6: Comparison of selected bond lengths of $Ru(CO)_3$(dppe), $Ru(CO)_3$(dhpe), $Ru(CO)_3$(dpae) and $Ru(CO)_3$(dhae). Values for **P1** are taken from are experimental x-ray data taken from reference [180]

When the full ligand system is introduced, the metal-CO bond lengths remain unchanged, whereas the axial metal-As bond length increases slightly from 2.48 Å to 2.51 Å. The CO_{ax}-metal-As_{ax} bond angle decreases slightly from 177° to 173° and the CO_{eq}-metal-CO_{eq} bond angle decreases from 126.1° to 120.5°. This geometry is included in Figure 2.6, labelled as **A1a**. Hence, it can be seen that the geometry of $Ru(CO)_3$(dhae) obtained with the simple model is a reasonable match for the geometry obtained with the full model for $Ru(CO)_3$(dpae) (**A1a**); the geometry of **1** is also evidently similar to that of the experimental geometry for $Ru(CO)_3$(dppe) (as **P1**).

The fluxional behaviour of the starting complex $Ru(CO)_3(dhae)$ (**1**) was also investigated. A transition state **1a'** was located which is best described as a distorted square-based pyramid with one carbonyl ligand occupying the axial position. The axial-equatorial bond angles are between 100° and 105° and all equatorial bond angles are around 88°. This geometry is only +10.0 kJ mol^{-1} higher than that of the starting complex **1** indicating that this complex is fluxional. This is consistent with experiment; one signal from the carbonyl groups arose in the ^{13}C NMR spectrum.

2.3.3 Mechanism of ligand replacement

The experimental work undertaken by Adams *et al.* found that the addition of CO to the reaction mixture of **A1** with thermal initiation drastically reduced the size of the NMR proton signals from the products observed with *p*-H_2. It was therefore concluded that the reaction with hydrogen proceeds via CO dissociation rather than the initial de-chelation of one arm of the dpae ligand. For this reason, only a CO dissociative pathway is considered here.

The loss of a carbonyl group from **1** results in a 4-coordinate 16-electron geometry **4**[†], which can exist as an electronic triplet or singlet. Previous work has discovered that related complexes containing phosphorus rather than arsenic ligands complexes exist as 16-electron complexes in a singlet state in agreement with the observed hydride polarisation from *p*-H_2.[46] Two singlet geometries were identified for $Ru(CO)_2(dhae)$; one is a distorted square-planar geometry with the other best described as a distorted tetrahedral complex (butterfly geometry). Two triplet states of $Ru(CO)_2(dhae)$ were also identified and both found to be of higher energy than the most stable singlet geometries. This is in keeping with previous studies.[46] The four possible intermediates and relevant bond lengths and angles are illustrated in Figure 2.7. The geometries of these 16-electron intermediates here are labelled **4a–b**, and are similar to those of $Ru(CO)_2(dhpe)$ identified in previous studies.[46, 143] The two structures of $Ru(PH_3)_4$ are included; these intermediates allowed the cause of these geometries adopted to be identified.[150]

[†]the label **4** is used here to allow $Ru(H)_2(CO)_2(dhae)$ to be labelled as **3**, consistent with $Ru(H)_2(CO)_2(dpae)$ as **A3**

The triplet state of $Ru(PH_3)_4$ adopted a distorted square planar geometry where two ligands became almost *cis*, with an in-plane angle of 94° and the other two were still in a *trans* arrangement but the angle reduced to 159°. The singlet took a different structure which was only a slightly distorted square-planar geometry, with in-plane angles of 159° (butterfly geometry). This singlet structure is similar to intermediate **4b**. The structure of **4b** is also consistent with that of the related intermediate $Ru(CO)_2$(dhpe) reported in the literature. Eisenstein *et al.* reported Ru-CO bond lengths of 1.89 Å and P-Ru-C bond angles of 169.3° and 157.6°, with McGrady *et al.* reporting values of 1.87 Å, 174.2° and 149.9° respectively.[143, 182] The geometry obtained for $Ru(CO)_2$(dhpe) using the theoretical models in this thesis yields values of 1.90 Å, 171.1° and 153.9° which are consistent with those in the literature. The non-planar geometry arises from the presence of π–acceptor ligands which allow back-donation from the metal and stabilises the z^2 and xy orbitals (whilst destabilising the yz orbital).[183, 184] The weaker bonding of tertiary arsines with metals compared to the equivalent phosphines accounts for this reduction in stabilisation and therefore a more planar structure, reflected by the As-Ru-CO bond angles of 160.0° and 162.8° in **4b** here.

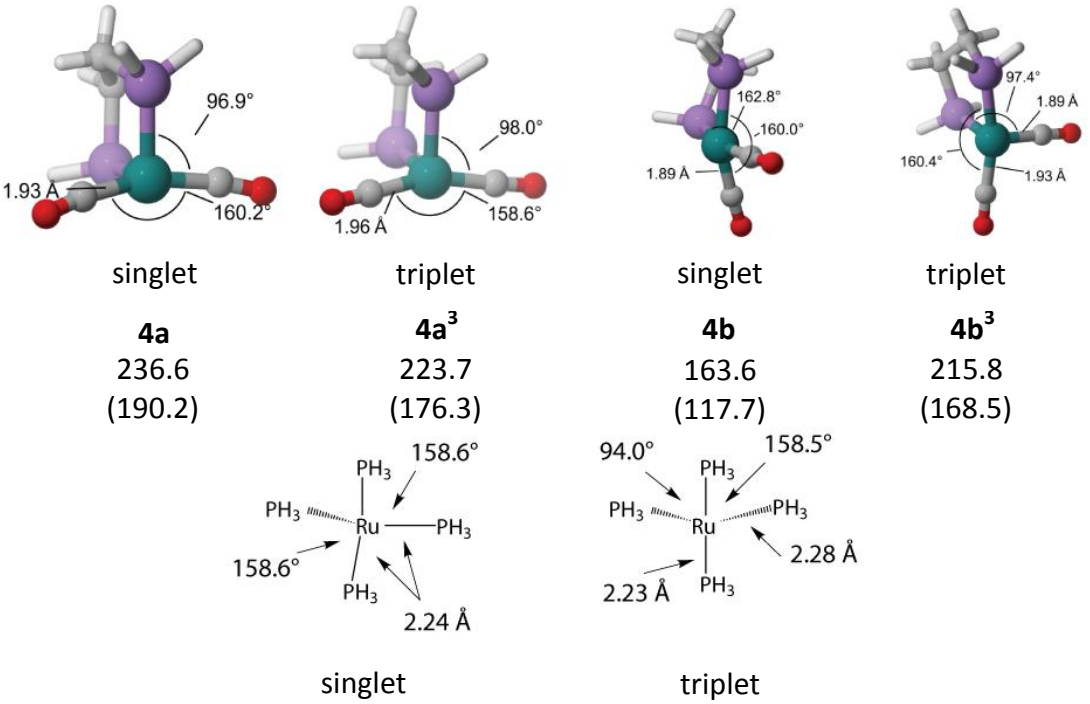

Figure 2.7: Comparison of selected bond lengths in $Ru(CO)_2$(dhae) as singlet or triplet states. Relative enthalpies to Ru(CO)3(dhae) are included, with free energies in brackets; values are in kJ mol^{-1}

The distortion of the triplet geometry of $Ru(PH_3)_4$ away from square planar was assigned to the destabilisation of a non-bonding *d*-orbital and the stabilisation of an unoccupied metal *p*-orbital, resulting in the lowering of the HOMO-LUMO gap.[185] Interestingly, the relative energies of the two triplets formed from $Ru(CO)_3$(dhae) are of a similar energy (enthalpies of +224 kJ mol^{-1} and +216 kJ mol^{-1}) but more surprising is the similar energy of the singlet when the carbonyl ligands are *trans* (enthalpy of +237 kJ mol^{-1}). A previous study into the behaviour of $Ru(CO)_2(PH_3)_2$ found the dominant geometry had the phosphine groups in a *trans* arrangement (*ct*) - this isomer is not able to form in this study as the bidentate ligand limits the binding to occur in a *cis* configuration.

The dominant 16-electron intermediate of $Ru(CO)_2$(dhae) identified here is **4b**. The enthalpy of this intermediate is 163.6 kJ mol^{-1} above that of **1** thereby indicating that CO loss is not feasible at room temperature. This is consistent with the experimental observations, where heating a mixture of **A1** in toluene with a headspace of *p*-H_2 allowed the gradual detection of **A3** upon reaching 308 K. The same reaction was possible at 263 K with *in-situ* photolysis (UV laser pulses centred at 325 nm) thereby indicating that this photolysis allows the generation of the 16-electron intermediate(s) involved via a more efficient route. The significantly lower thermodynamic pathway for the formation of **4b** from **1** (compared to **4a** and triplet states $\mathbf{4a^3}$ and $\mathbf{4b^3}$) means that this intermediate is also likely to dominate the photochemical route. The relative free energy of **4b** is also consistent with experimental evidence; the calculated value of 117.7 kJ mol^{-1} indicates that this reaction should be feasible at elevated temperatures. It is noted that the formation of two species from one species will lead to an over-estimation of the entropic effects and lower the free energy term. This inaccuracy has been addressed by various methods in the literature but no ideal procedure has yet been identified.[186-188]

The use of photochemical initiation means that it is possible for the less stable geometry **4a** to form, but it is still over 70 kJ mol^{-1} above **4b**. A low energy route from **4a** to **4b** exists (Figure 2.8) and hence reactivity via **4b** is still likely to dominate with photochemical initiation.

Investigations into the addition of H_2 to the intermediates formed by phosphine loss from $Ru(CO)_2(dppe)(PPh_3)$ (**P3**) using model complexes of $Ru(CO)_2(dhpe)(PH_3)$ and $Ru(CO)_2$(dhpe)

revealed the creation of three model isomers of $Ru(H)_2(CO)_2$(dhpe).[143] The most stable isomer had a *cis,cis,cis* geometry with one hydride *trans* to a carbonyl ligand and the other *trans* to a phosphorus centre. The second isomer was +9 kJ mol^{-1} higher in energy than the first and had the two hydrides both *trans* to phosphorus and the carbonyls *trans* to each other (*cct*-CO). The third isomer was +27 kJ mol^{-1} higher than the first and had the two hydrides *trans* to each other and the remaining ligands *cis* (*cct*-H). The calculations in the current work on $Ru(CO)_3$(dhae) (**1**) reveal the creation of the three isomers of $Ru(H)_2(CO)_2$(dhae) (labelled as **3a-c**), analogous to those computed for $Ru(H)_2(CO)_2$(dhpe). These are illustrated in Figure 2.9 along with the potential routes to their formation.

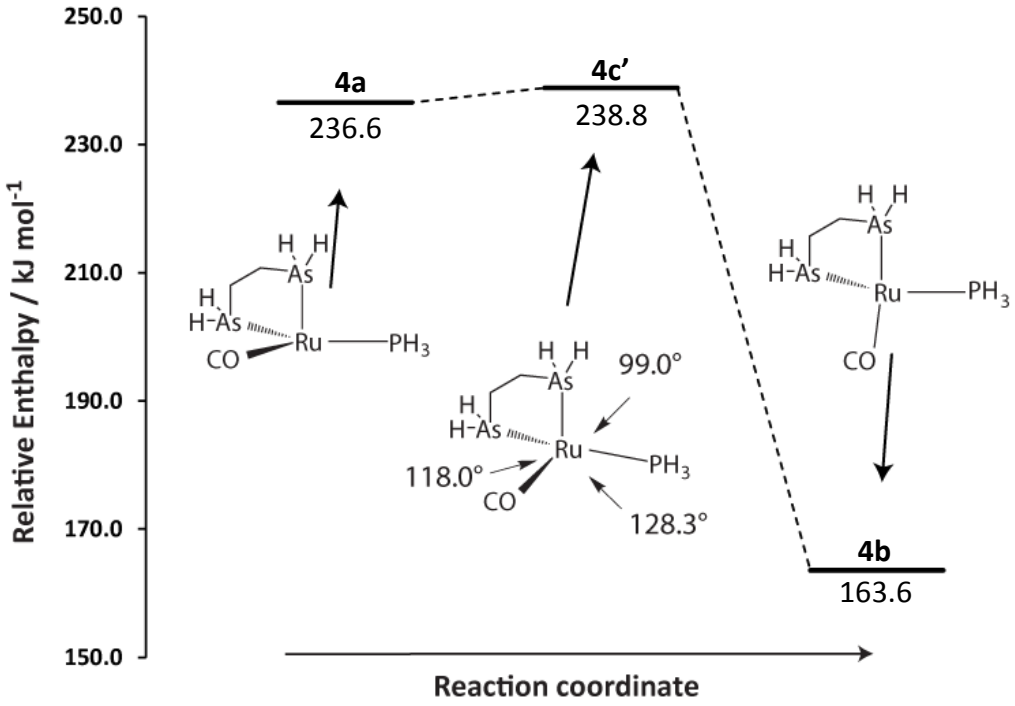

Figure 2.8: Transition state linking the intermediates $Ru(CO)_2$(dhae) **4a** and **4b**

Complex **3a** is the corresponding *ccc* product, lying +36 kJ mol^{-1} above **1** and is formed via intermediate **4b**. Complex **3b** is the *cct*-CO isomer and lies +7 kJ mol^{-1} above **3a**, and could potentially be formed via intermediates **4a** or **4a**^{3}. The remaining potential product **3c** is the *cct*-H isomer which lies +16 kJ mol^{-1} above **3b** but cannot be formed directly. The triplet resulting from equatorial carbonyl loss (**4b**^{3}) does not undergo hydrogenation and is not involved in the formation of **3**. As the singlet state lies below the triplet, there is no possibility for system crossing and a role for this triplet can therefore be discounted.

Additionally, no barrier was found for the approach of H_2 to any 16-electron singlet and no presence of binding through a η^2-dihydrogen mode was found prior to optimisation of the local minimum of **3a**. These geometries and thermodynamics are consistent with the experimental evidence given Section 2.2.1 and previous work on related complexes.

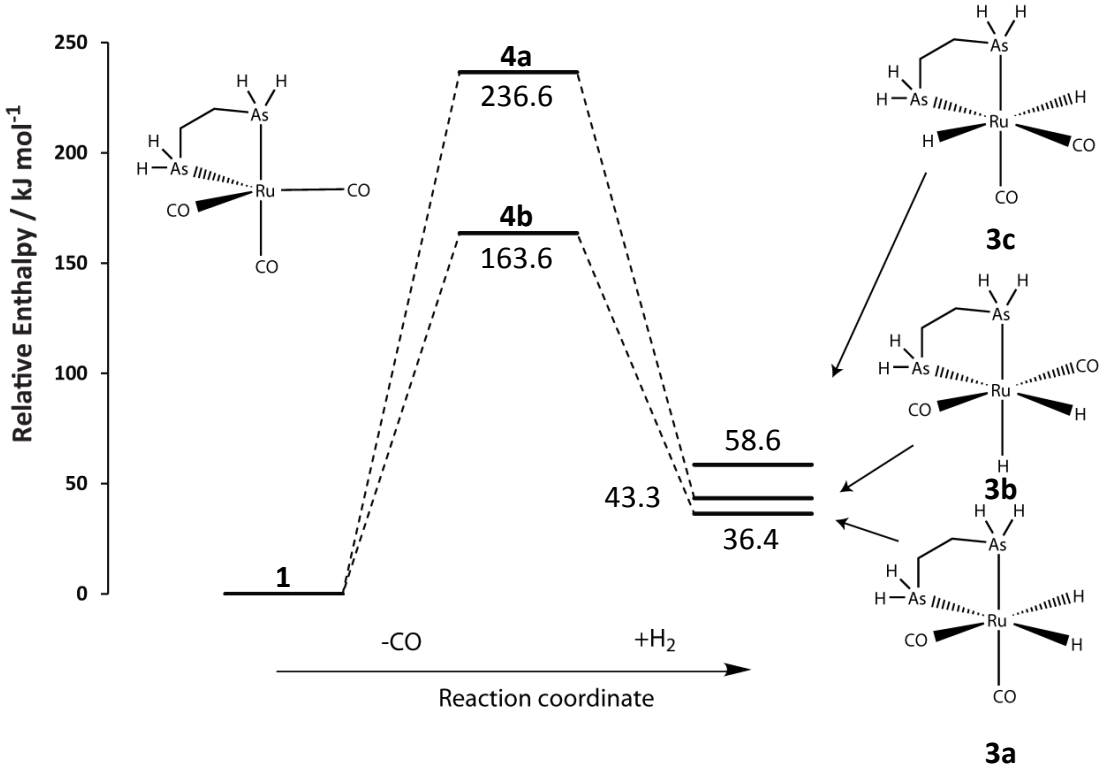

Figure 2.9: Relative energies of hydrogenation products and the mechanistic paths of formation. The pathway from **4a** to **3b** is unlikely and only included to show a potential pathway.

The enthalpies of dihydrides **3a-c** relative to **1** reveal that their formation is unfavourable. The free energies for their formation are also unfavourable, with values for **3a-c** of 30.8, 35.6 and 53.0 kJ mol^{-1} respectively. This reaction from **1** to **3a** results in no net change in the number of species and so the free energy values calculated are likely to be more realistic than those determined for **4a-b**. Importantly, the experimental evidence showed dihydride **A3** to be stable after depletion of *p*-H_2; this is likely to arise from the experimental conditions. Once CO is lost from **1**, it can enter the solvent and then be lost into the gaseous headspace in the NMR tube. This can also mean that the back reaction is inhibited and so allows dihydride **A3** to remain present in solution as a stable complex. Additionally, the presence of 3 atm. of *p*-H_2 in the NMR tube used in the reaction will

potentially disfavour H_2 loss. The determination of dihydride **3a** to be the most stable geometry is consistent with the experimental evidence, where dihydride **A3** adopts the same geometry.

The formation of the related dihydride complexes $Ru(H)_2(CO)_2(dhpe)$ and $Ru(H)_2(CO)_2(PH_3)_2$ from $Ru(CO)_3(dhpe)$ and $Ru(CO)_3(PH_3)_2$ were modelled to verify whether the corresponding hydrogenation reaction was favourable. The formation of the equivalent geometry of **3a** for reaction of $Ru(CO)_3(dhpe)$ was calculated to be unfavourable, with an enthalpy change of 36.9 kJ mol^{-1}; the formation of the *cct*-L geometry of $Ru(H)_2(CO)_2(PH_3)_2$ from $Ru(CO)_3(PH_3)_2$ was more favourable with an enthalpy change of 26.9 kJ mol^{-1}. It can therefore be concluded that there must be experimental factors driving the reaction that are not taken into account in the model.

When the full ligand system is introduced, the thermodynamic values and geometries obtained are similar. The relative enthalpies for the two models are compared in Table 2.1.

Table 2.1: Comparison of the relative enthalpies for the 16-electron intermediates and dihydride products formed from $Ru(dpae)(CO)_3$ and $Ru(dhae)(CO)_3$ via CO loss

	4a	**4a[3]**	**4b**	**4b[3]**	**3a**	**3b**	**3c**
Simple	+236.6	+223.7	+163.6	+215.8	+36.4	+43.3	+58.6
Full	+238.1	+225.7	+156.8	+212.6	+30.8	+42.2	+43.7

The most significant difference in the relative enthalpies between the full and simple systems is with **3c**, which is more stable with the full system. This can be attributed to the low steric interaction of the hydride ligands with the arsenic centre these are *cis* with. It is still however the least stable isomer of $Ru(H)_2(CO)_2(dpae)$. These values and the geometry comparison in Figure 2.6 indicate that the differences in results between the simple and full model, while substantial, do not change the conclusions; this can be attributed to the small size of the exchanging ligands and the limited geometries of the complexes imposed by the chelating ligand.

2.3.4 Fluxional behaviour of the dihydride $Ru(H)_2(CO)_2(dpae)$

The detected dihydride **A3** was previously found by Adams *et al.* to undergo hydride exchange with activation parameters of $\Delta H^{\ddagger}$ = 94 ± 6 kJ mol^{-1} and $\Delta S^{\ddagger}$ = 55 ± 20 J mol^{-1} K^{-1}. The exchange processes for the dihydride complex **3a** were limited here to those processes identified as viable by Albright.[162] Six transition states were located for the hydride site interchange in dihydride **3a**. Two of these states are rotations of the η^2-dihydrogen unit in the square-based pyramid geometry (pseudo-rotation). Transition state **3xA'** (named as such as it is a transition state from the fluxional nature from **3**) is formed via a clockwise rotation relative to dihydride **3a** and leads to the same geometry, **3a**. Transition state **3xB'** corresponds to the anti-clockwise rotation and also leads to the same geometry. However, the rotation mechanism for **3xA'** interconverts only one position of the hydrides; one hydride remains *trans* to a carbonyl whilst the other changes the arsenic centre it is *trans* to. In the mechanism of **3xB'**, both hydrides fully exchange position and so their chemical shifts reflect this conversion. This is shown graphically in Figure 2.10. These two transition states have similar energies and are compared to the experimental values in Table 2.2.

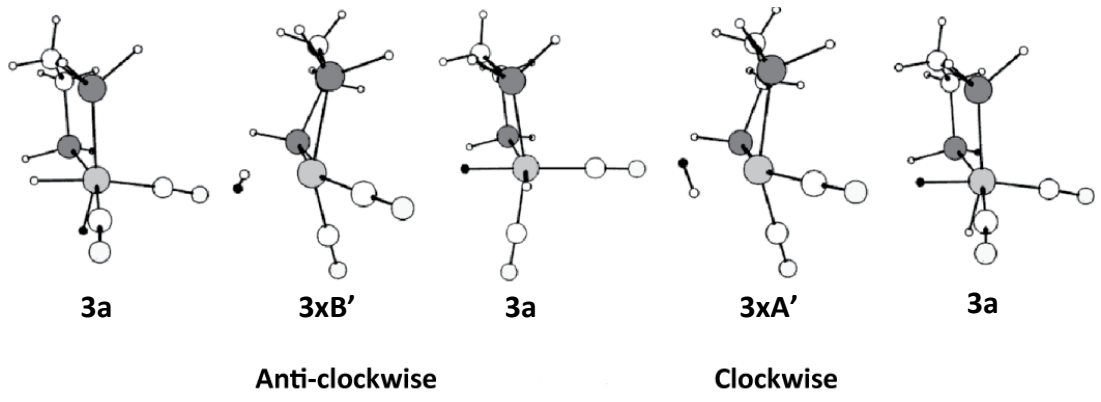

Figure 2.10: Transition states and product geometries involved in the pseudo-rotation of $Ru(H)_2(CO)_2(dhae)$ with isomer **3a**

Table 2.2: Relative thermodynamic changes for the two theoretical transition states of **3xA'** and **3xB'**, along with the experimentally determined activation parameters

	Experimental	3xA'	3xB'
$\Delta E_{SCF+ZPE}$ / kJ mol^{-1}		+78.6	+82.7
ΔH / kJ mol^{-1}	+94 ± 6	+78.1	+83.3
ΔG_{298} / kJ mol^{-1}	+78 ± 12	+81.8	+83.2
ΔS / J mol^{-1} K^{-1}	+55 ± 20	-12.2	-0.5

The calculated thermodynamic values for transition states **3xA'** and **3xB'** match the experimentally determined activation parameters reasonable well and so this provides validation for the details described in Section 2.3.1 (although clearly the full model would be better). It is worth noting the error in the experimental enthalpy was ± 6 kJ mol^{-1}. The optimisation with the B3PW91* functional and basis sets previously used yield enthalpies for the clockwise and anticlockwise transition states of +81.6 kJ mol^{-1} and +86.2 kJ mol^{-1} respectively and so the two methods give similar energetics. The use of a GGA functional (BP86) for optimisations and then the use of the hybrid functional (PBE0) to get energies in this way has been reviewed[189, 190] and the use of PBE0 is recommended for transition metals. This method also requires less computational power than optimisation with a hybrid functional. One issue raised by these calculations is that the formation of the η^2-dihydrogen unit decreases the entropy of the system whereas the positive value of the experimental entropy indicates a dissociative process. The experimental value had an error of ± 20 J mol^{-1} K^{-1} arising from the extrapolation of the Eyring plot. It is worth noting that this extrapolation can introduce a significant error with the value obtained for the entropy term.

Two alternative transition states have also been located, at energies higher than **3xA'** and **3xB'**. Transition states **3xC'** and **3xD'** also feature rotations of η^2-dihydrogen. The dihydrogen vibrations in **3xA'** and **3xB'** are high at 3060 cm^{-1} and 3203 cm^{-1} respectively whereas the vibrations in **3xC'** and **3xD'** are 2708 cm^{-1} and 2178 cm^{-1} respectively. This means that the H_2 unit in these latter two states are more strongly bound and so the barrier should be higher. The H_2 bond lengths in **3xA'** and **3xB'** are 0.84 and 0.83 Å respectively whereas in **3xC'** and **3xD'** the lengths are longer at 0.87 and 0.94 Å respectively. **3xC'** has a trigonal bipyramid type geometry with the H_2 unit sitting in an axial position and the bidentate dhae occupying two equatorial sites, with an As-Ru-As bond angle of 84°. The

geometry relaxes in both directions to form **3a** and the mechanism exchanges both hydrides, arsenic centres but only one carbonyl; the other carbonyl remains *trans* to an arsenic. Transition state **3xD'** is a similar trigonal bipyramidal structure but an arsenic centre occupies both an equatorial site and an axial site, with an As-Ru-As bond angle of 83°. Both arsenic centres and carbonyls exchange sites but one hydride remains *trans* to an arsenic centre. This geometry relaxes in one direction to **3a** whereas the other direction leads to **3b**. The geometries and negative vibrations of **3xC'** and **3xD'** are consistent with the trigonal twist mechanism with the H_2 unit forming a triangular face with the carbonyl ligand *trans* to arsenic. The thermodynamic changes of these four transition states and mechanisms are shown in Figure 2.12 with the routes involving **3xC'** and **3xD'** shown in red; note that the values are relative to the starting dihydride **3a**. The free energy difference between **3a** and **3b** with the full model is 11.2 kJ mol^{-1}; this corresponds to a population ratio of these isomers of 100:1. Therefore, if transition states **3xC'** and **3xD'** were experimentally possible, the dominant isomer will still be **3a**.

The fifth and sixth transition states do not involve a η^2-dihydrogen unit and the vibrational frequencies reveal each hydride ligand having hydride-metal vibrations rather than those of a dihydrogen unit. The fifth transition state **3xE'** again has a similar geometry to **3xD'** but the movement of the separate hydrides is a swing movement. Relaxation of the geometry leads to **3a** in both directions. The sixth transition state **3xF'** has a distorted octahedral structure, where the hydrides are between *cis* and *trans* alignments and the motion of the hydrides is in the direction of **3a** and **3c**. Relaxation of this transition state leads to the *cis* hydride species **3a** and the *trans* hydride species **3c**. Detailed illustrations of the six identified transition states are illustrated in Figure 2.11. These two transition states and their relative energies are shown in Figure 2.13.

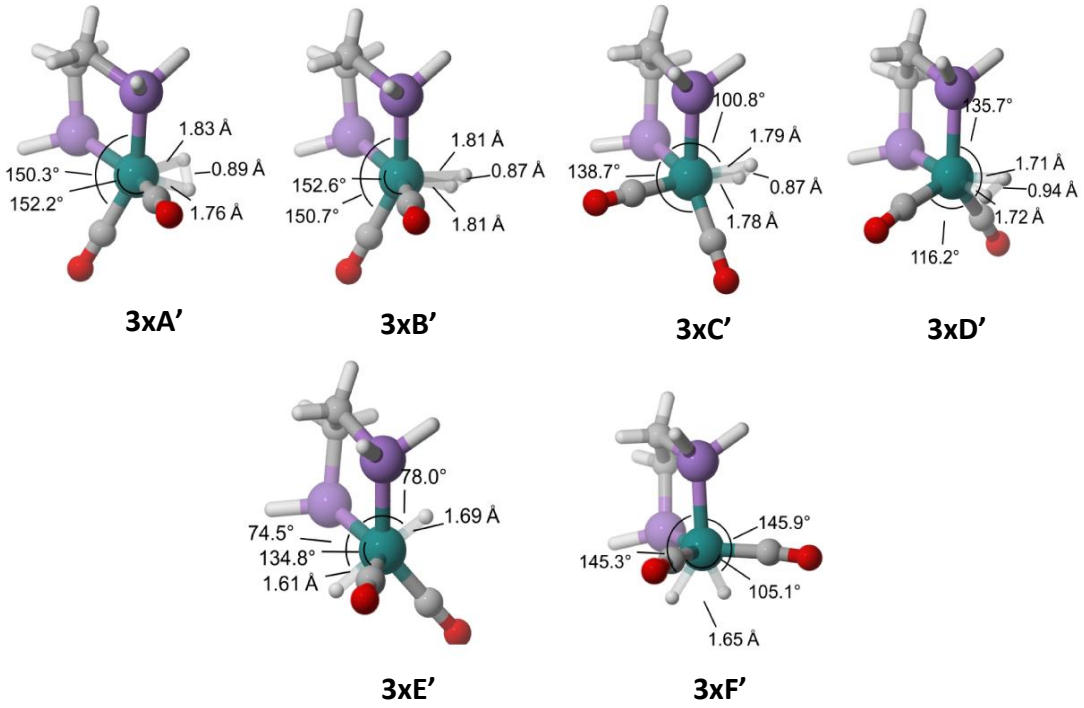

Figure 2.11: Detailed illustrations for the six identified transition states for the interchange between isomers of $Ru(H)_2(dhae)(CO)_2$

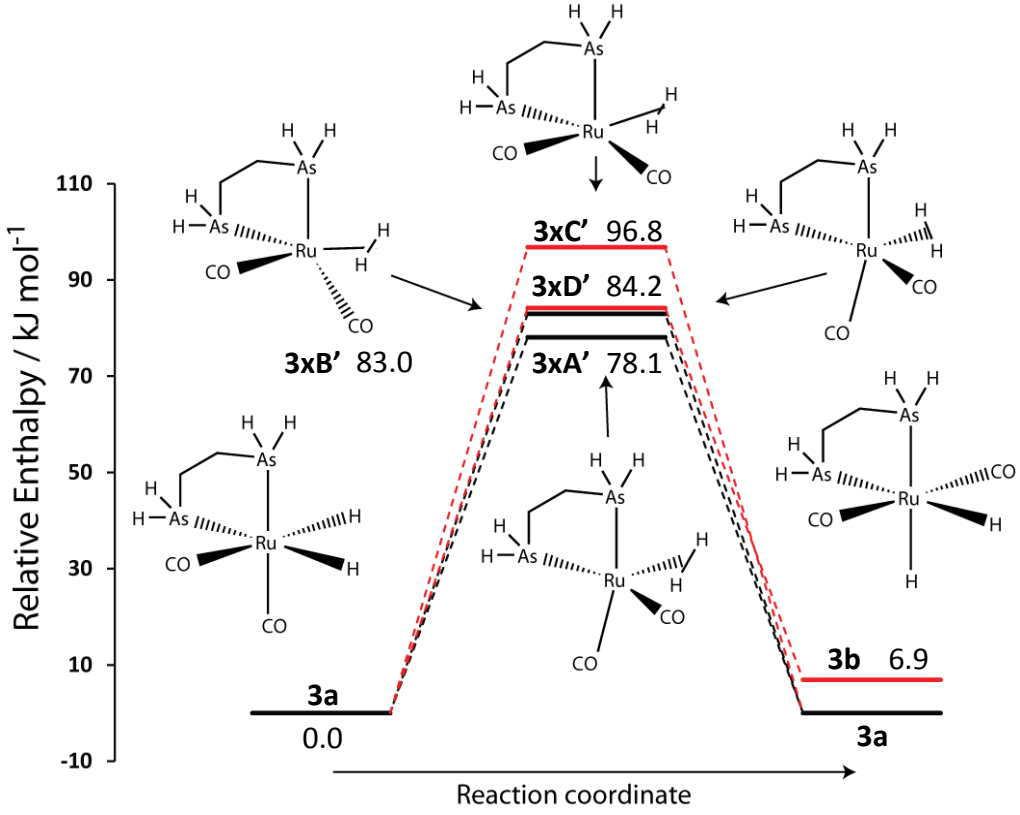

Figure 2.12: Relative enthalpy profile of transition states and products from $Ru(H)_2(CO)_2(dhae)$ involving a dihydrogen unit. Pathways through **3xC'** and **3xD'** are shown in red

All of these transition states have a similar energy meaning that all rearrangements are potentially feasible, the observation of only one dihydride species **3a** in the proton NMR spectrum indicates the dominance of this isomer. It should be noted however that the hydrides in **3b** and **3c** are arranged symmetric with respect to one another and so these products would not be expected to show any PHIP.

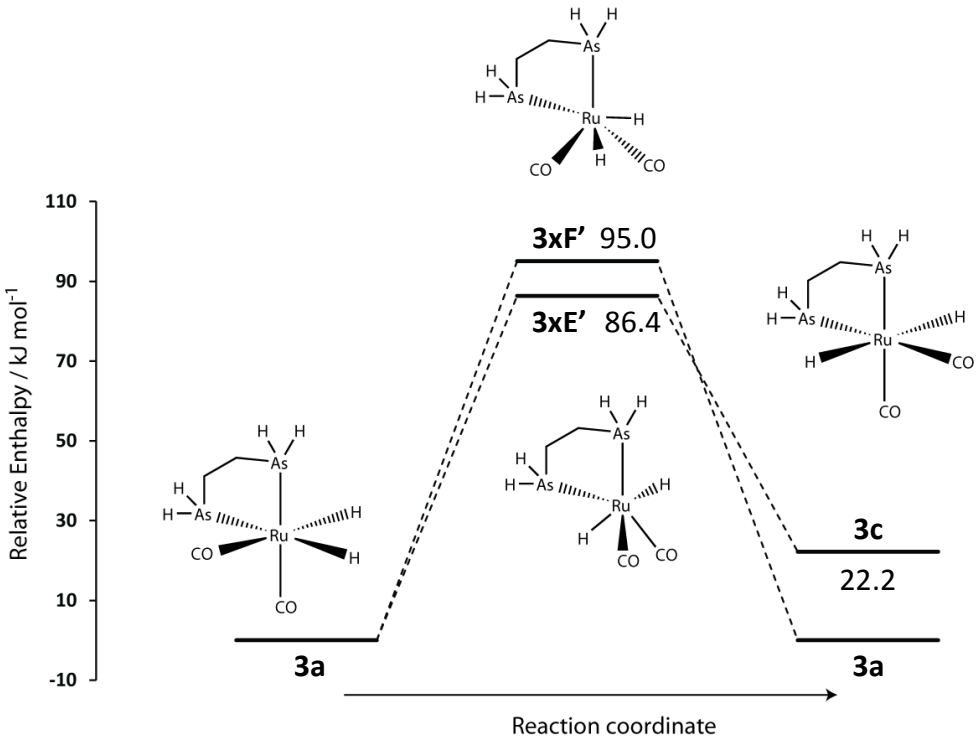

Figure 2.13: Relative enthalpy profile of transition states and products from $Ru(H)_2(CO)_2$(dhae) where no formation of a dihydrogen unit is involved

The two lowest transition states **3xA'** and **3xB'** were modelled with the full model; the thermodynamic values were found to increase. The relative enthalpy and free energy of **3xA'** increase, from 78.1 and 81.8 kJ mol^{-1} to 81.1 and 101.9 kJ mol^{-1} respectively. The relative enthalpy and free energy of **3xB'** also increase from 83.3 and 83.2 kJ mol^{-1} to 86.9 and 102.7 kJ mol^{-1} respectively. The transition state **3xE'** was also modelled with the full model (this transition state leads to geometry **3c**); this transition state did not increase in relative enthalpy from 86.4 but the free energy was raised from 89.5 kJ mol^{-1} to 105.7 kJ mol^{-1}. Whilst this transition state is therefore predicted to feasibly lead to the unobserved geometry **3c**, the free energy difference to **3a** of 14.2 kJ mol^{-1} means that **3c** would only be present in a ratio of 100:0.3.

These collective increases when the complexity of the model is increased are low in terms of enthalpy, suggesting that the electronic effects from dhae and dpae have a low impact on the transition states. The increase in free energy in contrast can be attributed to the increase in steric bulk of dpae over dhpe. The change in entropy for these transition states is not consistent with experiment; for **3xA'** a value of -70 J K^{-1} mol^{-1} is obtained, **3xB'** yields a change of -53.1 J K^{-1} mol^{-1} and **3xE'** yields a change of -64.7 J K^{-1} mol^{-1}. These values are of similar magnitude to the experimental value of +55 J K^{-1} mol^{-1} but the sign is opposite. The related complex $Ru(H)_2(CO)_2$(dppe) was determined to be fluxional, with the activation values determined to be $\Delta H^{\ddagger}$ = 85.5 (2) kJ mol^{-1} and $\Delta S^{\ddagger}$ = 34 (7) J K^{-1} mol^{-1}.[154] The pathway for this fluxionality was proposed to involve the η^2-H_2 unit rotation used in this work. There was no evidence with this complex for loss of phosphine or CO ligands which does contrast with the increase in entropy determined. The related complex $Fe(H)_2(CO)_2$(dppe) was also found to be fluxional, with exchange thermodynamic values of $\Delta H^{\ddagger}$ = 48 ± 6 kJ mol^{-1} and $\Delta S^{\ddagger}$ = -10 ± 20 J K^{-1} mol^{-1}.[46] The pathways were modelled theoretically and a good agreement obtained for the relative enthalpies. The entropy values calculated were not in agreement with experiment, with the discrepancy attributed to the level of theory not fully representing the entropic effects arising from the phenyl substituents present in the experimental system. The use of the full system here has revealed a more significant loss of entropy in the transition states than with the simple system. The negative term is consistent with the ordering of the complex in the transition state and so it is possible that another pathway is involved in the exchange process. It is also possible that the models employed here do not properly model the long range interactions or solvent effects.

2.3.4.1 Conclusions into the fluxional nature of $Ru(H)_2(CO)_2$(dpae) and related complexes

The work presented here has revealed that the interconversion of equivalent groups in $Ru(H)_2(CO)_2$(dpae) is likely to be based on the model followed here. The dominant isomer is the c*c*-isomer of $Ru(H)_2(CO)_2$(dhae), although a higher energy *trans* hydride isomer lies 22 kJ mol^{-1} above it (an equilibrium position of 1:8000 is predicted at 298 K). This situation changes when the full ligand system is considered as the energy difference falls to 12.9 kJ mol^{-1} but the ratio would still be 1:185 at 298 K.

These data are consistent with the detection of the *cc* isomer through PHIP and suggest that a chelating ligand without a mirror plane should be employed to search for the second isomer (**3b**). Ultimately, *cc*-$Ru(H)_2(CO)_2$(dhae) results, for both thermal and photochemical initiation. It arises from the common intermediate $Ru(CO)_2$(dhae), as **4b**, and has the greatest stability as $Ru(H)_2(CO)_2$(dhae) (**3a**).

2.3.5 Formation of 14-electron Ru(CO)(dpae)

Photochemical initiation of the reaction with $Ru(CO)_3$(dpae) (**A1**) was observed to lead to $Ru(H)_2(CO)_2$(dpae), **A3** as the sole photoproduct. This could involve single carbonyl loss, as described, or 14-electron Ru(CO)(dpae). Previous studies indicate this double ligand loss product is involved with the phosphine analogues.[142, 143] The loss of two carbonyls from **1** was therefore modelled and three intermediates identified as **5a**–**b**^{3}. Intermediates **5a** and **5a**^{3} have similar structures with the remaining carbonyl approximately *trans* to an arsenic centre whereas in **5b**^{3}, the CO ligand lies out of the dhae-metal plane. The geometries of these three structures are in shown in Figure 2.14 and it can be seen that **5a** and **5a**^{3} are of similar energy whereas **5b**^{3} is higher in energy.

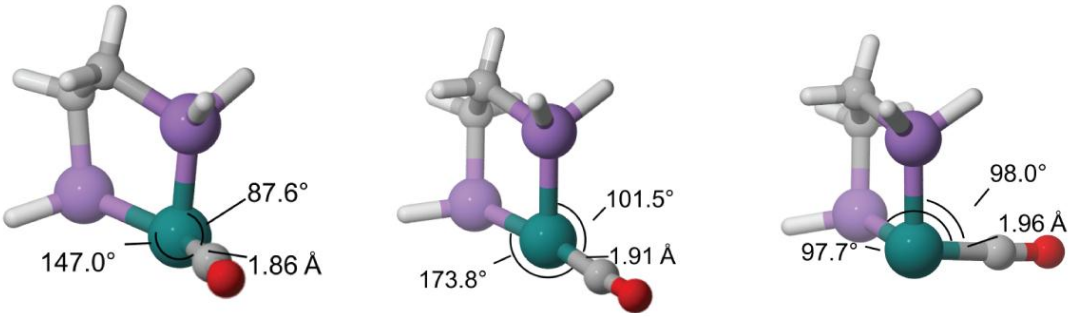

singlet	triplet	triplet
5a	**5a**^{3}	**5b**^{3}
397.8	391.8	406.4
(311.4)	(298.5)	(315.4)

Figure 2.14: Geometries and thermodynamic values of the identified 14 electron intermediates of Ru(CO)(dhae)

The thermodynamic values calculated here reveal no significant preference for the formation of one 14-electron species over another. Importantly, the formation of singlet **5a**

is potentially favoured, as it requires no spin flip transition during its formation. These three 14-electron species can interact with solvent, dihydrogen or one of the dissociated carbonyls in the next step. Interaction with the toluene solvent is addressed in Section 2.3.6. The recombination of a carbonyl ligand to singlet **5a** results in singlet 16-electron **4b**. The formation of singlet **4a** would require an unfavourable rearrangement and so only **4b** is formed. This results in only one 16-electron isomer which reacts with dihydrogen to form **3a**. Intermediate **4b** can reform **1** by adding a second carbonyl ligand. The addition of CO to the two 14-electron triplet intermediates can also occur, creating 16-electron triplets. In these reactions, no spin-flip is required and so is feasible. It is also worth noting that none of the 14-electron intermediates identified are accessible thermally due to the significant thermodynamic cost of their formation. Due to the significant enhancement from *para*-hydrogen observed experimentally, any pathway involving a triplet species is minor and so not considered further.

The addition of dihydrogen to singlet **5a** results in 16-electron $Ru(H)_2(CO)(dhae)$ (**6a**), where one hydride ligand is *trans* to the carbonyl ligand, the other hydride being *trans* to a vacant site. This geometry is thermodynamically the most favourable as hydride ligands are most stable when no ligand is present *trans* to them; this maximises the electron density they share with the metal in unsaturated systems. The subsequent binding of CO to **6a** results in the formation of **3a** as the sole product. The binding of another dihydrogen molecule to **6a** results though in dihydride-dihydrogen species, **6b**, which is unable to undergo further reaction. Whilst the binding of the dihydrogen ligand is favourable, the free energy change is favourable by only -51 kJ mol^{-1} compared to the change of -88 kJ mol^{-1} in terms of enthalpy. This means that the recombination of a carbonyl is preferred to form **3a**. These structures and their relative energies are shown in Figure 2.15. The experimental data showed no difference in the reaction products with thermal or photochemical initiation (apart from the intensity increase of 3.4 fold for the signals arising from **A3** with photolysis at 333 K), with dihydride **3a** observed as the only reaction product. The complexes identified here, with associated thermodynamic values, are consistent with these findings. One significant result shown in Figure 2.15 is that **5a** results in the formation of only the starting complex and dihydride **3a** in keeping with experimental findings.

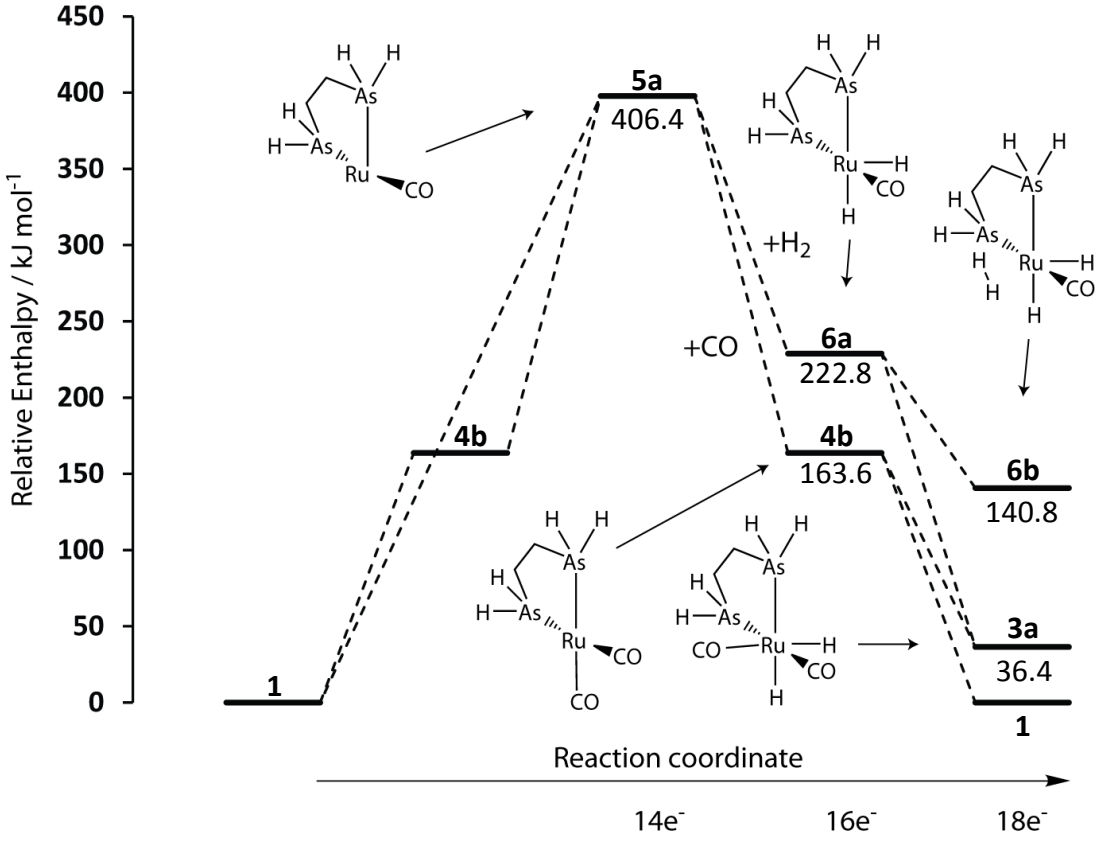

Figure 2.15: Relative enthalpy profile for the reactions of 14-electron Ru(CO)(dhae) as **5a** (formed via photochemical initiation) with CO or H_2

When the full ligand system is introduced, the geometries of the three 14-electron states and reaction thermodynamic values remain very similar to those of the simple model. These are summarised in Table 2.3 along with the equivalent simple ligand model energies. As can be seen from the table, the simple model results in values which match the full model to within 10 kJ mol^{-1}, although for only 2 out of 8 values does the simple model produce a lower energy solution. The difference in electronic effects between the dhae and the dpae ligand is therefore relatively small here. Additionally, as the phenyl rings in dpae are directed away from the metal centre, together with the small size of H_2 and linear bonding mode of CO with the metal centre here, little steric difference is encountered.

Table 2.3: Comparison of the relative enthalpies of the 14-electron species potentially formed by photolysis of Ru(dpae)$(CO)_3$ (**1**) with the simple and full theoretical models. All values are in kJ mol^{-1}

Label	Formula	Electronic State	Formed from	Simple Model	Full model
5a	Ru(CO)(dhae)	Singlet	2x CO loss from **1**	397.8	392.4
$5a^3$	Ru)(CO)(dhae	Triplet	2x CO loss from **1**	391.8	392.3
$5b^3$	Ru(CO)(dhae)	Triplet	2x CO loss from **1**	406.4	398.9
6a	$Ru(H)_2(CO)$(dhae)	Singlet	H_2 addition to **5a**	228.8	226.3
6b	$Ru(H)_2(CO)$(dhae)(H_2)	Singlet	H_2 addition to **6a**	140.8	136.7
4b	$Ru(CO)_2$(dhae)	Singlet	CO addition to **5a**	163.6	156.8
$4b^3$	$Ru(CO)_2$(dhae)	Triplet	CO addition to **$5a^3$**	223.7	225.7
$4a^3$	$Ru(CO)_2$(dhae)	Triplet	CO addition to **$5a^3$** or **$5b^3$**	215.8	212.6

2.3.5.1 Summary of the reactions of $Ru(CO)_3$(dpae) with H_2

The DFT calculations therefore predict that $Ru(CO)_3$(dhae) or $Ru(CO)_3$(dpae) can produce $Ru(H)_2(CO)_2$(dhae) (**3a**) and $Ru(H)_2(CO)_2$(dpae) upon reaction with H_2 via singlet **4b**. The work presented here is therefore consistent with previous experimental and theoretical studies.[142] The triplets of $Ru(CO)_2$(dhae) are higher in energy than the singlet, in agreement with the observation of PHIP. The formation of **5a** is unfeasible with thermal initiation and photochemical initiation would be required. Ultimately, if formed, 14-electron **5a** leads to the same stable 18-electron species as through 16-electron **4b**.

2.3.6 Role of solvation for ligand loss and oxidative addition of hydrogen

In order to establish the sensitivity of the model system to solvation, the reactions shown in Figure 2.16 were considered. Given that these species are neutral it was expected that these data would confirm a simple continuum model was appropriate.

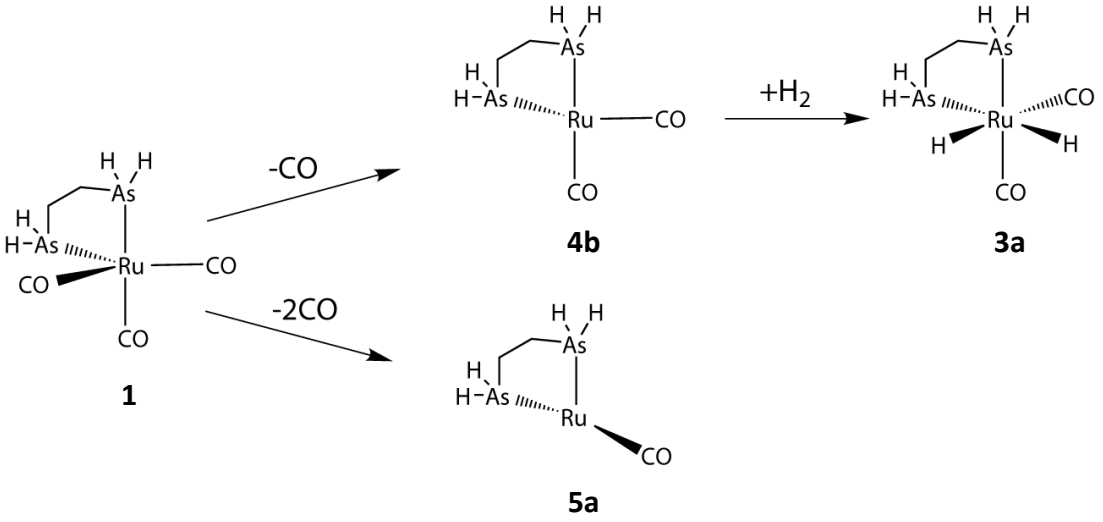

Figure 2.16: Geometries and reaction considered for the preliminary investigation

The calculations previously mentioned were modelled in the gas phase at 0 K with thermodynamic corrections at 298.15 K applied, whereas the reactions were carried out in toluene-d_8. The effect of solvation was examined using both implicit and explicit solvent models. Implicit solvation was performed using the Integral Equation Formalism Polarisable Continuum Model (IEFPCM)[191-193] with the solvent specified as toluene. The inclusion of PCM solvation was tested using two methods; the first method included the PCM model in the single point calculations using the PBE0 functional, whereas the second method also included the solvation model in the geometry optimisation and frequency analysis. For the explicit solvent investigation, the toluene molecule was substituted for benzene to eliminate multiple conformers when the ring is bound in a η^2- mode. Explicit solvation was investigated in the reactions of **1** to form **4b** and **5a** in two separate ways. In the first way, the calculations were performed in the gas phase whereas in the second way implicit PCM solvation was also included.

The use of single point calculations with PCM solvation only affects the thermodynamic values calculated with the geometries used unaffected; these are summarised in Table 2.4. The calculated values exhibit little difference to the gas phase values reported previously. This is in keeping with the low dielectric constant of toluene. Additionally, whilst the continuum solvation model does allow for the inclusion of solvent effects, it does not fully model the true interaction of the solvent with solute, such as hydrogen bonding. Using the implicit PCM model for geometry optimisation and thermodynamic analysis had little impact on the obtained geometry for **1**, 16-electron **4b** or 14-electron **5a** formed by CO loss, or the hydrogenation product **3a**.

Table 2.4: Relative energies for the initial reactions of CO loss and H_2 addition with $Ru(CO)_3$(dhae) (**1**) with and without PCM solvation

	4b		**5a**		**3a**	
	ΔH / kJ mol^{-1}	**ΔG / kJ mol^{-1}**	**ΔH / kJ mol^{-1}**	**ΔG / kJ mol^{-1}**	**ΔH / kJ mol^{-1}**	**ΔG / kJ mol^{-1}**
Gas phase	163.6	117.7	397.8	311.4	36.4	30.4
PCM SP	161.8	115.9	387.8	301.4	37.3	31.3
PCM optimised	161.4	115.2	389.3	301.9	36.8	30.5

The inclusion of explicit solvation did affect the geometries of the intermediates obtained in contrast. The carbonyl ligands in **4b** both have similar CO-Ru-As bond angles of around 161° (as illustrated in Figure 2.7); explicit solvation results in the change in one bond angle to 129°, whilst the other angle does not change significantly. The geometry obtained is a trigonal bipyramid, with the benzene ligand present in the trigonal (or equatorial) plane. For the 14-electron intermediate **5a**, the CO-Ru-As bond angle is changed from 147° (Figure 2.14) to 168°. These geometries are illustrated in Figure 2.17. The thermodynamic values for explicit solvation are summarised in Table 2.5.

It can be seen that the free energy terms all increase, consistent with the coordination of a ligand to the complex compared to the sole release of CO in the reaction. The enthalpy term lowers in size as expected, with the most significant stabilisation for the explicit solation with no PCM solvation; this indicates the reactivity of these intermediates. However, whilst the use of explicit solvation does lower the enthalpies, these results have revealed that solvation is unlikely to be critical in the analysis of reaction pathways of these

complexes and intermediates. In a more polar and coordinating solvent, like pyridine, it is likely that the inclusion of solvation would be necessary. It should be noted that as improved solvation models are created, the inclusion of solvent effects for toluene in this system may need to be necessary to fully model the reactions.

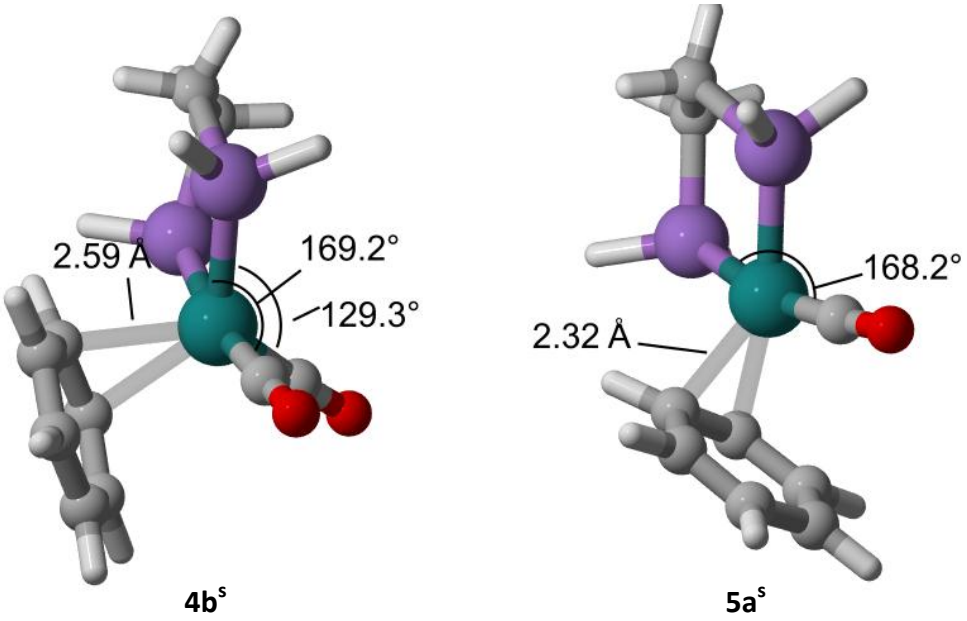

Figure 2.17: Detailed illustration of the geometries of 16-electon **4b** and 14-electon **5a** when optimised with explicit solvation (labelled as **4b^s** and **5a^s**)

Table 2.5: Comparison of relative energies for the initial CO loss and H_2 addition reactions with implicit and explicit solvation models

	4b / 4b^s		**5a / 5a^s**	
	ΔH / kJ mol^{-1}	**ΔG / kJ mol^{-1}**	**ΔH / kJ mol^{-1}**	**ΔG / kJ mol^{-1}**
Gas phase, no solvation	163.6	117.7	397.8	311.4
Explicit	124.9	127.2	296.3	256.1
Explicit + PCM Optimised	142.4	144.9	311.9	272.8

2.3.7 Theoretical modelling of $Ru(CO)_2(dpae)(PPh_3)$

$Ru(CO)_2(dhae)(PH_3)$, **2**, was found to exist with a similar trigonal bipyramidal structure to $Ru(CO)_3(dhae)$, **1**. However, the PH_3 group can be located in the equatorial plane (**2a**) or the axial plane (**2b**). These two forms differ in energy by 3.4 kJ mol^{-1}, with **2a** being more stable. This small energy difference predicts that both forms are accessible and any reactivity studies on **2** needs to consider both. However, when this is extended to the full model, the location of the PPh_3 group in the axial position is more stable by 4.9 kJ mol^{-1}. This change in stability could arise from the steric crowding around the metal centre; when the phosphine is in the equatorial plane, it is *cis* to both ends of the dpae ligand (bond angles of 100.7° and 107.6° for the axial and equatorial ends respectively). In the axial position, the phosphine is only *cis* to the end of the dpae ligand that lies in the equatorial plane (bond angle of 99.2°). The effect of the phosphine on the relative difference in energies of the two geometries was investigated. With the phosphine as PF_3, the equatorial position was favoured by 7.4 kJ mol^{-1} whereas with the phosphine as PMe_3, the axial position was favoured by 19.4 kJ mol^{-1}. Significantly, the bulkier phosphine $P(C_6F_5)_3$ (bulkier than PPh_3) revealed a preference for the equatorial position by 19.1 kJ mol^{-1}. This means that the difference in energy arises not from steric effects but from electronic effects. The equatorial positions in trigonal bipyramidal geometries are preferentially preferred by good π-acceptors, which is in agreement with PH_3, PF_3 and $P(C_6F_5)_3$. With the PPh_3 and PMe_3 ligands, the equatorial positions are occupied by the two CO ligands. This reveals that the simple model simplification used in this work does not fully model some of the important chemistry needed in this work. For the chelating dhae ligand, it is always forced to coordinate in *cis*-positions and so the difference between dhae and dpae is reduced; for PH_3 and PPh_3 this difference is more pronounced and can result in a reversal of stabilities. Whilst the stabilities of the two isomers reverse with the use of the simple model, the simple model will be continued, but certain results will be verified with the full model. The relative enthalpies given in this section are to the lowest enthalpy geometry of $Ru(CO)_2(dhae)(PH_3)$ as **2a**.

The fluxional nature of the starting complex $Ru(CO)_2(dpae)(PPh_3)$, **A2**, was also investigated. Previous studies found the related complex $Ru(CO)_2(dppe)(PPh_3)$ (**P3**) to exist as two different isomers with the phosphine group occupying an axial or an equatorial position.[143]

The exchange processes connecting two isomers **2a** and **2b** were modelled and two low lying transition states located; both involve a square-based pyramidal structure. The first transition state **2c'** had both carbonyl ligands close to being *trans* to each end of the dhae ligand and the phosphine group *cis* to the dhae ligand, with bond angles of between 101° and 106°. The second transition state **2d'** had the phosphine group swapped with one of the carbonyl ligands, with the carbonyl *cis* to both ends of the dhae ligand and the bond angles being slightly smaller than **2c'**, at 100° and 105°. Transition state **2c'** was found to be +2.4 kJ mol^{-1} above **2a** and -1.0 kJ mol^{-1} (relative enthalpy) below **2b**. Transition state **2d'** was calculated to be slightly higher; +14.4 kJ mol^{-1} above **2a** and +11.0 kJ mol^{-1} above **2b**. Whilst the vales for **2c'** are less than **2b**, the SCF energy of **2c'** is above **2b** by 2.5 kJ mol^{-1} confirming the transition state - the loss of vibrational mode means that the enthalpy correction is lowered slightly resulting in this discrepancy. These low barrier heights explain the experimental observation that $Ru(CO)_2(dpae)(PPh_3)$ (**A2**) is highly fluxional. The transition states for the related complex $Ru(CO)_2(dppe)(PPh_3)$ (**P3**) (modelled as the simple complex $Ru(CO)_2(dhae)(PH_3)$ were located and similar low barrier heights obtained. These states and additional energies are shown in Figure 2.18 with the accompanying numbers referring to the relative enthalpies in kJ mol^{-1} (free energies in brackets).

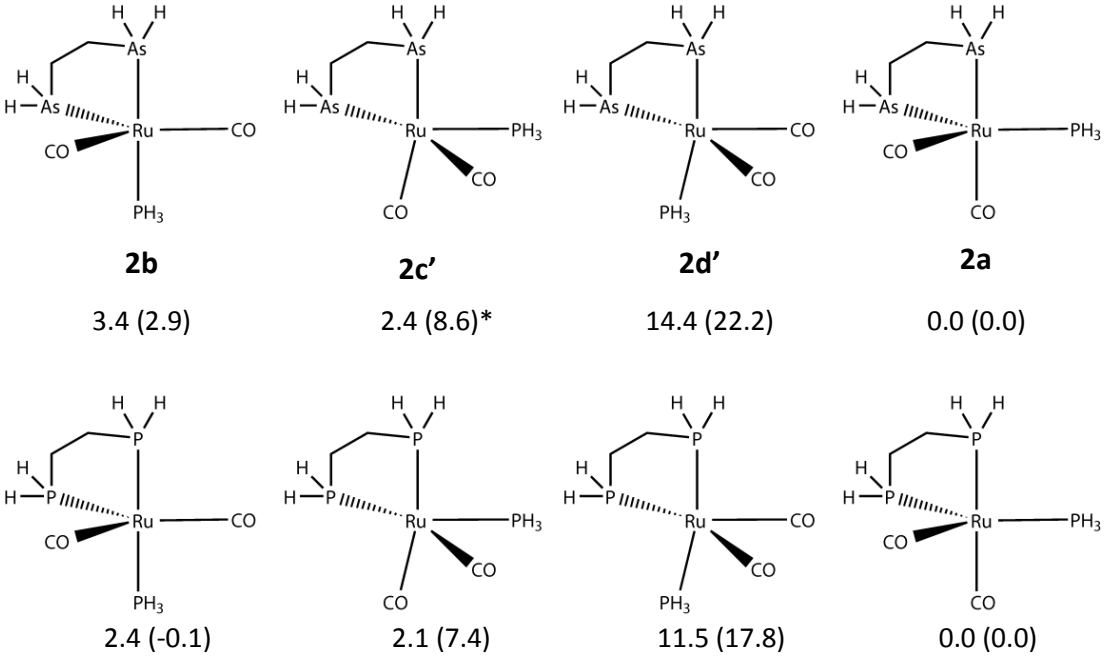

Figure 2.18: Geometries and enthalpies for the isomers and transition states arising from the fluxional nature of $Ru(CO)_2(dhae)(PH_3)$ and $Ru(CO)_2(dhpe)(PH_3)$. The lower enthalpy of **2c'** (marked by *) relative to **2b** is discussed in the text. Free energies are included in brackets.

Ligand loss from $Ru(CO)_2(dhae)(PH_3)$ can occur by phosphine or CO loss; phosphine loss can result in the formation of the 16-electron intermediates **4a** and **4b** previously described in Section 2.3.3; **4b** will be the dominant intermediate formed. The formation of **4b** by phosphine loss results in a lower change in enthalpy; the formation from **1** previously described resulted in an enthalpy change of 163.6 kJ mol^{-1}, whereas the formation from **2a** results in an enthalpy change of 116.9 kJ mol^{-1}. This is in keeping with the stronger ruthenium-CO bond compared to the ruthenium-PH_3 bond. This means that the loss of the phosphine will dominate in thermal reactions.

With photochemical initiation, it is possible that a ruthenium-CO bond is broken. For CO loss from **2a** and **2b**, four 16-electron intermediates were located in this investigation. These can potentially go on to form **7a**-**7d** which are discussed later; the 16-electron intermediates here are labelled **8a–8c^3**. The 16-electron singlet intermediate with a distorted square-planar structure optimized to a local minimum (**8b**). The P-Ru-As bond angle is *ca.* 180° while the OC-Ru-As bond angle is 147°. The formation of **8b** is in keeping with previous studies by Eisenstein *et al.* on $Ru(CO)_2(PH_3)_2$.[184] This isomer also has the CO ligand occupying a position out of the plane, which allows stabilisation of the z^2 and xy orbitals previously described for the geometry of **4b**. Triplet **8c^3** adopts a similar geometry, but has the PH_3 group distorted out of the plane. The remaining two intermediates **8a** and **8a^3** have similar geometries to intermediate **4a**, where the dhae ligand is in the equatorial positions of the butterfly geometry and PH_3 and CO in the axial positions. These geometries are illustrated in Figure 2.19 together with their relative enthalpies (free energies in brackets). The enthalpies and free energies for the formation of the intermediates **8a-8c^3** all show that the thermodynamic changes involved are sizeable and not facile. This is consistent with the experimental data, where the major species observed in the thermal reactions of **A2** were the dihydride $Ru(H)_2(CO)_2(dpae)$ (**A3**) previously described.

The fluxional nature of the 16-electron intermediates of $Ru(CO)(dhae)(PH_3)$ (**8a** and **8b**) was also examined. The transition state **8d'** obtained was different to that for the similar conversion between isomers of $Ru(CO)_2(dhae)$. This transition state has a smaller distortion of the CO and PH_3 ligands from the positions in starting intermediate **8a**, but importantly the barrier created by **8d'** of 2.7 kJ mol^{-1} means that if this is a true barrier, any **8a** produced will spontaneously convert to intermediate **8b**. This transition state and thermodynamic

values (enthalpy relative to **2a** listed first with free energy in brackets) are illustrated in Figure 2.20. The dominance of **8b** will mean any reaction of $Ru(CO)_2(dhae)(PH_3)$ from either isomer will be likely though this intermediate.

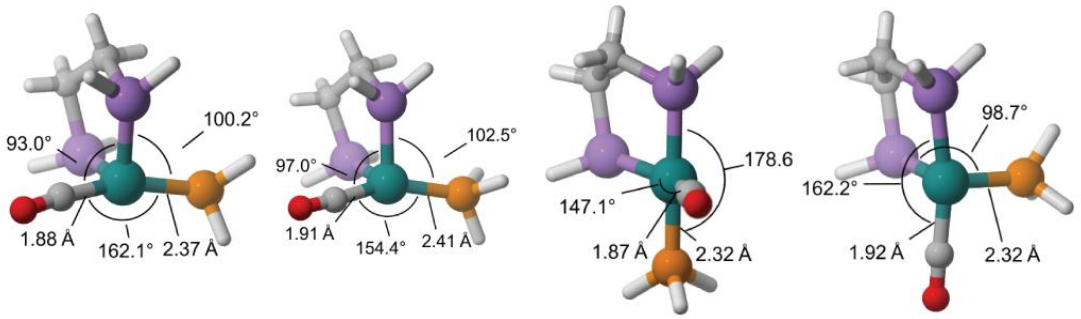

8a	**8a**[3]	**8b**	**8c**[3]
242.3 (196.7)	228.9 (178.3)	177.8 (131.8)	221.8 (171.6)
singlet	triplet	singlet	triplet

Figure 2.19: Comparison of selected geometric values and relative enthalpies (free energies in brackets) for the 16-electron species of $Ru(CO)(dhae)(PH_3)$; values are in kJ mol^{-1}

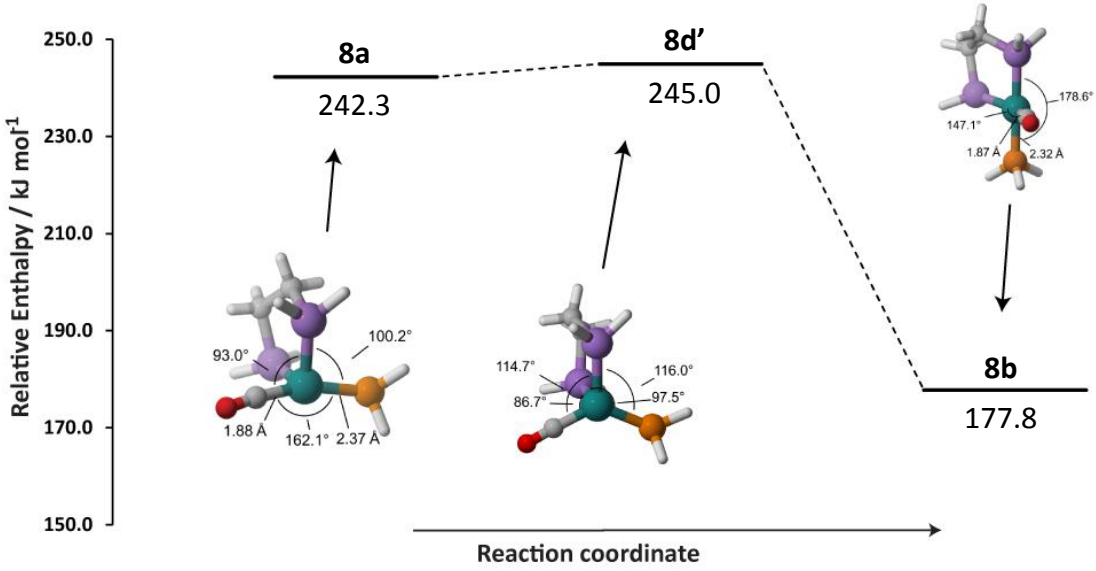

Figure 2.20: Geometry and enthalpies for the transition state linking the two singlet 16-electron isomers of $Ru(CO)(dhae)(PH_3)$ (**8a** and **8b**)

The use of *in-situ* photolysis for initiation with $Ru(CO)_2(dpae)(PPh_3)$ (**A2**) led to the detection of two isomers of $Ru(H)_2(CO)(dpae)(PPh_3)$ (**A7a** and **A7b**) and so reactions are possible where the phosphine group is retained in the complex. The results here show that CO loss from **2a** will occur primarily through 16-electron intermediate **8b**. The potential geometries of the subsequent hydrogenation products of $Ru(H)_2(CO)(dhae)(PH_3)$ were modelled and structures obtained with similar geometries to those identified with the phosphorus analogue.[143] Two isomers were located, both with one hydride occupying a site *trans* to one arsenic centre and *cis* to the other with the other hydride is *cis* to both arsenics. These two isomers differ in the location of the PH_3 and CO ligands; in **7a** the PH_3 is *trans* to an arsenic whereas in **7b** it is *trans* to a hydride. Interestingly, these two isomers have very similar relative energies. The third possible isomer **7c** has both hydrides *trans* to arsenic with the carbonyl *trans* to the phosphine. The fourth isomer **7d** has the hydrides in a *trans* configuration with the arsenic centres *trans* to the carbonyl and the PH_3 group. Both **7c** and **7d** are less stable than **7a** or **7b**. The thermodynamic values for the formation of these complexes can be found in Figure 2.21.

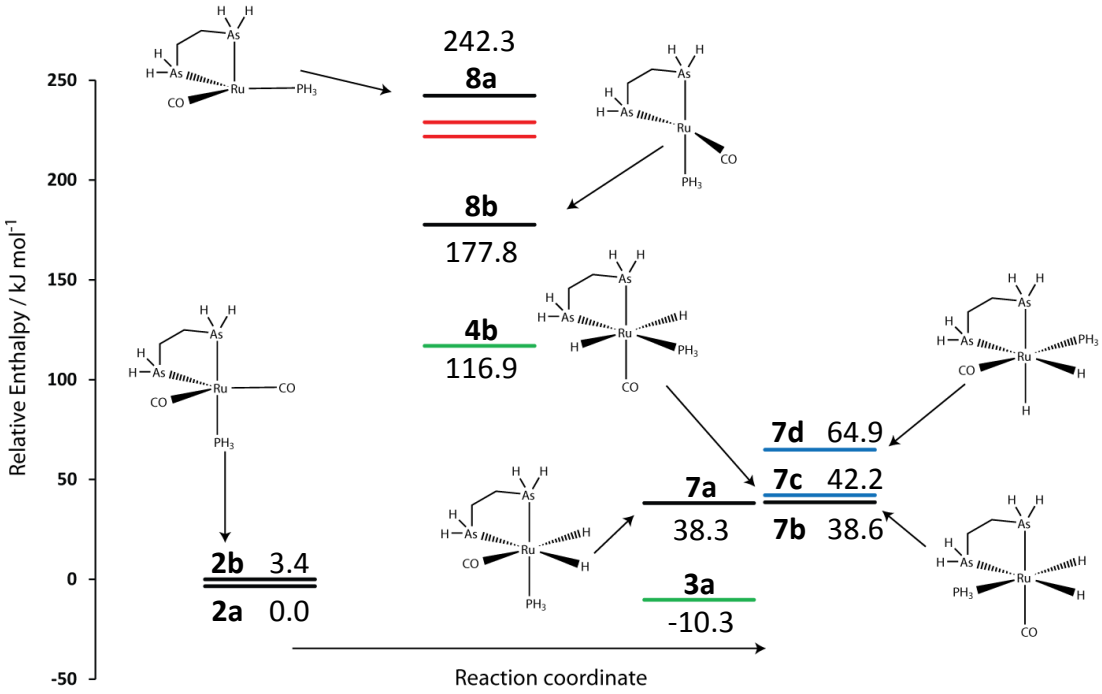

Figure 2.21: Relative enthalpies of intermediates and hydrogenation products from $Ru(CO)_2(dhae)(PH_3)$. The unlikely triplets **8a**^{3} and **8c**^{3} are shown in red, the dihydrides **7c** and **7d** inconsistent with experimental data in blue. The intermediate **4b** and dihydride **3a** formed by PH_3 loss are included to show the likely thermal reaction route (in green). The intermediates and products in black are likely to be accessible via photochemical initiation

This figure also shows how these intermediates react with H_2. It is clear that the reactivity of **8b** dominates with both **7a** and **7b** reflecting the preferred reaction products if CO is lost. However, **3a** would be the preferred product if PH_3 is lost. Experimentally, when this reaction is initiated thermally, **A3** is seen but under irradiation **A7a** and **A7b** are observed in the ratio 11:1, consistent with these theoretical findings.

The relative energies of **7a** and **7b** reveal their formation is unfavourable from **2a** and **2b**. This was also calculated for the formation of dihydride **3a** from **1** in Section 2.3.3. The stability of **7a** and **7b** will also rely on the loss of CO into solution, and the need of photolysis for their formation also reduces the likelihood for their reverse reaction (providing **7a** and **7b** are photo inactive). The favourable enthalpy change for the formation of **3a** from **2a** and **2b** is also consistent with experimental observations.

When the full ligand system is introduced, the thermodynamic values and geometries obtained are similar, with some notable differences. The relative enthalpies for the simple model and the full model are compared in Table 2.6. It should be noted that the values are all given relative to the lowest energy geometry (**2a**, with the simple, **2b** with the full model).

Table 2.6: Comparison of the enthalpies and free energies for the reaction intermediates and products from **2a** and **2b** for the simplex and full ligand systems. Values are relative to **2a** for the simple model, **2b** for the full model; values are in kJ mol^{-1}

			Simple Model		**Full Model**	
Label	**Electronic State**	**Formed from**	**ΔH**	**ΔG**	**ΔH**	**ΔG**
8a	Singlet	**2a**	242.3	196.7	195.5	159.2
$8a^3$	Triplet	**2a**	228.9	178.3	221.6	163.5
8b	Singlet	**2b**	177.8	131.8	177.1	123.3
$8c^3$	Triplet	**2b**	221.8	171.6	221.9	166.4
7a	Singlet	**8b**	38.3	32.4	29.0	21.8
7b	Singlet	**8b**	38.6	31.2	50.1	46.5
7c	Singlet	No direct route	42.2	35.5	65.1	75.2
7d	Singlet	No direct route	64.9	57.6	49.1	53.2

The difference in stability of the starting complex with the two model systems has already been noted. For the 16-electron intermediates, similar stabilities are calculated for **8a**[3], **8b** and **8b**[3], whereas the value for **8a** is significantly lower. This arises from an interaction of the phosphine ligand with the metal centre. The geometries of **8a** and **8b** are illustrated in more detail in Figure 2.22.

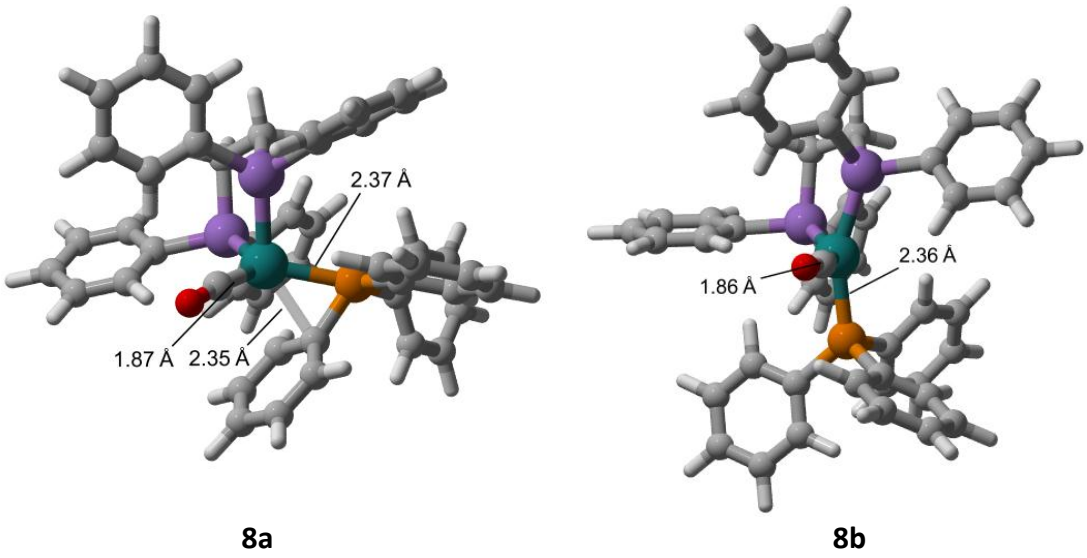

Figure 2.22: Illustrations of the geometries of the 16-electron intermediates **8a** and **8b** with the full model system

With the full model, **8b** maintains the geometry obtained with the simple model; for **8a** an interaction between the ruthenium centre and a phenyl ring in PPh_3 is present. This results in the formation of a trigonal bipyramidal geometry, with the phenyl ring occupying an axial position, which stabilises intermediate. With the simple system, **8a** was calculated to be the least stable intermediate. With the full model, this interaction is not strong enough to stabilise the geometry satisfactorily, as intermediate **8b** is still more stable than **8a** despite this stabilisation.

The 18-electron products from the hydrogenation of these intermediates (**7a-d**) show similar values but there is disagreement between the simple and full model systems. **7a** is still calculated to be the most stable geometry of $Ru(H)_2(dpae)(CO)(PPh_3)$ but it is the most stable geometry by a considerable amount (*ca.* 20 kJ mol^{-1}). This can be attributed to steric effects, as the phosphine group is only *cis* to one end of the dpae ligand; the other geometry with this alignment has the hydrides in an unfavourable *trans* arrangement (**7d**).

Both **7b** and **7c** are less stable than **7a** which can be attributed to this steric effect. The relative stabilities of **7c** and **7d** are reversed in the full system; this is likely to arise from the steric crowding in **7c** compared to **7d**. This was confirmed by the use of models with increasing numbers of phenyl groups present; models of **7c** and **7d** with structures of $Ru(CO)_2(dhae)(PPh_3)$ and $Ru(CO)_2$(bis-hydridophenylphosphinoethane)(PPh_3) still show **7c** as more stable than **7d**. These findings have shown that the intermediates and pathways identified so far in this work can be satisfactorily modelled by the simple model, but care needs to be taken for bulkier ligands like PH_3/PPh_3 – the steric and electronic effects influence the stability of important geometries. For the dpae/dhae ligand, only small influences are identified.

The previous work on the phosphorus analogues of these complexes postulated that the approach of the incoming dihydrogen is barrierless and that the H_2 unit aligns with the equatorial and axial planes of the lowest isomer of $Ru(CO)(dppe)(PPh_3)$ to form the two isomers.[143] Work by Eisenstein and co-workers also found that the approach of H_2 to $Ru(PH_3)_4$ was also barrierless.[150] It was found that at around 1.84 Å the H_2 unit started to re-orient into an η^2-mode followed by H-H bond elongation at 1.64 Å resulting in the dihydride species. The approach of H_2 to **8b** leads to the formation of both **7a** and **7b** depending on the orientation of addition. Figure 2.23 illustrates how **7a** is formed in this process.

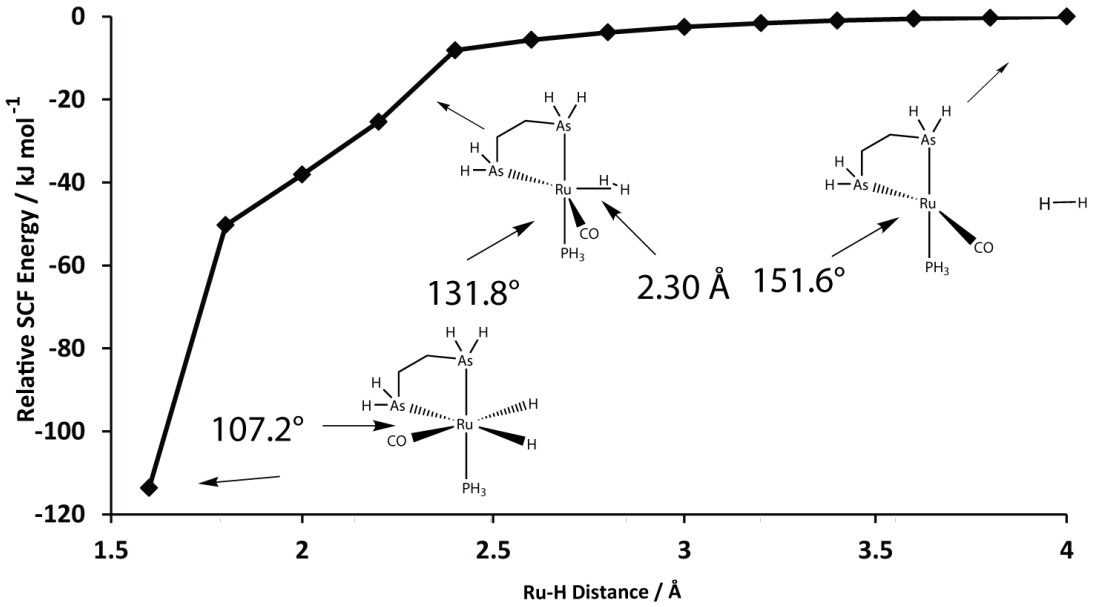

Figure 2.23: Reaction profile for the approach of dihydrogen to 16-electron **8b** and formation of **7a**

The bending of the As-Ru-CO bond angle in **8b** from 180 degrees in a square planar geometry to 147.0° here results in the favoured addition of dihydrogen across this axis; this results in the dominant isomer as **7a**.

The use of photochemical initiation with $Ru(CO)_2(dpae)(PPh_3)$ (**2**) led to the detection of dihydrides **A7a** and **A7b** whereas the thermal initiation led to primarily the dihydride **A3**. This is rationalised as arising from the lower relative energy for loss of PH_3 of +117 kJ mol^{-1} compared to +178 kJ mol^{-1} for the loss of a carbonyl ligand under thermal conditions.

2.3.7.1 Formation of 14-electron Ru(dpae)(PPh_3)

It has been postulated that a 14-electron intermediate is important when photochemical initiation is used with $Ru(CO)_2(dppe)(PPh_3)$ and $Ru(CO)_3(PPh_3)_2$.[142, 143] Two potential 14-electron intermediates can be formed from $Ru(CO)_2(dpae)(PPh_3)$ (**A2**); Ru(CO)(dpae) (modelled as **5a–5b^3** when modelled with the simple ligand system) and Ru(dpae)(PPh_3). Using the model systems, whereas the enthalpy of dominant **5a** relative to **1** is +398 kJ mol^{-1}, the relative enthalpy of this 14-electron complex to **2a** is lower at +351 kJ mol^{-1} arising from the lower bond energy of Ru-PH_3 compared to Ru-CO. Three geometries for Ru(dhae)(PH_3) were located as **9a**, **9a^3** and **9b^3**. The singlet state **9a** has a geometry where the PH_3 group occupied a site *cis* to one arsenic centre (bond angle of 91.0°) and approximately *trans* to the other, with a P-Ru-As bond angle of 154.6°. Triplet state **9a^3** has a similar geometry to **9a** but PH_3 forms a larger bond angle with one *trans* arsenic at 171.2° whilst the *cis*-arsenic bond angle is greater at 103.2°. The third isomer **9b^3** adopts a different geometry, where the PH_3 group lies *cis* to both arsenic centres, with bond angles of 103.5° and 100.5°. These geometries are illustrated in Figure 2.24.

The energies of these intermediates were found to sit closely together, differing in enthalpies by only 17 kJ mol^{-1}, with triplet **9a^3** being the lowest in energy at +409 kJ mol^{-1}, triplet **9b^3** slightly higher at +413 kJ mol^{-1} and the singlet **9a** the highest at +426 kJ mol^{-1}. Singlet **9a** is likely to dominate if Ru(dhae)(PH_3) is formed under photolysis, as its formation does not require a spin-flip transition. With the full model, the enthalpies and free energies of the triplet species are similar, with values of 407.3 and 305.0 kJ mol^{-1} for **9a^3**, and 412.4 and 342.5 kJ mol^{-1} for **9b^3** respectively. The singlet state is significantly lower in both

enthalpy and free energy, with values of 382.5 and 289.5 kJ mol^{-1} respectively. This arises from an interaction of a phenyl ring in the PPh_3 group with the metal centre to form a distorted square planar geometry. This interaction will be weak and unlikely to prevent any further reaction; it does increase the likelihood of reaction through the singlet state rather than a triplet state and so potentially preserve polarisation from *p*-H_2.

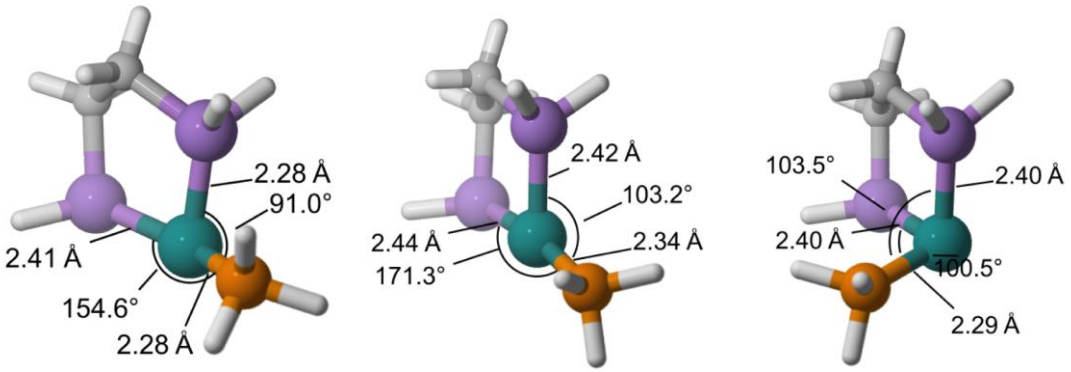

9a
429.0
(339.4)

9a^3
412.0
(314.3)

9b^3
416.2
(321.6)

Figure 2.24: Geometries of the 14 electron intermediates of Ru(dhae)(PH_3) (**9a**, **9a^3** and **9b^3**). Relative enthalpies are included, with relative free energies in brackets; values are in kJ mol^{-1}

Singlet **9a** can undergo reaction with CO or H_2, with CO forming the 16-electron singlet Ru(CO)(dhae)(PH_3) as **8b**. The addition of H_2 to **9a** results in barrierless oxidative addition and forms Ru$(H)_2$(dhae)(PH_3) as **10a** with a change in enthalpy of -183.2 kJ mol^{-1}. The oxidative addition is perpendicular to the As-Ru-P bond and the resultant complex has one hydride *trans* to the dhae ligand and the second hydride *trans* to a vacant site on the metal. The addition of CO to **10a** was found to be favourable, with an enthalpy change of -204.1 kJ mol^{-1} forming the major isomer **7a** of Ru$(H)_2$(CO)(dhae)(PH_3). The addition of PH_3 to Ru$(H)_2$(CO)(dhae) (**6a**) could also potentially occur if **6a** is formed from Ru(CO)(dhae) (**5a**); this would require the reaction of this intermediate with free phosphine in solution and would result in the minor isomer **7b** to form. This pathway could be a minor competing pathway for the formation **7b**. The work on the related complex Ru$(CO)_2$(dpae)(PPh_3) (**P3**) proposed that a pathway where both PPh_3 and CO were lost competes with the loss of both CO and PPh_3.[143] This proposal is consistent with the results reported here; the loss of PPh_3 and CO to form **5a** is of lower energy and leads to both **3a** and **7a** depending on the

pathways that then follow, with the recoordination of the phosphine more likely than the addition of dihydrogen. The lower energy CO loss from **2a** or **2b** results in the formation of intermediate **8b** which can then form the dihydride species **7a** and **7b**, consistent with experimental evidence. The dominant pathways for the reaction of $Ru(CO)_2(dhae)(PH_3)$ via 14- and 16-electron complexes are illustrated in Figure 2.25; red routes indicate CO loss and green PH_3 loss. Only **4b** is predicted to be thermally accessible.

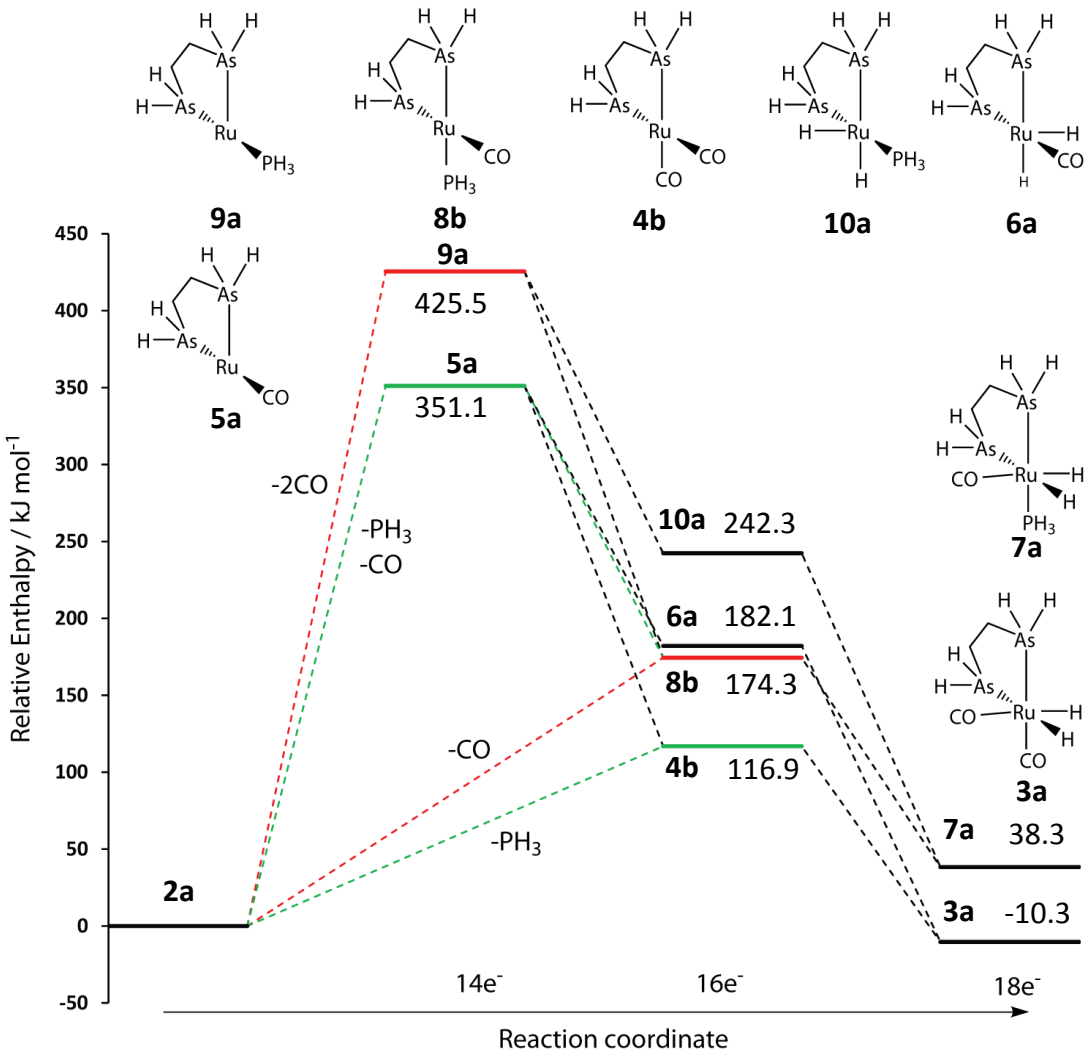

Figure 2.25: Primary reactions of $Ru(CO)_2(dhae)(PH_3)$ with hydrogen through singlet 14-electron intermediates. Enthalpies are shown for intermediates and products red routes indicate CO loss and green PH_3 loss.

2.3.7.2 Discussion into the reactions of $Ru(CO)_2(dpae)(PPh_3)$ with H_2

The main reactions formed from the ligand loss from $Ru(CO)_2(dhae)(PH_3)$ via electronic singlet species are illustrated in Figure 2.25. The dominant 16-electron species generated are **4b** (from PH_3 loss by thermal initiation) and **8b** (from CO loss by photochemical initiation) and these lead to the formation of $Ru(H)_2(CO)_2(dhae)$ as **3a** and $Ru(H)_2(CO)(dhae)(PH_3)$ as **7a** as the dominant products, in agreement with experimental evidence. The generation of 14-electron intermediates can involve both the formation of **5a** (loss of one CO ligand and the phosphine) or **9a** (loss of both carbonyls); these lead to the formation of the observed complexes **3a** and **7a** as the dominant complexes. The reactions of $Ru(CO)_2(dhae)(PH_3)$ were identified to be more facile than the reactions of $Ru(CO)_3(dhae)$ (**1**) due to the lower bond energy of the metal phosphine-bond in **2a** (phosphine in the equatorial plane) compared to the metal-CO bond in **1**.

2.3.8 Fluxional behaviour of the dihydride $Ru(H)_2(CO)(dpae)(PPh_3)$

The dihydride $Ru(H)_2(CO)_2(dpae)$ (**A3a**) was experimentally found to undergo hydride exchange; this process has been discussed in detail, with six potential processes and transition states identified. The fluxional behaviour of $Ru(H)_2(CO)(dpae)(PPh_3)$ (**A7a**) was also investigated by NMR methods by Adams *et al.* No hydride exchange was observed, but elimination of dihydrogen was observed. This latter process was examined in further detail by the use of EXSY experiments and the activation parameters of this process obtained from the respective Eyring plot were $\Delta H^{\ddagger} = 109 \pm 12$ kJ mol^{-1} and $\Delta S^{\ddagger} = 65 \pm 34$ J mol^{-1} K^{-1}. This contrasts from the investigations into the phosphine analogue of **A7a** as $Ru(H)_2(CO)(dppe)(PPh_3)$, where the activation parameters for hydride exchange were calculated to be $\Delta H^{\ddagger} = 95 \pm 6$ kJ mol^{-1} and $\Delta S^{\ddagger} = 26 \pm 17$ J mol^{-1} K^{-1}.[143] Further experiments showed no exchange in the ^{31}P spectra obtained in ^{31}P-2D-NOESY NMR experiments and no elimination of dihydrogen was observed. A similar theoretical investigation was undertaken to examine the fluxional nature of **7a**. The same types of interchange were attempted as for $Ru(H)_2(CO)_2(dhae)$ (**3a**) and 8 separate transition states located.

The first pair of transition states located is the clockwise and anticlockwise rotation of an η^2-dihydrogen unit in a square based pyramid geometry. These two transition states are the equivalent of **3xA'** and **3xB'** in Section 2.3.4. In the clockwise rotation transition state (**7xA'**), one hydride does not interchange and remains *trans* to an arsenic centre, the other hydride changes from a *trans*-CO to a *trans*-PH_3 position. In the anticlockwise rotation transition state (**7xB'**), one hydride changes from being *trans*-CO to *trans*-As whereas the other hydride changes from *trans*-As to *trans*-PH_3. Interestingly, the two transition states have virtually the same relative energies, in contrast to that found for **3xA'** and **3xB'** given in Table 2.2.

Two additional transition states involving η^2-dihydrogen units have been located here. Transition states **7xC'** and **7xD'** have trigonal bipyramidal geometries with one arsenic centre in the axial position (*trans* to the H_2 unit) and the other in the equatorial position. A subtle alignment difference in the H_2 unit creates two separate transition states; the unit in **7xC'** is parallel to the direction of the carbonyl ligand whereas the direction is perpendicular to the carbonyl ligand in **7xD'**. These two transition states do not relate to **7a** and instead link **7b** with **7c**.

The fifth transition state (**7xE'**) has a similar trigonal bipyramidal geometry except that the hydrogen ligands are coordinated as hydrides ligands rather than in a dihydrogen unit, with a separation of 1.67 Å. This distance is slightly greater than that defined for a compressed dihydride of 1.6 Å by Ess and Devarajan, which discusses transition state geometry for dihydrogen activation.[194] The PH_3, CO and one end of the dhae ligand form a triangular face, with the plane of the hydrides sitting perpendicular to that of the Ru-P bond. The motion of the imaginary frequency is for the movement of the two hydrides across the equatorial Ru-As bond, linking **7a** with **7b**. The sixth transition state (**7xF'**) has a similar trigonal bipyramidal geometry with no indication of the dihydrogen unit (separation of 1.65 Å). This geometry differs to **7xE'** as the hydride ligand plane is perpendicular to the Ru-As bond. The motion of the imaginary frequency was for the movement of the two hydrides across the equatorial Ru-PH_3 bond, linking **7a** with **7c**.

The seventh transition state (**7xG'**) also adopts a trigonal bipyramidal geometry except that this geometry has the two arsenic centres in the equatorial plane (with the bite angle of

dhae at 85.4° imposing strain on the geometry) along with PH_3. This transition state does not have a dihydrogen unit and the two hydrides are separated by 1.65 Å. The motion of the imaginary frequency is a 'swing' of the two hydride across the Ru-PH_3 bond, interconverting **7a** to another isomer of **7a**. The final transition state (**7xH'**) is consistent with the Ray-Dutt mechanism with the hydrides being significantly separated by 3.06 Å. The imaginary frequency for this transition state leads to one hydride moving from *trans* to arsenic to the position that the carbonyl had occupied. This transition state links dihydride **7a** with dihydride **7d**. The detailed illustrations of the geometries of these transition states are shown in Figure 2.26.

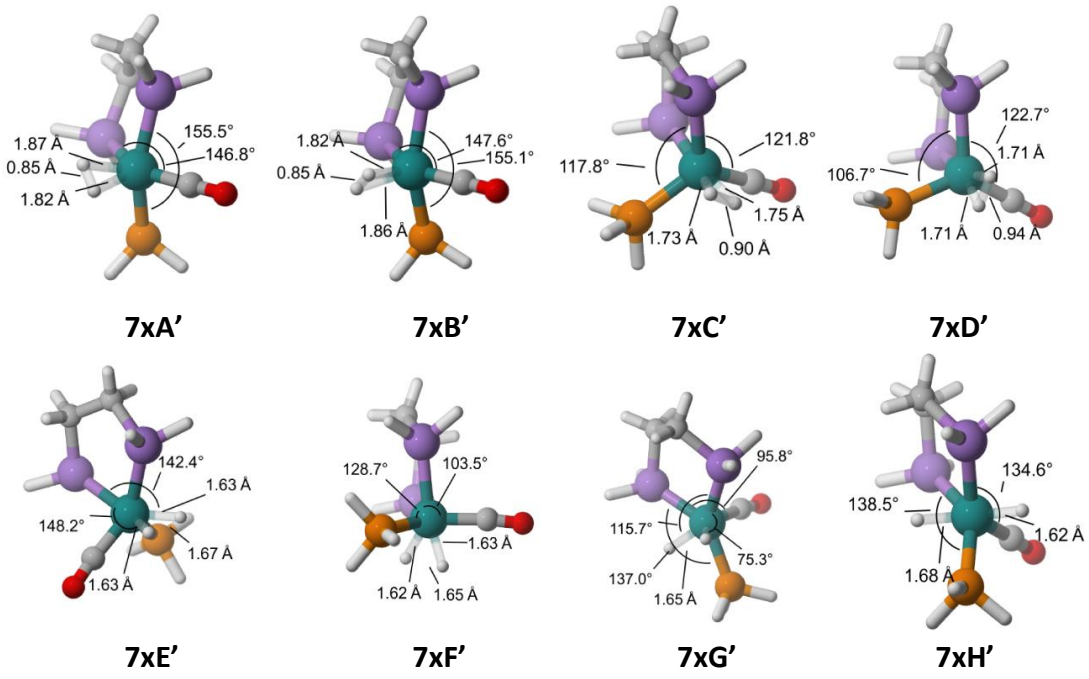

Figure 2.26: Detailed illustrations for the eight identified transition states for the interchange between isomers of $Ru(H)_2(dhae)(CO)(PH_3)$ (**7a-d**)

The relative thermodynamic changes for these eight transition states are shown in Table 2.7, Figure 2.27 and Figure 2.28 respectively. The relative energies of **7xC'** and **7xD'** are shown in italics in Table 2.7 because these energies are relative to **7a** but the transition states do not explicitly involve this isomer.

The relative energies obtained from this investigation reveal no obvious reason why compound **7a** showed no hydride exchange in the NMR experiments. The energies of the

main routes of rearrangement via **7xA'** and **7xB'** are similar to the rearrangement routes identified in Section 2.3.4 for $Ru(H)_2(CO)_2$(dhae) (**3a**) and so hydride exchange should be predicted.

Table 2.7: Relative energies for the eight possible transition states involved in the fluxional nature of $Ru(H)_2(CO_2)$(dhae)$(PH)_3$

Transition State	$\Delta E_{SCF+ZPE}$ / kJ mol^{-1}	ΔH / kJ mol^{-1}	ΔG / kJ mol^{-1}	Linking
7xA'	+88.9	+88.3	+92.0	**7a** to **7b**
7xB'	+89.3	+88.9	+92.2	**7a** to **7b**
7xC'	*+95.0*	*+95.0*	*+95.0*	**7b** to **7c**
7xD'	*+87.0*	*+86.2*	*89.6*	**7b** to **7c**
7xE'	+92.9	+92.4	+93.8	**7a** to **7b**
7xF'	+98.0	+97.7	+99.4	**7a** to **7c**
7xG'	+108.2	+107.7	+109.5	**7a** to **7a**
7xH'	+86.0	+84.9	+89.1	**7a** to **7d**

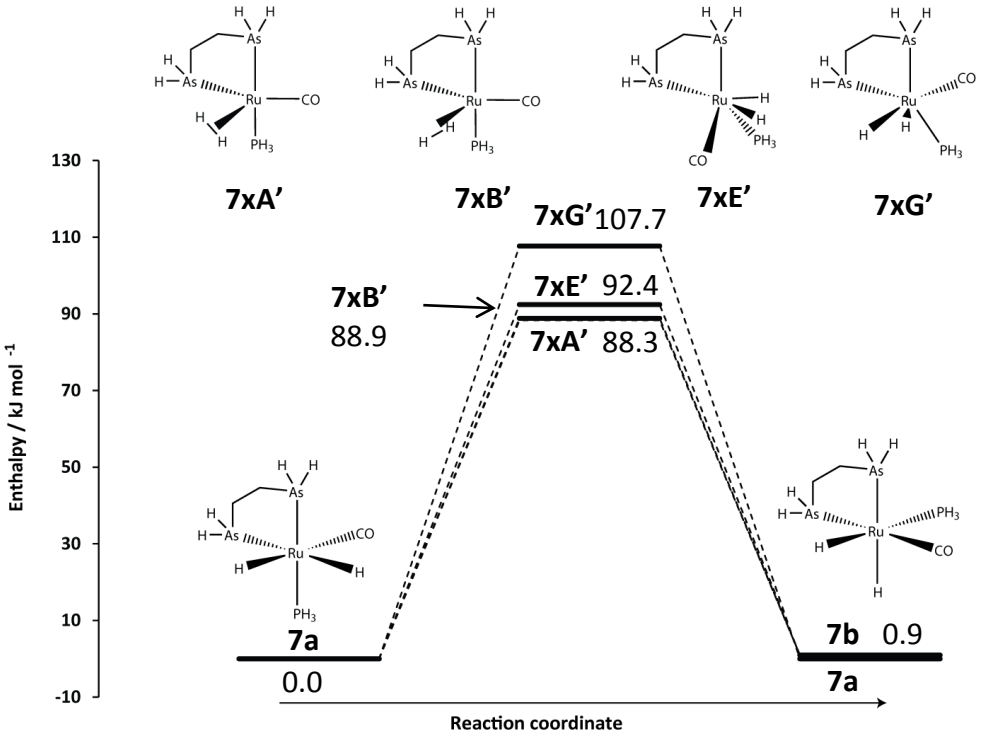

Figure 2.27: Relative enthalpy profiles for transition states involving η^2-H_2 units, for the fluxional nature of $Ru(H)_2(CO)$(dhae)(PH_3)

The calculated relative energies for the loss of H_2 from **7a** to form **8b** are $\Delta H^{\ddagger}$ = 139.5 and $\Delta G^{\ddagger}$ = 99.3 kJ mol^{-1} and so these values offer one reason for the observed reductive elimination of H_2 observed in the NMR experiments. However, the same values for $Ru(H)_2(CO)_2(dhae)$ (**3a**) from the theoretical calculations are $\Delta H^{\ddagger}$ = 127.2 and $\Delta G^{\ddagger}$ = 87.3 kJ mol^{-1}. These calculations therefore predict that **7a** is not more likely to undergo reductive elimination of H_2 than **3a**.

The change of the bidentate ligand to dpae from dppe is unlikely to hinder exchange and so the lack of evidence from the NMR data for **A7a** may not exclude exchange. The use of $AsRH_2$ in the models will change the electronic density at the metal centre and neglect the sterics already identified as causing discrepancies with the simple model and experimental evidence.

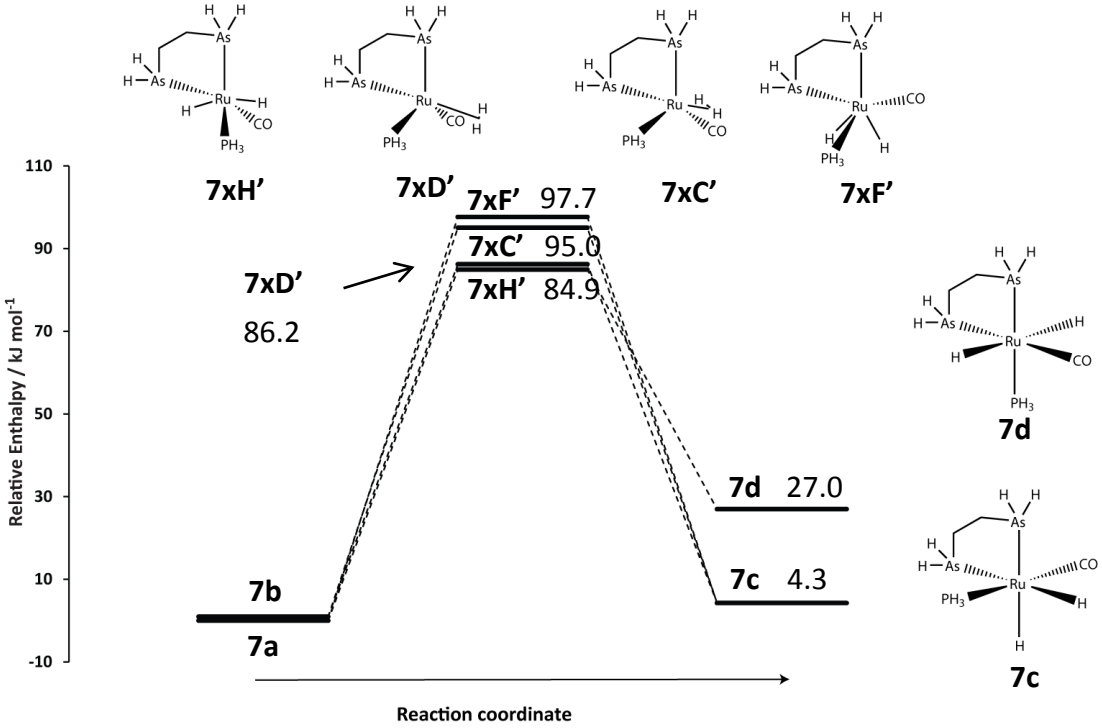

Figure 2.28: Relative enthalpy profiles for additional transition states for the fluxional nature of $Ru(H)_2(CO)(dhae)(PH_3)$

Selected transition states were modelled with the full system; the transition states calculated to have a high barrier (**7xC'**, **7xF'** and **7xG'**), did not involve **7a**, (**7xD'**) or led to **7c** or **7d** (**7xH'**) were not modelled. The difference in stabilities of **7c** and **7d** compared to **7a** and **7b** was previously described in Section 2.3.7 and so even if these transition states were

possible their pathways would not be dominant. Transition states **7xA'**, **7xB'** and **7xE'** were therefore modelled. The thermodynamic values were found to increase for all three transition states. For **7xA'**, the relative enthalpy and free energy rose from 88.3 and 92.0 kJ mol^{-1} to 113.0 and 133.1 kJ mol^{-1} respectively. For **7xB'**, the relative enthalpy and free energy rose from 88.9 and 92.2 kJ mol^{-1} to 115.8 and 145.5 kJ mol^{-1} respectively. For **7xC'**, the relative enthalpy and free energy rose from 92.4 and 93.8 kJ mol^{-1} to 109.4 and 136.7 kJ mol^{-1} respectively. These values are significantly higher than those observed for in the rearrangements of **3a** (81.1-86.9 kJ mol^{-1} enthalpy and 101.9-102.7 kJ mol^{-1} free energy changes). Additionally, for **3a** the reductive elimination of H_2 with the full model (forming **4b**) was predicted to result in changes in enthalpy and free energy of 126.0 and 84.6 kJ mol^{-1} respectively; here the formation of **8b** from **7a** with the full model changes from respective values of 139.5 and 99.3 kJ mol^{-1} with the simple model to 153.0 and 109.3 kJ mol^{-1}. This reductive elimination process now has a lower free energy change than any modelled rearrangement transition state and so is consistent with the experimental observations.

2.3.8.1 Conclusions into the fluxional nature of $Ru(H)_2(CO)_2$(dpae) and related complexes

The work presented has revealed that the interconversion of different geometries of $Ru(H)_2(CO)_2(dhae)(PH_3)$ is likely when using the model complexes examined here. This is inconsistent with experimental evidence. The use of the full model finds that these rearrangement pathways become less favourable and that the reductive elimination of H_2 becomes more likely to dominate. Similar calculations of the full model with $Ru(H)_2(CO)_2(dppe)(PPh_3)$ could be undertaken to examine whether similar pathways will compete with the reductive elimination. It is noted that this is not a trivial task. The activation parameters for this complex containing dppe were measured experimentally to be $\Delta H^{\ddagger}$ = 95 ± 6 kJ mol^{-1} and $\Delta G^{\ddagger}_{350}$ = 86.2 ± 0.1 kJ mol^{-1} and so the rearrangements are likely to be more facile than the reductive elimination, which had a comparable $\Delta G^{\ddagger}_{350}$ of 96 kJ mol^{-1}. It is clear how a role for the full model is demonstrated here

2.3.9 De-chelation of the bidentate arsino ligand

A further ligand loss possibility was proposed by Dunne *et al.* for the related phosphorus complex $Ru(CO)_3(dppe)$.[142] This was the de-chelation of the bidentate dppe ligand to form $Ru(H)_2(CO)_2(\kappa^1\text{-dppe})(sol)$ and ultimately $Ru(H)_2(CO)_2(sol)_2$ where pyridine (a coordinating solvent) was used. Hydrides with chemical shifts in the region of -12 to -16 ppm were observed in ^1H NMR spectra and assigned to hydrides *trans* to nitrogen. This de-chelation was also proposed for the complex $Ru(CO)_2(dppe)(PPh_3)$ where $Ru(H)_2(CO)(\kappa^1\text{-dppe})(PPh_3)_2$ was proposed as a minor product (at ca. 5% of the level of $Ru(H)_2(CO)(dppe)(PPh_3)$ as **P4a**) under photolysis in benzene. This complex allowed characterisation to determine that three inequivalent phosphorus centres coupled to the hydride ligands, and that four phosphorus centres were present – one of these was consistent with the shift of a non-coordinated centre. The potential for $Ru(CO)_3(dpae)$ (**A1**) and $Ru(CO)_2(dpae)(PPh_3)$ (**A2**) to undergo such a reaction was investigated.

2.3.9.1 De-chelation with $Ru(CO)_3(dpae)$ (A1)

The de-chelation of the dhae ligand from the complex $Ru(CO)_3(dhae)$ (as **1**) was modelled and found to proceed through transition state **1b'**, which has the de-chelated arsenic at a distance of 4.8 Å from the metal centre. This creates a barrier of 107.3 kJ mol^{-1} and the pathway ends with a change in enthalpy of +93.0 kJ mol^{-1} from **1**, and a free energy of +101.3 kJ mol^{-1}. These values are lower than those for the loss of a CO ligand (forming **4b**). Only one geometry for the de-chelated complex was located, as **1b**. This intermediate could potentially then undergo hydrogenation to form $Ru(H)_2(CO)_3(\kappa^1\text{-dhae})$ (**1c**). This hydrogenation product was calculated to have a relative enthalpy of -15.3 kJ mol^{-1} relative to **1**, with a free energy of +5.2 kJ mol^{-1} (which becomes accessible when *p*-H_2 is present in excess by using a headspace of 3 atm). The bond enthalpy for the carbonyls in the equatorial plane (*trans* to the hydrides) is expected to be lower in **1c** than in the 5-coordinate starting material (**1**). However, the difference is minimal with the bond enthalpy for the carbonyl *trans* to hydride being slightly higher at +170.6 kJ mol^{-1} compared to enthalpy for an carbonyl in the equatorial trigonal plane, at +163.6 kJ mol^{-1} in **1**. The free energy for this loss is also higher at +125.2 kJ mol^{-1} compared to +117.7 kJ mol^{-1} for **1**. Such a loss of a carbonyl ligand leads to the formation of the square-based pyramidal $Ru(H)_2(CO)_2(\kappa^1\text{-dhae})$ as **3d**, with the vacant site *trans* to a hydride ligand.

The recoordination of the free end of the κ^1-dhae ligand could then occur through transition state **3d'**, as the vacant site is in a *cis*-position to the coordinated end. This occurs through a barrier of 6.1 kJ mol^{-1} and leads to the formation of **3a**. This coordination is favourable, with an enthalpy change of -118.9 kJ mol^{-1}. The coordination of dihydrogen to the 5-coordinate d^6-complex $Ru(H)_2(CO)_2(\kappa^1$-dhae) **3d** could also occur resulting in a dihydrogen complex. This coordination has a change in enthalpy of -71.8 kJ mol^{-1} with the free energy being lower at -32.9 kJ mol^{-1}, forming **6c**. This means that this coordination is possible, but would likely be reversible, competing with the recoordination of the free end of the κ^1-dhae ligand. These thermodynamic changes are illustrated in Figure 2.29. The change in enthalpy for the loss of CO from **1** and **1c** are similar, at 163.6 and 170.6 kJ mol^{-1} respectively. Whilst the loss of a CO ligand from **1c** could be facilitated by the *trans* effect of the hydride ligands, the formal change in electron count for the ruthenium from d^8 to d^6 upon oxidative addition of dihydrogen to form **1c** results in similar bond strengths. It is possible that de-chelation with **3a** can also occur to form a second isomer of $Ru(H)_2(CO)_2(\kappa^1$-dhae) as **3e**; this will be discussed in Chapter 3.

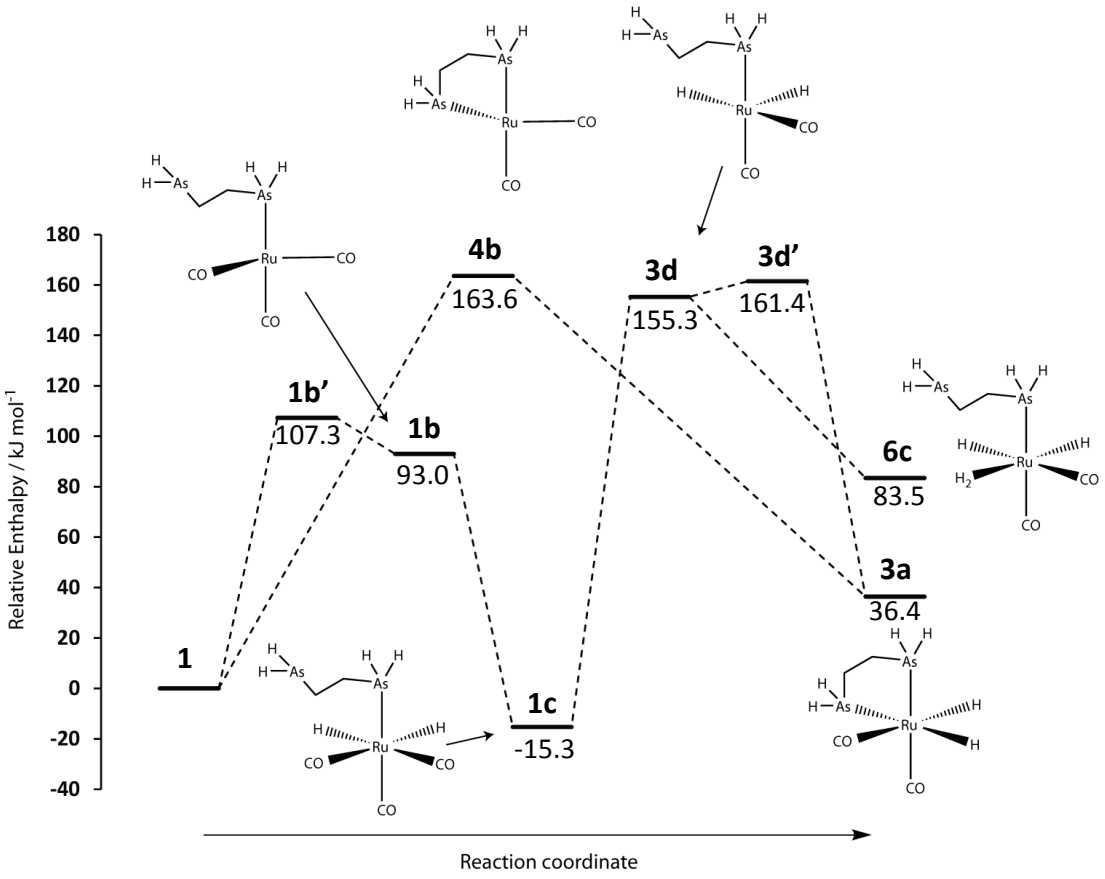

Figure 2.29: Relative enthalpy profile for carbonyl loss and unhooking pathway for **1** with dihydrogen

Experimental evidence found that the addition of CO to **A1** with *p*-H_2 led to the reduction of the dihydride signals under thermal initiation. This indicates that the primary route to form **3a** is via CO loss, which is less favourable according to these calculations. The chelate effect can be used to account for this discrepancy, primarily the model proposed by Schwarzenbach.[195] Whilst the bond strength of the ruthenium-arsenic ligand is lower than that of ruthenium-CO, because the dissociated end of dhae is held close to the metal, its effective concentration is significantly higher than that of any other reactive species, in this case H_2. As the reactions are based on collisions of molecules, the likelihood of any encounter will be for the re-coordination of the free end of the dhae ligand. The low barrier of 14.3 kJ mol^{-1} from **1b** to **1b'** means that the formation of **1b**, whilst possible, will ultimately result in the recoordination of the free end of dhae and reform **1**. The encounter with H_2 whilst de-chelated is possible but this will be a minor pathway. It should be noted that dihydride **1c** would not be likely to show and PHIP due to the symmetrical hydride ligands and lack of coupling to the arsenic centre.

2.3.9.2 De-chelation with $Ru(CO)_2(dpae)(PPh_3)$ (A2)

Whilst the de-chelation of the bidentate ligand is unlikely for reasons described here, Adams and Eguillor *et al.* proposed complexes for de-chelation products (**A5** and **A6**) from **A2**. Two geometries for Ru(κ^1-dhae)$(CO)_2(PH_3)$ were identified; both of these were butterfly geometries in keeping with the work presented here. Significantly, the change in dhae upon going to a monodentate form means that the *ct-L* isomer is now accessible. These two geometries are illustrated in Figure 2.30 along with selected bond lengths and bond angles.

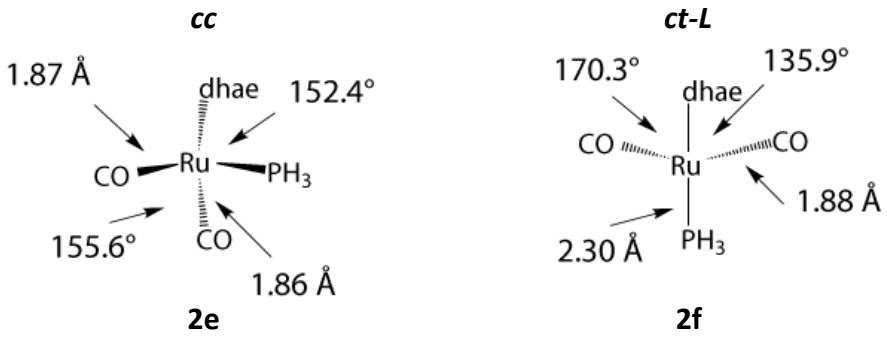

Figure 2.30: 16-electron intermediates formed from de-chelation of the dhae ligand in Ru$(CO)_2(\kappa^2$-dhae$)(PH_3)$

Intermediate **2e** has a relative enthalpy of +95.6 kJ mol^{-1} and free energy of +79.7 kJ mol^{-1} above **2a**; **2f** has similar values of +93.6 kJ mol^{-1} and +77.7 kJ mol^{-1}. The bond enthalpy for PH_3 was previously calculated as +116.9 kJ mol^{-1} from **2a** which is higher than the enthalpies for the two de-chelation possibilities. The free energies for the phosphine loss (+71.0 kJ mol^{-1}) and de-chelation are similar; the formation of two species by PH_3 loss is likely to be responsible for the lower free energy for PH_3 loss despite the lower bond strengths of Ru-As. With the full model, **2e** is calculated to be 109.0 kJ mol^{-1} above **2b** (free energy of 104.9 kJ mol^{-1}) and **2f** is 85.6 kJ mol^{-1} above **2b** (free energy of 68.7 kJ mol^{-1}). These values compare to the loss of PPh_3 from **2b** of 117.1 and 50.7 kJ mol^{-1} in terms of enthalpy and free energy respectively (forming **4b**). This means that **2f** will be the dominant isomer of $Ru(H)_2(CO)_2(\kappa^1\text{-dhae})(PH_3)$ and so only pathways from this will be considered here. The formation of **2f** proceeds via **2b'** which results in a barrier for de-chelation of 99.0 kJ mol^{-1} (free energy barrier of 92.9 kJ mol^{-1}). The reverse reaction with **2f** through **2b'** has a barrier of only 5.4 kJ mol^{-1} and so the primary reactions from **2a** and **2b** is via phosphine loss.

The possible addition of dihydrogen to **2f** was found to be favourable and barrierless with two the formation of more dihydride species becoming possible. Addition across the CO-Ru-CO plane results in **10b** with an enthalpy change of -114.8 kJmol^{-1}. Addition across the bent κ^1-dhae-Ru-PH_3 plane results in **10c** with a change in enthalpy of -118.3 kJ mol^{-1}. A relaxed constrained optimisation revealed the preference of dihydrogen to add over the CO-Ru-CO plane preferentially, meaning **10b** will be the dominant isomer. Complex **10b** is notably more stable than the starting complex; it is also consistent with the experimentally observed complex **A5**. This means that the de-chelation route is likely to be possible, but significantly only as a minor pathway.

The loss of the phosphine ligand could occur from **10b** to form of $Ru(H)_2(CO)_2(\kappa^1\text{-dhae})$ as **3f**. This formation results in an enthalpy change of +188.9 kJ mol^{-1}, but **3f** cannot undergo direct re-coordination of the κ^1-dhae ligand directly as the vacant site is *trans* to this ligand. If this recoordination were to occur, a rearrangement would be required; the movement of a CO ligand into this vacant site creates a vacancy *cis* to the κ^1-dhae ligand. Whilst this rearrangement is favourable, (**3d** resulting in a reduction in enthalpy of -52.1 kJ mol^{-1}), the barrier for this proceeds through transition state **3f'** and creates a barrier of +62.6 kJ mol^{-1}. This pathway is therefore unlikely to occur. If **3d** were to be formed, it would then lead to

3a as previously identified. These unfavourable thermodynamic changes reveal **10b** to be a stable complex, consistent with the experimental complex **A5**. These complexes and thermodynamic changes are illustrated in Figure 2.31. Since this de-chelation pathway is a minor pathway, the formation of the minor isomer of **10c** is unlikely.

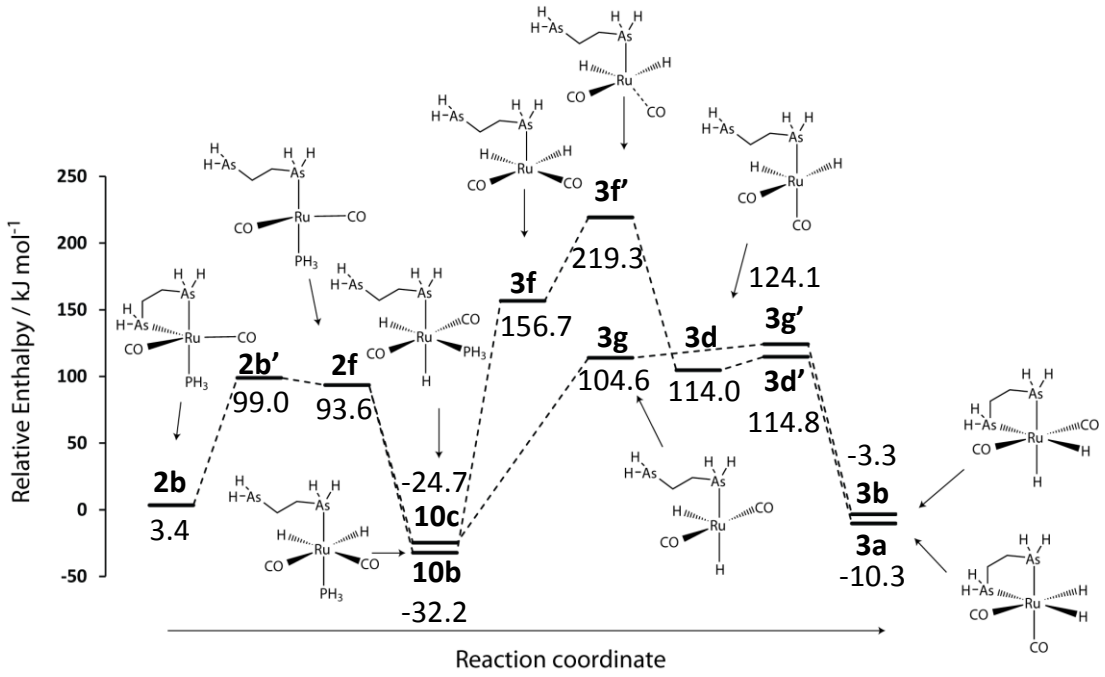

Figure 2.31: Relative enthalpy profile for reactions of **2b** (through **2f**) via initial de-chelation of dhae

When the full model is introduced, similar thermodynamic values are obtained; these are summarised in Table 2.8.

Table 2.8: Relative enthalpies (free energies in brackets) for pathways involving initial de-chelation from $Ru(CO_2)(dhae)(PH)_3$ and $Ru(CO_2)(dpae)(PPh_3)$. Values are in kJ mol^{-1}

Label		**Simple Model**		**Full Model**	
		Change	Value	Change	Value
2f	De-chelation	93.6 (77.1)	93.6 (77.1)	90.6 (76.5)	85.6 (68.7)
10b	H_2 addition	-125.7 (-84.6)	-32.2 (-7.5)	-110.8 (-69.9)	-25.2 (-1.2)
10c	H_2 addition	-118.2 (-82.1)	-24.7 (-5.0)	-94.4 (-48.4)	-8.7 (20.3)
3f	Phosphine Loss	188.9 (142.4)	156.7 (134.9)	196.3 (134.2)	171.1 (133.0)
3g	Phosphine Loss	138.7 (96.0)	114.0 (91.0)	145.4 (75.2)	136.6 (95.5)

The values from the simple model compare poorly with the full model, with some values underestimated and others over-estimated. The formation of **10c** is predicted to be less likely than with the simple system, as **10b** is significantly more stable. Dihydride **10b** is calculated to be more stable than **2b** in terms of enthalpy but about the same stability in terms of free energy. This could be the reason that the experimentally observed species **A5** is observed as a minor product; its formation is not significantly favourable from **2b**.

A similar investigation into de-chelation from $Ru(H)_2(CO)(dhae)(PH_3)$ (**7a**) reveals two pathways; one with the loss of an arsenic centre *trans* to PH_3 and the other *trans* to a hydride ligand. The de-chelation of arsenic *trans* to PH_3 was found to require an enthalpy change of +152.5 kJ mol^{-1} and free energy change of +135.8 kJ mol^{-1}. The other de-chelation pathway was found to be lower, with an enthalpy change of +116.1 kJ mol^{-1} and a free energy change of +100.3 kJ mol^{-1}. These values potentially indicate that the change in observed products when **2** is examined with *p*-H_2 is possibly linked to the lowering in energy of de-chelation of the dpae ligand. This could combine with the lower barrier for phosphine loss than carbonyl loss to make **2** more reactive than **1**.

2.3.10 Summary of the de-chelation of the bidentate arsino ligand

The thermodynamic values reported here show that de-chelation should be expected from the two complexes of $Ru(CO)_3(dhae)$ and $Ru(CO)_2(dhae)(PH_3)$ if only the thermodynamic changes from these models are considered. The lack of experimental observation for these possible processes contradicts these predictions (except for the minor complex **A5**). This is due to the chelate effect, where the most likely reaction if de-chelation occurs is the re-coordination of the free end of the ligand. In previous work on $Ru(CO)_3(dppe)$ (**P1**) the solvent used was pyridine, which is likely to be able to trap any de-chelated intermediate.[142] For $Ru(CO)_2(dppe)(PPh_3)$ (**P3**), the presence of PPh_3 in solution following liberation can essentially trap the de-chelated intermediate formed.[143] This trapping is less likely due to the concentration of free phosphine and accounts for this pathway leading to a significantly minor product. The addition of free PPh_3 to **A2** was also investigated by Adams and Eguillor – it was found that the formation of $Ru(H)_2(CO)_2(PPh_3)_2$ at elevated temperatures was possible, meaning that de-chelation and total displacement of dpae is possible.

2.3.11 Theoretical comparison to related systems

The reactions of $Ru(CO)_3$(dpae) (**A1**) and $Ru(CO)_2$(dpae)(PPh_3) (**A2**) could be similar to those of the phosphorus analogues (**P1** and **P3**), as the change in phosphorus centre for arsenic is subtle; it is worth noting that previous studies have found significant differences between the stability of observed isomers of $Ru(H)_2(CO)_2(PMe_2Ph)_2$ and $Ru(H)_2(CO)_2(AsMe_2Ph)_2$.[153] With these complexes, the *ccc* and *cct*-L geometries for the arsenic complex were observed in a 4:3 ratio whereas the phosphorus complex geometries are detected in the ratio 96:4.

To examine the change in reactions, the geometries and thermodynamic corrections were calculated for $Ru(CO)_3$(dhpe) and $Ru(CO)_2$(dhpe)(PH_3). The thermodynamic values obtained are compared to those previously identified as the dominant pathways in Table 2.9.

Table 2.9: Comparison of the thermodynamic values calculated for dominant pathways with $Ru(CO)_3$(dhLe) and $Ru(CO)_2$(dhLe)(PH_3) with L = P or As. All values are in kJ mol^{-1}

	Label	dhae complexes		dhpe complexes	
		ΔH	**ΔG**	**ΔH**	**ΔG**
$Ru(CO)_3$(dhLe) -CO	**4b**	163.6	117.7	159.5	113.0
$Ru(CO)_2$(dhLe) + H_2	**3a**	36.4	30.4	36.9	30.9
$Ru(CO)_3$(dhLe) de-chelation	**1b**	117.6	101.3	123.2	105.4
$Ru(CO)_3$(dhLe-κ^1) + H_2	**1c**	-15.3	5.2	9.5	34.0
$Ru(H)_2(CO)_2$(dhLe-κ^1) -CO	**3d**	159.3	136.8	177.2	163.6
$Ru(H)_2(CO)_2$(dhLe) – CO	**6a**	228.8	177.2	227.1	175.7
$Ru(CO)_2$(dhLe)(PH_3) – PH_3 (rel. **2a**)	**4b**	116.9	71.0	115.9	69.5
$Ru(CO)_2$(dhLe) +H_2 (rel. **2a**)	**3**	-10.3	-19.1	-6.7	-12.6

It can be seen that the pathways from $Ru(CO)_3$(dhLe) are not significantly affected by the atom present in the bidentate ligand. De-chelation is more significantly affected in contrast, with the complexes and intermediates formed by this route lower in enthalpy and free energy with arsenic when compared to phosphorus. This is in keeping with the weaker metal-arsenic bond compared to the metal–phosphorus bond. The thermodynamic values for the reactions from $Ru(CO)_2$(dhLe)(PH_3) do not vary much between the two possible forms with L = As or P. The final two rows for L = P can also be compared to the previously published work with a benchmarked computational model, where values were reported for $Ru(CO)_2$(dhpe) and $Ru(H)_2(CO)_2$(dhpe) of +122 and 2 kJ mol^{-1} respectively.[143]

Work with $Ru(CO)_3(dppe)$ has shown that its reaction with various nitroaromatics proceeds via CO loss.[196] Studies with hydrogen has also shown that the reaction proceeds via CO loss to form the dihydride species $Ru(H)_2(CO)_2(dppe)$ with both thermal and photochemical initiations.[46, 142, 154, 197] The related monodentate complex $Ru(CO)_3(PPh_3)_2$ has also been studied in great detail due to its catalytic properties. This complex was studied by Wilkinson *et al*. and determined to undergo CO dissociation and subsequent H_2 addition to form the active species $Ru(H)_2(CO)_2(PPh_3)_2$.[142, 146, 147, 197, 198] This species was later found to exist primarily in the *cct*-L form with the *ccc* form detectable with *p*-H_2 as a minor isomer.[142, 199] The thermodynamic values for these two isomers and their formation from $Ru(CO)_3(PPh_3)_2$ are shown in Table 2.10 for calculations with both the simple ligand system and the full system with phenyl rings included.

Table 2.10: Calculated thermodynamic values for pathways from the monodentate complexes $Ru(CO)_3(PH_3)_2$ and $Ru(CO)_3(PPh_3)_2$. All values are in kJ mol^{-1}

Species	**Reaction**	**Simple Model**		**Full Model**	
		ΔH	**ΔG**	**ΔH**	**ΔG**
t-L $Ru(CO)_3(L)_2$		0.0	0.0	0.0	0.0
c-L $Ru(CO)_3(L)_2$		0.3	0.9	32.1	45.2
$Ru(CO)_3(L)$	*t-L* $Ru(CO)_3(L)_2$ -L	106.4	65.3	193.4	147.3
t-L $Ru(CO)_2(L)_2$	*t-L* $Ru(CO)_3(L)_2$ -CO	145.9	104.2	148.3	104.2
cct-C $Ru(H)_2(CO)_2(L)_2$		33.3	27.1	75.0	84.8
ccc $Ru(H)_2(CO)_2(L)_2$		29.6	26.4	64.0	73.6
cct-L $Ru(H)_2(CO)_2(L)_2$		26.9	23.7	43.6	43.3

The relative stabilities of the two geometries for the starting complex $Ru(CO)_3(L)_2$ are poorly reproduced with the simple model. The *t*-L $Ru(CO)_3(L)_2$ geometry is more stable than the equivalent *c*-L geometries due to the sterics associated with the bulky phosphines, with no significant difference for which π-acceptor ligands occupy equatorial positions in the trigonal bipyramids. Experimental studies with similar compounds have also found this geometry to dominate.[200, 201] With the full model, the difference in stability between the two geometries is significant and the *t*-L geometry predicted to dominate. For the simple model, the loss of a phosphine ligand is preferred to that of CO loss by 39.5 kJ mol^{-1}. Conversely, the prediction is reversed with the full model, with CO loss being more facile by

45.1 kJ mol^{-1}. The hydrogenation products are calculated to form favourably from the CO loss intermediates with both models. With the simple system, the *cct-L* geometry of $Ru(H)_2(CO)_2(L)_2$ is the most stable with the *ccc* and *cct-C* geometries lying higher in enthalpy, by 2.7 and 6.4 kJ mol^{-1} respectively. For the full model, the *cct-L* geometry is predicted to dominate, with the *ccc* and *cct-C* geometries being higher in enthalpy by 20.4 and 31.4 kJ mol^{-1} respectively. This highlights the agreement of both models for the dominant isomer of the dihydride species and agrees with that determined experimentally.[201] Importantly, the full model is needed to obtain meaningful stability energy differences; the simple model would predict the presence of all three geometries whereas the full model predicts the *cct-L* isomer to dominate

The related dihydride complexes $Ru(H)_2(CO)_2(LMe_2Ph)_2$ where L = P or As were also studied in detail by NMR measurements. With these systems, a significant difference was encountered with the isomers detected; only one geometry was detected when L = P, as the *cct*-L form whereas initially two isomers were detected for L = As (*cct*-L and *ccc*, in a 4:3 ratio).[202] The use of *p*-H_2 with these complexes did allow the detection of the third *cct*-CO isomer when L = As (at a level of 1-2% of the *cct*-L).[153, 154] It was also reported in the *p*-H_2 studies that the *ccc* isomer for L = P could be detected thermally, but a significant number of transients was needed to be able to obtain the hydride signals; the ratio of 96:4 for the *cct*-L and *ccc* forms was reported. This difference in behaviour for the two dihydride complexes was investigated theoretically to see if the correct results were obtained. The calculations were performed on both the simple and full ligand systems and the results are summarised in Figure 2.32.

For the phosphine geometries, both the simple and full model predict the *cct*-L geometry to be the most stable, with the *cct*-C geometry highest in energy. However, the simple model predicts the energies to be similar and so all geometries would be observed. With the full model, the *cct*-L geometry is predicted to dominate, with the *ccc* isomer lying at an enthalpy of 13 kJ mol^{-1} above. For the arsine geometries, the ccc geometry is predicted to be the most stable with the simple model, with the *cct*-L geometry the least stable. The difference in enthalpy is also predicted to be low, with a difference from the most stable to the least of 6.3 kJ mol^{-1}. For the full model, the *cct*-L geometry is correctly predicted to be the most stable, with the *ccc* geometry 4 kJ mol^{-1} higher in enthalpy. The *cct*-C geometry is

predicted to be the least stable, but the enthalpy difference of 13.7 kJ mol^{-1} means that is it likely to be present in low amounts.

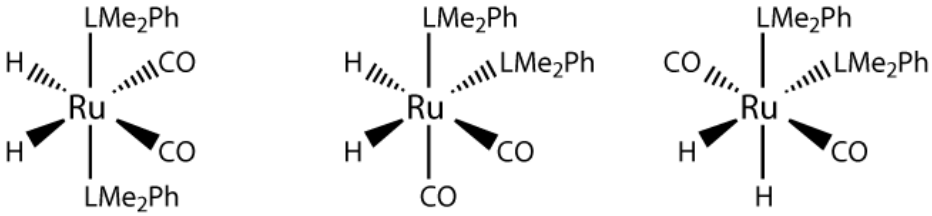

	cct-L	**ccc**	**cct-C**
L = P			
Simple	0.0	2.7 (2.7)	6.4 (3.4)
Full	0.0	13.2 (10.2)	29.0 (22.8)
L = As			
Simple	0.0	-6.3 (-7.7)	-4.4 (-8.2)
Full	0.0	3.9 (6.3)	13.7 (15.9)

Figure 2.32: Calculated relative enthalpies (free energies in brackets) for the three isomers of $Ru(H)_2(CO)_2(LMe_2Ph)_2$ (L = As or P) using the simple and full models. Values are in kJ mol^{-1}

These values fit the experimental values reasonably well, with the free energy difference between the *cct*-L and *ccc* forms for L=PMe_2Ph being determined as 7.8 kJ mol^{-1}. For L=AsMe_2Ph, the experimentally determined free energies were 0.7 kJ mol^{-1} and *ca.* 10 kJ mol^{-1} for the *ccc* and for c*ct*-C geometries above the *cct*-L geometry.[154]

These results show that the full model is needed to accurately predict the geometries and relative energies of the different isomers for both arsines and phosphines. The simple model does often predict reasonable values and trends but the results need to be carefully considered. The use of a bidentate ligand limits possible geometries and so the failings of the simple model are limited in this work. When the monodentate phosphine ligand is retained in the complex, the full model is needed to calculate reliable results.

2.4 Discussion into the reactions of the two ruthenium complexes with *p*-H_2

The work outlined in this chapter has covered the reactions of the two complexes $Ru(CO)_3(dpae)$ and $Ru(CO)_2(dpae)(PPh_3)$ with *p*-H_2, and evaluated the behaviour of the resulting products. The possibility of multiple pathways and interconversion of isomers were identified along with the different routes available for reaction depending on the method of initiation.

The two complexes $Ru(CO)_3(dhae)$ and $Ru(CO)_2(dhae)(PH_3)$ were identified to be highly fluxional with rearrangement of the equatorial and axial ligands found to occur via low lying transition states of a few 10s of kJ mol^{-1}. For the model complex $Ru(CO)_3(dhae)$ there is no essential change of isomer on rearrangement, whereas for $Ru(CO)_2(dhae)(PH_3)$ the phosphine group can occupy an axial or equatorial position. Complex **2b**, with the phosphine in the axial plane was calculated to be slightly less stable than isomer **2a** with the phosphine in the equatorial plane when using the simple model. The loss of the phosphine potentially leads to two isomers of $Ru(CO)_2(dpae)$, with **4b** being substantially more stable than **4a**. The more stable intermediate **4b** is formed by the loss of the phosphine from **2a** with no rearrangement required; for **2b** a small rearrangement would be needed to result in **4b**. The interconversion of **4a** to **4b** was also calculated to have a low energy barrier. The use of toluene as the solvent limits the potential for solvent coordination and so rearrangement is likely prior to reaction. It has been shown that rearrangements of intermediates and products via fluxional exchange pathways need to be carefully considered with subsequent reactions e.g. homogeneous catalysis.

The finding of key 16-electron intermediates as electronic singlets has been previously identified as the reason *p*-H_2 derived polarisation is observed for ruthenium complexes but not for the analogous iron complexes. In the system investigated here, the lowest energy 16-electron intermediate of $Ru(CO)_2(dhae)$ is also most stable as a singlet (as **4b**), with another singlet geometry and triplet states at higher energy. When thermal initiation is used, the lower energy intermediate **4b** will dominate. If photochemical initiation is used, the higher energy triplets could be accessible. This formation would require a spin-flip transition, and no evidence for triplet intermediates in the dominant pathway was

observed in the experimental evidence. For the 14-electron intermediates of Ru(CO)(dhae) and Ru((dhae)(PH_3) possibly generated by photochemical initiation, viable electronic triplets were again identified. Importantly, if the triplet states are formed under photolysis, experimental evidence shows that they have a limited role in the pathways as the polarisation observed reveals that singlet pathways are involved. The modelling with the full system revealed a favourable interaction of a phosphine phenyl group with the metal which stabilised the singlet; this could also account for the observed reactions. The approach of the incoming ligands has also been shown to be important for some reactions, where the addition of hydrogen across two possible planes in the 16-electon intermediate of Ru(CO)(dhae)(PH_3) could lead to two distinct isomers. Experimental evidence found their ratio to be 11:1; the models used in the calculations here revealed the preference to add dihydrogen over the CO-Ru-As plane and form the dominant isomer of $Ru(H)_2$(CO)(dhae)(PH_3) consistent with the experimental findings (isomer **7a/A7a**).

One area where the results from the DFT models have to be carefully interpreted is with the loss of a ligand which is not overly soluble in the solvent. The loss of CO from $Ru(CO)_3$(dhae) has to overcome a bond enthalpy of +163.6 kJ mol^{-1}, but the free energy change is lower due to the increase in disorder (from an increase in the number of species) at +117.7 kJ mol^{-1}. Notably, this reaction has a further driving force; the solubility of CO in toluene is low, with an Ostwald coefficient of 0.1857 at 308 K.[203] This means that if any CO dissociates, it can potentially come out of solution and enter the headspace of the NMR tube and the reaction can be classed as irreversible. The pressure of 3 atm. of *p*-H_2 will increase the amount of dissolved any dihydrogen in the solution and drive any reaction with the ruthenium complex forward, to dihydride complexes and possibly dihydrogen complexes. However, although the enthalpy change for the coordination of another dihydrogen to $Ru(H)_2$(CO)(dhae) (**6a**) is -87.6 kJ mol^{-1} (to form **6b**), the free energy change is less, at -50.6 kJ mol^{-1}. With $Ru(H)_2(CO)_2(\kappa^1$-dhae) as **3d**, this coordination leads to **6c** with an enthalpy change of -71.8 kJ mol^{-1} and a free energy change of -32.9 kJ mol^{-1}. This change, combined with the fact that no further reaction with any other ligand is then possible without another ligand loss, is likely to mean that the presence of any dihydrogen complex will be limited. Any dihydrogen complex is also unlikely to be detected on the NMR time-scales and would also show limited polarisation from *p*-H_2. This loss of CO could account for

the formation of $Ru(H)_2(CO)_2$(dpae) as **3a**, calculated to be unfavourable, but is experimentally observed as a stable dihydride complex.

The solvent has also been shown to have an important influence on reactions observed in the literature able to coordinate to the complex. The detection of such solvent complexes using pyridine indicates that this solvent would need to be considered in the models. The interaction with toluene or benzene was shown here to have limited interaction. The benzene solvent complexes were calculated to have little thermodynamic drive and so current solvent models appear to offer no significant advantage over the gas phase calculations here. It is noted that this could change as models available become more complete at describing the solvent effects in systems.

Dihydride complexes $Ru(H)_2(CO)_2$(dhae) (**3a**) and $Ru(H)_2(CO)_2$(dhae)(PH_3) (**7a**) have been predicted to be highly fluxional using the simple model system, which were formed from $Ru(CO)_3$(dhae) (**1**) and $Ru(CO)_2$(dhae)(PH_3) (**2**). Several different types of rearrangement were examined and the trigonal twist mechanism and mechanisms involving the formation of a (η^2-dihydrogen) unit found to be likely. The simple model was not consistent with experimental results for the phosphine dihydride $Ru(H)_2(CO)_2$(dpae)(PPh_3) (**A7a**). This complex is not observed to undergo rearrangement whereas the barriers predicted imply that rearrangement should occur. The related complex $Ru(H)_2(CO)_2$(dppe)(PPh_3) did show fluxionality in contrast; the discrepancy in the calculated and measured barriers was attributed to the use of a simple model where the bulky phenyl groups are neglected.[143] The use of the full model here revealed that the barriers were indeed higher than with the simple model, attributable to the steric bulk of the phosphine and arsine ligands. With the full model, the likelihood of reductive elimination of dihydrogen was predicted to be more favourable, which is also consistent with experimental observations.

The prediction of the metal-phosphine bond enthalpy has been an active field in the literature due to the importance of the Grubbs series of catalysts.[204] With these catalysts, the first step has been determined to be the loss of the phosphine; theoretical results disagree with experiment where standard DFT predicts the ruthenium-tricyclohexyl phosphine bond enthalpy in the second generation catalysts to be lower than first-generation catalysts.[205] Other studies have found that standard DFT can yield reasonable

thermodynamics[177] but it is clear that correctly modelling the bond is challenging. It is noted that the inclusion of dispersion corrections in the calculations in this thesis could alter the values obtained. Initial work with these corrections has found that the loss of phosphine from $Ru(CO)_2(dpae)(PPh_3)$ has a similar SCF energy to that of de-chelation; this similarity was also found with the simple model and so further work could be undertaken to examine the scope of such a correction on the complexes here.

The difference in bond energy between the ruthenium-carbonyl bond and the ruthenium-arsine bond is significant but the difference in reactivity can be linked to the de-chelation of a bidentate ligand versus the release of a CO ligand. The retention of the free end of the de-chelated ligand in close to proximity of the metal centre means that the dominant pathway once de-chelated is recoordination of the free arm. If the concentration of another ligand was significantly high enough, it is possible that a favourable encounter could occur prior to re-coordination. This is observed for $Ru(CO)_3(dppe)$ in pyridine.[143] In the experimental work for the systems modelled here, de-chelated complexes were not observed for non-polar and limited coordinating solvents like benzene or toluene. When there is an excess of another ligand like PPh_3, de-chelation can result in stable enough 18-electron complexes which can be detected. The observation of complexes where de-chelation has occurred followed by total loss has occurred confirm that these routes are feasible in a solvent capable of stabilising the resulting complexes (e.g. $Ru(H)_2(CO)_2(PPh_3)_2$ and $Ru(H)_2(CO)_2(pyridine)_2$). In reaction systems where other substrates are present, de-chelation reactions should also be considered as potential pathways.

The use of the simple model for the ligand system does introduce a change in chemistry of the bidentate arsine ligand. This change is indicated by the change in Tolman Electronic Parameter of PH_3 compared to PPh_3.[206, 207] PH_3 has been reported to have an electronic parameter of 2083 cm^{-1} whilst PPh_3 has a value of 2069 cm^{-1}. The cone angles of the ligands, indicating the steric effects, are 87° and 145° for PH_3 and PPh_3 respectively. These values show that PH_3 and PPh_3 have similar electronic effects, but significantly different steric effects. Recently published work has proposed replacing the Tolman Electronic Parameter by a metal-ligand electronic parameter, obtained by calculation of the metal-ligand local stretching force constant obtained through DFT.[208] This theoretical work showed that this new value incorporates the electronic and steric effects and allowed the calculation of this

parameter for a large variety of potential ligands. With this work, the bond strength order value was derived allowing convenient comparison of ligands. For phosphines, PH_3 was shown to have a relatively low value of 0.431, arising from its reduced σ-donor capacity. The value for PPh_3 was slightly higher at 0.475, which arose from the steric repulsion between the phosphine and the carbonyl ligands in the Nickel complexes modelled. For the equivalent arsines, values of 0.382 and 0.477 were obtained for AsH_3 and $AsPh_3$ respectively. Both approaches described here yield values which show that the simple model used here does neglect important effects introduced by the phenyl rings. However, the use of the simple model for the bidentate ligand appears to have a less pronounced effect than for monodentate arsines or phosphines. This is illustrated by the similarity in thermodynamic values determined in this work for the loss of CO, reaction with H_2 or the de-chelation of dhae/dpae for the simple and full models. The thermodynamic values for the stability of the 16-electron complexes identified, along with the geometries of the identified dihydrides are also a reasonable match. When PPh_3 is modelled as PH_3, it is noted that significant differences are encountered between the two approaches. This is illustrated in many sections, such as the incorrect prediction of the ground state geometry of $Ru(CO)_2(dhae)(PH_3)$ (**2a** vs. **2b**). For the 16-electron intermediates with PH_3, no interaction was found of the phosphine with the electron deficient metal centre; with the full model, interaction of PPh_3 with the metal centre was identified (e.g. in **8a**). The simple model is useful in surveying pathways to identify likely routes, but it is shown here that the full model is needed to capture all aspects of reactivity. It is also noted that dispersion effects have not been included in the models; this could potentially increase barriers for ligand loss, or stabilise intermediates by interactions not fully modelled here.

The simple system has facilitated the location of transition states which link the different conformations of isomers of dihydride complexes; the location of these transition states with the full model is challenging due to the increase in the degrees of freedom of the molecule, with many attempts to locate transition states failing. This simple modelling is useful in identifying potential pathways and the identified transition state geometries are invaluable in locating the transition states with the full model. There is also significant additional computational expense in running the full model system, as the DFT method scales with N^4. The simple model $Ru(CO)_2(dhae)(PH_3)$ has 20 atoms and optimisations with the basis sets used here results in 235 basis functions; for $Ru(CO)_2(dhae)(PH_3)$, the increase

in atoms to 91 results in *ca.* 1160 basis functions. The results presented here suggest that when the bidentate arsine ligand is retained in the complex, the reactions do not change drastically between the simple and full model. The modelling of the phosphine as PH_3 does lead to differences compared to the full model utilising PPh_3 in contrast. This means that significant care needs to be taken in assessing whether the simple model is sufficient to model the reactions of these complexes. Once the phosphine ligand is lost, the simple model is likely to provide a reasonable indication of feasible reactions of the formed intermediates, providing the new reactants are sufficiently modelled by the simple system.

Chapter 3: Catalytic hydrogenation of diphenylacetylene

3.1 Previous findings with ruthenium-phosphine complexes

The catalytic hydrogenation of diphenylacetylene by $Ru(CO)_3(PPh_3)_2$ was studied by Duckett *et al.* in pyridine and toluene solvents.[142] Signals for the two dihydride complexes *cct*-$Ru(H)_2(CO)_2(PPh_3)_2$ and $Ru(H)_2(CO)_2(PPh_3)$(pyridine) were observed in pyridine with a 100-fold excess of diphenylacetylene, alongside weak *cis*-stilbene signals. The use of photochemical initiation allowed the improved detection of signals for *cct*-$Ru(H)_2(CO)_2(PPh_3)_2$ and *cis*-stilbene which demonstrates that $Ru(CO)_3(PPh_3)_2$ can undergo both thermal and photochemical initiation. EXSY proton NMR experiments revealed transfer of magnetisation from the hydride resonance of $Ru(H)_2(CO)_2(PPh_3)_2$ into *cis*-stilbene and free H_2, thereby directly implicating this species in the mechanism of hydrogenation. The rate of hydrogenation was measured as 2.2 s^{-1} and found to be independent of the ratio of starting complex to alkyne, indicating that the alkyne is not involved in the rate determining step. The introduction of 1 atm. of CO into the reaction mixture decreased the intensities of the dihydride complex $Ru(H)_2(CO)_2(PPh_3)_2$ and *cis*-stilbene signals but did not change the rate of hydrogen transfer. Furthermore, the addition of an excess of PPh_3 essentially quenched the hydrogenation reaction.

The related complex $Ru(CO)_3$(dppe) (**P1**) was also examined in pyridine with diphenylacetylene. The detection of the dihydride complexes $Ru(H)_2(CO)_2$(dppe) (**P2**), $Ru(H)_2(CO)_2(\kappa^1$-dppe)(pyridine) (**P2a**) and $Ru(H)_2(CO)$(dppe)(pyridine) (**P2c**) was facilitated alongside *cis*-stilbene. No transfer of magnetisation into *cis*-stilbene was detected, indicating that catalysis is slow with **P1**. As described in Section 2.1.1, this difference was probed as a function of phosphine and higher rates of reaction were seen for less electron donating phosphines. The bidentate dppe ligand based complex had the slowest rate and this was attributed to the chelate effect.

3.2 Experimental investigations into the hydrogenation of diphenylacetylene with the complexes $Ru(CO)_3(dpae)$ and $Ru(CO)_2(dpae)(PPh_3)$

The two arsenic containing complexes $Ru(CO)_3(dpae)$ (**A1**) and $Ru(CO)_2(dpae)(PPh_3)$ (**A2**) described in Chapter 2 were investigated for catalytic behaviour with *p*-H_2 and diphenylacetylene. Both complexes were examined with thermal and photochemical initiation, leading to different complexes and products. The experimental work was performed by Adams and Eguillor *et al.* where the complexes were prepared in toluene-d_8 solutions in the presence of a 100-fold excess of diphenylacetylene. For **A1**, with thermal initiation, polarised signals for $Ru(H)_2(CO)_2(dpae)$ (**A3**) were observed upon heating to 315 K (consistent with the initial investigation without diphenylacetylene, as described in Section 2.2.1) and polarised signals for *cis*-stilbene were observed upon heating to 335 K.

The analysis of the reaction mixture by gas chromatography-mass spectrometry (GC-MS) revealed the presence of both *cis*- and *trans*-stilbene along with the double hydrogenation product 1,2-diphenylethane. OPSY NMR sequences were used to observe these species.[49] This revealed additional signals for new complexes where the alkene is bound to the metal and tentative assignments were made. These products are illustrated in Figure 3.1.

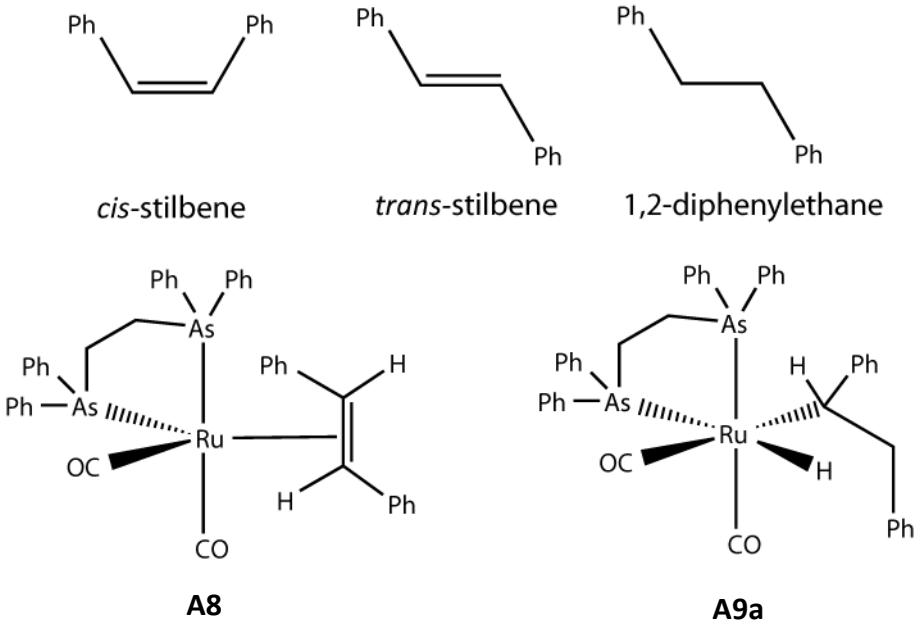

Figure 3.1: Detected species in the thermal reactions of **A1** with diphenylacetylene and *p*-H_2 in toluene

Signals for **A8** appeared at 2.8 ppm and 2.64 ppm and shared a common splitting of +15.3 Hz, thereby indicating a *trans* arrangement of the alkene. The use of labelled diphenylacetylene, as Ph-^{13}C≡C-Ph, allowed the connections of the proton signals to the carbon signals to be identified; the signal at 2.64 ppm in the proton spectrum connected with a ^{13}C resonance at 37.1 ppm, with the signal at 2.88 ppm in the proton spectrum connecting to a second ^{13}C signal at 38.5 ppm. The J_{HC} value of 132 Hz obtained between the signal at 2.64 ppm in the proton spectrum and the carbon signal indicated sp^3 hybridisation, along with electron density being donated from the metal to the alkene upon binding; the coupling value for the free species was determined to be 154 Hz. This species was observed in the reaction mixture at 343 K, but further heating to 353 K allowed the detection of Ru(H)$(CO)_2$(dpae)(CHPhCH_2Ph) as **A9a**. **A9a** yields a single hydride signal at -6.26 ppm, which coupled to another signal at 4.04 ppm with a coupling constant of +2.8 Hz, along with signals at 3.98 and 4.26 ppm. Correlation Spectroscopy (COSY) measurements confirmed that all four signals arose from the same species. The use of ^{13}C labelled diphenylacetylene allowed the correlation of the proton signals to common carbon signals. The chemical shift of the hydride signal was used to postulate that the hydride ligand was located *trans* to arsenic. EXSY experiments allowed the observation of magnetisation transfer from **A9a** into *cis*-stilbene at 358 K, showing that this species played a direct role in the semi-hydrogenation mechanism.

Photochemical initiation of **A1** (Ru$(CO)_3$(dpae)) at 295 K yielded signals for **A3** as well as signals for **A10**. This species gave rise to signals at 6.40 ppm and 1.56 ppm for the alkenic protons which showed a mutual coupling of +8 Hz. The use of isotopically labelled Ph-^{13}C≡^{12}C-Ph-d_{10} allowed proton-carbon couplings of 178 Hz (for the proton at 6.4 ppm) and 144 Hz to be determined which are consistent with sp^2 and sp^3 hybridisation respectively. The detection of this complex was consistent with the detection of 1,2,3,4-tetraphenylbutadiene in the reaction mixture by GC-MS. Low levels of a second isomer of Ru(H)$(CO)_2$(dpae)(CHPhCH_2Ph) (**A9b**) were detected at 295 K after 1024 scans in conjunction with *in-situ* photolysis. These two new species are illustrated in Figure 3.2.

The hydrogenation products *cis*- and, *trans*-stilbene and 1,2-diphenylethane were detected in the proton spectra using OPSY pulse sequences. A spatially resolving imaging experiment revealed that *cis*- and *trans*-stilbene signals showed a 5.5 fold increase in turnover, thereby

showing that photochemical initiation allowed improved hydrogenation. This could arise from the more facile loss of CO from **A1** required for the initiation step. The proportion of these species was found to change during photolysis. *Cis*-stilbene was found to be formed predominantly relative to *trans*-stilbene in the early stages of the reaction, with the signals from 1,2-diphenyethane increasing as its concentration built up during hydrogenation.

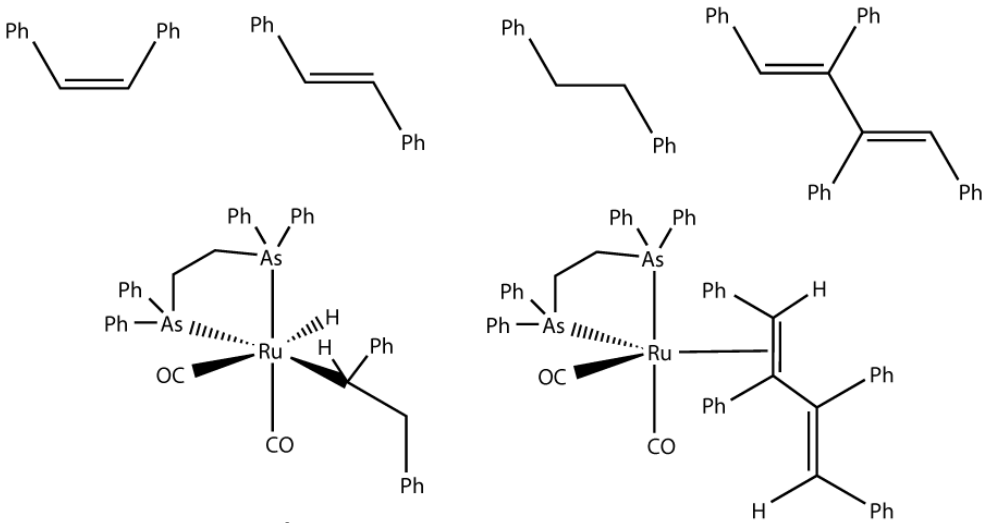

A9b **A10**

Figure 3.2: Detected species in the photochemical reactions of **A1** with diphenylacetylene *p*-H_2 in toluene

A series of photochemically initiated experiments were performed to determine the route to **A10**. This involved a preformed sample of **A3** that contained both diphenylacetylene and *p*-H_2. This mixture was found to have limited photochemical activity with irradiation at 325 nm, and it was therefore concluded that **A10** was not derived from **A3**. The addition of CO to the reaction mixture prior to reaction resulted in the sole detection of signals arising from dihydride **A3**. The introduction of a 50-fold excess of PPh_3 prior to reaction led to new products; two isomers of $Ru(H)_2(CO)(dpae)(PPh_3)$ (**A7a** and **A7b**) previously observed with $Ru(CO)_2(dpae)(PPh_3)$ (**A2)**. The ratio of these dihydride signals (**A3**:**A7a**: **A7b**) was measured as 110:11:1, with the ratio of **A7a**:**A7b** matching that observed when a sample of **A2** was photolysed. The ratio of **A3**:**A7** as a whole was 9:1 and deemed to be indicative that a pathway from **A1** involving the loss of two CO ligands contributes to at least 10% of the photoproducts. These findings were interpreted to suggest **A1** rather than **A3** as the source of **A10**. The photolysis of a sample of **A1** and *cis*-stilbene revealed no signals via PHIP in the

organic region of the proton spectra whereas signals for **A3** were observed. This was concluded to mean that the dimerisation product **A10** was not formed from *cis*-stilbene, and instead from the incorporation of *p*-H_2 into an organic species before *cis*-stilbene is formed.

Under thermal initiation, $Ru(CO)_2(dpae)(PPh_3)$ (**A2**) yielded dominant signals from **A10**, along with signals from **A9b** at 295 K. The species **A9b** was proposed to be responsible for the alkyl signals at 4.19, 4.06 and 3.18 ppm, along with a hydride signal at -11.34 ppm (identified through the COSY method). This species was proposed to have a geometry where the hydride was *trans* to CO.

Raising the temperature to 308 K allowed the detection of signals from **A3**, but further heating to 318 K caused the signals from **A9b** and **A10** to decrease in size. The signals from **A3** drastically increased though and signals for $Ru(H)_2(CO)_2(PPh_3)_2$, *cis*-*cis*-$Ru(H)_2(CO)_2(\kappa^1$-dpae)(PPh_3) (**A5**) and **A7a** become visible. Further heating to 328 K resulted in the signals from **A3** and $Ru(H)_2(CO)_2(PPh_3)_2$ dominating, but signals from *cis*-stilbene were also detected. Complex **A8** was observed after further heating to 338 K along with *trans*-stilbene. This process of chemical evolution reflects a change in the kinetics of H_2 exchange/addition.

The photochemical initiation of **A2** allowed the detection of **A7a** and **A7b** at 295 K with the same relative signal intensity as seen when **A2** was photolysed without diphenylacetylene. Photolysis at 308 K resulted in the detection of signals for both *cis*- and *trans*-stilbene and 1,2-diphenylethane. Interestingly, a spatially resolving imaging experiment performed with **A2**, revealed that the hydrogenation reaction is not accelerated by photolysis.

3.3 Theoretical modelling of the initiation step of catalytic hydrogenation

As detailed in Section 2.3.11, the complex $Ru(CO)_3(PPh_3)_2$ has been studied and the catalytically active species determined to be $Ru(H)_2(CO)_2(PPh_3)_2$.[142, 197] This species can then react via phosphine loss and add another ligand; if this is an alkyne or alkene, subsequent hydrogenation can occur. It has also been proposed that $Ru(H)_2(CO)_2(PPh_3)_2$ can undergo the dissociation of a CO ligand.[202] This CO loss would be assisted by the *trans*-labilizing effect of a hydride ligand. This proposal was supported by CO inhibition, but purging the reaction mixture with N_2 returned the reaction to its original rate. With a chelating ligand *L-L* (such as dppe or dpae), the loss of the phosphine reflects the dissociation of one end of this bidentate ligand; this has been previously discussed and so the loss of CO from the complex $Ru(H)_2(CO)_2(L\text{-}L)$ is likely to be the major pathway compared to de-chelation. It is worth noting that the reductive elimination of dihydrogen is also possible; no evidence was found for this in the experimental work of Adams and Eguillor with the ruthenium complex **A1** containing dpae ligands.

The isolable 16-electron complex $Ru(CO)_2(P^tBu_2Me)_2$ reported by Caulton *et al.* in 1996 for which the distortion of the square planar geometry to the butterfly geometry was identified,[184] is akin to the key intermediate identified in this work as $Ru(CO)_2$(dpae) (modelled as **4b**). This stable 16-electron complex was identified to rapidly react with diphenylacetylene and form $Ru(CO)_2(\eta^2\text{-PhC}{\equiv}\text{CPh})(P^tBu_2Me)_2$.[209] This complex was also proposed to be involved in the catalytic hydrogenation of diphenylacetylene.[210] This work also found that the reaction of this complex with phenylacetylene led to the detection of the alkynyl complex $Ru(H)(CO)_2(C{\equiv}CPh)(PMe_2Ph)_2$ thus indicating a complex reaction mechanism if oxidative addition of the alkyne is possible.

3.3.1 Theoretical models utilised

In order to rationalise these results, the modelling was performed using the same models as used in Chapter 2. This involved the optimisation and calculation of vibrational frequencies for structures with a combination of basis sets where ruthenium, phosphorus, and arsenic atoms used the lanl2dz basis sets (phosphorus and arsenic basis sets were augmented with polarisation functions) with associated ECPs, and the remaining ligands

used the 6-311G** basis sets.[165-170] The BP86 GGA functional allowed efficient optimisation of the geometries.[84, 87] The thermodynamic data was obtained from single point calculations which utilised the hybrid functional PBE0,[173] with the more modern basis set combination of Ahlrichs labelled def2-TZVP and the associated ECP for ruthenium.[175] The thermodynamic corrections obtained from the frequency calculations were then combined with the SCF energy obtained with the hybrid functional. Models were run in Gaussian09 software,[122] with the QST2/3 function being used to obtain transition state geometries.[171, 172] Transition state location was also aided by the use of relaxed constrained scans for the reaction pathway under investigation. The bulky phenyl rings in the dpae ligand were replaced by hydrogens to allow the calculations to be performed at reasonable computational efficiency. It is noted that this approximation will change the electronic and steric effects of dpae; this could change the predicted geometries of transition states, shield the metal centre and change the barriers and thermodynamic values calculated here. The requirement of dpae and dhae to always occupy sites on the metal in a *cis*-configuration will reduce the impact of this approximation, with the phenyl rings of dpae essentially being directed away from the metal centre and the *cct*-L isomer not able to form. The effect of the approximation was explored in detail in Chapter 2. The nomenclature used in Chapter 2 continues here. The suffix **T** is used to define complexes where the isomerisation of stilbene occurs. A capital **C** or **H** is used to define whether the transition state is forming a new carbon or hydrogen bond where relevant.

Atoms in Molecules (AIM) theory[211] was carried out in Multiwfn version 3.3.7.[212] To model the ruthenium atom, the all electron basis set of Jorge *et al.* was used.[213] This method was used to evaluate the agostic hydrogen interaction with the metal centre identified in the hydrogenation pathways.

3.3.2 Initiation step from $Ru(H)_2(CO)_2$(dpae)

The reactions of $Ru(H)_2(CO)_2$(dhae) with diphenylacetylene are discussed here. It is possible that the 16-electron intermediate $Ru(CO)_2$(dhae) (**4b**) forms following the dissociation of *cis*-stilbene The reaction with this 16-electron species will be considered, as the diphenylacetylene loading 100 times higher than that of the ruthenium complexes in these experiments.

3.3.2.1 Carbonyl ligand loss

The loss of a carbonyl ligand from $Ru(H)_2(CO)_2$(dhae) (**3a**) is likely to occur from a position *trans* to hydride, leading to $Ru(H)_2(CO)$(dhae), **6a**. This species was identified in Chapter 2 as being formed by H_2 addition to 14-electron Ru(CO)(dhae), **5a**. The loss of this carbonyl ligand results in an enthalpy change of +192.4 kJ mol^{-1} and a free energy change of 146.7 kJ mol^{-1}. These values compare to those of the carbonyl ligand loss from $Ru(CO)_3$(dhae) (**1**) as 161.4 and 115.1 kJ mol^{-1} respectively. The loss of the alternative carbonyl (forming **6c**) has a larger change in enthalpy by +41.7 kJ mol^{-1}, in keeping with the *trans* effect of the hydride ligands. It is unlikely therefore that **6c** will form directly and so the dominant pathway will be the formation of **6a**. Subsequent coordination of diphenylacetylene results in $Ru(H)_2(CO)$(dhae)(η^2-diphenylacetylene), where one hydride is *cis* to diphenylacetylene and the other hydride is *trans*. This forms **11a** with a relative enthalpy change of -108.6 kJ mol^{-1}. The structures of these complexes, and the enthalpy changes relative to **1** are illustrated in Figure 3.3.

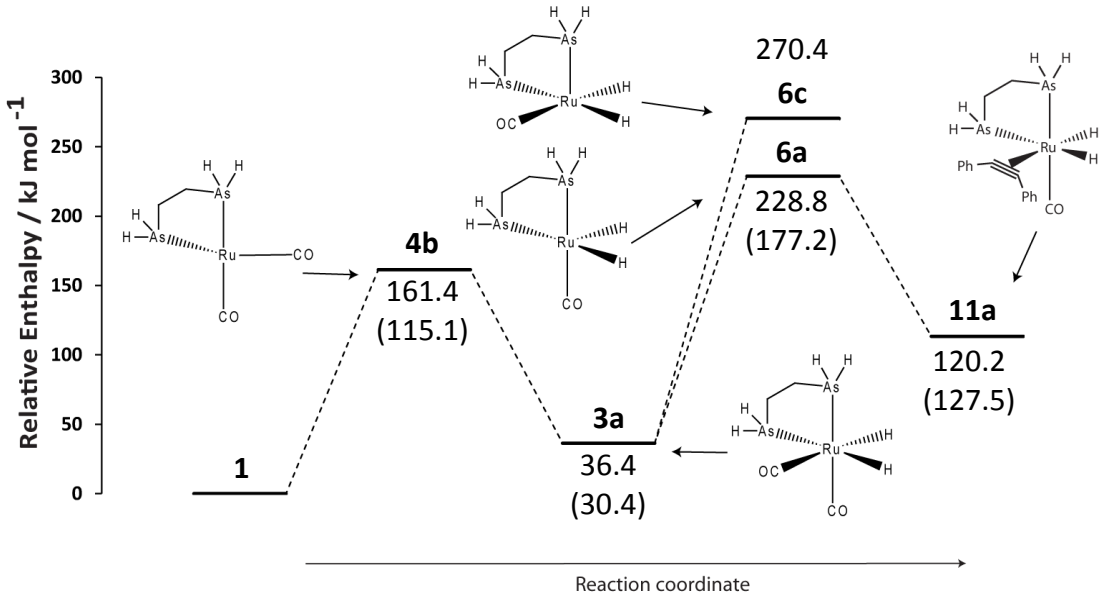

Figure 3.3: Relative enthalpy profile for the formation and reaction of **3a** with *p*-H_2 and diphenylacetylene via CO loss. Free energy terms are included in brackets

These thermodynamic changes reveal that formation of **11a** containing both diphenylacetylene and hydride ligands is unfavourable. **11a** is significantly less stable than

dihydride **3a**, by 83.8 kJ mol^{-1} (enthalpy). These predictions are consistent with the experimental observations that significant heating is required before catalysis commences.

3.3.2.2 Reductive elimination of H_2

Whilst no observation of the reductive elimination of dihydrogen from **A3** was observed experimentally, the possibility of this process should be considered. The reductive elimination of dihydrogen from **3a** is the reverse of the formation of **3a** from **1**. These changes are shown in Figure 3.3, with the associated change in enthalpy from **3a** to **4b** being 125 kJ mol^{-1} and free energy change being 84.7 kJ mol^{-1}. These values indicate that loss of dihydrogen is more facile than loss of CO.

Using the full model, the formation of **6a** via CO loss results in an enthalpy change of 195.8 kJ mol^{-1} (described in Chapter 2 for the reactions of Ru(CO)(dpae)); the free energy change for this process is 148.0 kJ mol^{-1}. These values compare to the values of reductive elimination of dihydrogen from **3a** to form **4b** of 126.0 and 84.6 kJ mol^{-1} respectively. The full model does not therefore change this deduction. However, it should be noted that the related complex $Ru(H)_2(CO)_2$(dppe) (**P2**) has been reported to undergo reductive elimination of H_2 with a barrier of 97 ± 10 kJ mol^{-1} (enthalpy).[46, 154] The failure to see such a process experimentally is therefore worthy of note.

3.3.2.3 De-chelation with $Ru(H)_2(CO)_2$(dpae)

A final possibility exists, where the bidentate dpae ligand in $Ru(H)_2(CO)_2$(dpae) (**A3**) de-coordinates one end and becomes monodentate. This pathway is the direct equivalent of phosphine loss from the related complex $Ru(H)_2(CO)_2(PPh_3)_2$ as previously discussed. Whilst de-chelation will lead to re-coordination of the free end of η^1-dpae due to the chelate effect, it is possible that a minor pathway exists where a successful collision with a molecule of diphenylacetylene occurs whilst de-chelated. This de-chelation step is therefore examined here.

De-chelation can occur from either position of $Ru(H)_2(CO)_2$(dhae) (**3a**); the loss of the arsenic centre is preferred when *trans* to the hydride ligand in the same way as noted for CO loss to form **6a** from **3a**. This de-chelation requires a change in enthalpy of 125.0 kJ

mol^{-1} to access transition state **3d'** and results in **3d**. The coordination of diphenylacetylene to **3d** is then favourable, with a change in enthalpy of -82.3 kJ mol^{-1} and results in Ru(H)$_2$(CO)$_2$(κ^{1}dhae)(η^2-diphenylacetylene) as **12a**. This complex is unfavourable relative to **3a**, which is more stable by 36.6 kJ mol^{-1} (enthalpy). This pathway is shown in Figure 3.4 along with the alternative de-chelation possibility (to **3e**). The free energy profile though **3d** is included in red.

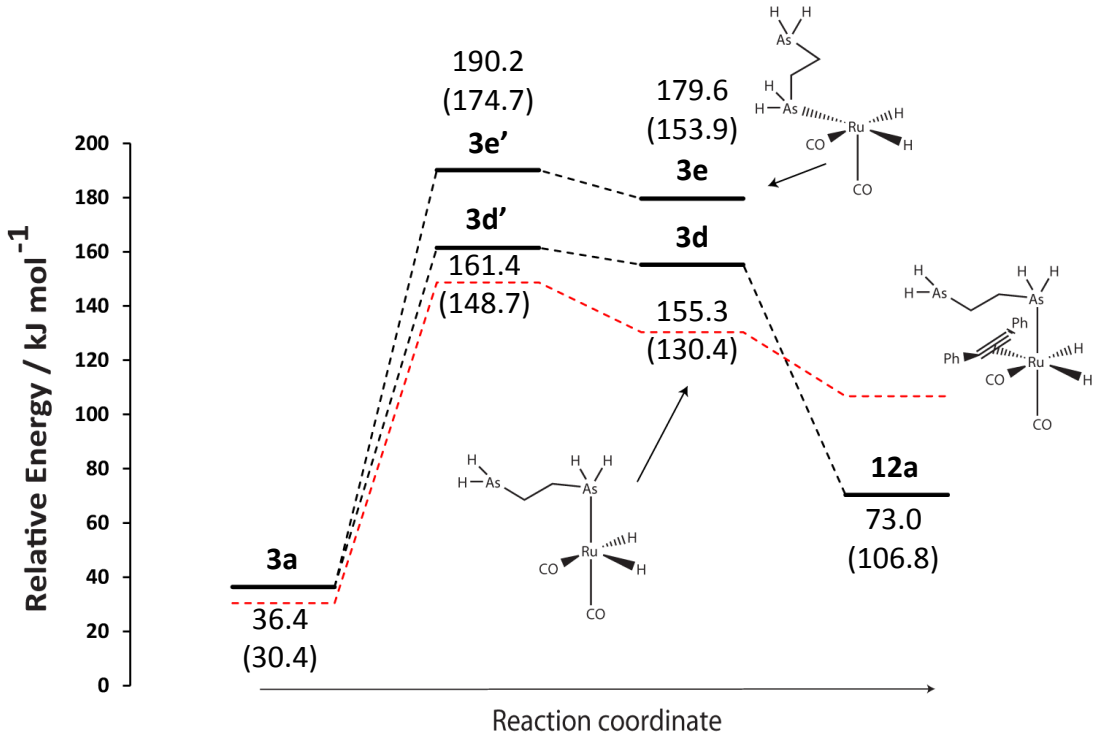

Figure 3.4: Relative enthalpy profile for the de-chelation of **3a** and subsequent reaction with diphenylacetylene. Free energy terms are included in brackets, and shown in red for the pathway through **3d**

The pathway resulting in Ru(H)$_2$(CO)$_2$(κ^{1}dhae)(η^2-diphenylacetylene), **12a**, is therefore predicted to be accessible. Hence, de-chelation should dominate over CO loss, with the free energy for H_2 loss calculated to be the most facile pathway. The de-chelation pathway is dominated by the chelate effect, with the reformation of **3a** the dominant outcome from de-chelation.

3.3.3 Reaction of diphenylacetylene with 16-electron $Ru(CO)_2(dpae)$

It is also possible that $Ru(CO)_2(dhae)$ (**4b**) could be formed from **1** (or **3a**) and react with diphenylacetylene prior to the coordination of dihydrogen. The related complex $Ru(CO)_2(P^tBu_2Me)_2$ has previously been shown to undergo this reaction with diphenylacetylene and so there is evidence for this pathway.[209]

The coordination of diphenylacetylene to $Ru(CO)_2(dhae)$ (**4b**) after initial CO dissociation from **1** results in a change in enthalpy of -119.6 kJ mol^{-1}, similar to that provided by the oxidative addition of dihydrogen (forming **3a**). This coordination results in a trigonal bipyramid where the η^2-bound diphenylacetylene occupies an equatorial position, with the plane of the carbon-carbon triple bond lying in the equatorial plane (**13**, label **12a** follows shortly). No alternative isomer was observed where η^2-diphenylacetylene occupied an axial position. This is consistent with work by Hoffman *et al*. who identified that the 3d-p π overlap is significantly greater with the geometry where the π-acceptor ligand occupies an equatorial position and the ligand is in the plane perpendicular to the axial plane.[214] The subsequent loss of either carbonyl ligand can then occur, with loss from the axial position being more facile. The two isomers of Ru(CO)(dhae)(η^2-diphenylacetylene) (**13a** and **13b**) that result are shown in Figure 3.5. **13b** has a distorted square-planar geometry, whereas **13a** is best described as having a distorted trigonal-planar geometry. The bond length of the diphenylacetylene ligand in **13a** is 1.34 Å whereas it is shorter at 1.30 Å in **13b**. This difference indicates that there is less back donation of electron density from a filled d-orbital on the metal into the π*-MO of diphenylacetylene in **13b**.

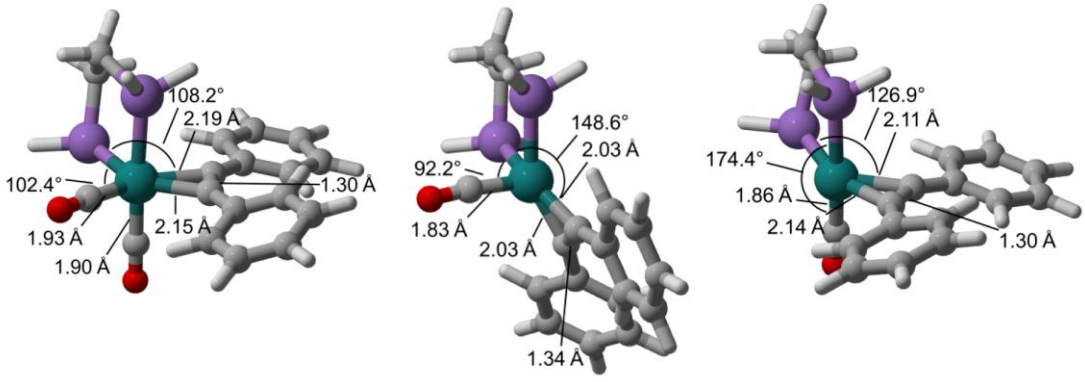

13 **13a** **13b**

Figure 3.5: Illustrations of isomers of **13a** and **13b** of Ru(CO)(dhae)(η^2-diphenylacetylene)

A transition state was located for the conversion of isomer **13b** to **13a** which had an enthalpy of only 0.1 kJ mol^{-1} (SCF energy difference is +2.8 kJ mol^{-1}) above **13b**; this means that if it were formed, it will rearrange instantaneously to **13a** and only pathways from this need to be considered.

The addition of dihydrogen to **13a** creates a dihydrogen species, Ru(CO)(dhae)(η^2-H_2)(η^2-diphenylacetylene), with a slightly unfavourable enthalpy change of +1.2 kJ mol^{-1} (with a free energy change of +39.0 kJ mol^{-1}) in the form of **11c**. The dihydrogen molecule lies in parallel with the carbon-carbon triple bond with the dihydrogen bond length as 0.82 Å. This dihydrogen containing complex converts through transition state **11c'**, with a barrier of +14.0 kJ mol^{-1}, to $Ru(H)_2$(CO)(dhae)(η^2-diphenylacetylene), as **11b**. The alternative approach of dihydrogen between the diphenylacetylene and CO ligands requires a significant rearrangement of the ligands; this occurs through a barrier of 32.0 kJ mol^{-1} (**13a'**). This transition state has the molecule 2.6 Å from the metal and the dihydrogen bond length as 0.76 Å – this means that no oxidative addition has occurred and the barrier is solely from the ligand rearrangement. The size of the barrier means that the pathway leading to **11b** is significantly more favourable. For this reason, the pathway through **13a'** is discounted. The enthalpies for these calculated complexes and intermediates are summarised in Table 3.1 for pathways via **13** and are illustrated relative to $Ru(CO)_3$(dhae) in Figure 3.6.

Table 3.1: Summary of reaction enthalpies for pathways involving CO, H_2 and diphenylacetylene via $Ru(CO)_2$(dhae)(η^2-diphenylacetylene), **13**

Label	Formed from	Reaction	Enthalpy change	Relative Enthalpy	Relative free energy
4b	**1**	Loss of CO	161.4	161.4	115.1
4b	**3a**	Reductive elimination of H_2	125.0	161.4	115.1
13	**4b**	Addition of diphenylacetylene	-119.6	41.7	56.5
13a	**13**	Loss of CO	120.1	161.8	130.4
11c	**13a**	Coordination of H_2	1.2	163.1	169.4
11c'	**11c**	Barrier for H_2 oxidation	14.0	177.1	185.1
11b	**11c**	H_2 oxidation	-17.0	146.1	151.9
13b	**13**	Loss of CO	187.5	229.2	197.8
13a'	**13a**	Barrier for H_2 approach	+32.0	189.9	192.6

The barrier for oxidative addition of dihydrogen from **13a** and subsequent stability of **11b** relative to **13a** means that this pathway is disfavoured. In free energy terms, **11b** is 21.5 kJ mol^{-1} less stable than **13a** despite **13a** being 4-coordinate. The coordination of diphenylacetylene must reduce the ability of the metal to stabilise the cleavage of the dihydrogen bond. The geometry of **11c** is essentially a strained trigonal bipyramid with the dhae and diphenylacetylene ligands in the equatorial plane; this means that the dihydrogen ligand occupies an axial position. This position reduces the orbital overlap of the σ*-H_2 molecular orbital with the metal[214] and allows dihydrogen bonding. With $Ru(CO)_2$(dhae) (**4b**), the addition of dihydrogen approaches the butterfly geometry across the equatorial plane. This allows significant interaction of the polarised xy orbitals with the σ*-H_2 molecular orbital, leading to barrierless oxidative addition of dihydrogen. This results in the encounter of **13a** with dihydrogen being unfavourable. The more favourable pathway from **13** is diphenylacetylene loss which results in **4b**. This is likely to be significantly more favourable if the effects of sterics are introduced by the inclusion of phenyl rings into the dhae model geometries. The free energies are highlighted for these pathways in red in Figure 3.6.

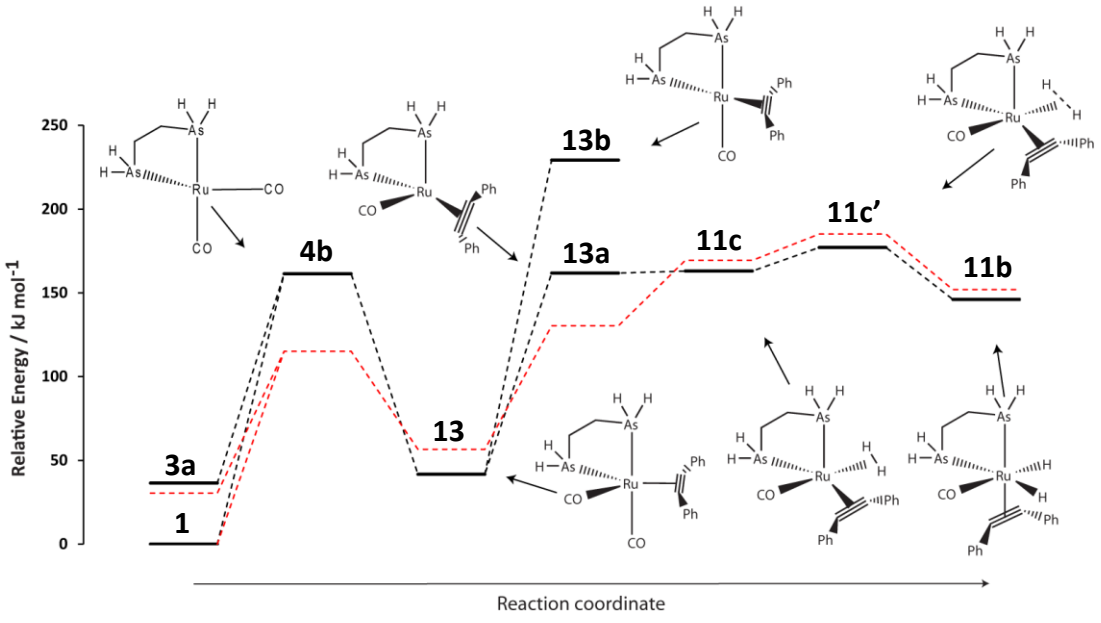

Figure 3.6: Relative enthalpy profile for the species formed in the reaction of **1** with *p*-H_2 and diphenylacetylene via CO loss. The reductive elimination of H_2 from **3a** is also included. The red profile represents the free energies

It has been determined here that initial CO dissociation from **1** followed by diphenylacetylene coordination is likely to be a minor pathway, with the formation of $Ru(H)_2(CO)_2$(dhae) (**3a**) the preferred stable complex formed from **1**. The reactions from this complex have already been discussed.

3.3.4 De-chelation of the dpae ligand

Whilst the de-chelation of the bidentate dppe ligand in $Ru(CO)_3$(dppe) has been found to be only significant when pyridine was used as the solvent,[142] it is a possibility that the presence of diphenylacetylene in excess could allow such a pathway to be feasible. These pathways are therefore considered here. The initial de-chelation steps were considered in Chapter 2; the pathway proceeds through transition state **1b'** and results in the formation of $Ru(CO)_3(\eta^1$-dhae) as **1b**. These changes have associated thermodynamic values of 107.3 and 93.0 kJ mol^{-1} as enthalpies, and free energies of 99.4 and 79.0 kJ mol^{-1} respectively.

$Ru(CO)_3(\kappa^1$-dhae) (**1b**) could subsequently undergo diphenylacetylene coordination, which results in trigonal bipyramidal (TBP) $Ru(CO)_3(\kappa^1$-dhae)(η^2-diphenylacetylene) (**14**) where diphenylacetylene lies in the equatorial plane with two CO ligands. This geometry has the preferred position for diphenylacetylene as discussed for **13**. The coordination is favourable with an enthalpy change of -134.0 kJ mol^{-1}. This addition is similar to that of the hypothetical oxidative addition of H_2 to **1b** modelled in Chapter 2 (forming **1c** with an enthalpy change of -132.9 kJ mol^{-1}). The subsequent loss from **14** of any carbonyl ligand results in a product with a distorted tetrahedral geometry (**14a**). The geometries of the key complexes are illustrated in Figure 3.7.

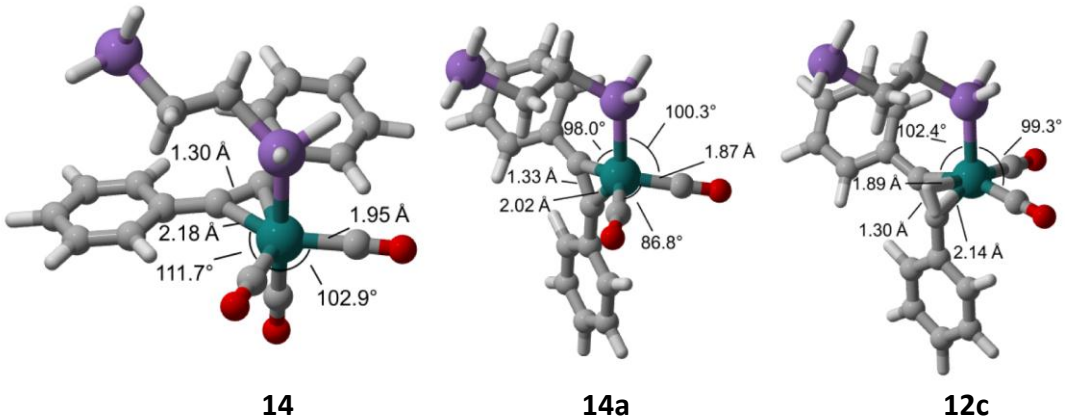

14 **14a** **12c**

Figure 3.7: Illustrations of key geometries for structures identified in the pathways through **14**

14a could then subsequently re-coordinate the free end of the dhae ligand and form $Ru(CO)_2$(dhae)(η^2-diphenylacetylene) as **13** previously described. The enthalpy for this recoordination reveals that it is favourable by 39.1 kJ mol^{-1}. If **13** is formed from the coordination of diphenylacetylene to $Ru(CO)_2$(dhae), the likelihood of de-chelation is significantly higher than with any other complex identified in this work. This de-chelation is analogous to the loss of phosphine from the 16-electron complex $Ru(CO)_2(\eta^2$-PhC≡CPh)($P^tBu_2Me)_2$.[209] In this work, it was found that upon the reaction of the preceding 16-electron species with diphenylacetylene, dissociation was possible above -40 °C to release free phosphine (<5%). This dissociation was proposed to arise from the steric interaction of the bulky phosphines with the coordinated diphenylacetylene. It was also suggested that the change in character of the alkyne from two electron donor to four electron donation upon phosphine loss provided additional stabilisation. The potential steric repulsion with dpae in the experimental complex considered here is less than the P^tBu_2Me ligands for two reasons; the dpae ligand occupies one axial and equatorial position in the TBP geometry, and the phenyl groups in dpae are more planar in nature and so the rings in the axial position of the dpae do not point towards the vacant site in the equatorial plane.

A dihydrogen addition pathway can also occur from $Ru(CO)_2(\eta^1$-dhae)(η^2-diphenylacetylene) as **14a** to form $Ru(CO)_2(\kappa^1$-dhae)(η^2-H_2)(η^2-diphenylacetylene) (**12c**). The formation of this complex is slightly unfavourable with a barrier for oxidative addition from transition state **12c'**, and dihydride complex **12b** would likely result. The enthalpies of these complexes and intermediates are listed in Table 3.2.

The free energy profiles reveal more information regarding the initial steps; the loss of CO from $Ru(CO)_3$(dhae) (**1**) involves a similar the same free energy change as de-chelation (115.0 vs. 99.4 kJ mol^{-1}). This is consistent with the experimental evidence for this loss, where CO loss was observed. The subsequent coordination of dihydrogen to $Ru(CO)_3(\kappa^1$-dhae)(η^2-diphenylacetylene) (**14a**) (if formed) is also unfavourable in terms of enthalpy and significantly unfavourable in free energy terms (**14a** to **12c'** is 86.2 kJ mol^{-1}). The reaction from **14a** involving the re-coordination of the free end of the κ^1-dhae ligand to form **13** is therefore favoured and the dominant pathway. This pathway has a barrier of only 10.0 kJ

mol^{-1} in this direction. This is illustrated in Figure 3.8 and the pathway to **14a** through **4b** is also included.

Table 3.2: Summary of reaction enthalpies and free energies for pathways via Ru(CO)$_3$(η^1-dhae)(η^2-diphenylacetylene), **14.** Values are in kJ mol^{-1}.

Label	Formed from	Reaction	Enthalpy change	Relative Enthalpy	Relative free energy
14	**1b**	Coordination of diphenylacetylene	-134.0	-16.4	29.2
14a	**14**	Loss of CO ligand	94.6	78.2	76.8
13'	**14a**	Barrier for of κ^1-dhae recoordination	10.0	88.2	83.2
13	**14a**	Recoordination of κ^1-dhae	-36.5	78.2	56.5
12c	**14a**	Coordination of H_2	10.3	88.6	125.1
12c'	**12c**	Barrier for H_2 oxidation	13.9	102.4	163.0
12b	**12c**	H_2 oxidation	-2.4	86.2	123.9

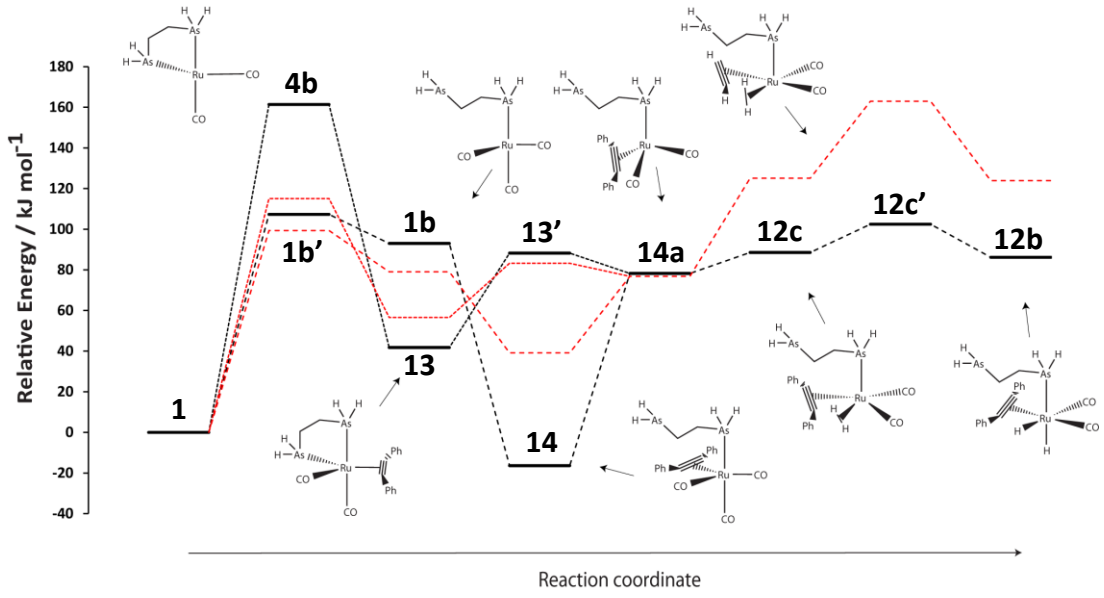

Figure 3.8: Relative enthalpy and free energy (shown in red) profile for the pathways involved in de-chelation of the bidentate dhae ligand in Ru(CO)$_3$(dhae) (**1**) and subsequent reaction with *p*-H_2 and diphenylacetylene

These results show that the initial de-chelation is not significantly favoured prior to the coordination of diphenylacetylene, which is compounded by the chelate effect. The de-

chelation of the dhae ligand in **13** is thermodynamically feasible, but the subsequent reaction with dihydrogen is unfavourable. For these reasons, this de-chelation is not considered as a starting point for the potential catalytic hydrogenation of diphenylacetylene. The formation of **11b** and **12a** are possible, but can be considered as being minor pathways in catalytic hydrogenation.

3.3.4.1 Discussion

The results presented here have shown that the likely start of catalytic hydrogenation is $Ru(H)_2(CO)(dhae)(\eta^2$-diphenylacetylene), as **11a**, formed by CO loss from $Ru(H)_2(CO)_2(dhae)$ (**3a**). Pathways formed by de-chelation of the bidentate dhae ligand are disfavoured by the chelate effect and reaction thermodynamic changes

3.3.5 Initial reactions in the photochemical initiation of $Ru(CO)_3$(dpae)

The photochemical behaviour of $Ru(CO)_3$(dpae) (**A1**) was investigated, with the formation of a mixture of $Ru(CO)_3$(dpae), diphenylacetylene and *p*-H_2, the potential 14-electron intermediate Ru(CO)(dpae) (formed following double CO ligand loss via photochemical initiation) could react with free CO or dihydrogen as described in Chapter 2. The initial reaction of the 14-electron singlet complex Ru(CO)(dhae) (**5a**) with dihydrogen leads to the dihydride intermediate $Ru(H)_2(CO)(dhae)$ (**6a**) as previously described; reaction with CO leads to $Ru(CO)_2$(dhae) as **4b**. However, coordination of diphenylacetylene to Ru(CO)(dpae) (**5a**) could occur and possibly lead to a new set of reaction pathways. If the initial reaction proceeds with diphenylacetylene, Ru(CO)(dpae)(η^2-diphenylacetylene) as **13a** and **13b** result (Section 3.3.3), with **13b** able to rearrange to **13a** via an almost barrierless pathway. The structures of these complexes and the associated enthalpy changes are illustrated in Figure 3.9.

Interestingly, the coordination of diphenylacetylene to **5a** results in a very similar enthalpy change to that of CO coordination. This contrasts the coordination of diphenylacetylene to $Ru(CO)_2$(dhae) (as **4b** forming **13**) where CO coordination (to reform **1**) was more favourable by 41.8 kJ mol^{-1}.

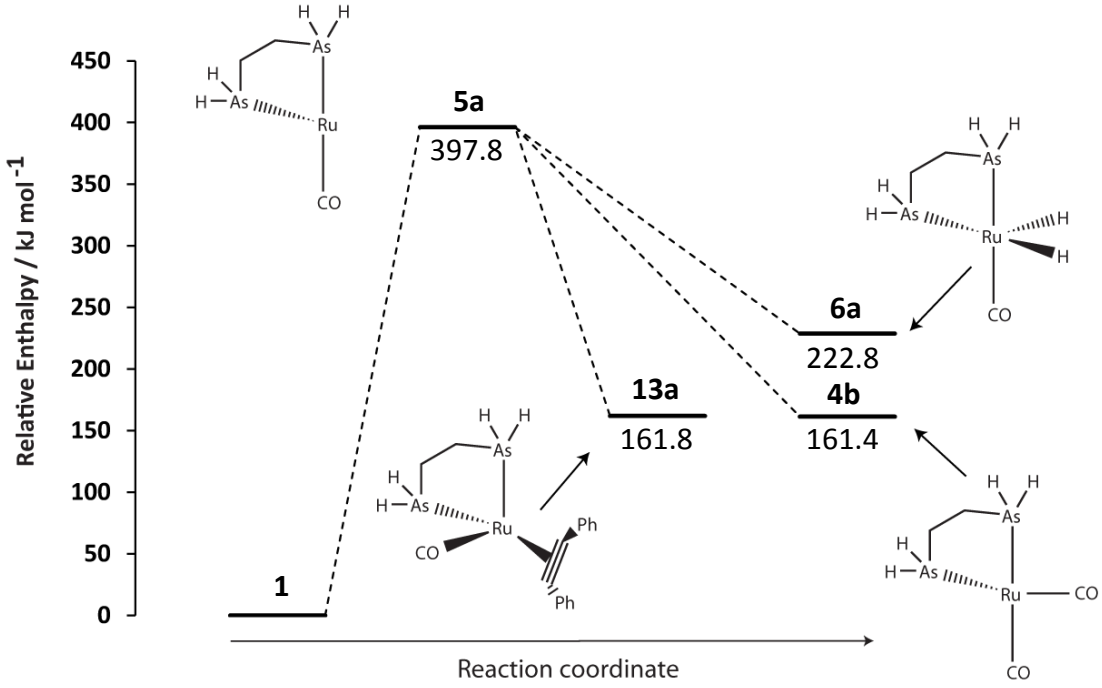

Figure 3.9: Species formed in the reaction of **1** with *p*-H_2 and diphenylacetylene under photochemical initiation, which could form from the 14-electron intermediate Ru(CO)(dhae) (**5a**)

3.3.6 Initial reactions of $Ru(CO)_2(dpae)(PPh_3)$

The analogous reactions with $Ru(CO)_2(dpae)(PPh_3)$ (**A2**), diphenylacetylene and *p*-H_2 are likely to be similar to those of $Ru(CO)_3(dpae)$ (**A1**), but the thermodynamic values will be different due to the weaker ruthenium-phosphine bond when compared to the ruthenium-carbonyl bond. Thermal initiation will result in the formation of $Ru(CO)_2(dpae)$ with subsequent formation of $Ru(H)_2(CO)_2(dpae)$ (**A3**)or $Ru(CO)_2(dpae)(\eta^2$-diphenylacetylene). Evidence for this was found in the experimental NMR spectra, where $Ru(H)_2(CO)_2(dpae)$ was the dominant species when the reaction was carried out with *p*-H_2 in toluene. This matches with the fact that phosphine loss (as PH_3 here) from $Ru(CO)_2(dhae)(PH_3)$ proceeds to **4b** with an enthalpy change of 116.9 kJ mol^{-1}, compared to the 177.6 kJ mol^{-1} needed for CO loss (forming **8b**). The dominant thermal reaction is therefore likely to lead to $Ru(CO)_2(dhae)(\eta^2$-diphenylacetylene) (as **13**) or $Ru(H)_2(CO)_2(dhae)$ (as **3a**). Pathways from these two complexes have already been detailed. As shown in Chapter **2**, the formation of dihydride **3a** from **2** is favourable, with **3a** being 10.3 kJ mol^{-1} more stable than **2a**; with the full model this difference becomes more pronounced, with changes in enthalpy and free energy of -13.9 and -41.6 kJ mol^{-1} respectively.

The photolysis of $Ru(CO)_2(dpae)(PPh_3)$ (**A2**) led to the detection of the hydrogenation products *cis* and *trans*-stilbene along with 1,2-phenylethane at 308 K. Two isomers of the dihydride complex $Ru(H)_2(CO)(dpae)(PPh_3)$ (**A7a** and **A7b**) were also detected as the major ruthenium based products, at the same intensities as without diphenylacetylene. The use of chemical shift imaging experiments revealed that the hydrogenation product intensities were not affected by photolysis. It was therefore concluded that the photochemical initiation of **2** did lead to any hydrogenation. It is therefore most likely that the hydrogenation products are formed from thermal reactions involving the loss of phosphine. For these reason, pathways from **8b**, formed by CO loss from **2a** or **2b**, are not considered here further.

3.3.7 Possibility of multiple diphenylacetylene coordination

The detection of 1,2,3,4-tetraphenylbutadiene by GC-MS means that two molecules of diphenylacetylene are brought into contact at the ruthenium centre. This could happen either before any hydrogenation reaction steps have occurred, or after the first hydride migration. These possibilities will be considered in Section 3.5.

3.3.8 Summary of the initial step of catalytic activation

The calculations performed into the initial reactions of $Ru(CO)_3(dpae)$ and $Ru(CO)_2(dpae)(PPh_3)$ (when modelled with the simple ligand system) with diphenylacetylene have revealed that the order of reaction can influence the final complex, and that the direction of ligand approach can have an effect. It has also revealed that two isomers of $Ru(H)_2(CO)(dhae)(\eta^2$-diphenylacetylene) are possible (**11a** and **11b**). These are formed via different pathways, with **11a** formed by CO loss from $Ru(H)_2(CO)_2(dhae)$ (**3a**) and subsequent addition of diphenylacetylene, and **11b** formed by the addition of diphenylacetylene to $Ru(CO)_2(dhae)$ (**4b**), and then subsequent CO loss and dihydrogen addition. The formation of **11b** has been identified to be a minor pathway. A second minor pathway has been identified where addition of diphenylacetylene occurs after de-chelation from $Ru(H)_2(CO)_2(dhae)$ (**3a**); this leads to the formation of $Ru(H)_2(CO)_2(\kappa^1$-dhae)$(\eta^2$-diphenylacetylene) as **12a** but is dependent on the successful collision of diphenylacetylene with $Ru(H)_2(CO)_2(\kappa^1$-dhae) before re-coordination of the free end of κ^1-dhae.

The geometries of the potential starting points for the hydrogenation of diphenylacetylene are illustrated in Figure 3.10, together with selected structural parameters. Table 3.3 details the possible starting points for catalysis.

Table 3.3: Relative energies of diphenylacetylene based intermediates accessible during catalysis

Complex	Relative enthalpy / kJ mol^{-1}	Relative free energy / kJ mol^{-1}
11a	120.2	127.5
11b	146.1	151.9
12a	70.3	106.8

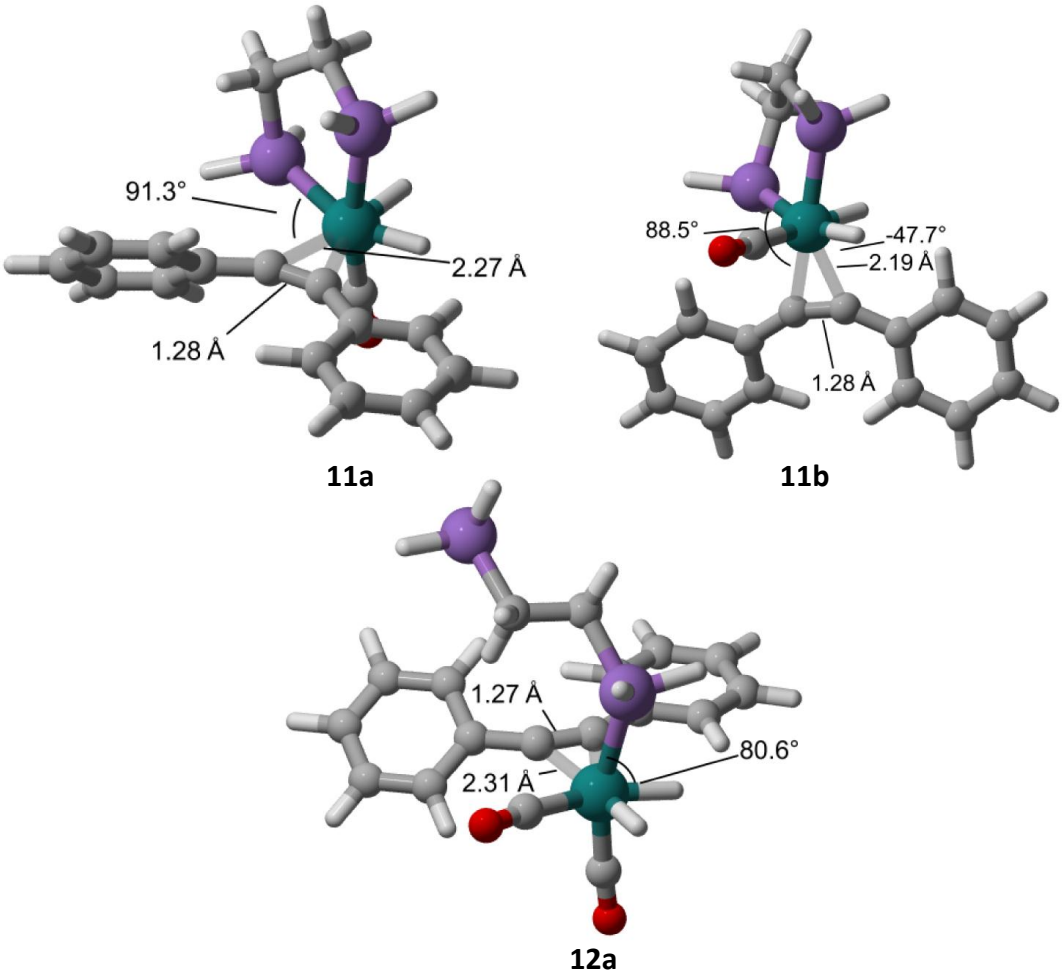

Figure 3.10: Detailed illustrations of the two identified isomers of $Ru(H)_2(CO)(dhae)(\eta^2$-diphenylacetylene) and the isomer of $Ru(H)_2(CO)_2(\kappa^1$-dhae)(η^2-diphenylacetylene)

In intermediates **11a**, diphenylacetylene is aligned with the As-Ru-H plane, which will be slightly more stable than the alternative orientation with the diphenylacetylene in the

vicinity of the CO ligand This also brings diphenylacetylene into the correct alignment for the successful transfer of the *cis* hydride ligand. In **12a**, diphenylacetylene is orientated in the CO-Ru-H direction, which reduces the steric interaction with the arsenic centre in κ^1-dhae, and will also allow interaction with the hydride ligand required for catalysis. In **11b**, it would be expected that diphenylacetylene would be orientated along the CO-Ru-H plane to minimise the interaction with the dhae ligand. Diphenylacetylene sits between this plane and the alternative plane formed by the As-Ru-H ligands, with a dihedral angle of approximately 45° with the two hydride ligands. This means that either hydride ligand can potentially be involved in the first step of the catalytic pathways.

All three of these complexes, where diphenylacetylene is coordinated to the metal together with hydride ligands, are formed unfavourably from $Ru(CO)_3$(dhae) (**1**). This is consistent with the experimental evidence where heating is required before any new products are observed (under thermal initiation). The positive pressure of hydrogen and the excess of diphenylacetylene used in the experiments means that any 16-electron intermediates can essentially be trapped and drive the reaction forward. It is noted that any subsequent reactions from these three complexes need to be favourable and proceed through low barriers for catalysis.

The most stable complex determined here is that of $Ru(H)_2(CO)_2(\kappa^1$-dhae)(η^2-diphenylacetylene) as **12a**, where retention of two CO ligands with a κ^1-dhae ligand yields a more stable product than the retention of only one CO ligand with a κ^2-dhae ligand. Isomer **11a**, $Ru(H)_2(CO)$(dhae)(η^2-diphenylacetylene), is calculated to be more stable than **11b** and would also dominate. As catalysis with $Ru(CO)_2$(dpae)(PPh_3) (**A2**) was found to occur at a lower temperature than that involving **A1** when thermal initiation was used, the lower bond enthalpy of the metal-phosphine group relative to the metal-carbonyl group is important in promoting catalysis.

3.4 Catalytic behaviour of the ruthenium complexes

The theoretical investigation into the reactions of $Ru(CO)_3(dpae)$ and $Ru(CO)_2(dpae)(PPh_3)$ with *p*-H_2 and diphenylacetylene (discussed previously) identified $Ru(H)_2(CO)(dhae)(\eta^2$-diphenylacetylene), as **11a**, along with **11b** and $Ru(H)_2(CO)_2(\kappa^1$-dhae)(η^2-diphenylacetylene) as **12a** as potential starting points for hydrogenation. All of these isomers have hydride ligands in a *cis* position relative to diphenylacetylene and so hydrogenation is possible. It is therefore feasible that three separate catalytic cycles exist. These cycles are modelled here and with Cycle 1 via **11a** being dominant.

3.4.1 Proposed catalytic cycles for $Ru(H)_2(CO)(dhae)(\eta^2$-diphenylacetylene)

The general inner sphere catalytic cycle for hydrogenation of an alkyne starts with a complex where both the alkyne and dihydrogen (as hydride ligands) are brought into the coordination sphere of the metal centre. A hydride in a *cis*-position to the alkyne can then undergo an intra-molecular hydride transfer reaction (alternatively described as insertion of the alkyne into the metal hydride bond). If the remaining hydride is *cis* to the σ-bound α-carbon in the newly formed vinyl group, a further hydride transfer reaction can take place to form the π-bound alkene, which can then allow the complex to react with dihydrogen.

The key points of such a cycle for $Ru(H)_2(CO)(dpae)(\eta^2$-diphenylacetylene) (**A**) with the equivalent geometry to **11a** are illustrated in Figure 3.11 which is labelled as Cycle 1.

Only one hydride ligand is *cis* to diphenylacetylene in **A**, and so only this hydride ligand can be transferred. As the remaining hydride is *trans* to the vinyl group a rearrangement must occur to form **B**. This 16-electron complex can then bind dihydrogen, or undergo a second hydride transfer reaction with the remaining hydride ligand to form **C** (neglecting other options at this stage). The coordination of dihydrogen between the vinyl group and hydride ligand before rearrangement could prevent the transfer of the hydride ligand. Coordination of dihydrogen before or after the second transfer reaction leads to the same dihydride complex **E**. Dihydride **E** can then undergo loss of *cis*-stilbene, and the product can react with a new diphenylacetylene molecule to reform **A**. Complex **E** can alternatively undergo a third hydride transfer reaction to form the 16-electron intermediate **F**, which can only occur

through the hydride ligand *cis* to the *cis*-stilbene. Again, the remaining hydride ligand is *trans* to the disubstituted ligand and so rearrangement of the complex will be required. Intermediate **G** could then undergo a fourth hydride transfer reaction to form 1,2-diphenylethane; the release of this compound would form the high energy 14-electron Ru(CO)(dpae) intermediate (**5a**) which has been previously shown to be very reactive. For this reason, this route has not been considered and only coordination of dihydrogen prior to the final hydride transfer reaction is shown in Figure 3.11. The release of diphenylacetylene reforms $Ru(H)_2(CO)(dpae)$ which can coordinate diphenylacetylene and reform complex **A**.

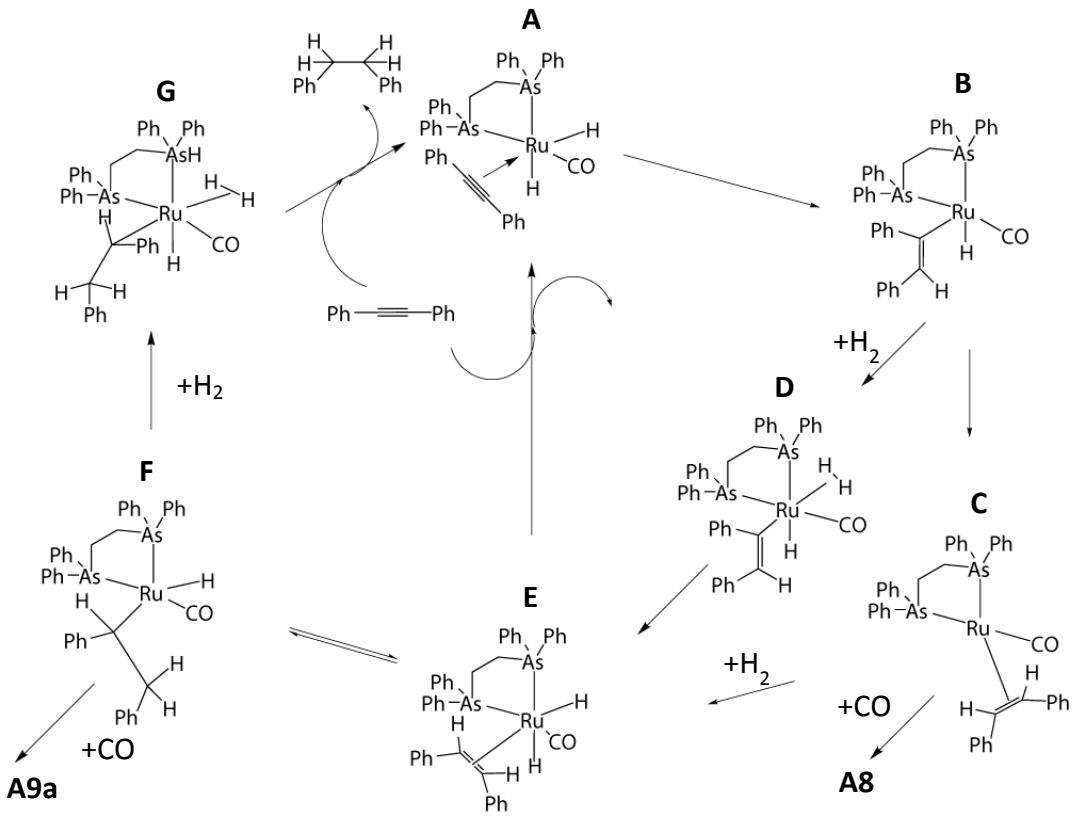

Figure 3.11: Idealised catalytic cycle for the hydrogenation of diphenylacetylene where the initial complex **A** has the equivalent geometry to **11a** (Cycle 1)

3.4.2 Hydrogenation of diphenylacetylene

3.4.2.1 Conversion of diphenylacetylene into stilbene through Cycle 1

The first hydride transfer reaction proceeds through transition state **11a'** where the hydride ligand is 1.53 Å from diphenylacetylene. This reaction leads to Ru(H)(CO)(dhae)(η^1-CPh=CPhH), as **15a**, with the remaining hydride ligand *trans* to the vacant site on the metal and the vinyl group *trans* to dhae. The barrier for from this reaction (**11a'**) is 36.7 kJ mol^{-1} and the overall reaction is favourable by -34.1 kJ mol^{-1}. The second hydride transfer reaction can then proceed through transition state **15a'** which has a significant barrier of 74.6 kJ mol^{-1}. This transition state has the hydride ligand at a distance of 1.51 Å from the vinyl α-carbon, with the hydride adding to the vinyl group on the same face as the first hydride, forming *cis*-stilbene. The reaction then proceeds through a rearrangement where the CO ligand moves *cis* to both ends of the dhae ligand. This rearrangement leads to a more stable geometry and a further stabilisation occurs via interaction with the phenyl ring of the vinyl ligand. This forms species **16a** from **15a**, with an enthalpy change of -69.6 kJ mol^{-1}. This difference in stability with position of the CO ligand was previously reflected in the formation of two isomers of Ru(CO)(dhae)(η^2-diphenyacetylene) as **13a** and **13b**.

The addition of dihydrogen to 16-electron **16a** proceeds via a barrierless oxidative addition forming Ru(H)$_2$(CO)(dhae)(η^2-*cis*-stilbene) (**17b**, **17a** is discussed shortly), with an enthalpy change of -28.2 kJ mol^{-1}. This complex has a different arrangement of the hydride and CO ligands, that is more akin to **11b**, where both hydrides are *cis* to *cis*-stilbene. This change results in the rearrangement of the ligand sphere during the transition from **15a'** to **16a**. The dissociation of *cis*-stilbene from **17b** then forms 5-coordinate Ru(H)$_2$(CO)(dhae) (previously identified **6c**) with an enthalpy change of +120.4 kJ mol^{-1}. The free energy change from this loss is more favourable at +63.1 kJ mol^{-1} but this value will be larger than the true value due to the over estimation of the entropic effects from forming two species from one in the gas phase. The free energy profile is revealed to be similar to that of the enthalpy profile, with the coordination of dihydrogen to **16a** being slightly unfavourable due to the loss of entropy when two molecules combine to form one. Detailed illustrations of the key geometries identified are illustrated in Figure 3.12.

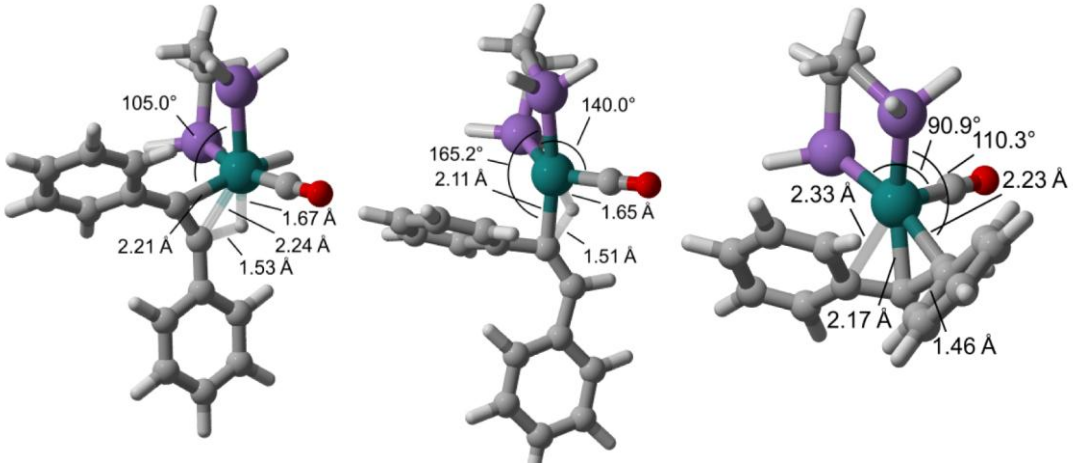

11a' **15a'** **16a**

Figure 3.12: Illustrations of key geometries involved in the beginning of Cycle 1

The incorporation of dihydrogen into Ru(H)(CO)(dhae)(η^1-CPh=CPhH) (**15a**) prior to the second hydride transfer reaction was examined. This addition was found to be favourable by -26.7 kJ mol^{-1} and leads to Ru(H)(CO)(dhae)(η^2-H_2)(η^1-CPh=CPhH) (as **16b**). This modest stabilisation reflects the coordination of dihydrogen and results in an 18-electron complex without oxidative addition. The second hydride transfer reaction can then proceed through transition state **16b'** to form coordinated *cis*-stilbene. The dihydrogen ligand is simultaneously oxidised and the dihydride complex **17a** forms. The barrier to this migration is 44.2 kJ mol^{-1}, and is lower than the barrier from Ru(H)(CO)(dhae)(η^1-CPh=CPhH) as **15a**. The resultant complex $Ru(H)_2$(CO)(dhae)(η^2-*cis*-stilbene), as **17a**, is analogous to the starting complex **11a**, with one hydride *cis* to *cis*-stilbene and the second hydride *trans* to it. The loss of *cis*-stilbene reforms $Ru(H)_2$(CO)(dhae) as **6a** which can then recoordinate diphenylacetylene and reform **11a** and start the cycle again. This loss is unfavourable in terms of enthalpy and free energy, with changes of 98.4 and 38.9 kJ mol^{-1} respectively. The geometry of transition state **16b'** and the final geometries of $Ru(H)_2$(CO)(dhae)(η^2-*cis*-stilbene) as isomers **17a** and **17b** are illustrated in Figure 3.13.

It is also feasible that a second molecule of diphenylacetylene can coordinate to the complex whenever a vacant site is created; the coordination to **15a** is discussed in Section 3.5. Coordination to Ru(CO)(dhae)(η^2-*cis*-stilbene) (**17b**) is significantly unfavourable; the steric repulsion of the phenyl rings in the coordinated *cis*-stilbene effectively shields the metal and makes the approach of an incoming molecule of diphenylacetylene unlikely. This

contrasts the approach of dihydrogen which is significantly smaller and able to approach the metal centre successfully. The thermodynamic values for the reactions identified here are listed in Table 3.4. The profiles for these thermodynamic changes are illustrated in Figure 3.14.

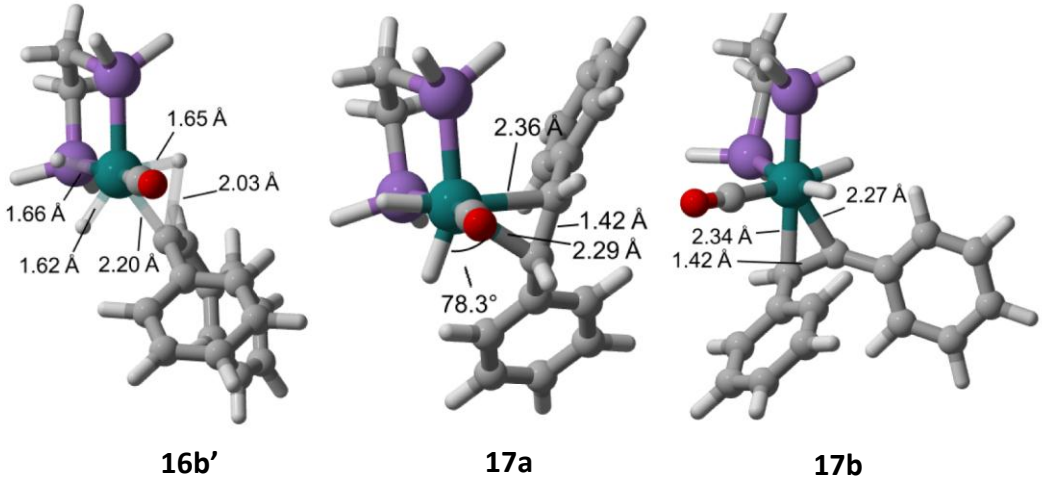

Figure 3.13: Detailed illustrations of transition state **16b'** and later-stage complexes of Cycle 1

Table 3.4: Summary of the thermodynamic values for diphenylacetylene hydrogenation according to Cycle 1. Values are in kJ mol^{-1}

Label	Formed from	Reaction	Relative Enthalpy	Relative free energy
11a'	**11a**	Hydride migration barrier	157.0	166.5
15a	**11a**	Hydride migration	86.1	93.7
15a'	**15a**	Hydride migration barrier	160.7	165.5
16a	**15a**	Hydride migration	16.5	32.9
17b	**16a**	Oxidative addition of H_2	-11.7	37.3
16b	**15a**	Coordination of H_2	59.4	103.2
16b'	**16b**	Hydride migration barrier	103.6	153.8
17a	**16b**	Hydride migration	-31.4	20.0

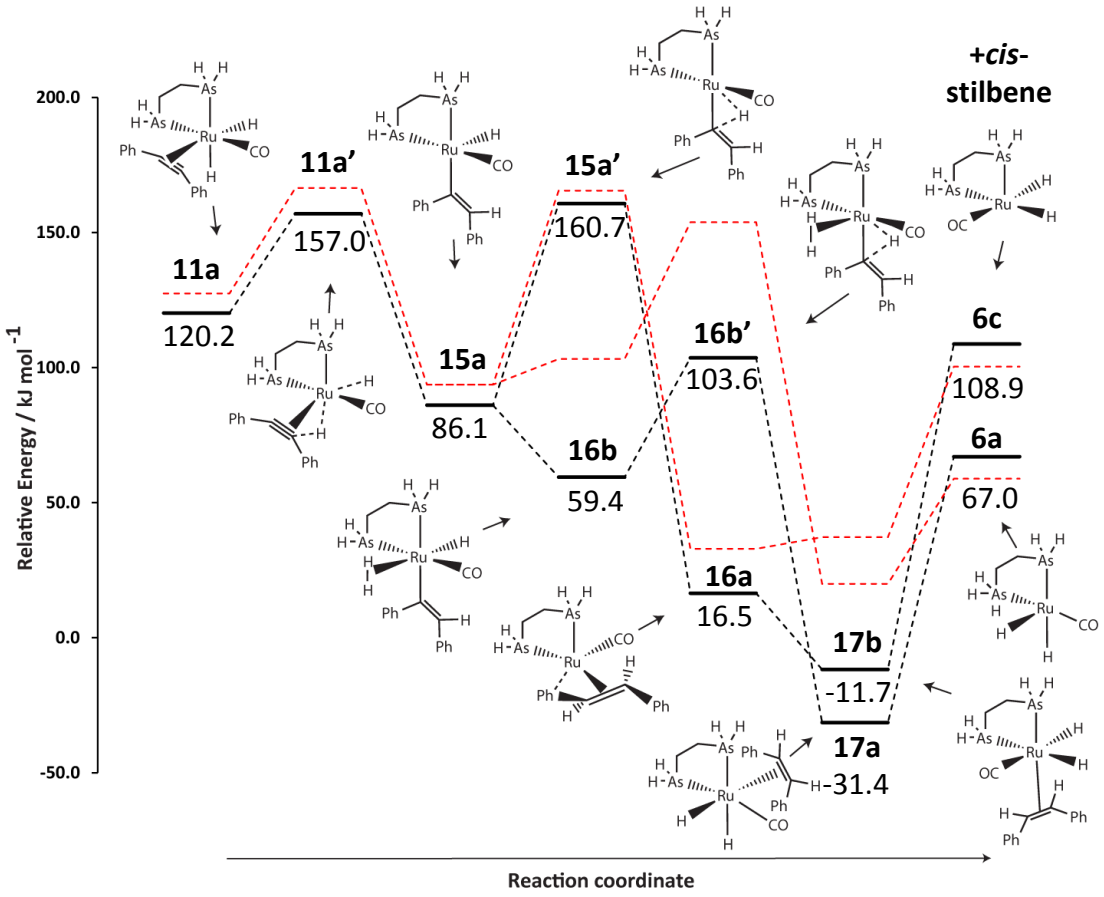

Figure 3.14: Relative enthalpy profile for the catalytic hydrogenation of diphenylacetylene starting from $Ru(H)_2(CO)(dhae)(\eta^2$-diphenylacetylene) as **11a**, forming *cis*-stilbene (Cycle 1). The free energy profile is shown in red.

The loss of *cis*-stilbene from $Ru(H)_2(CO)(dhae)(\eta^2$-*cis*-stilbene) as isomers **17a** and **17b** results in the formation of $Ru(H)_2(CO)(dhae)$, as intermediates **6a** and **6c** respectively; the reaction of **6a** has been described in Section 3.3.2.1 and forms **11a**. **11b** can result from the favourable addition of diphenylacetylene to **6c**, with relative enthalpy and free energy changes of -124.3 and -66.7 kJ mol^{-1} respectively. It should be noted that the feasible reaction to form **17b** means that the minor starting complex **11b** is likely to become the dominant species in the hydrogenation of diphenylacetylene once hydrogenation has been initiated. This is due to the reaction with the stable complex **16a** being more likely than the intermediate **15a**, as **16a** requires the approach of another ligand whereas **15a** can react further without involving another molecule.

3.4.2.1 Conversion of diphenylacetylene into stilbene through Cycle 2

Cycle 2 starts with $Ru(H)_2(CO)(dhae)(\eta^2$-diphenylacetylene) as **11b**, where diphenylacetylene is *trans* to one end of the dhae ligand and *cis* to both hydride ligands. Diphenylacetylene is not aligned with either plane formed by the other ligands and forms 45° dihedral angles with both hydride ligands, illustrated in Figure 3.10 in **11b**. This alignment reduces the steric interaction between the phenyl rings and any other ligand in the complex. Both hydride ligands are capable of undergoing hydride transfer to diphenylacetylene but only the hydride *trans* to CO is considered, as this will create less steric repulsion in the resulting transition state. If the models used included the phenyl rings on dhae, this steric interaction would be more significant.

Hydride migration proceeds through transition state **11b'** which creates a low barrier of 15.3 kJ mol^{-1} to the formation of $Ru(H)(CO)(dhae)\eta^1$-CPh=CPhH) as **15b**. The remaining hydride ligand is *cis* to the vinyl group and so the second hydride migration reaction is possible. This migration proceeds through transition state **15b'** which forms a barrier of 62.2 kJ mol^{-1}. This transition state leads to *cis*-stilbene, and these transition states are illustrated in Figure 3.15.

A subtle rearrangement in **15b** was identified which changes the pathway of the second hydride transfer, which involves a minor barrier of 2.1 kJ mol^{-1} as **15c'**. This rotation, involving the vinyl ligand, changes the orientation of the transferred hydrogen on the β-carbon and the phenyl ring on the α-carbon such that it is directed towards the arsenic centre rather than the hydride ligand and leads to the formation of **15c**, which is 6.0 kJ mol^{-1} more stable than **15b**.

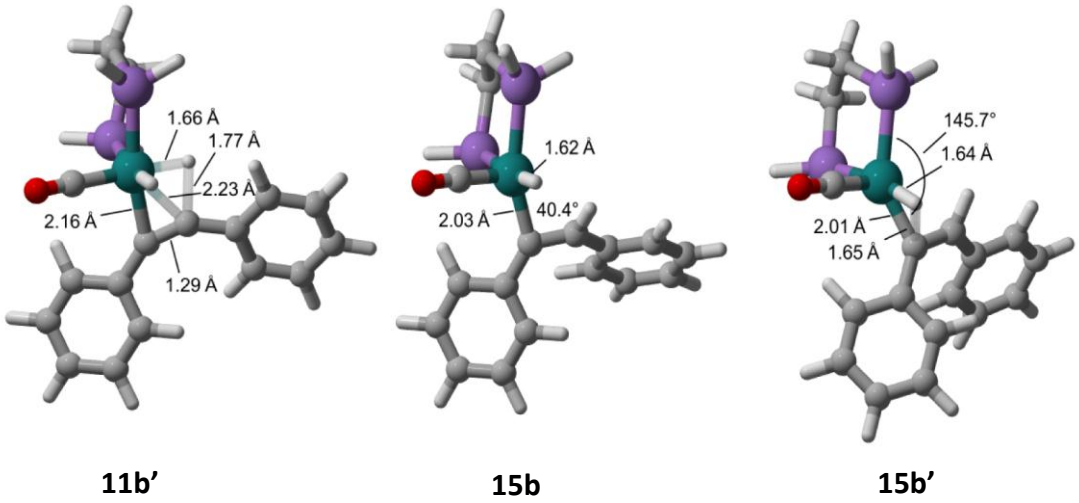

Figure 3.15: Illustrations of selected intermediates identified at the beginning of Cycle 2

Hydride transfer in **15c** has a low barrier of 9.7 kJ mol^{-1} and therefore likely to dominate. Importantly, this hydride migration proceeds to the opposite face of the alkene bond and forms *trans*-stilbene. Relaxed constrained scans showed that the transition state **15d'** leads to the *trans* isomer regardless of the initial vinyl alignment. Additionally, a similar scan with the full model (where dhae was replaced by dpae) revealed *trans*-stilbene formation to still occur. The resulting complex, **16c**, is formed favourably, with an enthalpy change of 110.1 kJ mol^{-1} and is stabilised by an interaction with a phenyl ring of stilbene as seen with **16a**. Addition of dihydrogen to **16c** forms **17c**, which is of similar geometry to **17b** but contains *trans*-stilbene.

Coordination of dihydrogen to Ru(H)(CO)(dhae)(η^1-CPh=CPhH) (as **15b** or **15c**) prior to the second hydride transfer reaction forms Ru(H)(CO)(dhae)(η^2-H_2)(η^1-CPh=CPhH) as **16d**. The subsequent reaction via **16d'** involves the simultaneous oxidation of dihydrogen and the second hydride transfer. The barrier for this is significant at 63.3 kJ mol^{-1}, and higher than the route without dihydrogen addition. This transition state leads to *cis*-stilbene, and results in Ru(CO)(dhae)(η^2-H_2)(η^2-*cis*-stilbene) as isomer **17b**. The barrier from **16d'** is in keeping with that calculated in Cycle 1 as **15b'**, leading to the formation of *cis*-stilbene. The geometries of selected intermediates and transition states are illustrated in Figure 3.16. The exact pathway followed will therefore depend on the concentration of H_2. Hence, the pathways will operate in competition.

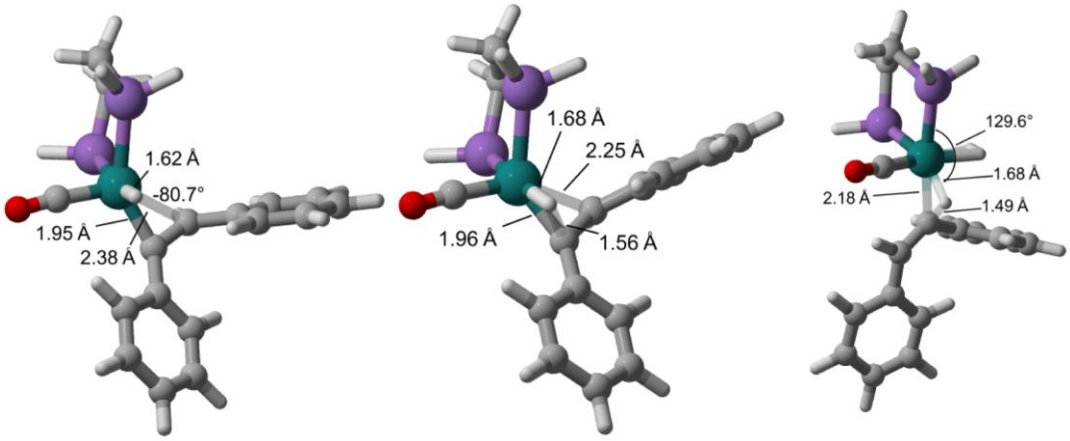

Figure 3.16: Illustrations of selected major intermediates identified for Cycle 2

$Ru(H)_2(CO)(dhae)(\eta^2$-*cis*-stilbene), as **17b**, can then undergo dissociation of *cis*-stilbene and the formation of 16-electron **6c** as previously detailed. Loss of *trans*-stilbene from **17c** also leads to the formation of **6c**, which involves an enthalpy change of 102.8 kJ mol^{-1} and a lower free energy change of 43.2 kJ mol^{-1}. Intermediate **6c** can then add another diphenylacetylene ligand and can re-enter the hydrogenation cycle. This addition was also described for Cycle 1. The reaction enthalpies, and free energies changes are detailed in Table 3.5, with the pathways illustrated in Figure 3.17. The rearrangement from **15b** to **15c** is not included for clarity.

Table 3.5: Summary of the thermodynamic values for diphenylacetylene hydrogenation via Cycle 2. Values are in kJ mol^{-1}

Label	Formed from	Reaction	Relative Enthalpy	Relative free energy
11b'	**11b**	Hydride migration barrier	161.4	168.8
15c	**11b**	Hydride migration	112.9	125.9
15d'	**15c**	Hydride migration barrier	128.6	138.9
16c	**15c**	Hydride migration	8.8	25.1
17c	**16c**	Coordination of H_2	-14.1	31.2
16d	**15c**	Coordination of H_2	66.8	109.3
16d'	**16d**	Hydride migration barrier	130.1	174.7
17b	**16d**	Hydride migration	4.1	49.9

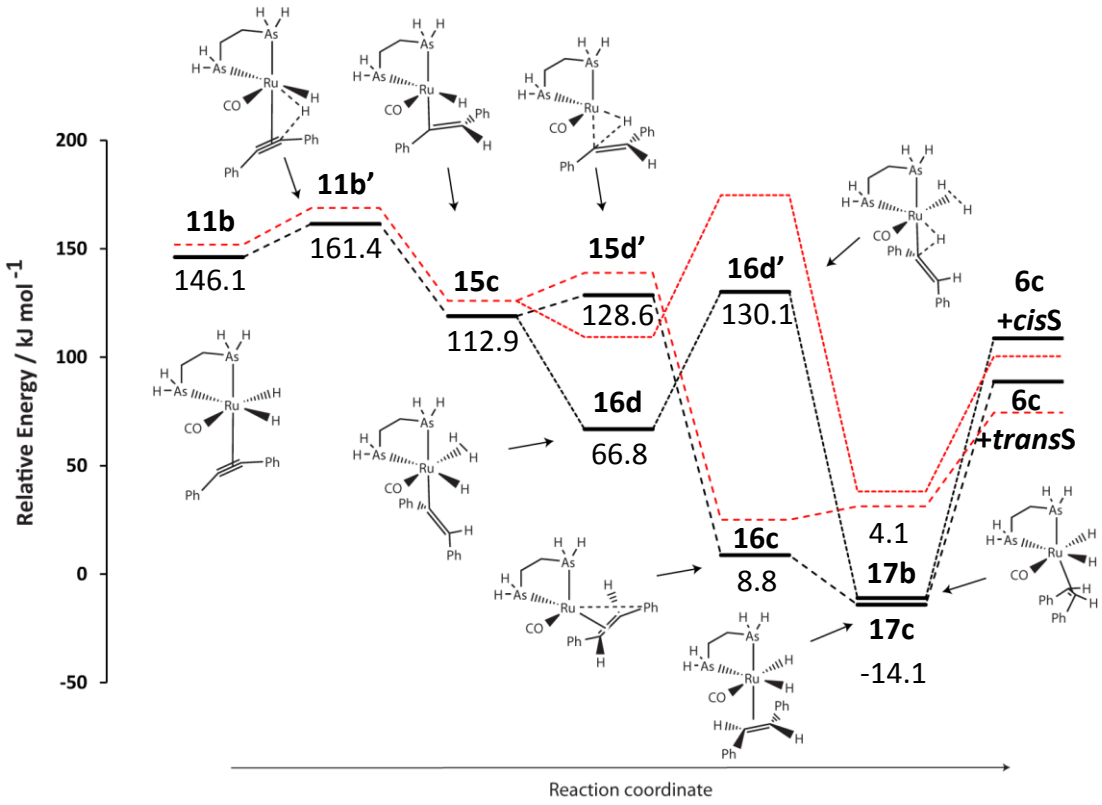

Figure 3.17: Relative enthalpy profile for the catalytic hydrogenation of diphenylacetylene starting from complex **11b**, forming *cis* and *trans*-stilbene (Cycle 2). The free energy profiles are shown in red. The terms *cis*S and *trans*S refer to *cis*- and *trans*-stilbene respectively.

The binding of another molecule of diphenylacetylene to intermediate Ru(H)(CO)(dhae)(η^1-CPh=CPhH) as **15c** is discussed in Section 3.5. The binding of diphenylacetylene to the vacant site in Ru(H)(CO)(dhae)(η^2-*trans*-stilbene), as **16c**, is unfavourable due to the steric repulsion from the *trans*-stilbene ligand; this ligand also interacts with the metal to shield the vacant site.

3.4.2.2 Conversion of diphenylacetylene into stilbene through Cycle 3

Only one hydride ligand is *cis* to diphenylacetylene in $Ru(H)_2(CO)_2(\kappa^1$-dhae)(η^2-diphenylacetylene), as **12a**, and so hydride transfer proceeds through this route (transition state **12a'**). This process is downhill with a barrier of 22.1 kJ mol^{-1} (from **12a'**, forming **12c**) with a rearrangement to **18a** having a barrier of 9.6 kJ mol^{-1}. The complex produced via **12c'** (**18a**) is 45.5 kJ mol^{-1} more stable than **12a**. The second hydride migration via **18a** has a sizable barrier of 86.5 kJ mol^{-1} via transition state **18a'** and is therefore disfavoured. Alternatively, dihydrogen can add to **18a** forming Ru(H)(CO)(η^1-dhae)(η^2-H_2)(η^1-CPh=CPhH) as **19a**. The second transfer reaction then involves transition state **19a'** and a barrier of 79.5 kJ mol^{-1}. The most likely pathway is now however recoordination of the free end of the η^1-dhae ligand. Recoordination occurs through a small barrier of 7.3 kJ mol^{-1} (from **18aR'**) and forms complex $Ru(H)(CO)_2$(dhae)(η^1-CPh=CPhH), as isomer **20a**. The second hydride transfer reaction then occurs through transition state **20a'** with a barrier of 73.8 kJ mol^{-1} (enthalpy), to form $Ru(CO)_2$(dhae)(η^2-*cis*-stilbene) as **20b**. This complex is similar to experimentally identified **A8**. Whilst the barrier for this second hydride transfer reaction is the same as those calculated with **18a'** and **19a'**, the recoordination of the free end of η^1-dhae is likely due to the chelate effect. Selected key transition states are also illustrated in Figure 3.18.

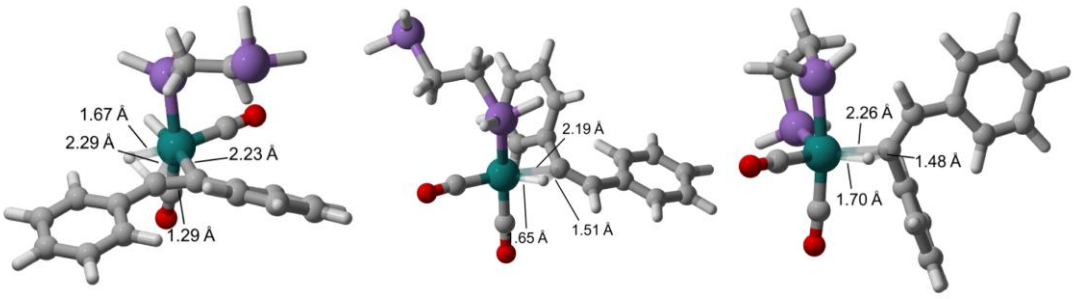

12a' **18a'** **20a'**

Figure 3.18: Detailed illustrations of key transition states identified in Cycle 3

The loss of *cis*-stilbene from **20b** is unfavourable by +92.1 kJ mol^{-1} and forms $Ru(CO)_2$(dhae), as **4b**, as identified previously. The free energy change is more favourable at 31.1 kJ mol^{-1}. This 16-electron intermediate can then react with diphenylacetylene or hydrogen as previously described. These geometries and thermodynamic profiles are illustrated in Figure 3.19, with the reaction enthalpies and free energies shown in Table 3.6.

Table 3.6: Summary of thermodynamic values for diphenylacetylene hydrogenation via Cycle 3. Values are in kJ mol^{-1}

Label	Formed from	Reaction	Relative Enthalpy	Relative free energy
12a'	**12a**	Hydride migration barrier	92.4	127.6
12d	**12a**	Hydride migration	64.0	101.9
12d'	**12d**	Rearrangement barrier	73.6	115.3
18a	**12d**	Rearrangement	18.5	58.9
18a'	**18a**	Hydride migration barrier	86.5	138.4
19a	**18a**	Coordination of H_2	0.3	69.8
19a'	**19a**	Hydride migration barrier	79.8	177.5
18aR'	**18a**	Recoordination of η^1-dhae barrier	25.8	72.6
20a	**18a**	Recoordination of η^1-dhae	-51.2	4.7
20a'	**20a**	Hydride migration barrier	22.6	87.0
20b	**20a**	Hydride migration	-92.5	-34.3

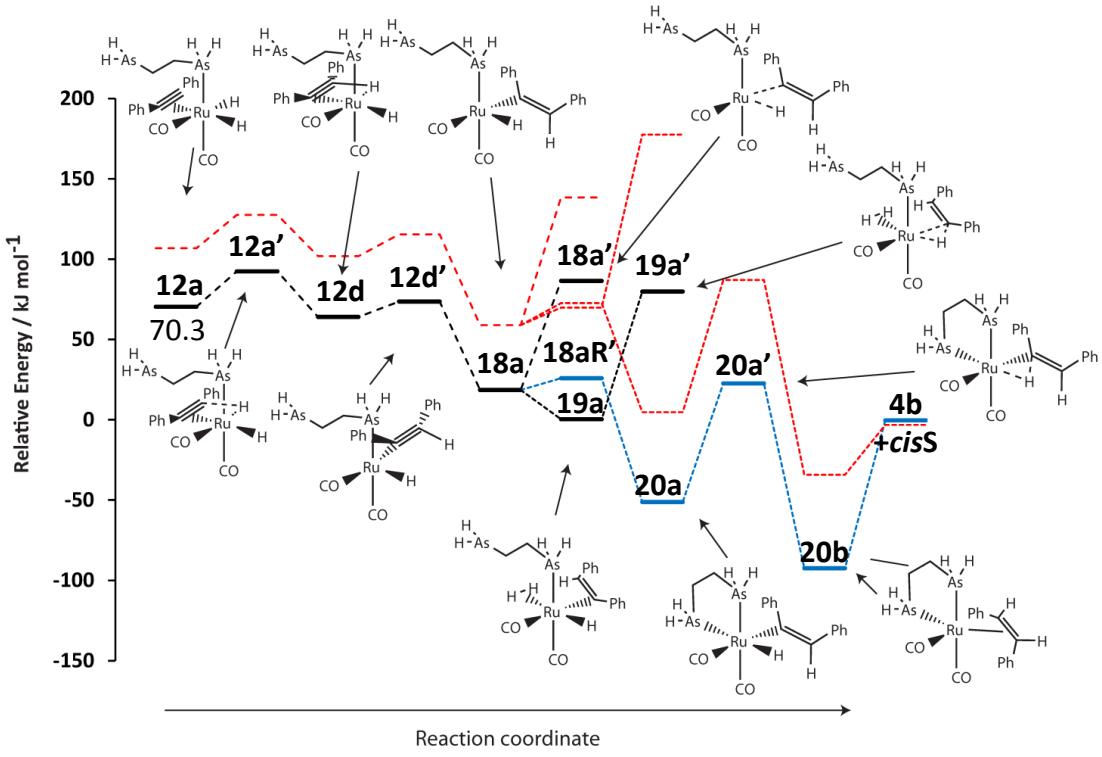

Figure 3.19: Catalytic cycle for the hydrogenation of diphenylacetylene from complex **17a** (Cycle 3). The pathway shown in blue is for the recoordination of the free end of η^1-dhae with **18a**. The free energy profile is illustrated in red

It should be noted that the barriers for recoordination of the chelate could be significantly lower here than in the real system, due to the simplification of dpae to dhae.

It is possible that de-chelation can occur with **20b** in competition with the loss of *cis*-stilbene to form **4b**. However the analysis of the thermodynamic changes for this reaction revealed that *cis*-stilbene dissociation was favoured. Formation of **4b** allows the reformation of $Ru(H)_2(CO)_2$(dhae), as **3a**, which was previously determined to be a stable species in Chapter 2. Hence, the hydrogenation of either isomer of stilbene though a de-chelation route can be considered to be negligible.

3.4.2.3 Summary of diphenylacetylene hydrogenation pathways

The pathways identified for the three starting species all lead to *cis*-stilbene according to the calculations performed here. It has been found that the formation of *trans*-stilbene is also possible, but this appears to require the correct distribution of inner sphere ligands to allow rotation of the C=C bond of the vinyl ligand. This rotation allows the second hydride transfer reaction to take place on the opposite face to that of the β-CH group formed during the first hydride transfer pathway.

The first hydride transfer reaction was found to proceed through relatively low barriers, with the second transfer proceeding through significantly higher barriers, except that of **15d'** in Cycle 2. These low barriers are consistent with the failure to experimentally detect any complexes of the type $Ru(H)_2(CO)$(dpae)(η^2-diphenylacetylene). The sizeable barriers predicted for the second hydride transfer reaction mean that the lifetime of the 16-electron intermediates of the type Ru(H)(CO)(dpae)(η^1-CPh=CPhH) can be significant enough for a successful collision to occur with another ligand, potentially changing the products formed. The steric crowding of the metal centre could still allow the coordination of another ligand, indicated by the barriers predicted for the recoordination of the free end of the η^1-dhae ligand with Cycle 3.

The role of the alkene in these reactions was not innocent. The interaction of the phenyl groups in *cis* or *trans*-stilbene with the metal centre did not prevent coordination of dihydrogen to form a dihydride complex capable of further hydrogenation, although, it should be noted that such complexes were not seen experimentally. The ability of these

complexes to further react could account for this observation. The steric bulk of *cis*-stilbene was found to aid in its dissociation from the metal complex more than the dissociation of *trans*-stilbene. This is consistent with the alignment of the phenyl rings. Crowding of the metal centre by either isomer of stilbene provides a barrier to the coordination of a second molecule of diphenylacetylene in contrast to the approach of dihydrogen.

3.4.3 Hydrogenation of stilbene

3.4.3.1 Hydrogenation of *cis*-stilbene through Cycle 1

The significant barrier for the loss of *cis*-stilbene from $Ru(H)_2(CO)(dhae)(\eta^2$-*cis*-stilbene) (as **17a**) (enthalpy and free energy changes of 98.4 and 38.9 kJ mol^{-1} respectively) means that the further hydrogenation of *cis*-stilbene is possible. **17a** has only one hydride ligand *cis* to *cis*-stilbene (*trans* to the dhae ligand) and so only one hydride transfer reaction is possible. This reaction proceeds though transition state **17a'** and forms an isomer of $Ru(H)(CO)(dhae)(\eta^1$-$CPhH\text{-}CPhH_2)$ (**21a**) where the hydrogen atom transferred forms an agostic β-H-bond to the ruthenium centre. This reaction is unfavourable but the change in enthalpy is lower than for dissociation of *cis*-stilbene to form **6a** (49.0 vs. 98.4 kJ mol^{-1} respectively). The nature of the agostic bond was confirmed by the Ru-H distance; it was modelled as 1.79 Å which satisfies the definition given by Brookhart *et al.*[215] The C-H bond length is also lengthened to 1.26 Å, whilst the non-interacting C-H bond length is 1.10 Å.

To investigate this interaction, Atoms In Molecules (AIM) theory was used.[211] This method evaluates the electron density of the system along with the gradient vector field of the electron density. This allows critical points in the density to be identified where the gradient field is zero. The maxima in the gradient field are identified as the location of the nuclei and are referred to as nuclear critical points (NCP). Second-order saddle points usually appear between attractive atom pairs and are referred to as bond critical points (BCP). First-order saddle points usually appear at the centre of ring systems and are referred to as ring critical points (RCP). Local minima in the gradient field are referred to as cage critical points and usually appear in the centre of cage systems.[216] This method has been shown be helpful in understanding agostic interactions,[217] with a recent study classifying the different types of interaction.[218] The analysis of the electron density and gradient vector field was undertaken and critical points identified. The examination of the

Poincaré-Hopf relation found this was satisfied for **21a**, indicating that all critical points had been identified.

The electron density gradient profile for this analysis is shown in Figure 3.20.

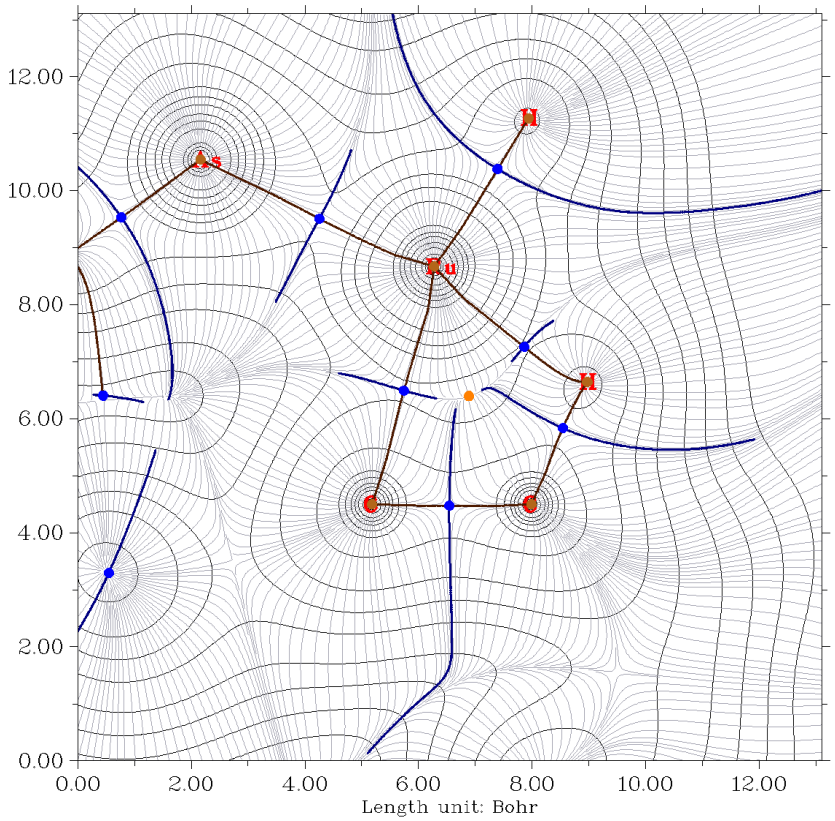

Figure 3.20: Electron density plot taken through the Ru-CPh-CPH_2 plane of intermediate **21a**. NCPs are coloured brown, BCPs are coloured blue and RCPs are coloured orange. Paths between NCPs which run through BCPs are coloured brown and interbasin paths are coloured blue. The agostic interaction is shown between the β-hydrogen and the metal centre

This analysis shows that bond critical points are present between the β-carbon and the hydrogen, together with this hydrogen and the metal centre. A ring critical point was located in the centre of the 5-membered ring that this interaction creates. This analysis is consistent with the presence of the agostic interaction.

The final hydride transfer reaction cannot occur directly from **21a** as the hydride is not in the required *cis* position. The movement of the remaining hydride into the position occupied by the agostic hydrogen was calculated to occur through a sizeable barrier of 54.8

kJ mol^{-1}, through transition state **22a'**. Two additional transition states were identified, **22b'** is the barrier for approach of dihydrogen between the hydride ligand and the agostic hydride; the coordination results in a reaction where the dihydrogen bond breaks and is reformed with the hydride ligand. This results in a hydride ligand *cis* to the partially hydrogenated *cis*-stilbene and the dihydrogen ligand *trans*. A similar approach can also occur with CO, with the approach simultaneously forcing the remaining hydride in to the *cis* position through transition state **22c'**. These reaction enthalpies and free energies are detailed in Table 3.7, with the pathways illustrated in Figure 3.21.

Table 3.7: Thermodynamic values for the start of the possible hydrogenation of *cis*-stilbene by Cycle 1. Values are in kJ mol^{-1}

Label	Formed from	Reaction	Relative Enthalpy	Relative free energy
17a'	**17a**	Hydride migration barrier	28.0	78.7
21a	**17a**	Hydride migration	17.6	68.3
22a'	**21a**	Rearrangement barrier	72.4	122.8
22b'	**21a**	Approach of dihydrogen	78.4	168.6
22c'	**21a**	Approach of CO	74.8	178.4
6a	**17a**	Release of *cis*-stilbene	67.0	58.9

These calculations predict that the hydrogenation of *cis*-stilbene is likely to constitute a minor pathway due to the significant barriers for rearrangement of the ligand sphere. The formation of **21a** is unfavourable and so dihydride complex **17a** will dominate, with the barrier for the reformation of **17a** from **21a** now being 10.4 kJ mol^{-1}. The free energy change for the loss of *cis*-stilbene from complex **21a** to form $Ru(H)_2(CO)(dhae)$ (as **6a**) of 38.9 kJ mol^{-1} means that this is the most likely pathway.

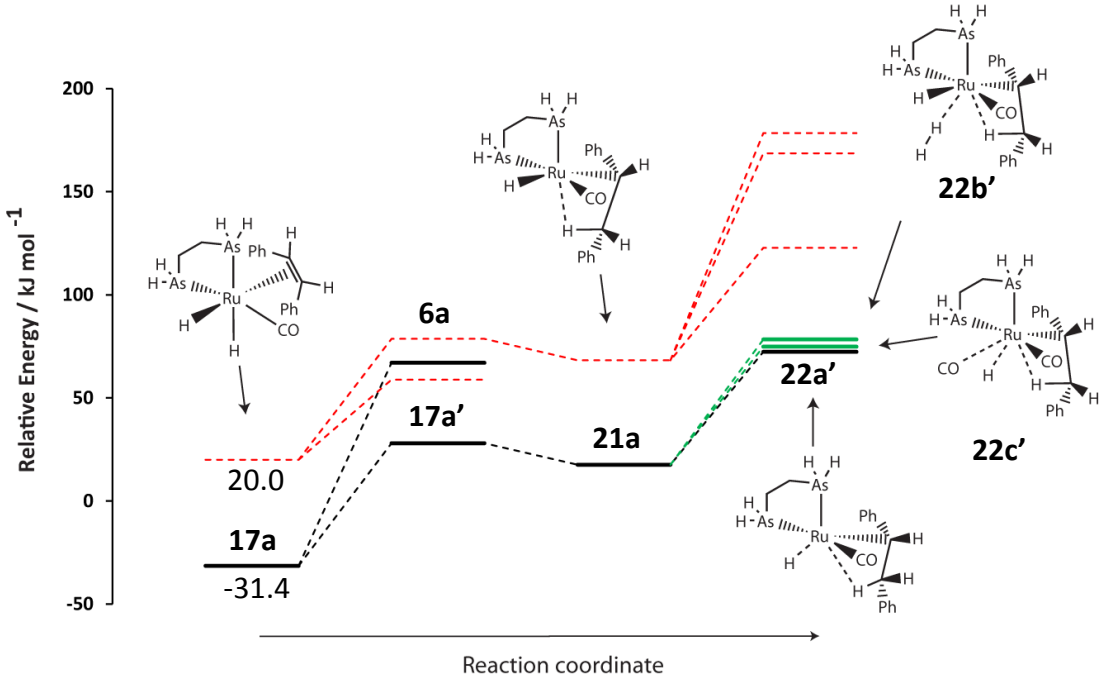

Figure 3.21: Relative enthalpy profile for the start of the hydrogenation of *cis*-stilbene from complex **17a**, forming 1,2-diphenylethane ethane (Cycle 1). The barriers formed for the approach of H_2 or CO are shown in in green. The free energy profiles are shown in red

If rearrangement did occur, the resulting complex Ru(H)(CO)(dhae)(η^1-CPhH-CPhH$_2$), as **22a**, can react with CO or dihydrogen. The addition of dihydrogen results in **22b**. The final hydride transfer reaction can occur from this species, with a low barrier from transition state **22d'** of 16.2 kJ mol^{-1}. This barrier is low as the transition state is stabilised by the simultaneous oxidation of the dihydrogen ligand to form two new hydride ligands. This leads to the formation of 1,2-diphenylethane which is released from the complex and the formation of **6a**, with a favourable enthalpy change of -18.3 kJ mol^{-1}. These thermodynamic values are summarised in Table 3.8.

The reaction of CO with **22a** leads to the formation of **23a**, which is favourable by -195.0 kJ mol^{-1}. The final hydride transfer reaction can occur from this complex, which leads to the formation of Ru(CO)$_2$(dhae) as **4b** and the release of 1,2-diphenylethane. This proceeds through transition state **23a'** which creates a barrier of 72.4 kJ mol^{-1}, with the overall pathway unfavourable in terms of enthalpy by 27 kJ mol^{-1}. It is predicted to be favourable in terms of free energy by -34.6 kJ mol^{-1}.

Table 3.8: Thermodynamic values for the hydrogenation of *cis*-stilbene via Cycle 1. Values are in kJ mol^{-1}

Label	Formed from	Reaction	Relative Enthalpy	Relative free energy
22a	**21a**	Complex rearrangement	44.1	88.7
22b	**22a**	Coordination of H_2	-38.2	44.6
22d'	**22b**	Hydride transfer barrier	-16.6	71.9
6a	**22b**	Release of alkyl species	-56.5	-31.3
23a	**22a**	Coordination of CO	-150.9	-58.8
23a'	**23a**	Hydride transfer barrier	-78.5	18.2
4b	**23a**	Release of alkyl species	-123.9	-93.4

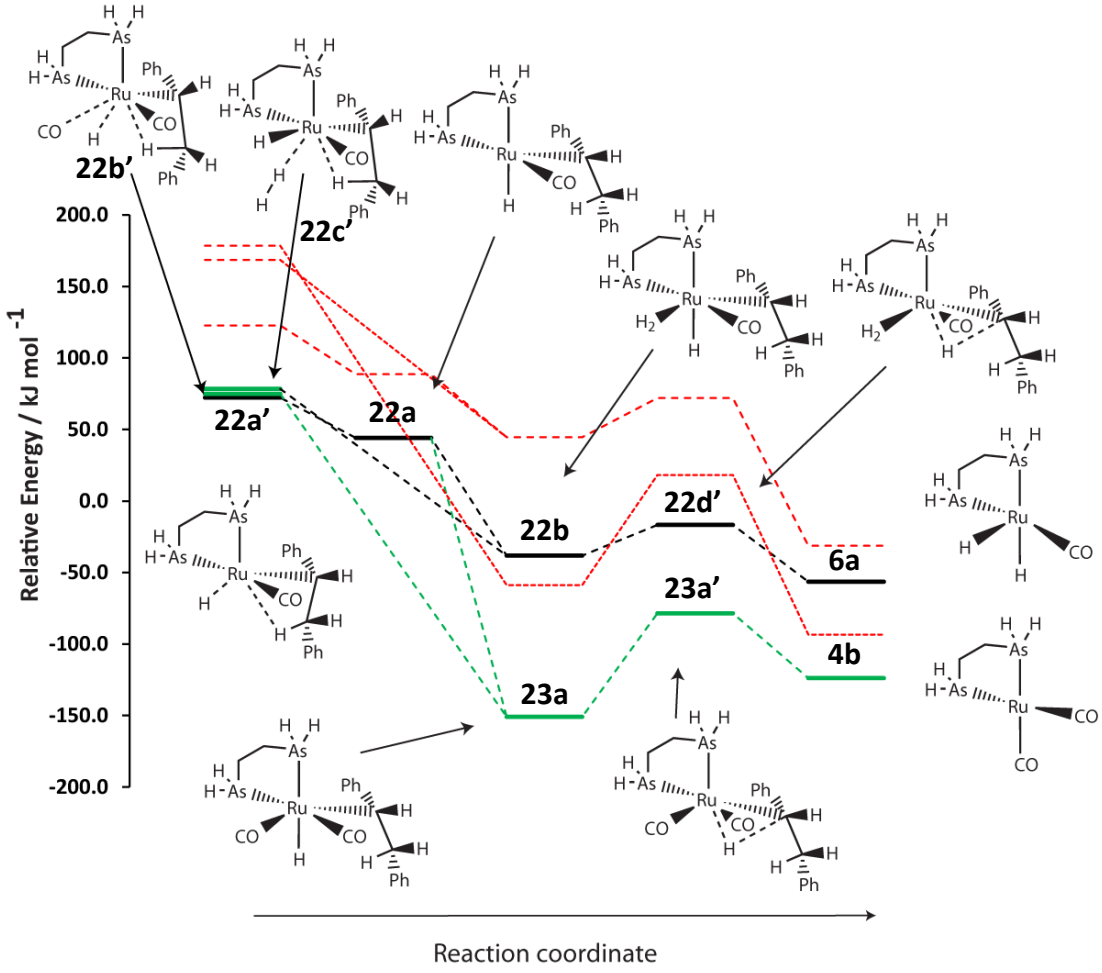

Figure 3.22: Relative enthalpy profile for the hydrogenation of *cis*-stilbene from complex **17a** forming 1,2-diphenylethane (Cycle 1). The addition of CO is shown by the green profile. The free energy profiles are shown in red

3.4.3.2 Hydrogenation of stilbene through Cycle 2

The isomer of $Ru(H)_2(CO)(dhae)(\eta^2$-*trans*-stilbene), as **17c**, has *trans*-stilbene in a position which is *cis* to both hydride ligands. This results in the potential for hydride migration to occur with either hydride ligand. The hydride *trans* to CO is considered here, as this involves a less sterically demanding centre than would be necessary for the other hydride. It is noted that the simplified model used here does not map such steric interactions fully.

This first hydride transfer leads to $Ru(H)(CO)(dhae)(\eta^1$-$CPhH\text{-}CPhH_2)$, as **21b**, which contains a β-agostic C-H bond. This interaction was confirmed by AIM, with bonding critical points being identified between the β-hydrogen and the carbon centre, and the metal centre, with a ring critical point also identified for the 5-membered ring that results. It is preceded by a barrier of 13.1 kJ mol^{-1}, for transition state **17c'**. This barrier is significantly less than that calculated for the equivalent reaction with **17a**. With transitions state **17a'**, the hydride-carbon distance is 1.40 Å whereas with **17c'** this distance is longer, at 1.68 Å. This means that the transition state occurs much earlier in the reaction coordinate. Further reactions of **21b** require rearrangement or coordination of another ligand, in line with **21a** of Cycle 1. The movement of the fourth hydride ligand into the position occupied by the agostic hydrogen occurs via transition state **22e'**. The barrier to this is 124.3 kJ mol^{-1} and therefore this pathway is unlikely and is not considered further**.** The coordination of dihydrogen to **21b** is possible and proceeds by transition state **22f'**. The dihydrogen molecule then occupies the position *trans* to CO, as **22f**. Intermediate **22f** has the dihydrogen molecule again in line with the metal-hydride ligand and so reaction can proceed by simultaneous oxidation of the dihydrogen ligand and the final hydride transfer reaction. This results in $Ru(H)_2(CO)(dhae)$ as isomer **6c** and 1,2-diphenylethane and proceeds through transition state **22g'**, with barrier 74.0 kJ mol^{-1}.

Alternatively, CO can approach $Ru(H)(CO)(dhae)(\eta^1$-$CPhH\text{-}CPhH_2)$ as **21b** and coordinate to the metal centre. This pathway proceeds through transition state **22h'** which creates the lowest barrier identified here of 34.8 kJ mol^{-1}. This barrier is less than that for the approach of dihydrogen and so the addition of CO is preferred. Hence, the selected pathway will depend upon the concentration of these ligands in solution. The addition of CO leads to $Ru(H)(CO)_2(dhae)(\eta^1$-$CPhH\text{-}CPhH_2)$, as **23b**, which has the CO ligands in a *trans* arrangement.

This addition is favourable by -111.0 kJ mol^{-1}, with the free energy reduced but still favourable, at -70.9 kJ mol^{-1}. The final hydride transfer reaction then has a barrier of 88.3 kJ mol^{-1} arising from transition state **23b'**. This reaction also leads to the rearrangement of the CO ligands to form the butterfly geometry of 16-electron $Ru(CO)_2$(dhae) as **4b**. Whilst this transfer is not favourable in terms of enthalpy, with a change of 8.0 kJ mol^{-1}, the free energy change is favourable at -48.6 kJ mol^{-1}. These thermodynamic changes and geometries are illustrated in Figure 3.23, with the reaction enthalpies and free energies detailed in Table 3.9.

Table 3.9: Summary of thermodynamic values during hydrogenation of *trans*-stilbene via $Ru(H)_2(CO)$(dhae)(η^2-*trans*-stilbene), **17c** via Cycle 2. Values are in kJ mol^{-1}

Label	Formed from	Reaction	Relative Enthalpy	Relative Free energy
17c'	**17c**	Hydride migration barrier	-1.0	44.7
21b	**17c**	Hydride migration	-20.9	26.1
22e'	**21b**	Rearrangement barrier	103.4	163.2
22f'	**21b**	Approach of H_2	31.0	106.3
22f	**21b**	Coordination of H_2	-26.3	51.0
22g'	**22f**	Hydride migration barrier	47.7	125.9
6c	**22f**	Hydride migration	-14.8	10.2
22h'	**21b**	Approach of CO	13.9	97.4
23b	**21b**	Coordination of CO	-131.9	-44.8
23b'	**23b**	Hydride migration barrier	-43.6	52.9
4b	**23b**	Hydride migration	-123.9	-93.4

The barriers for reaction from Ru(H)(CO)(dhae)(η^1-CPhH-$CPhH_2$), **21b**, have to compete with the barrier for the dissociation of *trans*-stilbene from $Ru(H)_2(CO)$(dhae)(η^2-*trans*-stilbene), **17c**. This forms **6c** and free *trans*-stilbene, with associated enthalpy and free energy changes of 102.8 and 43.2 kJ mol^{-1} respectively. These barriers are with the experimental data, where *cis* and *trans*-stilbene were observed first, with signals for 1,2-diphenylethane building during the reaction.

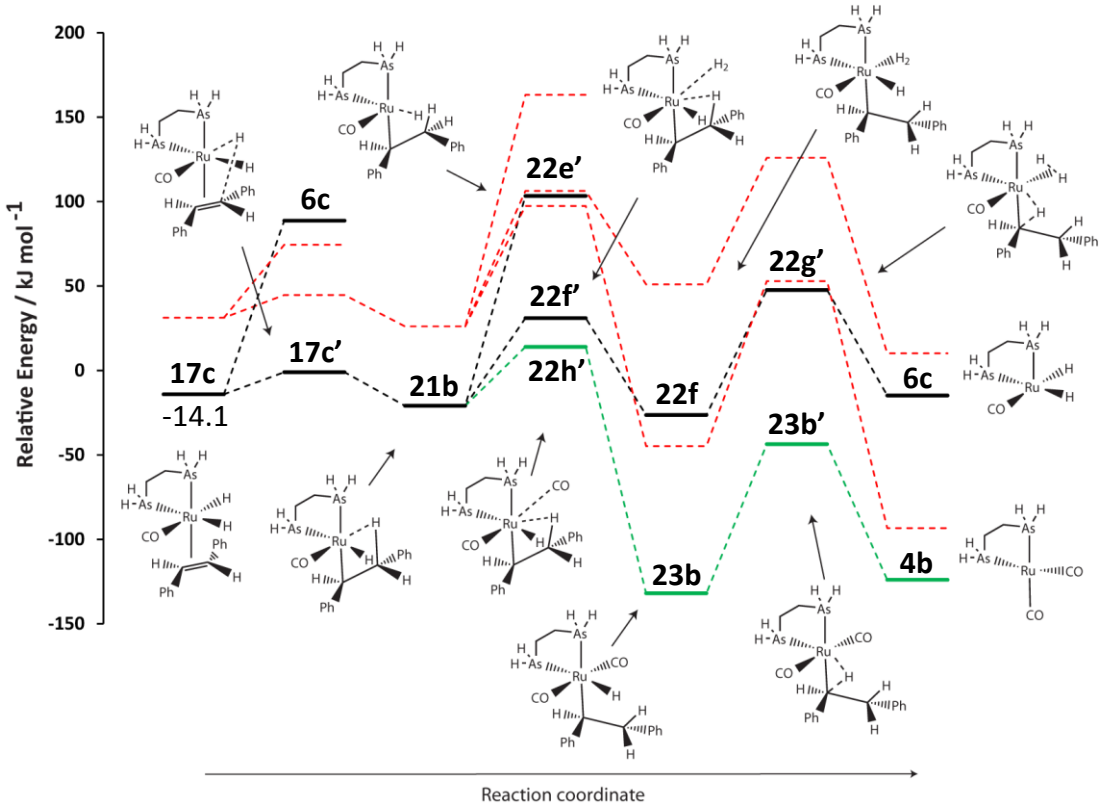

Figure 3.23: Relative enthalpy profiles *trans*-stilbene hydrogenation starting from complex **17c** (Cycle 2). The formation of **6c** and **4b** are accompanied by either *trans*-stilbene or 1,2-diphenylethane. The pathway involving the addition of CO is shown in green. The free energy profiles are illustrated in red

Hydrogenation of *cis*-stilbene can also occur from Ru(H)(CO)(dhae)(η^2-*cis*-stilbene), as **17b**, formed from the addition of dihydrogen to the metal complex prior to the 2nd hydride transfer reaction. This involves the same hydride ligand as previously described for **17c** and the pathway proceeds through a similar barrier of 13.1 kJ mol^{-1}, arising from transition state **17b'**. This transfer leads to the favourable formation of Ru(H)(CO)(dhae)(η^1-CPhH-CPhH$_2$), **21c**, with an enthalpy change of -12.2 kJ mol^{-1}. **21c** also exhibits the interaction of a β-hydrogen with the metal centre, with a distance between these two nuclei of 1.90 A. The movement of the remaining hydride ligand occurs through a high energy transition state, with a barrier of 111.5 kJ mol^{-1} (**22e'**) and so this route is not considered any further. Lower energy pathways were found which involved the approach of dihydrogen or CO; the barrier for dihydrogen approach (transition state **22i'**) is 45.8 kJ mol^{-1}, with the barrier for CO approach slightly higher at 49.5 kJ mol^{-1}. These pathways lead to **22f** and **23b** respectively,

as previously identified. These steps are summarised in Table 3.10 and the illustrated in Figure 3.24.

Table 3.10: Summary of thermodynamic values predicted during the hydrogenation of *cis*-stilbene via Ru(H)(CO)$_2$(dhae)(η^2-*cis*-stilbene) as **21b** via Cycle 2. Values are in kJ mol^{-1}

Label	Formed from	Reaction	Relative Enthalpy	Relative Free energy
17b'	**17b**	Hydride migration barrier	11.4	49.9
21c	**17b**	Hydride migration	-8.1	59.9
22e'	**21c**	Rearrangement barrier	103.4	163.2
22i'	**21c**	Approach of H_2	37.7	122.9
22f	**21c**	Coordination of H_2	-26.3	51.0
22j'	**21c**	Approach of CO	41.4	140.2
23b	**21c**	Coordination of CO	-131.9	-44.8

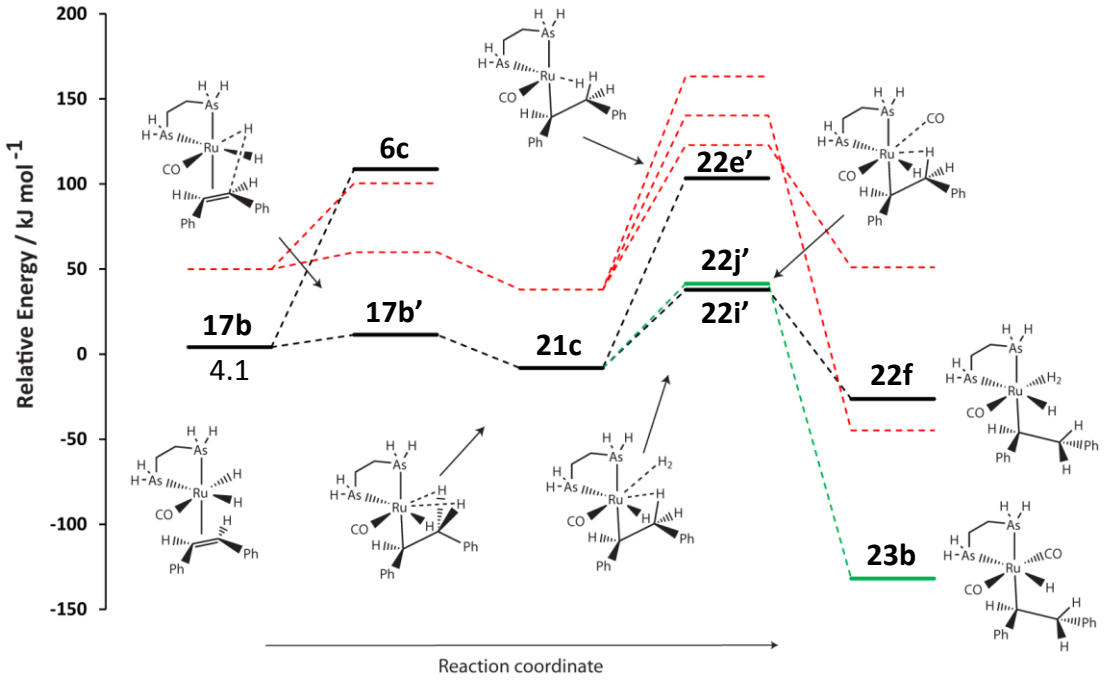

Figure 3.24: Relative enthalpy profile for the hydrogenation of *cis*-stilbene starting from complex **17b** (Cycle 2). The formation of **6c** is accompanied by *cis*-stilbene. The free energy profiles are illustrated in red. The subsequent reactions from 22f and 23b are shown in Figure 3.23.

The barriers for reaction from Ru(H)(CO)(dhae)(η^1-CPhH-CPhH_2) as **21c** also have to compete with the barrier for the dissociation of *cis*-stilbene from Ru$(H)_2$(CO)(dhae)(η^2-*cis*-stilbene) as **17b**. This dissociation again forms **6c** and free *cis*-stilbene, with associated enthalpy and free energy changes of 104.6 and 50.5 kJ mol^{-1} respectively.

The calculations here have shown that both *cis*- and *trans*-stilbene can be hydrogenated via **17b** and **17c** to form 1,2-diphenylethane. This hydrogenation also requires the interaction of a second ligand with the complex to overcome the hydrogen interaction with the metal. This can happen either with dihydrogen or CO. The resulting intermediates can then react with diphenylacetylene, and catalysis can occur once more. It is also possible that *cis*-or *trans*-stilbene can coordinate to a metal and undergo subsequent hydrogenation.

3.4.3.3 Summary of pathways for *cis*- and *trans*-stilbene hydrogenation

The barriers present in each cycle for the first transfer reactions to stilbene are generally high and result in products featuring agostic β-hydrogen-metal interactions. This interaction adds significant barriers to further reaction, whether by rearrangement or by the addition of another ligand. The overall pathway for hydrogenation is however downhill and hence thermodynamically favourable. The loss of 1,2-diphenylethane is likely to be the driving force behind its formation, with no feasible back reaction likely.

Multiple pathways exist depending upon the order of steps. The presence of a hydride ligand *trans* to CPhH-CPhH_2 throughout the hydrogenation reactions in Cycle 1 leads to a higher energy pathway than in Cycle 2.

Both *cis*- and *trans*-stilbene hydrogenation proceed via a by common pathway, when the agostic β-hydrogen-metal interactions are released. This is due to the rotation between the sp^3 hybridized carbons about the carbon-carbon bond, in the η^1-CPhH-CPhH_2 group. The barriers for the hydride transfer reactions into *cis*- and *trans*-stilbene also involve similar thermodynamic values, although the complexes containing *cis*-stilbene are predicted to be to be less stable than their *trans*-stilbene counterparts. This change arises from a steric interaction between the phenyl rings in *cis*-stilbene which makes coordination to the metal complex less favourable.

The addition of CO to the complexes formed after the first hydride transfer reaction to either *cis*- or *trans*-stilbene leads to relatively stable complexes of the type $Ru(H)(CO)_2(dhae)(\eta^1\text{-}CPhH\text{-}CPhH_2)$ which then exhibit significant barriers to further reaction. The isomer of **23a** identified in Cycle 1 is consistent with the experimentally detected complex **A9a**. The corresponding isomer $Ru(H)(CO)_2(dhae)(\eta^1\text{-}CPhH\text{-}CPhH_2)$ of Cycle 2, **23b**, is not consistent with formulation of **A9b**. It should be noted that **A9b** was identified on the basis of the detection of a complex with an alkyl group and a hydride ligand, which gave a signal at -11.34 ppm. It is therefore possible that the assumption the hydride ligand is *trans* to CO is not correct. It is also possible that other pathways exist that are not considered here; the addition of CO between the agostic β-hydrogen and the remaining hydride ligand is one such pathway. This would then prevent the final transfer of the hydride ligand and form a stable complex as the alkyl group would be *trans* to the hydride ligand.

3.4.4 Addition of CO to catalytic cycles

The formation of stable species, which could be detected by NMR (via enhancement with *p*-H_2), could also arise from the coordination of CO. This coordination could occur before or after the second hydride transfer reaction or before the fourth, meaning additional transition states are possible, where two CO ligands are present. The detection of a complex of the form $Ru(CO)_2(dpae)(stilbene)$ (**A8)** requires the coordination of CO to one of the intermediates identified in the Cycles 1-3 in competition with the addition of dihydrogen. It should be noted that for Cycle 3, the concentration of free CO is low as only one CO ligand is released during the formation of the starting complex **12a**, therefore is not considered here.

3.4.4.1 Addition of CO to prior to the addition of hydrogen

The addition of CO in Cycle 1 can occur to the first hydride transfer product $Ru(H)(CO)(dhae)(\eta^1\text{-}CPh{=}CPhH)$, as **15a**, which has a vacant site *trans* to the hydride ligand. This addition is significantly favourable and forms $Ru(H)(CO)_2(dhae)(\eta^1\text{-}CPh{=}CPhH)$, as **20c**. The associated enthalpy change is -127.1 kJ mol^{-1} and consistent with a strong metal CO bond. Hydride transfer from this complex results in $Ru(CO)_2(dhae)(\eta^2\text{-}cis\text{-}stilbene)$, as **20d**. It proceeds through transition state **20c'** with a barrier of 57.5 kJ mol^{-1} (enthalpy). This barrier

is slightly higher than the equivalent barrier when dihydrogen is bound to this complex (44.2 kJ mol^{-1} from **16b'**). The resulting complex, **20d**, is the most stable species identified here, consistent with the formation of a 5-coordinate 18-electron complex. This species can also form by the addition of CO to Ru(CO)(dhae)(η^2-*cis*-stilbene), **16a**.This complex can only undergo the loss of *cis*-stilbene, which results in the formation of Ru(CO)$_2$(dhae) as **4b** described in Section 3.3.3. The dissociation of *cis*-stilbene results in changes in enthalpy and free energy of 92.1 and 31.1 kJ mol^{-1} respectively. The free energy value indicates that this step is feasible. These pathways are illustrated in Figure 3.25. The thermodynamic values predicted for the pathway are summarised in Table 3.11

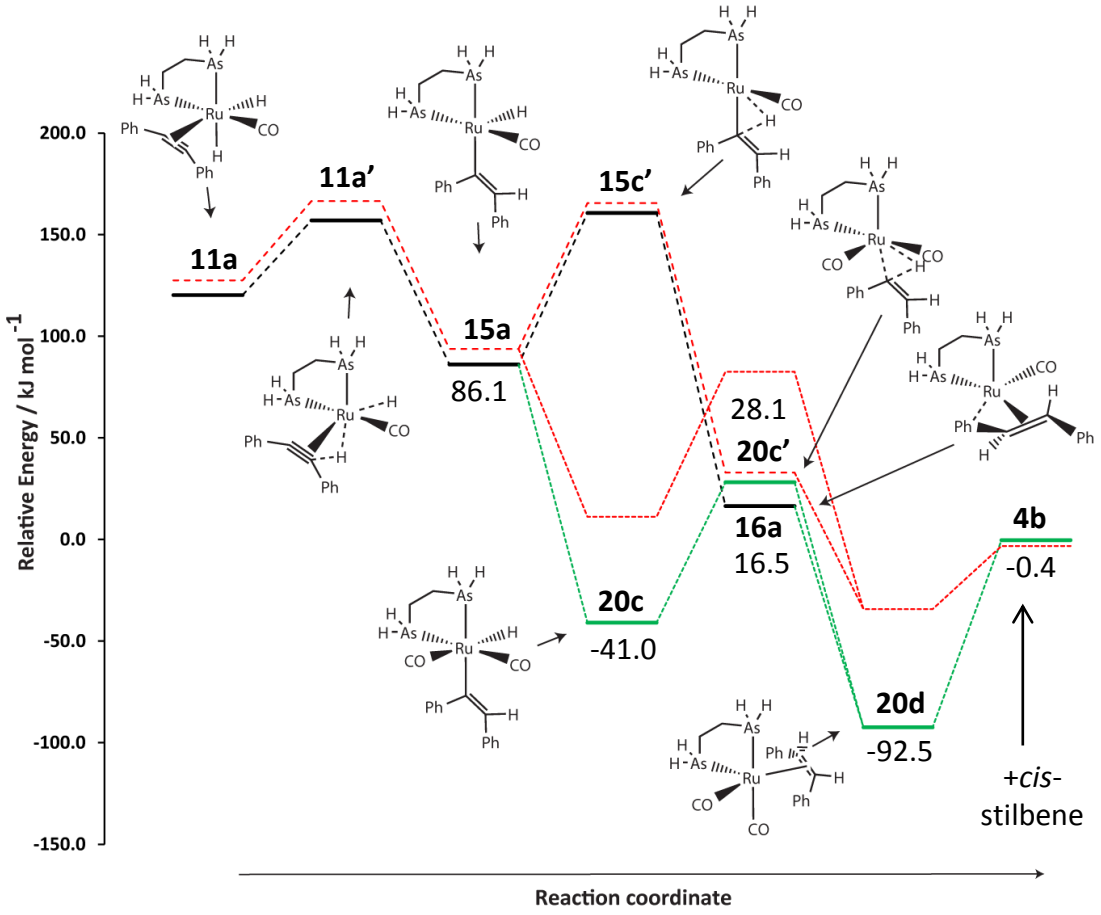

Figure 3.25: Relative enthalpy profiles resulting from the addition of CO in Cycle 1 to Ru(H)(CO)(dhae)(η^1-CPh=CPhH), as **15a** or Ru(CO)(dhae)(η^2-*cis*-stilbene), as **16a**, shown in green in Cycle 1. The free energy profiles are shown in red

It should be noted that no evidence was observed experimentally for *cis*-stilbene coordinated to the metal; this could arise from the favourable free energy of 29.2 kJ mol^{-1} for its dissociation if this pathway proceeds.

Table 3.11: Summary of thermodynamic values associated with CO addition to Ru(H)(CO)(dhae)(η^1-CPh=CPhH) as **15a** and Ru(CO)(dhae)(η^2-*trans*-stilbene) as **16a** in Cycle 1. Values are in kJ mol^{-1}

Label	Formed from	Reaction	Relative Enthalpy	Relative free energy
20c	**15a**	CO addition	-41.0	11.2
20c'	**20c**	Hydride migration barrier	16.5	82.5
20d	**20c**	Hydride migration	-92.5	-34.3
4b	**20d**	Dissociation of *cis*-stilbene	-0.4	-3.2
20d	**16a**	CO addition	--	--

The formation of Ru(H)$_2$(CO)(dhae)(η^2-diphenylacetylene), **11b**, has also been predicted. It goes on to form Ru(H)(CO)(dhae)(η^1-CPh=CPhH) as **15c** where the vacant site is *trans* to CO. CO coordination is favourable, with an enthalpy change of -158.7 kJ mol^{-1} to form Ru(H)(CO)$_2$(dhae)(η^1-CPh=CPhH), **20e**. Hydride transfer then proceeds through a barrier of 74.6 kJ mol^{-1} arising from transition state **20e'**. Once this barrier has been overcome, a rearrangement follows to form **20f**. This has a different stability to **20d** due to the orientation of *cis*-stilbene. In **20d**, the phenyl rings both are orientated away from the dhae ligand and towards the axial CO ligand. Here, the phenyl rings are directed in the opposite direction is different, resulting in a less stable complex by 11.4 kJ mol^{-1} (enthalpy). This is reflected in the loss of *cis*-stilbene from the complex; here the free energy change for this loss is 21.1 kJ mol^{-1} with **20f**, whereas it was higher from **20d**, at 31.1 kJ mol^{-1}. This pathway is illustrated in Figure 3.26, with the thermodynamic values summarised in Table 3.12.

Table 3.12: Summary of thermodynamic values associated with CO addition to Ru(H)(CO)(dhae)(η^1-CPh=CPhH, **15c**, and Ru(CO)(dhae)(η^2-*trans*-stilbene), **16c** in Cycle 2. Values are in kJ mol^{-1}

Label	Formed from	Reaction	Relative Enthalpy	Relative free energy
20e	**15c**	CO addition	-39.8	12.3
20e'	**20e**	Hydride migration barrier	34.8	93.7
20f	**20e**	Hydride migration	-82.1	-24.3
4b	**20f**	Dissociation of *cis*-stilbene	-0.4	-3.2
20g	**16c**	CO addition	-114.9	-57.6
4b	**20g**	Dissociation of *trans*-stilbene	-20.3	-29.2

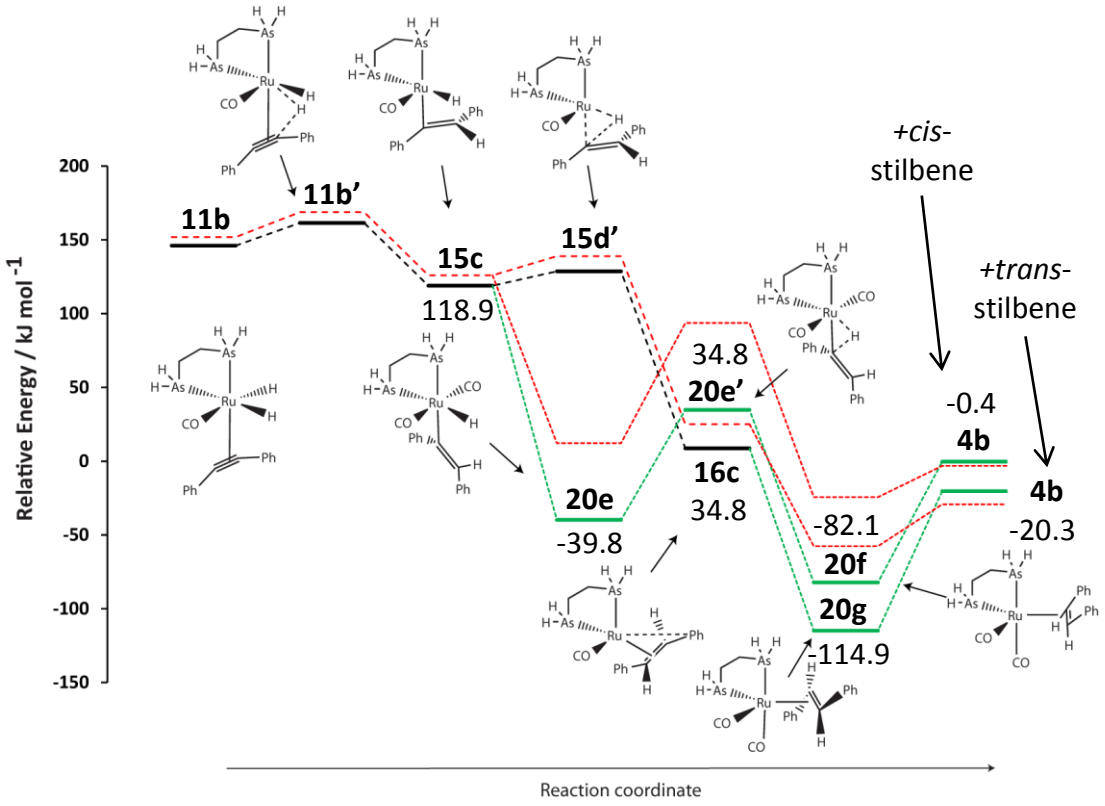

Figure 3.26: Relative enthalpy profiles for the addition of CO in Cycle 2 to Ru(H)(CO)(dhae)(η^1-CPh=CPhH) as geometries **15c** and Ru(H)(CO)(dhae)(η^2-*trans*-stilbene) as **16c**, shown in green in Cycle 2. The free energy profiles are shown in red

The transfer of the second hydride ligand to the vinyl ligand, prior to the coordination of another ligand can also result in the formation of Ru(H)(CO)(dhae)(η^2-*trans*-stilbene), **16c**. The coordination of CO to this complex is favourable, with a change in enthalpy of 149.8 kJ mol^{-1} and forms Ru(H)(CO)$_2$(dhae)(η^2-*trans*-stilbene), **20g**. This complex also adopts a trigonal bipyramidal geometry with *trans*-stilbene in an equatorial position. The dissociation of *trans*-stilbene then results in **4b**, with enthalpy and free energy changes of 94.6 and 28.5 kJ mol^{-1}. Notably, the formation of Ru(H)(CO)$_2$(dhae)(η^2-*trans*-stilbene), **20g** is consistent with the detection of the experimentally proposed complex Ru(H)(CO)$_2$(dpae)(η^2-*trans*-stilbene), **A8**.

CO coordination to Ru(H)(CO)(dhae)(η^1-CPh=CPhH), **15c**, has to compete with the second hydride transfer reaction which proceeds through transition state **15d'**, with a barrier of only 9.7 kJ mol^{-1} (enthalpy). This means that CO coordination is most likely to lead to Ru(CO)$_2$(dhae)(η^2-*trans*-stilbene), **20g** and fits with the detection of **A8** as proposed.

3.4.5 Formation of *cis* and *trans* isomers of stilbene

The ^{1}H NMR signals detected for coordinated stilbene in **A8** were measured to have a coupling constant of +15.3 Hz, consistent with a *trans* arrangement of an alkene. Additionally, free *trans*-stilbene was detected by NMR and GC-MS methods in the reaction mixture. It is feasible that *cis*-stilbene could be isomerised to the *trans* isomer during coordination to the metal centre. Any potential conversion must occur at the metal centre, as the required rotation of the C=C double bond is not energetically possible without this interaction. This conversion has previously been shown to involve the forward and back reactions of $Pd(H)(PEt_3)_2(CHPhCH_2\text{-}Ph)$[144, 219] and so the interconversion of the stilbene isomers was investigated. This occurs when the third hydride transfer reaction has taken place and the two carbon atoms are converted from sp^2 to sp^3 hybridisation. At this point, the single σ-bond allows the required rotation.

3.4.5.1 *Cis-trans* isomerisation in Cycle 1

In Cycle 1, isomerisation will occur via **21a** with sp^3 hybridised carbon environments in the η^1-CPhH-$CPhH_2$ group and a β-hydrogen agostic bond to the metal centre. A transition state was identified for the rotation of this β-$CPhH_2$ unit, where the metal-hydrogen distance to both hydrogens was increased to 2.5 Å, with the imaginary frequency for the rotation of the carbon-carbon bond. This transition state (**21aT'**) forms a barrier of 45.5 kJ mol^{-1} (enthalpy) which is lower than transition state **22a'**. Transition state **22a'** was previously identified as the most feasible transition state for the loss of the agostic interaction by the movement of the remaining hydride ligand. Significantly, the barrier imposed by **21aT'** is higher than that for the loss of *cis*-stilbene from **21a** (to form **6a**). If rotation did occur, the dominant pathway would lead to **21aT** and then $Ru(H)_2(CO)(dhae)(\eta^2$-*trans*-stilbene), as **17aT**. The thermodynamic and geometry changes during *cis-trans* isomerisation via this route are illustrated in Figure 3.27.

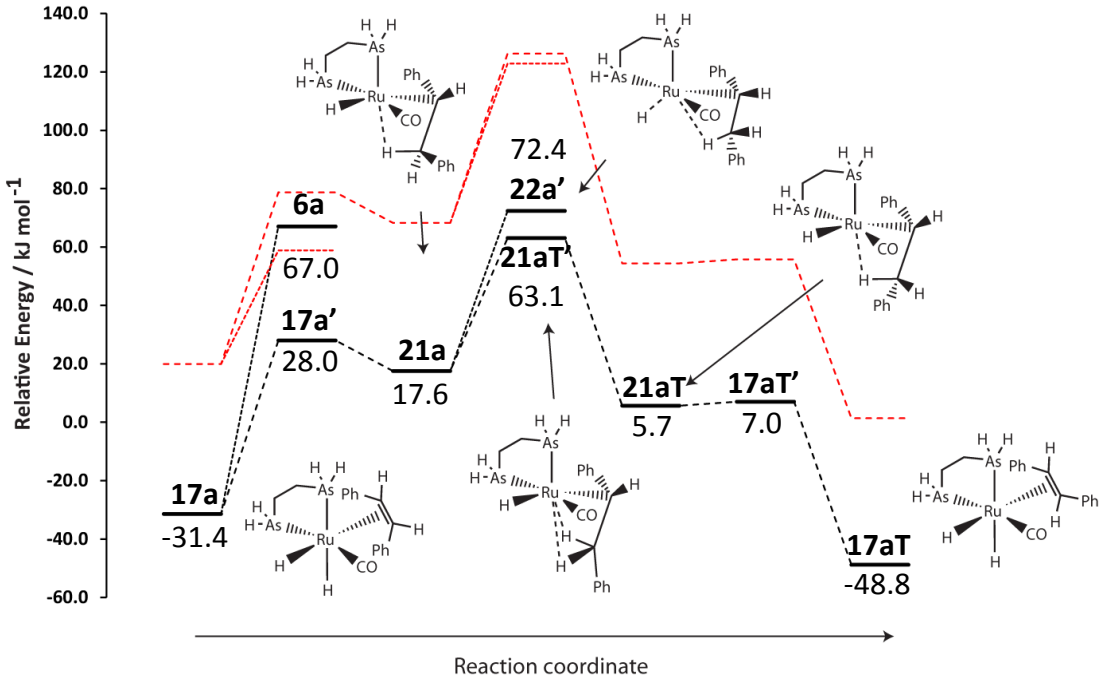

Figure 3.27: Relative enthalpy profile for the stilbene isomerisation via Cycle 1. The loss of *cis*-stilbene from **17a** and the barrier for rearrangement in **21a** are included. The free energy profiles are illustrated in red.

3.4.5.2 *Cis-trans* isomerisation in Cycle 2

In Cycle 2, two complexes of Ru(H)(CO)(dhae)(η^1-CPhH-CPhH$_2$) were identified to result from the third hydride transfer reaction. **21c** was formed from Ru(H)$_2$(CO)(dhae)(η^2-*cis*-stilbene) (**17b**) and **21b** was formed from Ru(H)$_2$(CO)(dhae)(η^2-*trans*-stilbene) (**17c**). It was identified that these complexes were more stable with an agostic interaction that with hydride ligands and stilbene coordinated via π-bonding. Both **21b** and **21c** potentially can undergo rotation about the carbon-carbon bond in the partially hydrogenated stilbene ligand. The two species are linked by a single transition state; this transition state (as **21bT'**) has two hydrogen atoms on the β-carbon at a similar distance to the metal (2.54 and 2.58 Å) with the imaginary frequency corresponding to the carbon-carbon bond rotation. The barrier created by this rotation is lower than for the loss of the agostic interaction, with a barrier height of 33.7 kJ mol^{-1} from complex **21c** and a barrier height in the reverse direction of 46.5 kJ mol^{-1} from complex **21b**. The barrier of 33.7 kJ mol^{-1} from **21c** reveals that the most favourable pathway via Ru(H)$_2$(CO)(dhae)(η^2-*cis*-stilbene) (**17b**) involves conversion to **21b**. These thermodynamic changes indicate that isomerisation is more likely

than loss of *cis*-stilbene from $Ru(H)_2(CO)(dhae)(\eta^2$-*cis*-stilbene) (**17b**). The reactions of this complex have been discussed previously. These pathways and thermodynamic changes are illustrated in Figure 3.28.

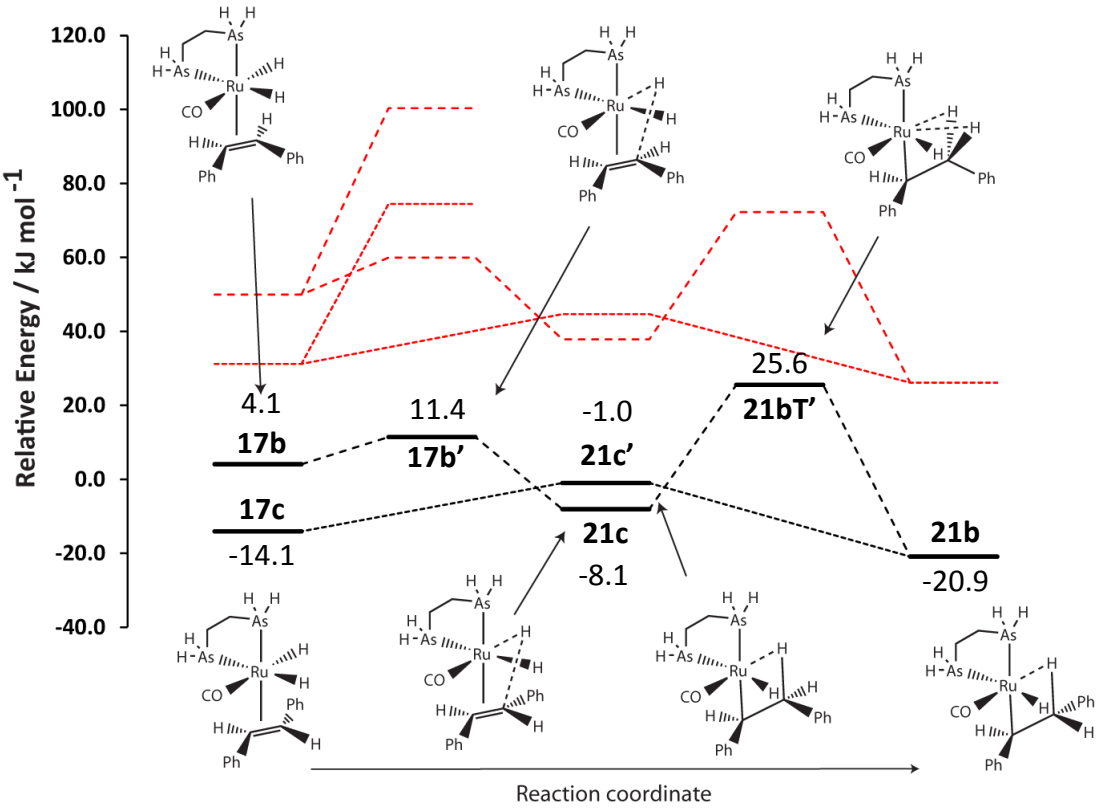

Figure 3.28: Relative enthalpy profile for the alkene isomerisation via Cycle 2. The free energy profiles are illustrated in red. The loss of *cis*-stilbene from **17b** and *trans*-stilbene from **17c** are also included in this profile.

3.4.5.3 Summary of *cis*/*trans* isomerisation of stilbene

The pathways for the *cis*/*trans* isomerisation of stilbene have revealed that rotation of the C-C bond is feasible following the third hydride transfer reaction. The increased stability of *trans*-stilbene over *cis*-stilbene and the increased ease of coordination to the metal centre are consistent with the experimental evidence. It is also possible that the dissociation of *trans*-stilbene from these metal complexes can be followed by the coordination of *cis*-stilbene (and vice-versa) which can isomerise the of stilbene mixture.

3.5 Formation of 1,2,3,4-tetraphenylbutadiene

The detection of 1,2,3,4-tetraphenylbutadiene along with **A10** has previously been described and so the possible mechanisms for the formation of this molecule were investigated. Experimental data showed that no reaction was observed when dihydride **A3** was used, indicating that these compounds are formed from the starting complexes. Further data from the reaction of **A1** with *cis*-stilbene showed the formation of the dihydride **A3** but no evidence of PHIP in the organic region of the spectra. It was interpreted that the enhanced resonances from **A10** arise from the introduction of *p*-H_2 into a diphenylacetylene dimerisation product. The experimental data were also interpreted to demonstrate that the formation of the dimer competes with CO or *p*-H_2 coordination along with the possible second hydride transfer reactions. The dimer was only observed when photochemical initiation was used with **A1** and when thermal initiation was used with **A2**. This can be attributed to the higher temperatures required for the thermal initiation of **A1** which will reduce the lifetime of any intermediate formed after the first hydride transfer reaction.

The coordination and subsequent reaction of diphenylacetylene to the different isomers of intermediate Ru(H)(CO)(dpae)(η^1-CPh=CPhH) is considered here. The change of diphenylacetylene bond to the metal upon hydride transfer (π- bonding to σ- bonding) frees up the inner coordination sphere to facilitate the approach of the second diphenylacetylene molecule. Two potential isomers of Ru(H)(CO)(dhae)(η^1-CPh=CPhH) and one isomer of Ru(H)$(CO)_2$(κ^1-dhae)(η^1-CPh=CPhH) were identified in Section 3.4.2. The coordination of a second molecule of diphenylacetylene to these isomers was therefore modelled as sensible starting points and the findings obtained are reported here.

3.5.1 Coordination of diphenylacetylene in Cycle 1

The coordination of diphenylacetylene to the vacant site of Ru(H)(CO)(dhae)(η^1-CPh=CPhH) as **15a** is first considered. This intermediate has the remaining hydride *trans* to the vacant site and the vinyl ligand *trans* to one end of the dhae ligand. The coordination of diphenylacetylene is favourable, with a change in enthalpy of -17.7 kJ mol^{-1} and results in Ru(H)(CO)(dhae)(η^1-CPh=CPhH)(η^2-diphenylacetylene), **24a**. The free energy change for this addition is unfavourable by 45.5 kJ mol^{-1}, reflecting both the loss of entropy from the

combination of two species into one, along with the steric bulk of the ligands. This product cannot undergo further hydride transfer to diphenylacetylene. Two alternative reactions are possible though; the formation of a new carbon-carbon bond or a hydride transfer to the vinyl ligand.

The formation of the new carbon-carbon bond proceeds via transition state **24aC'** with barrier of +85.0 kJ mol^{-1}. Transfer of the hydride to the vinyl ligand is more favourable, proceeding through transition state **24a'** with barrier 11.0 kJ mol^{-1} to form **24b**. This reaction proceeds favourably, with **24b** being -20.8 kJ mol^{-1} more stable than **24a**. The loss of *cis*-stilbene from this complex is then favourable resulting in Ru(CO)(dhae)(η^2-diphenylacetylene), **13a**, as described in Section 3.3.3. These geometries and thermodynamic changes are illustrated in Figure 3.29.with the thermodynamic values summarised in Table 3.13.

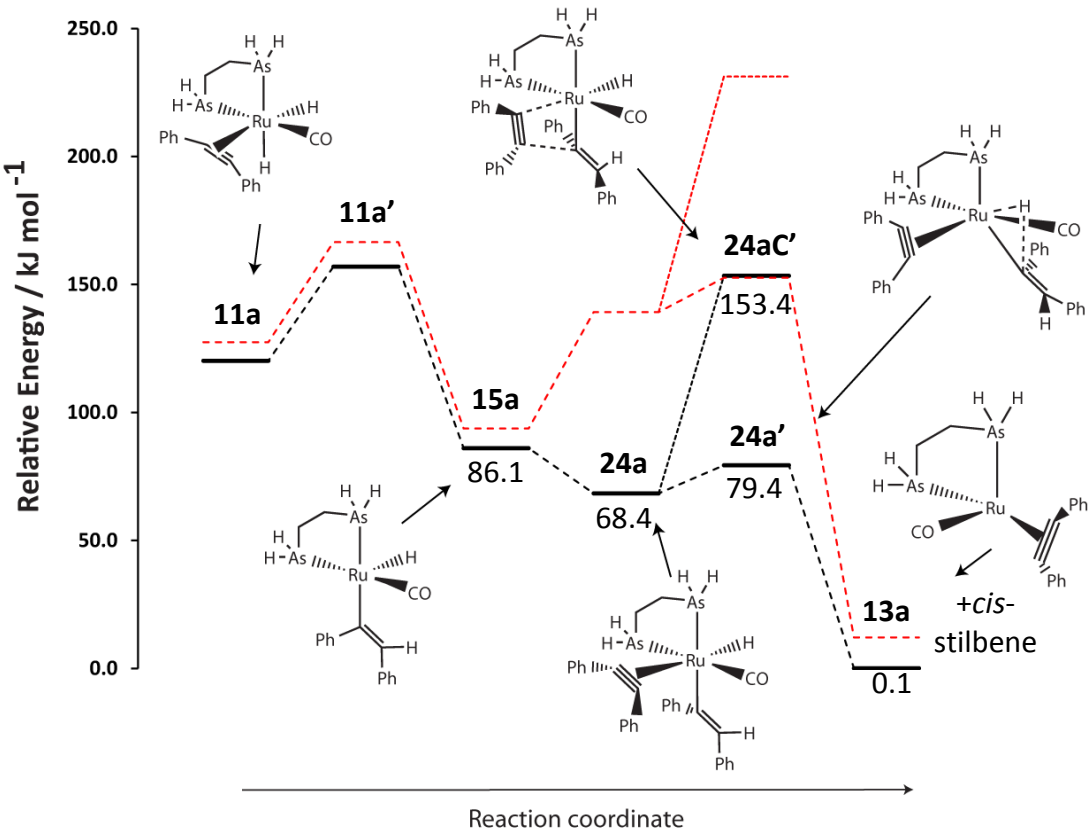

Figure 3.29: Relative enthalpy profile for the for the addition of diphenylacetylene to Ru(H)(CO)(dhae)(η^1-CPh=CPhH), as **15a**, of Cycle1; the formation of *cis*-stilbene and Ru(CO)(dhae)(η^2-diphenylacetylene) is predicted. The relative free energy profile is shown in red.

Table 3.13: Reaction enthalpies and free energies for the addition of diphenylacetylene to Ru(H)(CO)(dhae)(η^1-CPh=CPhH), as **15a** of Cycle 1. Values are in kJ mol^{-1}

Label	Formed from	Reaction	Relative Enthalpy	Relative free energy
24a	**15a**	Acetylene addition	68.4	139.2
24aC'	**24a**	C-C bond formation barrier	153.4	231.2
24a'	**24a**	Hydride migration barrier	79.4	152.6
24b	**24a**	Hydride migration	47.6	110.1
14a	**24b**	Dissociation of *cis*-stilbene	0.1	12.1

While the coordination of diphenylacetylene to **15a** is therefore feasible, it leads to the same overall process as previously described and does not account for the dimerisation product.

3.5.2 Coordination of diphenylacetylene in Cycle 2

The coordination of diphenylacetylene to Ru(H)(CO)(dhae)(η^1-CPh=CPhH), **15c**, was then considered. This intermediate has a vacant site *trans* to CO, and addition leads to Ru(H)(CO)(dhae)(η^1-CPh=CPhH)(η^2-diphenylacetylene), **24c**. This addition is favourable in terms of enthalpy, with a change of -52.3 kJ mol^{-1}. The free energy change is unfavourable by 8.1 kJ mol^{-1}, in contrast to that calculated for the coordination to **15a**.

Three possible reactions can then occur for Ru(H)(CO)(dhae)(η^1-CPh=CPhH)(η^2-diphenylacetylene). The dominant pathway will be the transfer of the hydride ligand to diphenylacetylene. This proceeds via transition state **24c'** and barrier 13.8 kJ mol^{-1}. The transfer is favourable and forms Ru(CO)(dhae)(η^1-CPh=CPhH)$_2$, **25a**, with an enthalpy change of -44.3 kJ mol^{-1}. The other two pathways have higher barriers for reaction; hydride transfer to the vinyl ligand has a barrier of 38.7 kJ mol^{-1} (from **24cV'**) and the barrier for the formation of a new carbon-carbon bond is 94.9 kJ mol^{-1} (from **24cC'**). These geometries and thermodynamic changes are illustrated in Figure 3.30, with the relative enthalpies and free energies shown in Table 3.14. The dominant transition states and intermediates described here are illustrated in Figure 3.31.

Table 3.14: Reaction enthalpies and free energies for the addition of diphenylacetylene to Ru(H)(CO)(dhae)(η^1-CPh=CPhH), **15c**, of Cycle 2. Values are in kJ mol^{-1}

Label	Formed from	Reaction	Relative Enthalpy	Relative free energy
24c	**15c**	Acetylene addition	60.6	128.6
24cC'	**24c**	C-C bond formation barrier	155.4	244.2
24cV'	**24c**	H transfer to vinyl ligand barrier	99.2	190.1
24c'	**24c**	H transfer to diphenylacetylene barrier	74.4	157.7
25a	**24c**	H transfer to diphenylacetylene	16.3	90.4

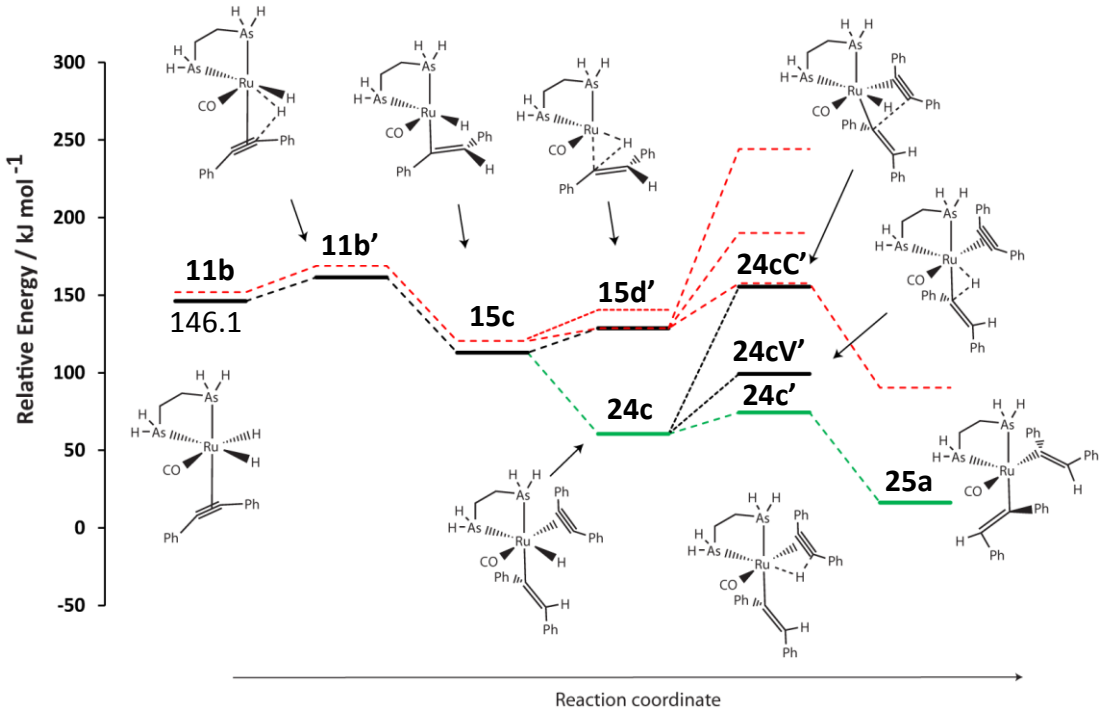

Figure 3.30: Initial pathways for the coordination and subsequent reaction of diphenylacetylene with Ru(H)(CO)(dhae)(η^1-CPh=CPhH), **15c**, of Cycle 2. The free energy profile is shown in red

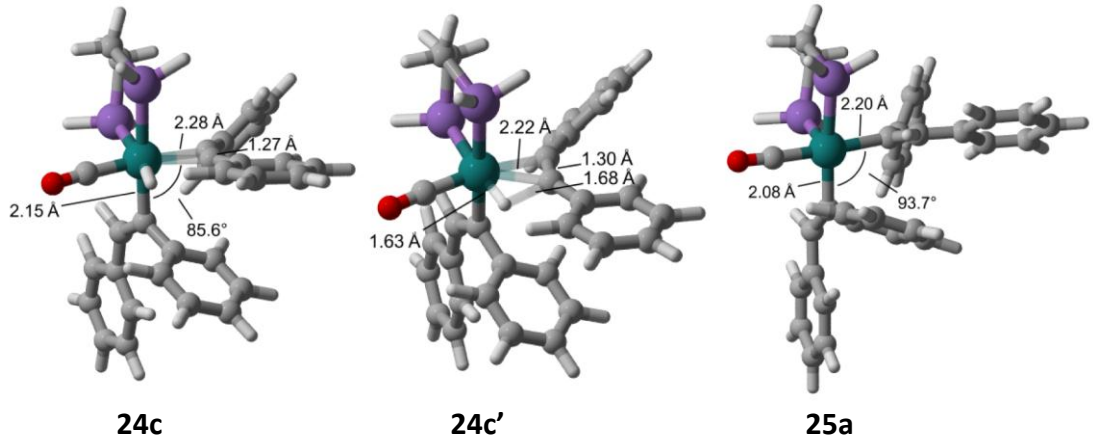

Figure 3.31: Illustrations of the dominant intermediates, and transition states, for the reaction of diphenylacetylene with Ru(H)(CO)(dhae)(η^1-CPh=CPhH), **15c**, of Cycle 2

Ru(CO)(dhae)(η^1-CPh=CPhH)$_2$ (as **25a**) can then undergo several further reactions; dimerisation of the vinyl ligands and coordination of CO or dihydrogen. The coordination of dihydrogen to the vacant site of **25a** is favourable, with an enthalpy change of -10.0 kJ mol^{-1} to create the dihydrogen species **26a**, whereas the free energy change is unfavourable at 12.1 kJ mol^{-1}. A small barrier was located for the transfer of one of the hydrogen atoms in the dihydrogen ligand to a vinyl ligand; this results in the creation of coordinated *cis*-stilbene and a new hydride ligand. This pathway has a low barrier of 14.3 kJ mol^{-1} from transition state **26a'**, which is for the reaction with the vinyl ligand in the same plane as the dihydrogen bond. Ru(H)(CO)(dhae)(η^2-*cis*-stilbene)(η^1-CPh=CPhH) (as **26b**) results, which is formed favourably by a change in enthalpy of -97.9 kJ mol^{-1}. The barrier for hydride transfer to the remaining vinyl ligand is then 59.9 kJ mol^{-1} (from transition state **26b'**) and leads to the formation of *cis*-stilbene which is liberated by the complex. This pathway forms **16a** of Cycle 1, with a favourable change in enthalpy and free energy of -41.1 and -96.8 kJ mol^{-1} respectively. The reaction between the vinyl ligands in **26a** could happen before the hydrogen transfer reaction; the barrier for this is significantly higher than **26a'**, with transition state **26aC'** forming a barrier of 102.5 kJ mol^{-1}.

Alternatively, CO can coordinate to Ru(CO)(dhae)(η^1-CPh=CPhH)$_2$ (as **25a**) to form Ru(CO)$_2$(dhae)(η^1-CPh=CPhH)$_2$ as **27a**. This addition is favourable, with an associated change in enthalpy of -130.4 kJ mol^{-1}. The barrier for the dimerisation of the two vinyl ligands is then 59.9 kJ mol^{-1}, via transition state **27a'**. This leads to the formation of Ru(CO)$_2$(dhae)(κ^1-CPhH=CPh-CPh=CPhH), **27b**. This dimerisation is now favourable, with **27b** being the most

stable species identified here, and formed with an enthalpy change of -41.4 kJ mol^{-1} from **27a**.

It is also possible that the dimerisation of the vinyl ligands can occur via Ru(CO)(dhae)(η^1-CPh=CPhH)$_2$, **25a**. This pathway proceeds through transition state **25a'** and barrier 66.1 kJ mol^{-1}. The resultant species **25b** is formed favourably, with an associated enthalpy change of -91.6 kJ mol^{-1}. This dimerisation product has both alkene bonds of 1,2,3,4-tetraphenylbutadiene bound, the addition of CO to the molecule can then potentially displace one of these, and form **27b**. It is noted that there would be a barrier for this process. These thermodynamic changes and pathways are illustrated in Figure 3.32, with selected intermediates and complexes illustrated in Figure 3.33. The enthalpies and free energies are summarised in Table 3.15.

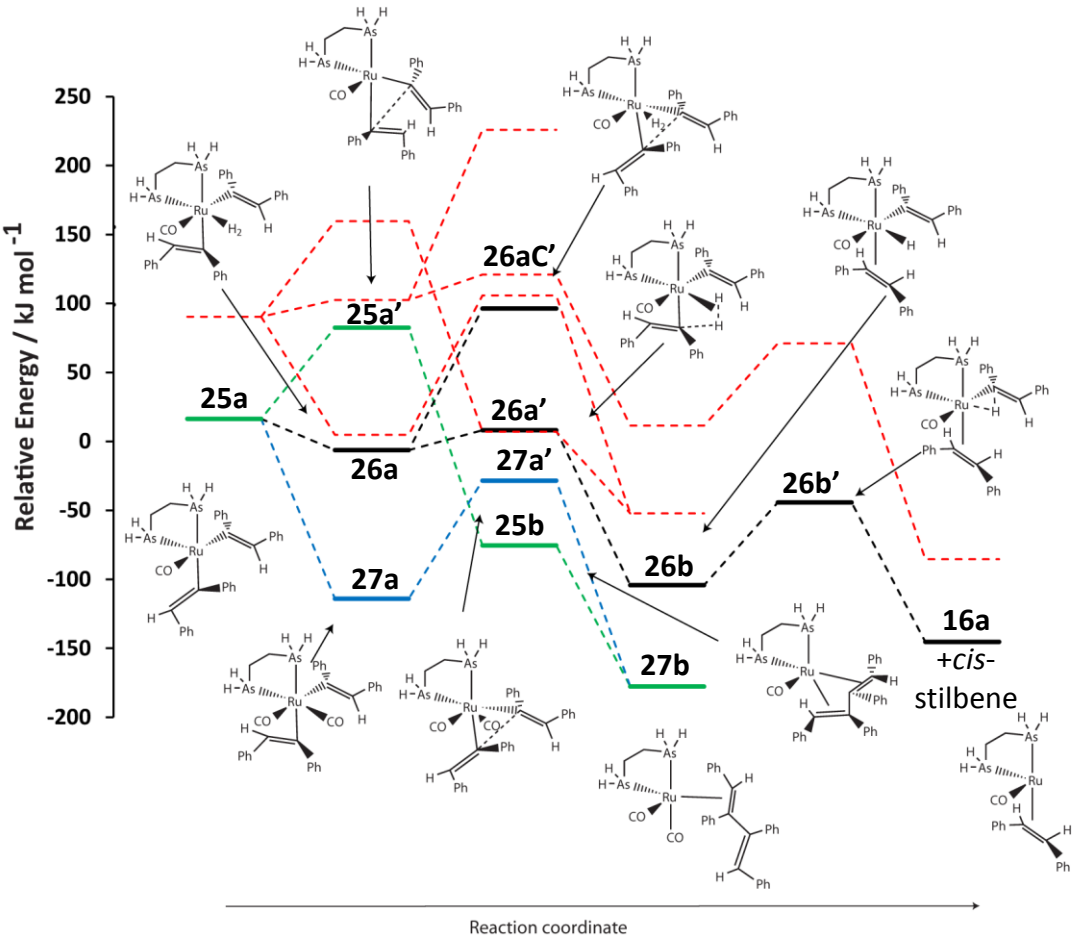

Figure 3.32: Relative enthalpy pathways involved in the reactions of Ru(CO)(dhae)(η^1-CPh=CPhH)$_2$, **25a**, in Cycle 2 to form 1,2,3,4-tetraphenylbutadiene. The pathway for CO addition is shown in blue and the pathway for initial dimerisation is shown in green. The free energy profiles are shown in red

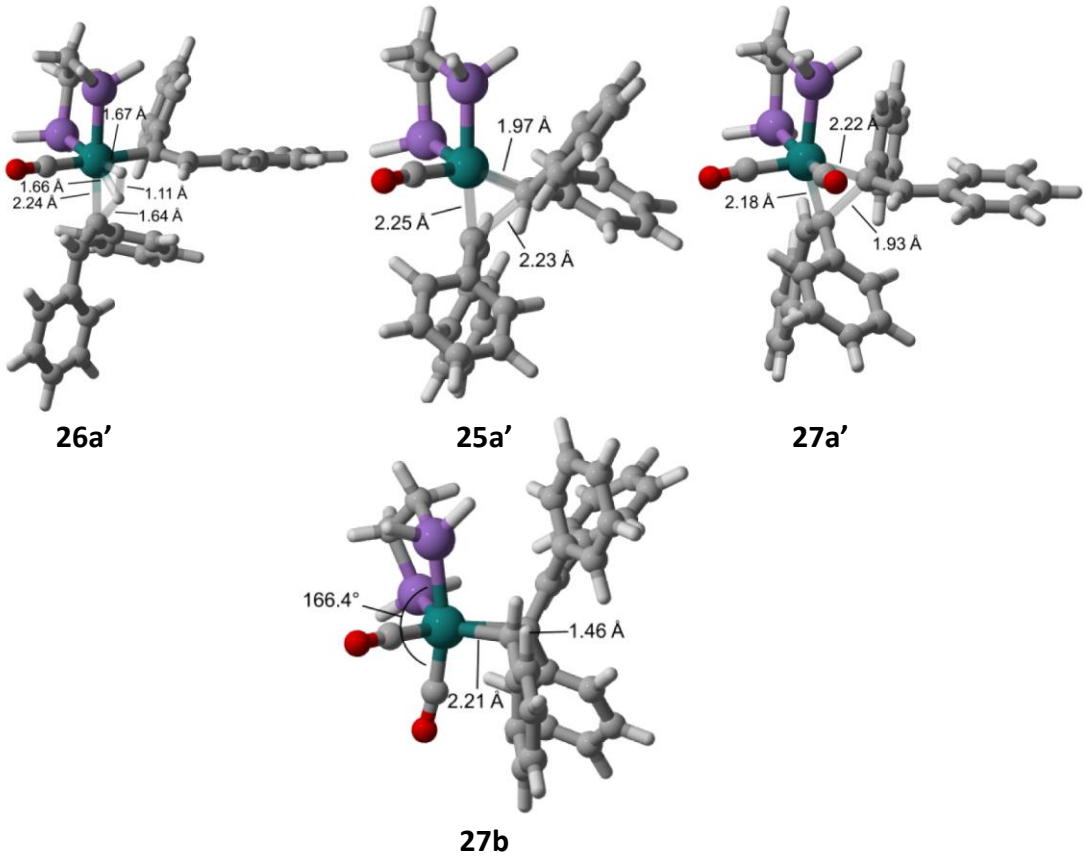

Figure 3.33: Detailed illustrations of selected intermediates and transition states involved in Figure 3.32

Table 3.15: Reaction enthalpies and free energies for the various pathways from Ru(H)(CO)(dhae)(η^1-CPh=CPhH)$_2$ as **25a** in Cycle 2. Values are in kJ mol^{-1}

Label	Formed from	Reaction	Relative Enthalpy	Relative free energy
26a	**25a**	Addition of dihydrogen	-6.3	102.5
26aC'	**26a**	C-C bond formation barrier	105.8	225.9
26a'	**26a**	H transfer to vinyl ligand barrier	8.0	121.0
26b	**26a**	Hydrogen transfer	-104.2	11.4
26b'	**26b**	H transfer to vinyl ligand barrier	-44.3	71.1
16a	**26b**	Formation and elimination of *cis*-stilbene	-145.3	-85.4
27a	**25a**	CO addition	-114.1	4.8
27a'	**27a**	Barrier for dimerisation	-28.4	105.8
27b	**27a**	Dimerisation	-177.7	-52.2
25a'	**25a**	Barrier for dimerisation	82.4	159.6
25b	**25a**	Dimerisation	-75.3	7.0
27b	**25b**	CO addition	-177.7	-52.2

The species $Ru(CO)_2$(dhae)(κ^1-CPhH=CPh-CPh=CPhH), **27b**, is analogous to **A10** from the experimental evidence. Its formation would also allow the detection of 1,2,3,4-tetraphenylbutadiene by GC-MS.

3.5.3 Coordination of diphenylacetylene in Cycle 3

For Cycle 3, a second molecule of diphenylacetylene could coordinate to Ru(H)$(CO)_2$(κ^1-dhae)(η^1-CPh=CPhH), **18a**, which is formed by the first hydride transfer reaction. It results in Ru(H)$(CO)_2$(κ^1-dhae)(η^1-CPh=CPhH)(η^2-diphenylacetylene), **28a**. This coordination is favourable in terms of enthalpy by -17.0 kJ mol^{-1} but unfavourable as free energy by 40.4 kJ mol^{-1}. This reflects the loss of entropy and the steric repulsion created by its coordination. This complex cannot undergo hydride transfer to diphenylacetylene due to the *trans* arrangement of the ligands. Two alternative reactions are possible; the formation of a new carbon-carbon bond or the hydride transfer reaction to the vinyl ligand (akin to those determined for Cycle 1, as **24a** and **24aC'**).

The formation of a new carbon-carbon bond between the diphenylacetylene and the vinyl ligand proceeds through transition state **28aC'** and a barrier of 75.6 kJ mol^{-1}, in keeping with similar barriers identified already for the formation of this carbon-carbon bond. This pathway leads to the formation of Ru(H)$(CO)_2$(κ^1-dhae)(κ^2-CPh=CPh-CPh=CPhH), **28b**, which cannot undergo the transfer of the hydride to the carbon atom bound to the metal due to the *trans* arrangement. The alternative reaction of **28a** is the transfer of the remaining hydride ligand to the vinyl ligand. It proceeds through a barrier of 40.1 kJ mol^{-1} (and so would be the dominant pathway if **28a** were formed) and arises from transition state **28a'**, resulting in the formation of $Ru(CO)_2$(κ^1-dhae)(η^2-*cis*-stilbene)(η^2-diphenylacetylene) as **28c**. This reaction is favourable, with an enthalpy change of -29.1 kJ mol^{-1}. Complex **28c** has *cis*-stilbene at a distance of 3.07 A (Ru-C) and the newly transferred hydrogen atom at a distance of 2.35 A from the metal. Recoordination of this ligand to the metal can occur, but the most favourable pathway leads to loss of *cis*-stilbene to form $Ru(CO)_2$(κ^1-dhae)(η^2-diphenylacetylene), **14a**, as previously identified in Section 3.3.4. This dissociation results in a change in enthalpy from **28c** of -55.9 kJ mol^{-1}. The thermodynamic values are illustrated in Table 3.16 and the pathways illustrated in Figure 3.34.

Table 3.16: Reaction enthalpies and free energies for the addition of diphenylacetylene to Ru(H)(CO)$_2$(κ^1-dhae)(η^1-CPh=CPhH), **18a**, in Cycle 3. Values are in kJ mol^{-1}

Label	Formed from	Reaction	Relative Enthalpy	Relative free energy
28a	**18a**	Acetylene addition	1.5	99.2
28aC'	**28a**	C-C bond formation barrier	77.0	183.4
28b	**28a**	C-C bond formation	-101.5	9.3
28a'	**28a**	Hydride migration barrier	41.5	146.2
28c	**28a**	Hydride migration	-27.6	59.8
14a	**28c**	Dissociation of *cis*-stilbene	-83.5	-41.5

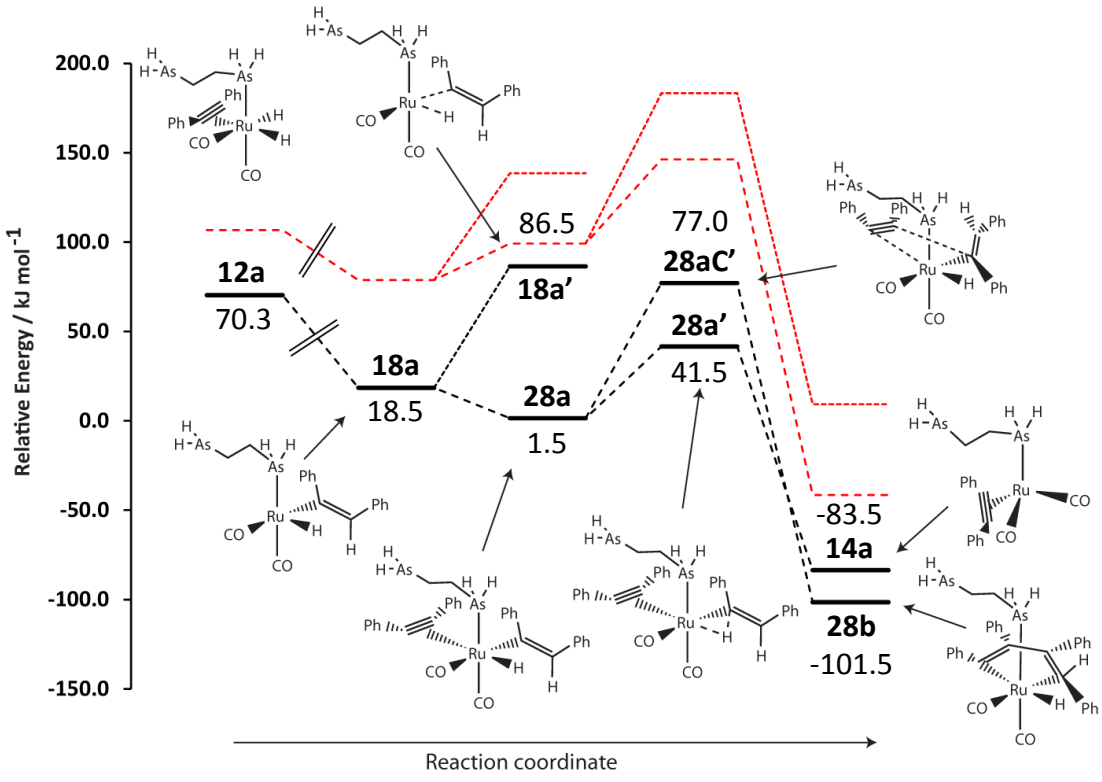

Figure 3.34: Relative enthalpy pathways for the addition of diphenylacetylene to Ru(H)(CO)$_2$(κ^1-dhae)(η^1-CPh=CPhH), **18a**, of Cycle 3; the formation of *cis*-stilbene and Ru(CO)$_2$(κ^1-dhae)(η^2-diphenylacetylene) is predicted. The relative free energy profile is shown in red.

Whilst the formation of a new carbon-carbon bond between η^2-diphenylacetylene and the vinyl ligand is possible, the low barrier for hydride transfer to the vinyl ligand means it will dominate.

3.5.4 Coordination of diphenylacetylene to14-electron Ru(CO)(dhae)(η^2-diphenylacetylene)

The photochemical formation of 14-electron Ru(CO)(dhae) (**5a**) was discussed in Chapter 2 and its reaction with diphenylacetylene described in Section 3.3.5, where it led to the formation of Ru(CO)(dhae)(η^2-diphenylacetylene), **13a**. It is possible that another diphenylacetylene molecule can coordinate to **13a** and react further. The coordination of diphenylacetylene to **13a** results in the formation of Ru(CO)(dhae)(η^2-diphenylacetylene)$_2$, **24d**, with a favourable enthalpy change of -38.3 kJ mol^{-1}. The free energy change of 22.6 kJ mol^{-1} is unfavourable in contrast. This complex has both diphenylacetylene ligands in equatorial positions of the trigonal bipyramid that results. This species can then undergo a dimerisation reaction; this was found to have a significant barrier of 156.4 kJ mol^{-1} arising from transition state **24d'**. An alternative pathway was identified, where the approach of dihydrogen to the complex resulted in the transfer of a hydrogen atom to one of the diphenylacetylene ligands. This is a favourable reaction to form Ru(H)(CO)(dhae)(η^2-diphenylacetylene)(η^1-CPh=CPhH) as **24e** with a change in enthalpy of -73.9 kJ mol^{-1}. The transfer of the remaining hydride ligand to the remaining diphenylacetylene ligand was found to be favourable, with an enthalpy change of -66.9 kJ mol^{-1}. This proceeds through transition state **24e'** which creates a barrier of 21.3 kJ mol^{-1} and leads to the formation of Ru(CO)(dhae)(η^1-CPh=CPhH)$_2$ as **25c**. This intermediate adopts a square-based pyramid with one of the vinyl ligands out of the basal plane.

The dimerisation of the two vinyl ligands can potentially occur via this species, which proceeds through a high energy transition state with a barrier of 159.6 kJ mol^{-1} (**25c'**). The complex that results is the same as **25b** that featured in Figure 3.32. This features a change in CO position in the complex and both alkene bonds in the resulting 1,2,3,4-tetraphenylbutadiene ligand. Dimerisation is favourable by -79.4 kJ mol^{-1}, and reaction with CO is favourable as previously detailed. Alternatively, CO could coordinate to **25c** which forms **27a** previously identified. This addition is favourable with an enthalpy change of -118.2 kJ mol^{-1}. The dimerisation can then occur through **27a'** (barrier of 85.7 kJ mol^{-1}) and both pathways end with the formation of Ru(CO)$_2$(dhae)(η^2-1,2,3,4-tetraphenylbutadiene) as **27b**. These thermodynamic values are summarised in Table 3.17, and the pathways are illustrated in Figure 3.35.

Table 3.17: Reaction enthalpies and free energies for the various pathways from Ru(CO)(dhae)(η^2-diphenylacetylene) as **13a**. Values are in kJ mol^{-1}

Label	Formed from	Reaction	Relative Enthalpy	Relative free energy
24d	**13a**	Addition of diphenylacetylene	123.5	153.0
25cC'	**24d**	C-C bond formation barrier	279.9	314.2
24e	**24d**	Addition of dihydrogen and hydride transfer	49.7	118.9
24e'	**24e**	Hydrogen transfer barrier to second alkyne	70.9	143.1
25c	**24e**	H transfer to vinyl ligand barrier	4.1	77.3
25c'	**25c**	Dimerisation barrier	163.6	258.2
25b	**25c**	Dimerisation	-75.3	7.0
27b	**25b**	Addition of CO	-177.7	-52.2
27a	**25c**	Addition of CO	-114.1	4.8
27a'	**27a**	Dimerisation barrier	-28.4	105.8

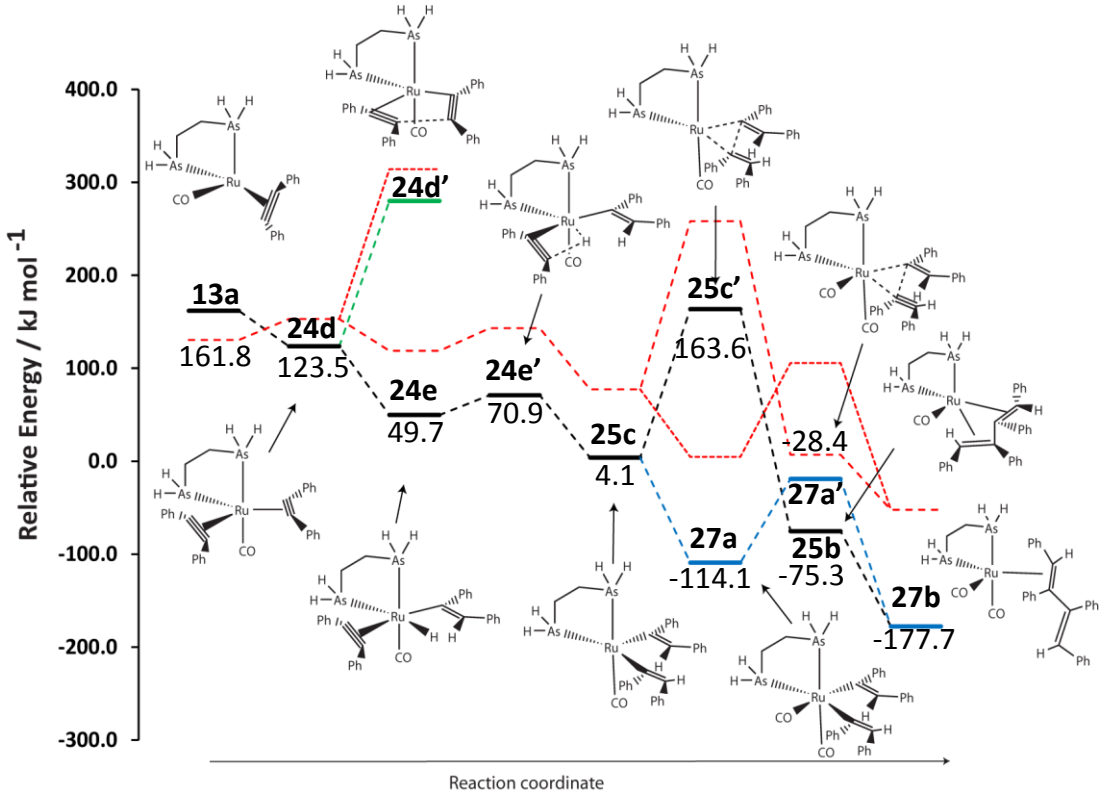

Figure 3.35: Relative enthalpy changes associated with the reaction pathways for the addition of diphenylacetylene to Ru(CO)(dhae)(η^2-diphenylacetylene), **13a**, formed from Ru(CO)(dhae), **5a**, by photochemical initiation. The initial dimerisation barrier is shown in green, and the coordination of CO prior to the dimerisation step is highlighted in blue. The relative free energy profile is shown in red.

3.5.5 Summary of the formation of 1,2,3,4-tetraphenylbutadiene

The investigations into the possible pathways of formation of the 1,2,3,4-tetraphenylbutadiene have revealed that the key carbon-carbon bond formation step can occur after the first hydride transfer reaction into diphenylacetylene, but only via Cycle 2. The first hydride migration creates a vacant site for the coordination of the second diphenylacetylene molecule to bind in, which is likely if an excess of ligand is present. This coordination is favourable and provides a complex set of new pathways. The barrier for the formation of a new carbon-carbon bond between the vinyl group and diphenylacetylene is sizeable. The dominant pathway will therefore be for the hydride ligand to transfer to the vinyl ligand and form *cis*-stilbene.

Pathways were found for the formation of 1,2,3,4-tetraphenylbutadiene involving the addition of CO to the complex. The butadiene group could form before or after CO addition; the addition prior to the dimerisation results in the coordination of only one end of the diene ligand to the metal. If the dimerisation occurs before the addition, the metal is able to coordinate both alkene groups. The addition of CO is favourable to the metal to release one of these groups but there will be a barrier associated with this. The addition of dihydrogen though is predicted to prevent dimerisation, with *cis*-stilbene being formed.

The formation of 1,2,3,4-tetraphenylbutadiene has also been predicted to be feasible via Ru(CO)(dhae)(η^2-diphenylacetylene)$_2$. It can react with H_2 to form a bis-vinyl species .The barriers for this transfer are low and is then followed by dimerisation, again proceeding through a reasonably small barrier. This pathway provides an alternative route to the formation of the butadiene group and the experimentally proposed complex Ru(CO)$_2$(dpae)(η^2-1,2,3,4-tetraphenylbutadiene), **A10**. The formation of Ru(CO)(dhae)(η^2-diphenylacetylene)$_2$ is unlikely to be viable through thermal initiation, but the formation of the 14-electron complex Ru(CO)(dhae) from Ru(CO)$_3$(dhae) with photochemical initiation is likely to be possible.

3.6 Discussion of the catalytic hydrogenation of diphenylacetylene

This investigation into the catalytic behaviour of the two related complexes $Ru(CO)_3(dpae)$ (**A1**) and $Ru(CO)_2(dpae)(PPh_3)$ (**A2**) towards the hydrogenation of diphenylacetylene has revealed a complex set of reaction pathways. The theoretical modelling validates the observation of *cis*-stilbene and *trans*-stilbene along with 1,2,3,4-diphenylacetylene and other key intermediates in the mechanism of reaction. These are now discussed in more detail.

The method of initiation plays a critical role in determining the reaction pathway. The use of thermal initiation with $Ru(CO)_3(dpae)$ provides the system with more energy; therefore when the diphenylacetylene and dihydrogen molecules are brought together on the metal centre, the hydrogenation reactions proceed faster. This results in a reduction of the lifetime of the 18-electron intermediates and allows pathways with higher barriers to occur. Thermal initiation via CO loss from $Ru(H)_2(CO)_2(dhae)$ (**3a**) (formed by CO loss and subsequent dihydrogen addition to $Ru(CO)_3(dhae)$ (as **1**) and subsequent reaction with diphenylacetylene), leads to the formation of $Ru(H)_2(CO)(dhae)(\eta^2$-diphenylacetylene) as isomer **11a** (shown in Figure 3.3). This isomer is then involved in Cycle 1. It was determined that a minor pathway was possible where de-chelation of dhae from $Ru(H)_2(CO)_2(dhae)$ (**3a**) could occur, followed by addition of diphenylacetylene; this results in the formation of $Ru(H)_2(CO)_2(\eta^1$-dhae)(η^2-diphenylacetylene) (**12a**) of Cycle 3. The coordination of diphenylacetylene would have to compete with the re-coordination of the free end of η^1-dhae, which is favoured by the chelate effect. The coordination of diphenylacetylene to 16-electron $Ru(CO)_2(dhae)$ (**4b**), formed by CO loss from $Ru(CO)_3(dhae)$ as **1**, was predicted here to be viable, but the subsequent CO loss and dihydrogen addition was calculated to be unfavourable and therefore a minor pathway (from **11b**) as Cycle 2.

The photochemical route also allows the potential 14-electron species Ru(CO)(dhae) **5a** to be formed, which can then combine with *p*-H_2, diphenylacetylene or CO to create three different intermediates. Importantly, photochemical initiation could allow these intermediates to form at lower temperatures and so the subsequent reaction pathways are

affected. These routes are illustrated in Figure 3.9, and an additional route to the dimer 1,2,3,4-tetraphenylbutadiene presented in Figure 3.35.

With $Ru(CO)_2(dhae)(PH_3)$ (**2**), the loss of phosphine would lead to the common 16-electron intermediate $Ru(CO)_2(dhae)$ (**4b**) that is generated from $Ru(CO)_3(dhae)$. When formed from **1**, it results in an enthalpy change of +163.6 kJ mol^{-1}, but for **2** it is lower at +116.9 kJ mol^{-1}. This is likely to be responsible for the different reactions seen in Chapter 2. It may also explain why $Ru(CO)_2(dpae)$(1,2,3,4-tetraphenylbutadiene) is detected in the thermal reaction of **2** but not **1**. The higher temperatures needed for **1** would reduce the lifetime of any intermediates and so reduce the potential for a second molecule of diphenylacetylene to bind.

The barriers for the hydride transfer reactions were also found to vary between the possible cycles, but were mostly low enough to allow the reactions to proceed. Table 3.18 summarises the barriers determined for the hydride transfer reactions, with the number representing the stage of the hydride transfer reaction.

Table 3.18: Comparison of the barrier heights for hydride transfer according to Cycles 1-3 (relative enthalpy, values in kJ mol^{-1})

Transfer reaction:	**1st**	**2nd**	**2nd+H_2**	**3rd**	**4th (with H_2)**
Cycle 1	36.8	74.6	44.2	59.4	77.0
Cycle 2	15.3	15.7	63.3	13.2	76.1
Cycle 3	22.1	68.0	79.5		

The lowest barriers encountered here were seen in Cycle 2, and associated with the formation of *trans*-stilbene. The barriers calculated for the first hydride transfer reactions were all low, in keeping with the electron density of diphenylacetylene, and the alignment of this ligand on the metal. The barriers for the second hydride transfer reaction are notably higher in Cycle 1 and 3 due to the alignment the vinyl ligand is required to adopt. In Cycle 2, the vinyl ligand is able to favourably interact with the metal centre during the transfer which allows considerable stabilisation. Cycles 1 and 3 also feature complexes where only one hydride ligand is *cis* to the diphenylacetylene/vinyl/stilbene ligand and so rearrangement of the ligand sphere is required to allow reaction to proceed. These cycles

also place this organic ligand *trans* to a hydride which is not favourable. A number of transition states also featured the simultaneous oxidative addition of a dihydrogen ligand (when present) which helped drive the reaction.

The dissociation of *trans*- and *cis*-stilbene from the complexes once formed was calculated to give rise to a high enthalpy change; the free energy for this dissociation was lower in keeping with the favourable increase in entropy. The barriers calculated here are in keeping with the total hydrogenation of diphenylacetylene to 1,2-diphenylethane along with the formation of free *cis*- and *trans*-stilbene – the retention of stilbene in the complex is feasible along with its dissociation.

The hydrogenation of *cis*- and *trans*-stilbene from complexes of $Ru(H)_2(CO)(dhae)(stilbene)$ are predicted here to involve complexes exhibiting an agostic interaction from the β-hydrogen to the metal centre. This is indicated by the distances between the atoms, the vibrational frequencies calculated and the use of AIM theory, with bonding critical points identified for this interaction. In Cycle 1, the formation of a complex with this interaction (**21a**) is unfavourable, whereas it is slightly favourable in Cycle 2 (**21b** and **21c**). Significantly, the barrier for further reaction must break this interaction, whether by the movement of a ligand in the coordination sphere, or by the reaction with another ligand. This creates a barrier and means the formation of 1,2-diphenylethane is hindered. The high barriers calculated for the transfer of the final hydride ligand also additionally hinder these reactions. The final transfer barriers were all approximately equal with those for the coordination of dihydrogen or CO to the metal to form am 18-electron complex. The hydride transfer reaction would result in the high energy 14-electron intermediate such as Ru(CO)(dhae) following the dissociation of 1,2-diphenylethane. These final barriers account for the observation of *trans*-stilbene, as isomerisation occurs via the rotation of the σ-bond between sp^3 hybridised carbons, formed by the third hydride transfer reaction. The reverse reaction then forms *trans*-stilbene, which is unlikely if the final fourth hydride transfer reactions were facile. It is worth noting that the formation of *trans*-stilbene can occur via Cycle 2, where the interaction of the vinyl ligand with the metal centre allows the alignment for the hydride ligand to transfer to the opposite face. This alignment was not possible in Cycles 1 or 3.

The detection of 1,2,3,4-tetraphenylbutadiene means that carbon-carbon bond formation occurs. The pathways modelled have thermodynamic values that indicate that this is only viable at elevated temperatures. These barriers are significantly higher than those encountered for the second hydride transfer reactions and are consistent with the observation of the dimer with high substrate excess, as the hydride transfer to vinyl ligand is more favourable. The ligand arrangements seen in Cycles 1 and 3 prevent this transfer; the transfer to the vinyl ligand creating *cis*-stilbene is significantly more favourable than the formation of the new carbon-carbon bond. The photochemical initiation and subsequent formation of Ru(CO)(dhae) (**5a**) was predicted to allow two diphenylacetylene molecules to coordinate to the metal centre and so provide a feasible route for the formation of the dimer; without this photochemical initiation this 14-electron species is not formed and so the dimer was not observed in the thermal reaction of **A1**.

The interconversion of the stable species identified in this work was not investigated here. The isomers of $Ru(H)_2(CO)_2$(dhae) (**3a**) in Chapter 2 were found to be fluxional and pathways identified. The dihydride containing complexes in this work could potentially have similar rearrangements; the barriers in these pathways are likely to be higher than for the loss of diphenylacetylene or *cis*/*trans*-stilbene. The loss of these species had substantially lower free energies than identified in the pathways for rearrangement.

The models employed here did not include solvation to represent the toluene solvent used in the experiments. The examination of the effect of implicit solvation in Chapter 2 found that it had little impact on the thermodynamic values obtained. It is noted that the approximation for the reaction pathways in the gas phase may lead to significant differences to those in solution. The key pathways occur at the metal centre and so the toluene solvent may not play a critical role in the catalysis. The inclusion of solvation would be more critical if a coordinating solvent like pyridine had been used in the experiments. Dispersion corrections were not included in the models; it is possible that their inclusion would change the barriers encountered here. The majority of the reactions modelled here are intramolecular and so it is possible that the reactions predicted to be the most favourable would continue to be the most favourable with dispersion. The use of the simplified ligand dhae in place of dpae is noted to affect the accuracy of the results. It is likely that this effect is less than with larger steric bulk from a ligand such as PPh_3, as

identified in Chapter 2. The requirement for a bite angle of dhae and dpae of 80° to 90° means that the ligand always occupies *cis* positions in octahedral geometries, and cannot occupy *cis* equatorial positions in a trigonal bipyramid. This limits the effect of the dhae ligand, as the phenyl rings in dpae are directed away from the metal centre. This will reduce the impact from using dhae in the models; it is noted that dhae will not fully allow certain geometries to be modelled correctly. The inclusion of the dispersion correction would also have a more significant impact if the dpae ligand had been modelled, to allow the Van der Waals interactions to affect the geometries. It is also noted that multiple conformations of the *cis*- and *trans*-stilbene ligand are possible, highlighted by the existence of two conformations of $Ru(CO)_2$(dhae)(η^2-*cis*-stilbene) as **20d** and **20f**; these had relative enthalpies of -92.5 and -82.1 kJ mol^{-1} respectively, caused by the alignment of *cis*-stilbene. This highlights the need for careful judgement with calculated geometries and energies.

The use of the TZVP family of basis sets with the PBE0 functional will lead to one set of reaction enthalpies; this combination allowed similar values to be obtained relative to the previous work using this basis set family and the B3PW91* functional.[151] The comparison of intramolecular barriers and reactions is also unlikely to vary significantly with model changes; the loss and coordination of ligands is more susceptible to model changes.

The intermediates detected experimentally were predominantly detected by the use of the OPSY pulse sequence;[49] this pulse sequence was only formulated in 2007, and so the work on the hydrogenation of diphenylacetylene by complexes containing monodentate phosphines and dppe predates this.[142, 209] It would be interesting to investigate the reactions and hydrogenations using OPSY to verify whether the intermediates proposed for the arsenic systems here were also generated with these. It would also be interesting to see if the use of pyridine changed the products and detected intermediates with the arsenic systems. The use of the monodentate ligand $AsPh_2Me$ should allow the chelate affect to be investigated in dpae, although the lack of usable coupling from the arsenic nucleus in NMR spectroscopy may limit the usefulness of such a study. The ligand 2,2'-Bis(diphenylphosphino)-1,1'-binaphthyl (BINAP) would also be an interesting ligand to use in this hydrogenation reaction; its effects on catalytic cycles has been widely investigated with its importance in the field of asymmetric hydrogenation.[220]

Chapter 4: Reactions of dihydrogen with $W(N_2)_2(dppe)_2$

4.1 Background

The majority of complexes presented in this thesis contain dihydrogen and form via barrierless oxidative addition[1]. It was speculated in 1959 that a three-centre transition state (η^2-M) could be involved in this process which is analogous to a Lewis base reaction,[221, 222] although others proposed a two-centre pathway.[4, 8] Subsequently, examples have been found where this three-centre dihydrogen binding mode is stable.[223]

The first example of this type of complex, $W(CO)_3(P^iPr_3)_2(H_2)$, was produced in 1984 by Kubas *et al.*[224] and a neutron structure confirmed that the dihydrogen ligand occupied a side-on position with respect to the metal centre. The hydrogen-hydrogen bond was measured as 0.82 Å, thereby indicating that the dihydrogen bond was still present. Later work found that this complex was in equilibrium with the 7-coordinate dihydride form which proved to be present at circa 20%.[6, 7] A further study revealed that the equilibrium constant for this reversible reaction was 4.0 at 24 °C and the associated enthalpy change was -5.0 kJ mol^{-1}.[225] Additionally, the activation parameters for this reaction were also low, with $\Delta H^{\ddagger}$ = +42.4 kJ mol^{-1} and $\Delta G^{\ddagger}$ = +67.2 kJ mol^{-1}.[226] It has also been shown that the reversible loss of dihydrogen creates a vacant site which in the case of P^iPr_3 is stabilised by an agostic bond of strength between 27 and 37 kJ mol^{-1}.[227]

When dinitrogen is lost from the related complex, *trans*-$[W(N_2)_2(dppe)_2]$, similar initial stabilisation via an agostic bond has been postulated by Hidai *et al.*[228] In this case, however, the formation of the *ortho*-metallated complex [W(*meso*-*o*-$C_6H_4(PPhCH_2CH_2PPh_2)_2(dppe)$] results. Caulton *et al.* observed the formation of the related *ortho*-metallated complex $W(H)_3((C_6H_4)PMe_2)(PMe_2Ph)_3$ when ^{t}BuLi reacts with $WH_2Cl_2(PMe_2Ph)_4$.[229] O*rtho*-metallation was first discovered in late 1960s,[223] with two of

the first *ortho*-metallated complexes (detailed in References [[230]] and [[231]]) shown in Figure 4.1.

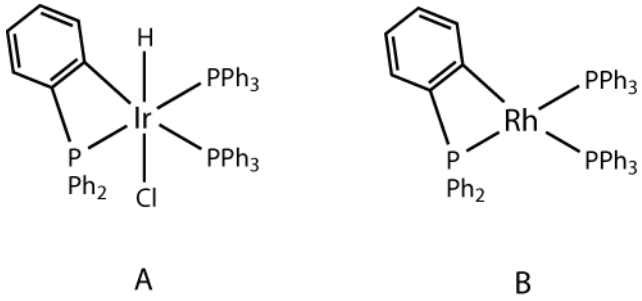

A B

Figure 4.1: Early *ortho*-metallated complexes: A is formed from $[IrCl(PPh_3)_3]$ and B is formed from $[RhMe(PPh_3)_3]$

Ortho-metallation reactions were traditionally referred to as *intra*molecular coordination but the terms *ortho*-metallated complex and cyclometallated complex have become favoured as the need to distinguish these two different classes of reaction has become apparent. *Ortho*-metallation is distinguished from cyclometallation by the formation of an aryl carbon-metal σ-bond at the *ortho* position. The reported reactions which lead to *ortho*-metallated complexes involve either thermal or photochemical activation.[223, 232] The formation of the new C-metal bond occurs alongside the formation of a new H-metal bond. This newly formed hydride ligand can undergo reductive elimination if a suitable anionic ligand is present and so does not remain part of the inner-coordination sphere of the detected/isolated complex. One notable exception to this is found in the chemistry of $IrCl(PPh_3)_3$ where the detection of the correspond *ortho*-metallated-hydride-product is possible.[233]

4.2 Investigation into the reactions of $W(N_2)_2(dppe)_2$ with *p*-H_2

A study carried out by Duckett *et al.*[45] used *p*-H_2 and $W(H)_2(CO)_3(PCy_3)_2$ to establish whether PHIP could be used to probe the dihydrogen-dihydride equilibrium described earlier. A sample of $W(H)_2(CO)_3(PCy_3)_2$ was first examined in the presence of *p*-H_2 at 298 K by ^1H NMR spectroscopy. While thermal signals were detected for the dihydride complex no PHIP was observed. *In situ* UV photolysis, using irradiation at 325 nm and 213 K, revealed signals for the dihydride complex, but again no PHIP. These observations were interpreted to mean that the rapid relaxation associated with coordinated dihydrogen

quenches the PHIP effect. This contrasts with the results of Bargon *et al.* which showed that PHIP can be observed in an organic hydrogenation product that is formed via a metal-based intermediate with dihydrogen ligand.[234]

It was then decided to test the behaviour of *p*-H_2 with $W(N_2)_2$(dppe-κ^2P)$_2$. The formation of $W(H)_4$(dppe-κ^2P)$_2$ was observed upon heating a sample of $W(N_2)_2$(dppe-κ^2P)$_2$ in THF-d_8 to 333 K. The hydride signal for $W(H)_4$(dppe-κ^2P)$_2$ in the resulting ^{1}H NMR spectrum appears as a polarized signal at -3.66 ppm and confirms the potential of using PHIP to study such complexes. The T_1(min) of the hydride signal of $W(H)_4$(dppe-κ^2P)$_2$ was determined as 0.58 s at 258 K and this value is consistent with the presence of four hydride ligands. It was expected that the formation of $W(H)_4$(dppe-κ^2P)$_2$ would proceed via $W(H)_2(N)_2$(dppe-κ^2P)$_2$ but no signals were observed for this species. When this experiment was repeated at lower temperatures, two further sets of polarized signals were detected at -2.69 and -2.93 ppm and found to couple by COSY methods. Surprisingly, they also coupled to a further signal at -0.14 ppm. These three signals were not consistent with the proposed dihydride intermediate and so low temperature irradiation studies were performed that aimed to form sufficient product for characterisation (see later).

It was subsequently noted that previous studies by Diamantis *et al.* found that the sole photoproduct formed from $W(N_2)_2$(dppe-κ^2P)$_2$ was W(dppe-κ^2P)$_2$ which then reacts with the released N_2 ligand to form $W(N_2)$(dppe-κ^2P)$_2$ and then $W(N_2)_2$(dppe-κ^2P)$_2$.[235] Flash photolysis determined that both of these reactions had first order rate constants, with the first process having a rate constant of 3.9 ± 0.8 x10^2 s^{-1} and the second having a rate of 1.6 ± 0.3 s^{-1}. These values were determined in THF solutions that were saturated with N_2 at 25 °C. A separate study by George *et al.* used ^{15}N labelling to suggest that the initial ligand loss process occurred through a sequential pathway.[236]

A series of DFT studies were therefore conceived to rationalise this behaviour. This work by Duckett and John *et al.* has been published (see Appendix 1).[45] In combination with the DFT study, the experimental results were interpreted to indicate that an *ortho*-metallation reaction had occurred, where a hydrogen in the *ortho* position of one of the phenyl rings moves to the metal. This leads to the complex $W(H)_3$(dppe-κ^2P)($Ph_2PCH_2CH_2PPh(C_6H_4)$-κ^2P) as illustrated in Figure 4.2. The work presented here takes the DFT study and extends it to

include a full-ligand description and the new results change some aspects of the published work.

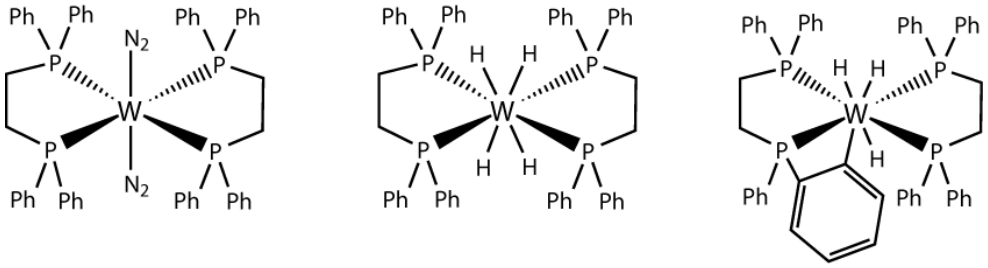

Figure 4.2: Complexes identified during the reaction *p*-H_2 with $W(N_2)_2$(dppe-κ^2P)$_2$

4.2.1 Experimental details

All DFT calculations were performed on the full molecule (without simplification) using the Gaussian 09 software package.[122] A small number of relaxed constrained optimisation scans were performed using a model with all phenyl substituents on the dppe ligands replaced by hydrogen, except for one ring to allow for the modelling of the *ortho*-metallation reaction. Structures were optimised using the BP86 DFT functional[84, 87] and the basis set family defined as def2-SVP from Ahlrichs[175, 237, 238] for all atoms with the associated ECP for tungsten[239] and the auxiliary basis sets from Weigend[240] to fit the Coulomb potentials in the density fitting approximation.[241, 242] Transition states were located using the STQN methods of Schlegel *et al.*[171, 172] and frequency calculations were used to confirm whether structures obtained were local minima or saddle points for transition states. The frequency calculations gave the zero-point and thermal corrections to energy at 298.15 K. All geometry optimisations and frequency calculations were carried out with solvent effects applied using the IEFPCM default model[191-193] with the solvent specified as THF. The implicit model for the solvent was included in the calculations as THF can be a coordinating solvent. Single point energy calculations were performed on the optimised structures using the same def2-SVP basis sets but with the PBE0 functional of Adamo *et al*.[173] and with the same solvation model applied. The energy corrections were then applied to obtain chemical enthalpies and free energies.[189, 190] This approach was used to minimise the computational cost, whilst utilising the PBE0 hybrid functional to calculate the reaction thermodynamics. This hybrid functional has been shown to perform

well for transition metals[243, 244] and a recent review of DFT by Tsipis recommends its use.[216]

The calculations were checked for Basis Set Superposition Errors (BSSE). The resulting counterpoise calculation[178, 179] revealed one dinitrogen ligand to have an error in its stabilisation energy of 0.00673 a.u., equal to 17.7 kJ mol^{-1}. Hence, all subsequent calculations were corrected for the BSSE. For complexes where *ortho*-metallation had taken place, the phenyl ring and hydrogen atom were not included in the BSSE correction whereas dihydrogen and the solvent were.

The results from the optimisation of $W(N_2)_2(dppe\text{-}\kappa^2P)_2$ (**1**) were validated by comparing selected bond lengths and bond angles with those of an *x*-ray structure of Englert *et al.*[245] These selected parameters are shown in Table 4.1.

Table 4.1: Comparison of selected bond lengths and angles between experimental and theoretical geometries of $W(N_2)_2(dppe\text{-}\kappa^2P)_2$

Bond length/ Bond angle	Experiment	Theory
W - N / Å	2.014(5)	2.03
W - P / Å	2.435(2) & 2.443(2)	2.52
N - W - N / °	180.0 (not given)	179.3
P - W - P (*cis*) / °	100.47(6)	100.5/99.4
P - W - P (chelating) / °	79.53(6)	80.3
P - W - P (*trans*) / °	180 (not given)	174.8

As can be seen, the model bond lengths for the tungsten-dinitrogen bonds and the tungsten-dppe bonds match the experimental lengths well. The bond angles also generally agree with the experimental values, although there is a discrepancy in the P-W-P (*trans*) bond angle. Two values for the P-W-P (*cis*) bond angle are given as the structure is not symmetric due to differences in the alignment of the phenyl rings. This difference is likely to cause of the difference in the P-W-P (*trans*) bond angle. It is for this reason that the bp86 DFT functional was felt to be appropriate for the use in in this study.

4.2.2 Theoretical formation of tetrahydride $W(H)_4(dppe\text{-}\kappa^2P)_2$ and tri-hydride $W(H)_3(dppe\text{-}\kappa^2P)(PPh(C_6H_4)CH_2CH_2Ph_2P\text{-}\kappa^2P)$

In order to map the reaction of $W(N_2)_2(dppe\text{-}\kappa^2P)_2$ (**1**) with dihydrogen, the intermediates shown in Figure 4.3 were modelled using the methodology set out in the previous section.

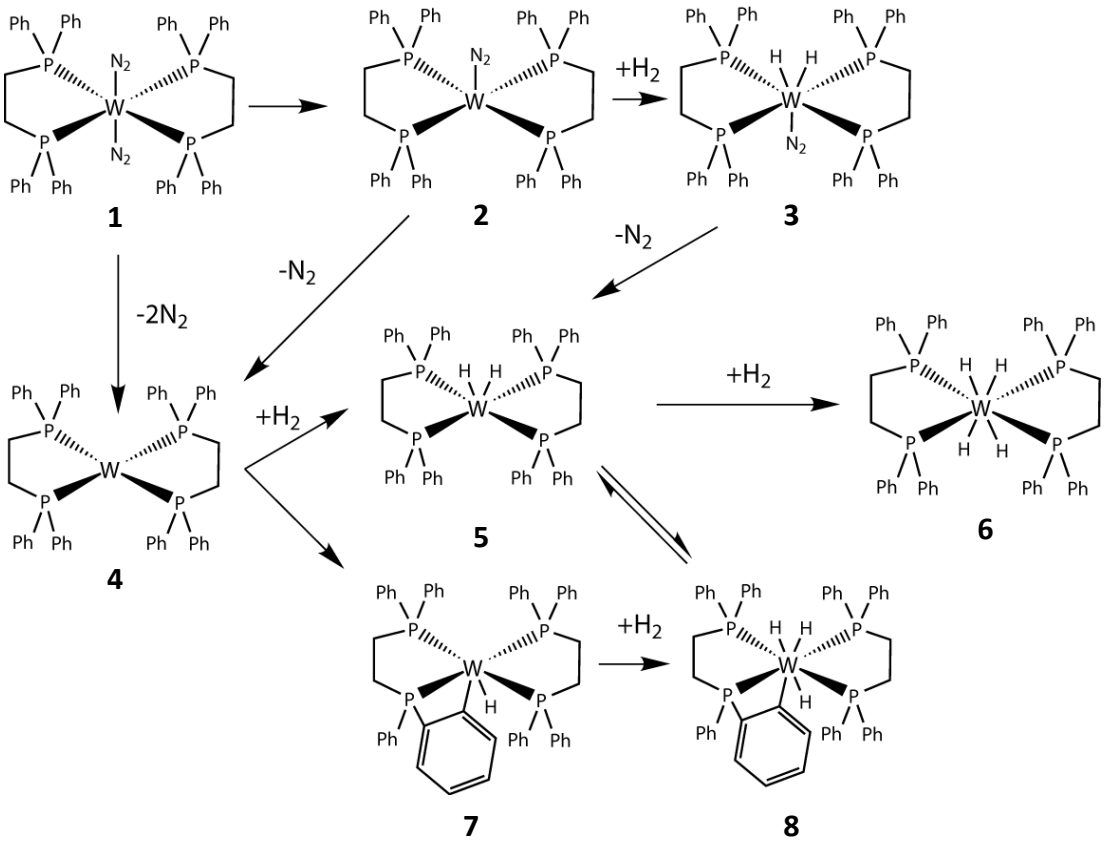

Figure 4.3: Complexes modelled for the reactions of dihydrogen with $W(N_2)_2(dppe\text{-}\kappa^2P)_2$

The geometry of $W(N_2)_2(dppe\text{-}\kappa^2P)_2$ (**1**) was used as the starting point for the optimisation of the subsequent product geometries. Structures **1** - **8** were all found to be local minima. All thermodynamic values are quoted relative to **1**; this complex therefore occupies the value of 0.0 kJ mol^{-1} on all of the following potential energy profiles. The loss of one dinitrogen ligand was calculated to result in an enthalpy change of +87.4 kJ mol^{-1} and results in the formation $W(N_2)(dppe\text{-}\kappa^2P)_2$ (**2**); however this intermediate is unlikely to be formed by photolysis for the reasons described in the introduction.

4.2.3 Geometry of 14-electron intermediate W(dppe-κ²P)₂

The 14-electron species W(dppe-κ^2P)$_2$ (**4**) was initially modelled as a square planar geometry in the same way as undertaken in the published work.[45] The double ligand loss product W(dppe-κ^2P)$_2$ (**4^1**) results in an enthalpy change of +282.2 kJ mol^{-1} after counterpoise correction and is therefore clearly very high in energy. An alternative geometry was located which was significantly lower in energy. This was the butterfly geometry already described in this thesis for numerous ruthenium intermediates. The key structural information for these two geometries is shown Figure 4.4.

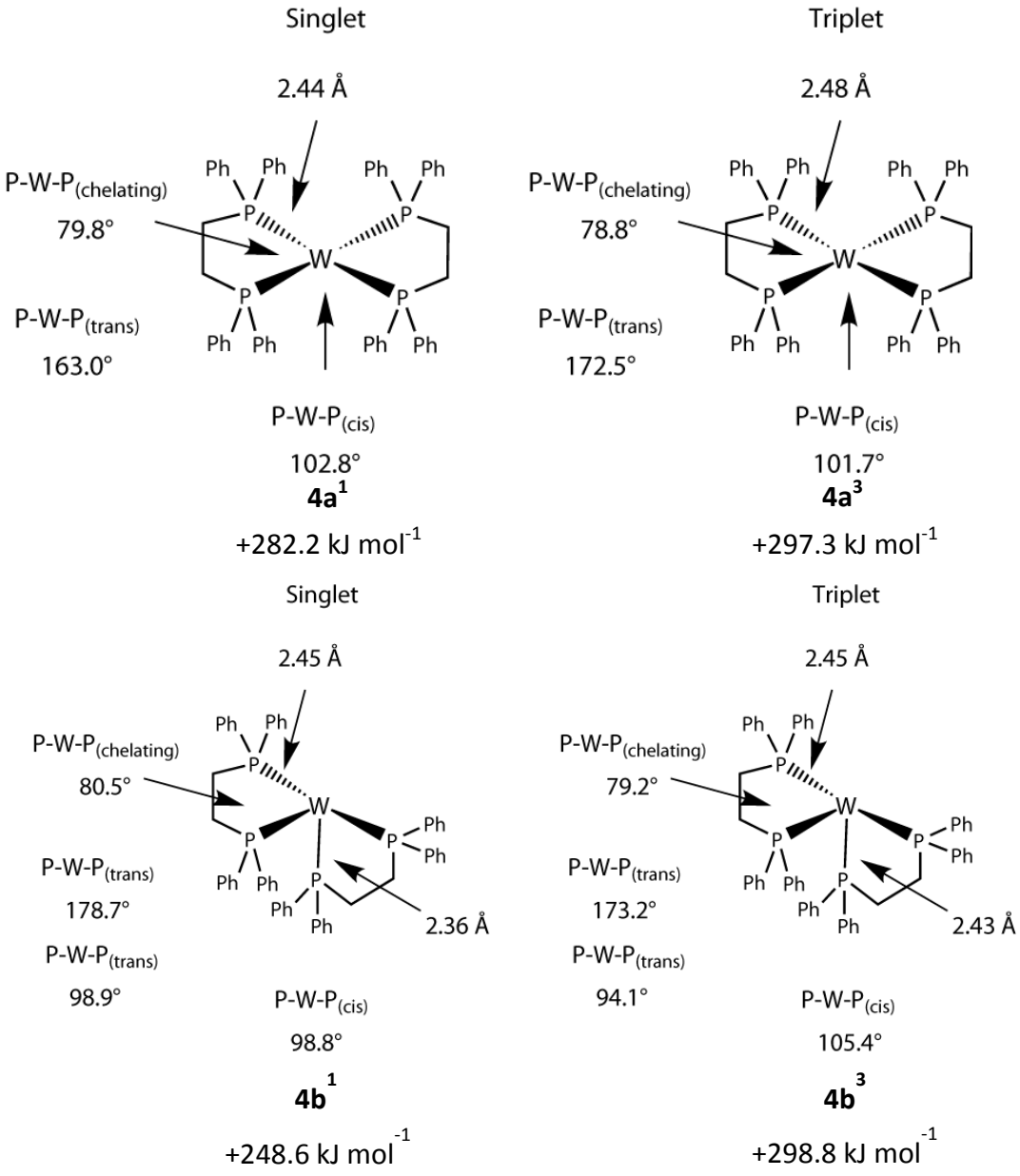

Figure 4.4: Comparison of the singlet and triplet geometries and enthalpies of W(dppe-κ^2P)$_2$

The butterfly intermediate **4b^1** was found to have an enthalpy of 248.6 kJ mol^{-1} above **1**, compared to **4a^1** with an enthalpy of 282.2 kJ mol^{-1}. Both geometries have the two dppe ligands with bite angles of 80° which is in keeping with the angle measured experimentally for **1** (shown in Table 4.1). The W-P bond lengths in **4a^1** are 2.44 Å whereas there are two different W-P bond lengths in **4a^3**. The phosphorus centres that are *trans* (the axial positions) have W-P bond lengths of 2.45 Å. The *cis* phosphorus centres (the equatorial positions) have shorter bond lengths of 2.36 Å, consistent with these centres being *trans* to vacant sites. The triplet geometry of **4a^3** adopts an almost perfect square-planar geometry with a P-W-P($_{trans}$) angles of 172.5° whereas the singlet **4a^1** adopts a distorted square-planar geometry with P-W-P($_{trans}$) bond angles of 163.0°. This distortion is not the same as that observed for the ruthenium butterfly geometries seen in the previous chapters as no CO ligands are present to allow significant π* back-bonding from the metal.

The two electronic states of the 14-electron butterfly complexes (**4b^1** and **4b^3**) have similar geometries, with their most significant difference being reflected in the equatorial planes W-P bond distances (2.36 Å vs. 2.44 Å). The higher enthalpy of triplet **4b^3** relative to singlet **4b^1** means that **4b^1** is going to the dominant photoproduct.

The difference in enthalpy between the lowest energy singlet **4b^1** and the lowest energy triplet **4a^3** is around 50 kJ mol^{-1}, with the singlet as the most stable species. This agrees with the experimental observation of PHIP in the subsequent reactions. Intermediate **4b^1** is considered to be the starting point in any further reactions.

The significantly high relative enthalpies for all identified states of W(dppe-κ^{2}P)$_2$ means that this 14-electron intermediate is only accessible by photochemical means.

4.2.4 Reactions of 14-electron intermediate W(dppe-κ²P)₂

Highly reactive **4b[1]** is predicted to be able to undergo four reactions; recoordination of the N_2 ligand, addition of H_2, *ortho*-metallation or addition of the solvent. The addition of dihydrogen after the recoordination of dinitrogen would result in the formation of $W(H)_2(N)_2(dppe\text{-}\kappa^2P)_2$ but this was not observed experimentally. The failure to see it suggests that one of the alternative pathways leads to a more stable product.

The addition of dihydrogen to **4b[1]** was found to occur via a barrierless reaction. It is favourable by -120.3 kJ mol^{-1} and leads to dihydride $W(H)_2(dppe\text{-}\kappa^2P)_2$ (**5b**). The relaxed potential energy profile scan for the approach of the dihydrogen during the formation of **5b** is illustrated in Figure 4.5 for the simple model $W(dhpe\text{-}\kappa^2P)(H_2PCH_2CH_2PHPh\text{-}\kappa^2P)$. The dihydrogen approaches with an end-on orientation which changes to side-on. After this point the dihydrogen ligand undergoes oxidative addition to form the dihydride complex $W(H)_2(dhpe\text{-}\kappa^2P)(H_2PCH_2CH_2PHPh\text{-}\kappa^2P)$. The preferred orientation of the resulting dihydrides is across the bent P-W-P plane (equatorial) as this results in the least steric hindrance of the ligands.

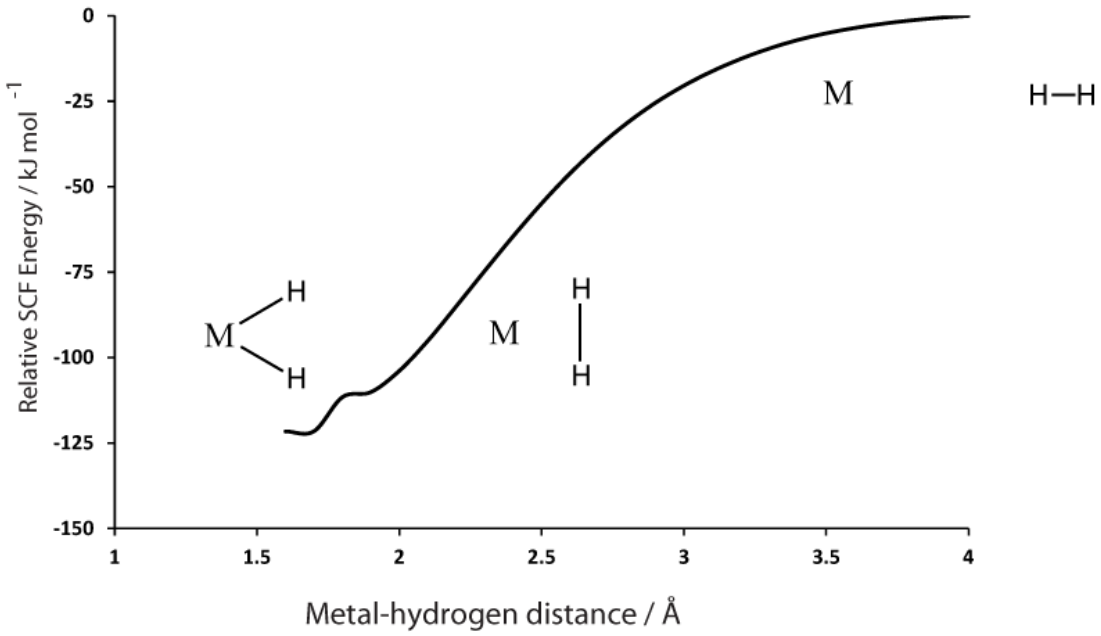

Figure 4.5: Relaxed potential energy profile scan for the approach of a dihydrogen molecule to the metal centre of $W(dhpe\text{-}\kappa^2P)(H_2PCH_2CH_2PHPh\text{-}\kappa^2P)$

The addition of a second hydrogen molecule to **5b** is also favourable and barrierless. It leads to square-based pyramidal $W(H)_4(dppe\text{-}\kappa^2P)_2$ (which has a phosphorus centre out of the basal plane, as **6b**) which is favourable by -80.5 kJ mol^{-1} but 105.6 kJ mol^{-1} less stable than the alternative isomer **6a** which has a square-planar $W(H)_4(dppe\text{-}\kappa^2P)_2$ core; there is no experimental evidence for **6b**. It was found that the approach of dihydrogen to **5b** between the equatorial ligands can result in the formation of **6a** which is in keeping with the experimental evidence. This is a higher energy approach than for hydrogen approaching the opposite face and leading to **6b**. and a low energy route from **4b^3** to **6a** is therefore implicated.

The *ortho*-metallation reactions were then investigated. For this type of reaction to occur, one of the phenyl rings on the dppe ligands has to approach the inner coordination sphere of the tungsten centre to allow interaction with an occupied d-orbital. Two *ortho*-metallation pathways from **4b^1** are possible involving a phenyl ring in the axial or equatorial plane. The equatorial phenyl ring reacts via transition state **9a'** and a barrier of 3.0 kJ mol^{-1} (enthalpy; the SCF energy difference is 41.7 kJ mol^{-1}) to form *ortho*-metallated **10a**. This intermediate is -51.2 kJ mol^{-1} more stable than **4b^1**. It then reacts with dihydrogen to form **11a**, which is favourable by -71.8 kJ mol^{-1}. It is worth noting that the addition of dihydrogen occurs between the phenyl ring and hydride on the metal centre.

The *ortho*-metallation reaction with an axial phenyl ring occurs through transition state **9b'** and a barrier of -28.1 kJ mol^{-1} (enthalpy; SCF energy difference is +5.7 kJ mol^{-1}). This negative barrier arises from the very small overall energy difference and loss of a vibrational mode in the transition state. Product **10b** is favoured by -57.5 kJ mol^{-1} and is slightly more stable than **10a**. This suggests that the route to **10b** would dominate. **10b** then reacts with dihydrogen, releasing 65.8 kJ mol^{-1} of energy to form **11b**. Both **11a** and **11b** have very similar energies (125.3 vs. 125.6 kJ mol^{-1}). Detailed representations of the two *ortho*-metallation transition states **10a** and **10b** are shown in Figure 4.6.

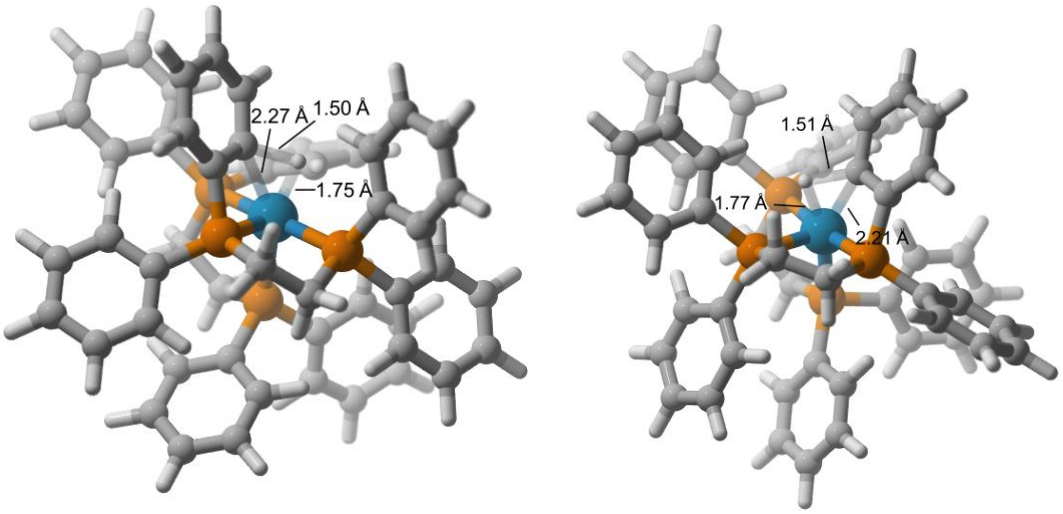

10a' **10b'**

Figure 4.6: Transition states **10a'** and **10b'** for *ortho*-metallation pathways from the butterfly geometry of W(dppe-κ^2P)$_2$ **4b**[1]

The addition of hydrogen and the formation of the *ortho*-metallation products with the resulting intermediates, overall reaction pathways, and associated thermodynamics are illustrated in Figure 4.7.

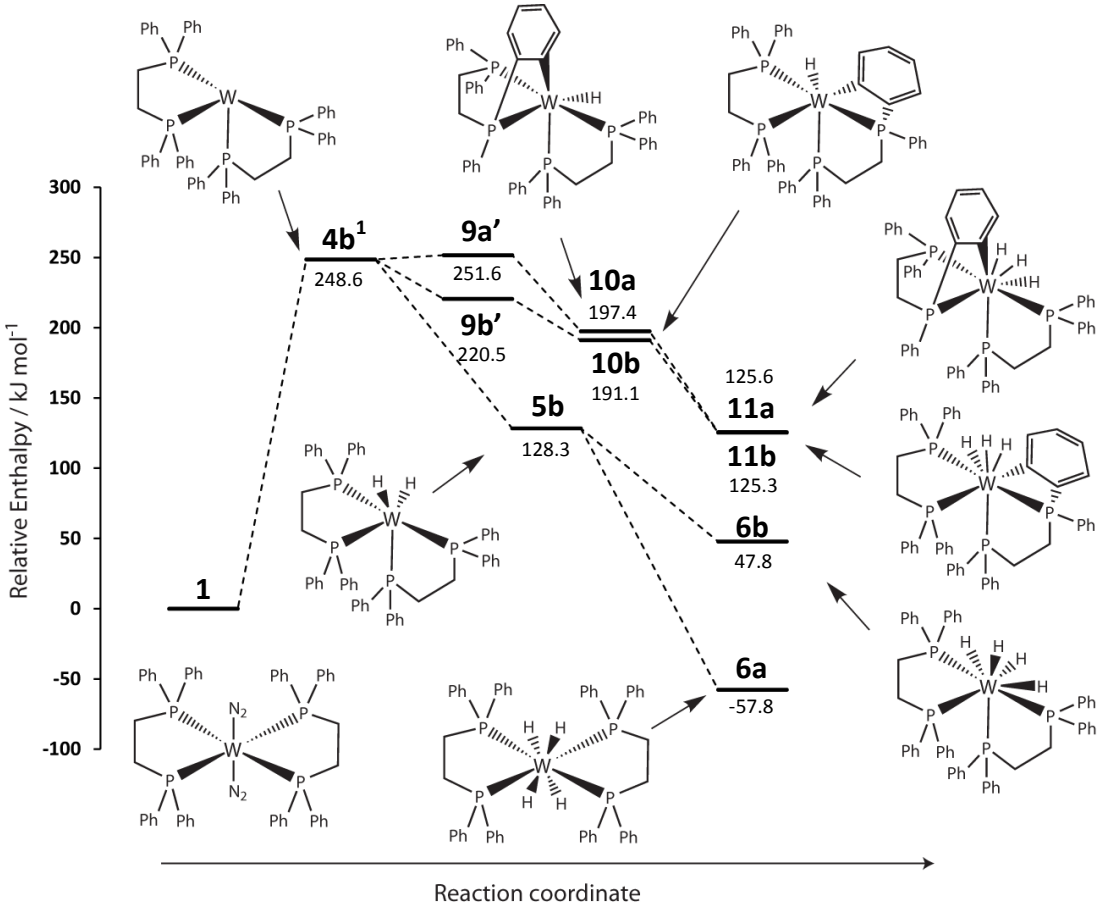

Figure 4.7: Relative enthalpy profile for the reactions of the butterfly intermediate of W(dppe-κ^2P)$_2$ (**4b^1**) via dihydrogen addition and *ortho*-metallation

The geometries of products **11a**, **11b** and **6b** do not fit with the experimental data. Hence, the geometries of the 16-electron species W(H)(dppe-κ^2P)(Ph$_2$PCH$_2$CH$_2$PPh(C$_6$H$_4$)-κ^2P) and W(H)$_2$(dppe-κ^2P)$_2$ were remodelled with all four phosphorus centres in the basal plane. The resulting product enthalpies are illustrated in Table 4.2. In all cases the square planar species have lower energy. It must therefore be concluded that interconversion between the two geometry forms is possible.

Table 4.2: Relative enthalpies of the identified butterfly geometry derived complexes and their square-planar derived equivalents

	Square-planar / kJ mol^{-1}	**Butterfly** / kJ mol^{-1}
W(dppe-κ^{2}P)$_2$	+282.2 (**4a^1**)	+248.6 (**4b^1**)
W(H)(dppe-κ^{2}P)(Ph$_2$PCH$_2$CH$_2$PPh(C$_6$H$_4$)-κ^{2}P)	+173.7 (**7a**)	+197.4 (**10a**)
		+191.1 (**10b**)
W(H)$_3$(dppe-κ^{2}P)(Ph$_2$PCH$_2$CH$_2$PPh(C$_6$H$_4$)-κ^{2}P)	+56.7 (**8a**)	+125.6 (**11a**)
		+125.3 (**1b**)
W(H)$_2$(dppe-κ^{2}P)$_2$	+92.1 (**5a**)	+128.3 (**5b**)
W(H)$_4$(dppe-κ^{2}P)$_2$	-57.8 (**6a**)	+47.8 (**6b**)

Low lying transition states were found for the conversion of the 16-electron butterfly derived complexes of W(H)(dppe-κ^{2}P)(Ph$_2$PCH$_2$CH$_2$PPh(C$_6$H$_4$)-κ^{2}P) and W(H)$_2$(dppe-κ^{2}P)$_2$-κ^{2}P). For **10a**, the equatorial P-W-P bond angle of 92.8° opens out to 111.0° and transition state **10a'** reflects a barrier of +15.9 kJ mol^{-1} to the formation of **7a**. For **10b**, the equatorial P-W-P bond angle of 105.3° opens out to 159.4° and transition state **10b'** reflects a barrier of +46.3 kJ mol^{-1} to **7a**. For complex W(H)$_2$dppe-κ^{2}P)$_2$ (**5b**), the equatorial P-W-P bond angle of 95.1° opens out to 121.5° and transition state **5a'** reflects a barrier of +10.3 kJ mol^{-1} to the formation of **5a**. Clearly intermediates **7a** and **5a** are accessible and can then react though a new set of pathways. These transformations are illustrated in Figure 4.10. Detailed illustrations for transition states **10b'** and **5c'** are shown in Figure 4.8 and Figure 4.9 respectively.

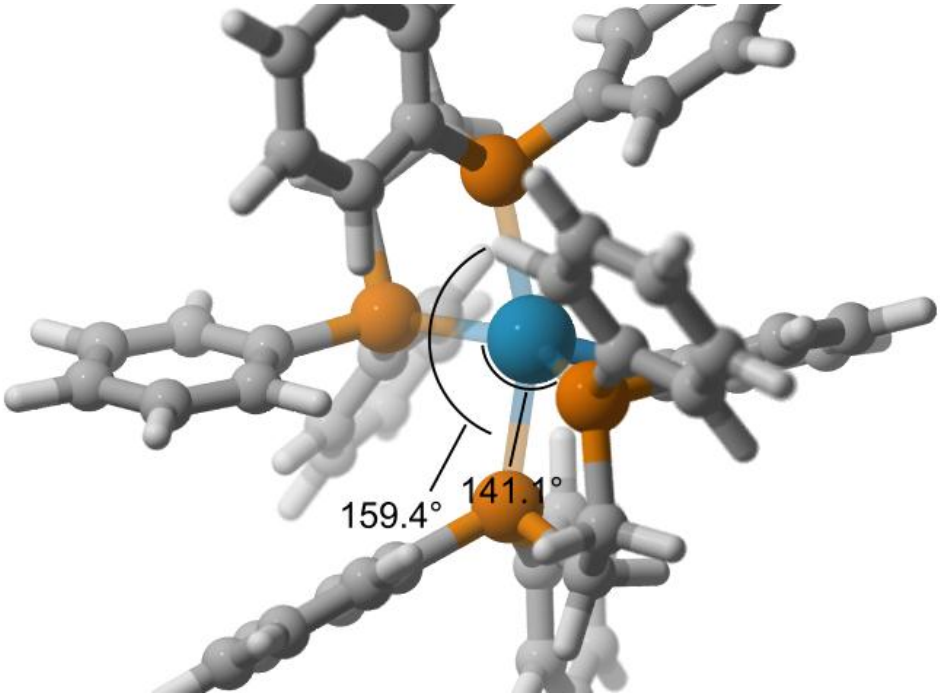

Figure 4.8: Detailed representation for transition state **10b'** which links the butterfly complex **10b** to **7a**

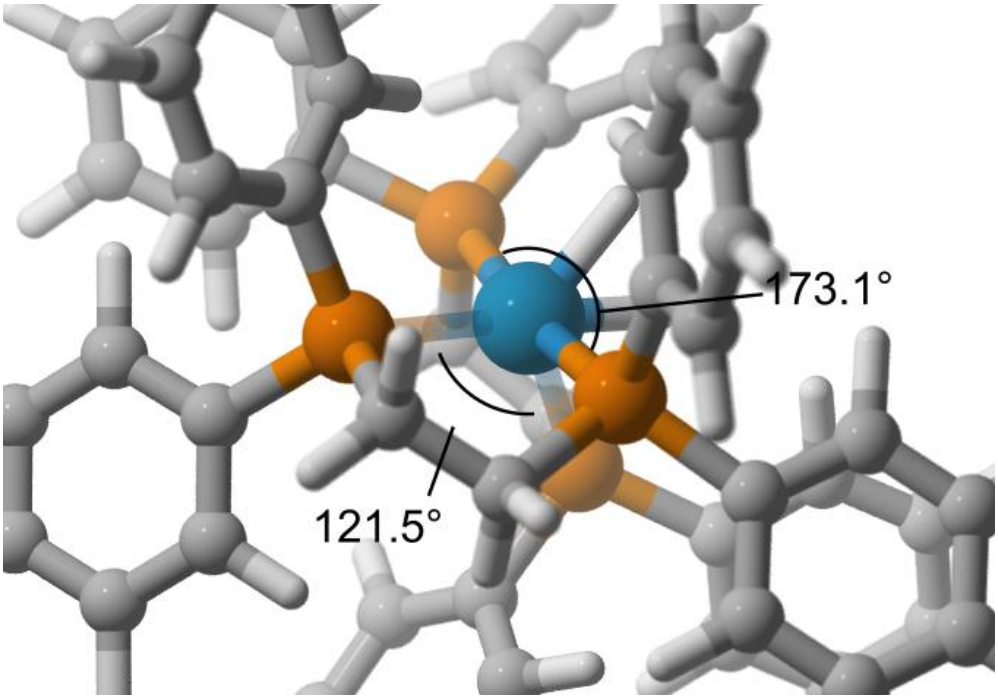

Figure 4.9: Detailed representation for transition state **5a'** which links the butterfly complex **5b** to **5a**

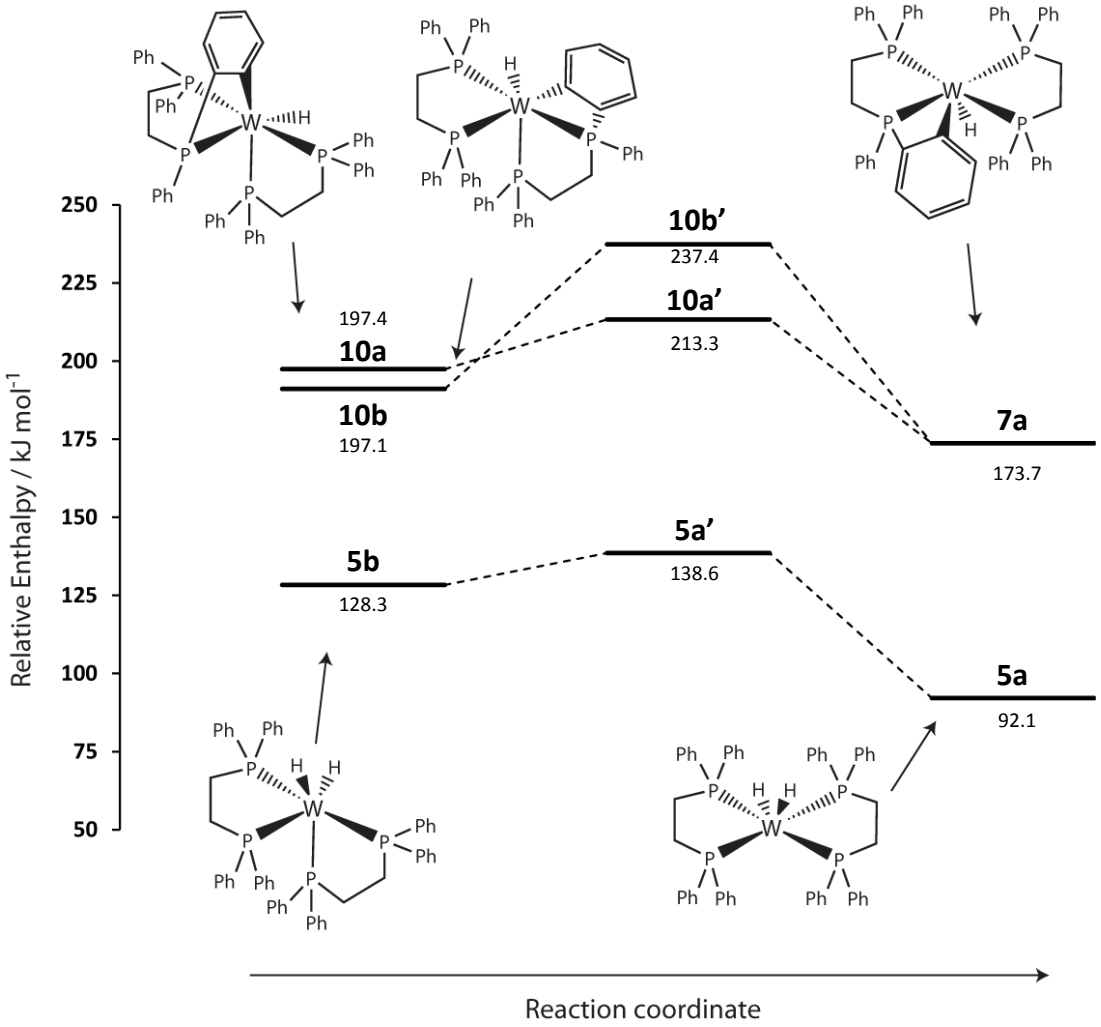

Figure 4.10: Relative enthalpy profiles for the interconversion of 16-electron butterfly derived complexes to their more stable square-planar counterparts

$W(H)_2$(dppe-κ^2P)$_2$ (**5a**) can then add dihydrogen to form the observed complex $W(H)_4$(dppe-κ^2P)$_2$, here modelled as **6a**, for which this reaction is favourable by **-**149.9 kJ mol^{-1}. The formation of this complex from $W(N_2)_2$(dppe-κ^2P) (**1**) is favourable by -57.8 kJ mol^{-1}. This addition is also barrierless according to the $W(H)_2$(dhpe-κ^2P)($H_2PCH_2CH_2PHPh$-κ^2P) model, with an end-on H_2 approach changing to side-on prior to full oxidative addition. This scan is illustrated in Figure 4.11.

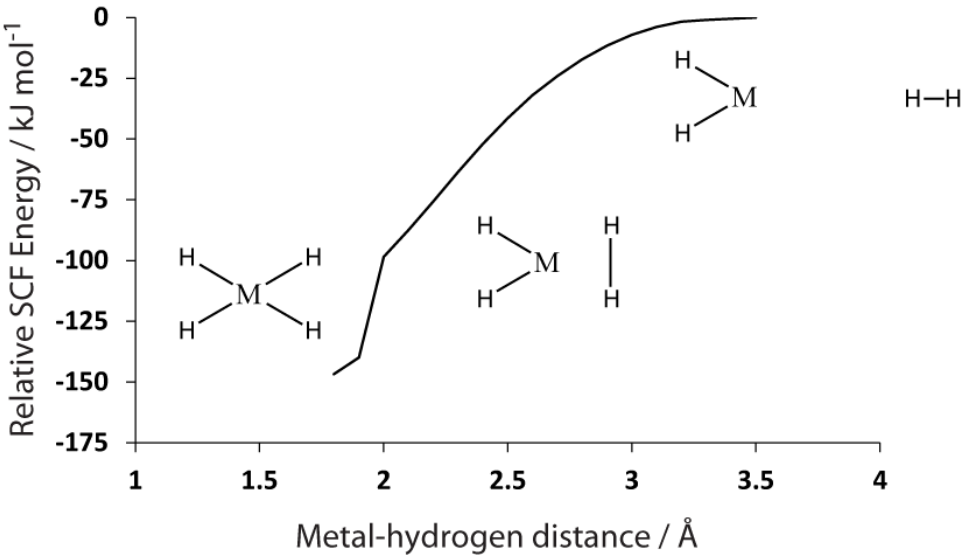

Figure 4.11: Relaxed potential energy profile scan for the approach of dihydrogen to $W(H)_2$(dhpe-κ^2P)($H_2PCH_2CH_2PHPh$-κ^2P)

The results presented so far show that the butterfly species has a role limited to the beginning of the pathways; reaction to any 16-electron species results in rearrangements to the dppe-κ^2P ligands forming a square-planar core. The predicted 16-electron *ortho*-metallated complex WH(dppe-κ^2P)($Ph_2PCH_2CH_2PPh(C_6H_4)$-κ^2P) (**7a**) was calculated to be more stable than **4b**[1] by -74.9 kJ mol^{-1} and is less stable than dihydride **5a** by +81.6 kJ mol^{-1}. This complex, illustrated graphically in Figure 4.12, has a metal-carbon bond of 2.15 Å and a metal-hydride bond of 1.72 Å. The phosphorus centre where the *ortho*-metallation reaction has taken place becomes bent out of the plane, and a P-W-P bond angle of 163.8° results. The other P-W-P bond angle is almost linear at 177.1°. This species was also shown to be more stable than the equivalent structures with the butterfly core (species **10a** and **10b**) and is formed via rearrangement from these through transition states **10a'** and **10b'**.

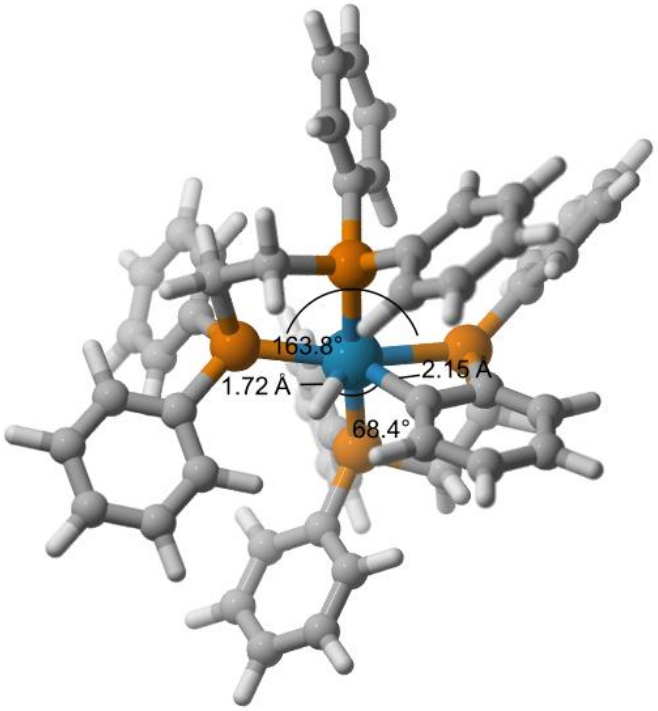

Figure 4.12: Representation of the o*rtho*-metallated complex WH(dppe-κ^2P)($Ph_2PCH_2CH_2PPh(C_6H_4)$-κ^2P) (**7a**)

This complex can then react with dihydrogen, again via a barrierless approach, to form 18-electron **8a**, as illustrated in Figure 4.13.

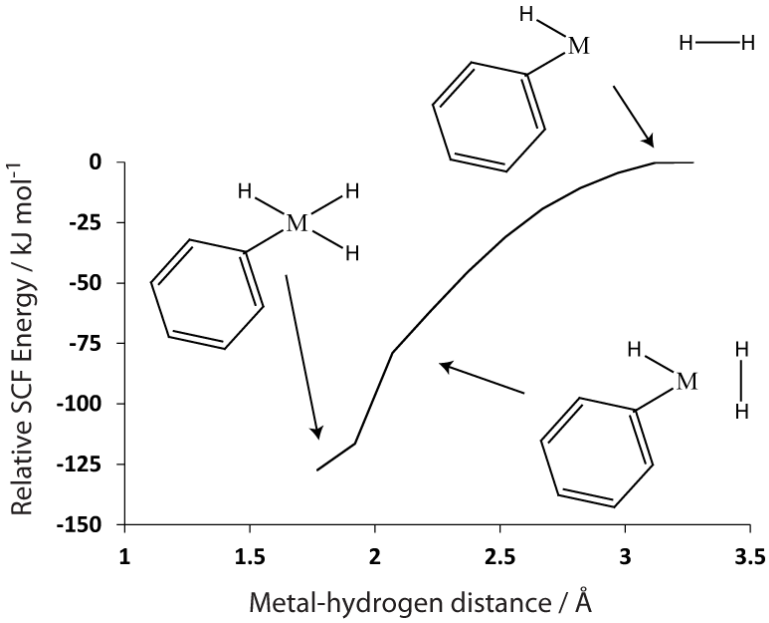

Figure 4.13: Relaxed potential energy profile scan for the approach of dihydrogen to the metal centre in W(H)(dhpe-κ^2P)($H_2PCH_2CH_2PH(C_6H_4)$)-κ^2P). Note; the simple model was used here

This second H_2 addition step is favourable by 117.0 kJ mol^{-1} with the product retaining a W(IV) oxidation state. **8a** is illustrated in detail in Figure 4.14. The P_{OM}-W-P bond angle is reduced upon the addition of dihydrogen from 163.8° in **7** to 151.8°, and the other P-W-P angle becomes distorted away from the linear angle of 177.1° and is now 162.6°. Importantly, the plane of the H-W-H ligands is perpendicular to that of the H-W-C plane of the ortho-metallated ring. These values and alignments are shown in Figure 4.14.

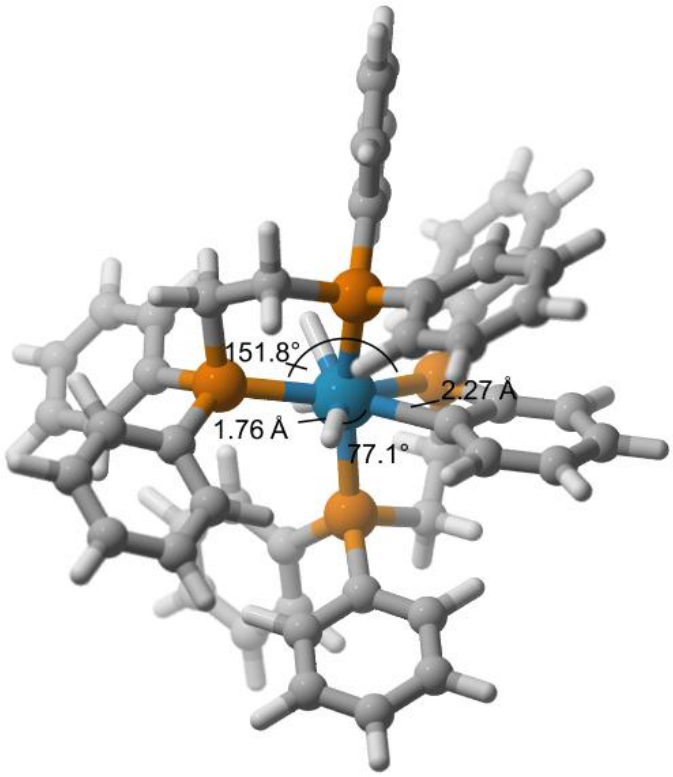

Figure 4.14: Representation of the o*rtho*-metallated complex $W(H)_3$(dppe-κ^2P)($Ph_2PCH_2CH_2PPh(C_6H_4)$)-κ^2P) (**8a**)

A second pathway to **8a** where the order of reaction is reversed is possible. The initial 16-electron dihydride (**5a**) contains two different environments for the phenyl rings due to the distortion imposed on the dppe ligands by the hydride ligands. This distortion is shown in detail in Figure 4.15, where the hydride ligands force the P-W-P bond angle for the atoms parallel to the H-W-H plane to become 160.6°. This means that the *ortho*-metallation reaction from **5a** can occur at two different sites. These two pathways exhibit different barriers. The different sites are labelled as A and B in Figure 4.15.

The *ortho*-metallation reaction at site A was found to lead to the formation **8a** with the same geometry as previously described and was favourable by 35.4 kJ mol^{-1}. The barrier for this reaction was determined to be sizeable, arising from transition state **5aA'**, at 64.6 kJ mol^{-1}. This transition state is illustrated in Figure 4.16. The motion of the imaginary frequency was for the cleavage of the C-H bond and optimised structures for two extremes of this vector confirmed the *ortho*-metallation reaction.

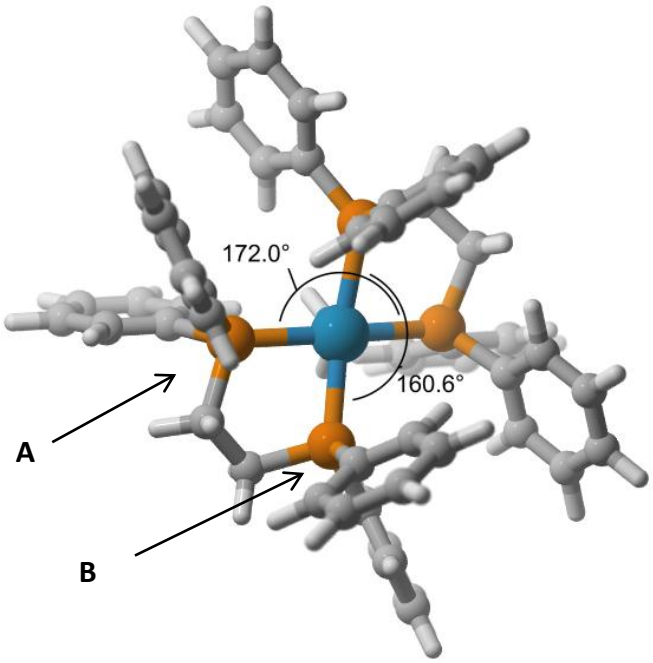

Figure 4.15: Representation of $W(H)_2(dppe\text{-}\kappa^2P)_2$ (**5a**)

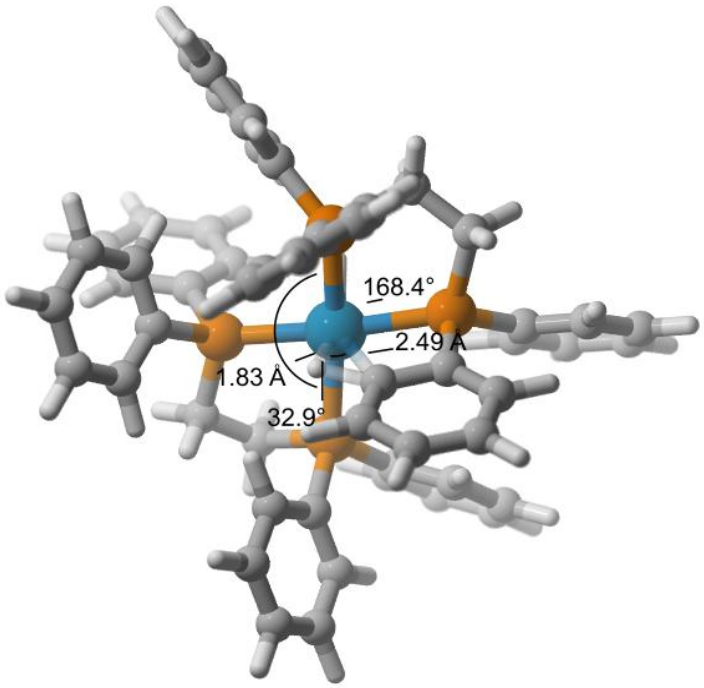

Figure 4.16: Detailed representation of the o*rtho*-metallation transition state $W(H)_2(dppe\text{-}\kappa^2P)_2$ (**5aA'**) arising from a phenyl ring in site A in **5a**

The *ortho*-metallation reaction at site B was found to lead to the formation of a new product geometry for $W(H)_3(dppe\text{-}\kappa^2P)(Ph_2PCH_2CH_2PPh(C_6H_4))\text{-}\kappa^2P)$ **8b**, which was favourable by just 12.9 kJ mol^{-1}. This geometry differs to that of **8a** by virtue of positions of the phenyl ring and hydride ligand relative to the pair of hydride ligands originating from **5a**. The geometry for **8b** is illustrated in Figure 4.17.

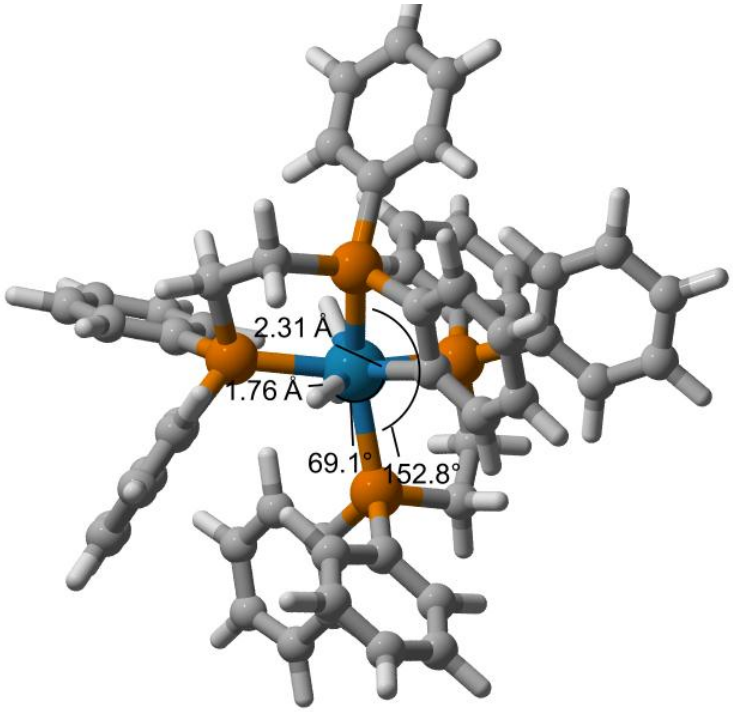

Figure 4.17: Representation of the new geometry of o*rtho*-metallated complex $W(H)_3$(dppe-κ^2P)($Ph_2PCH_2CH_2PPh(C_6H_4)$)-κ^2P) (**8b**)

In the geometry of **8b**, the C-W-H bond plane is perpendicular to that of the ortho-metallated phenyl ring, in contrast to that of **8a** where it is parallel. This geometry was found to be 22.5 kJ mol^{-1} less stable than that of **8a**. **8b** is formed via transition state **5aB'** which is now only 11.3 kJ mol^{-1} above **5a** and is significantly lower than the barrier arising from transition state **5aA'**. Transition state **5aB'** places the *ortho*-carbon on the reacting phenyl ring at a distance of 2.34 Å from the metal (in contrast to the distance of 2.49 Å in **5aA'**), with the *ortho*-hydrogen being closer at 1.82 Å, the motion of the imaginary frequency was for the breaking of the C-H bond. This geometry is shown in Figure 4.18.

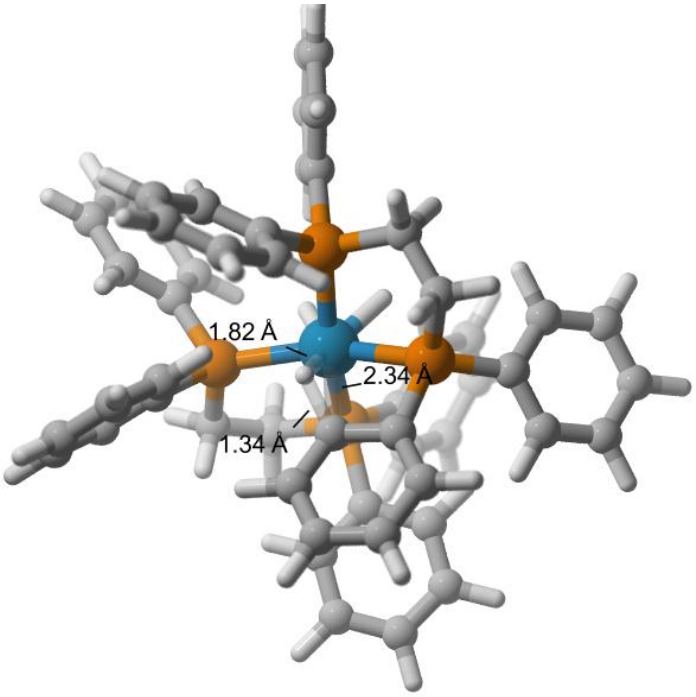

Figure 4.18: Detailed representation of the o*rtho*-metallation transition state $W(H)_2(dppe\text{-}\kappa^2P)_2$ (**5aB'**) arising from a phenyl ring in site B in **5a**

A pathway to interconvert **8b** and **8a** was located which proceeds through transition state **8b'** and is illustrated in Figure 4.19.

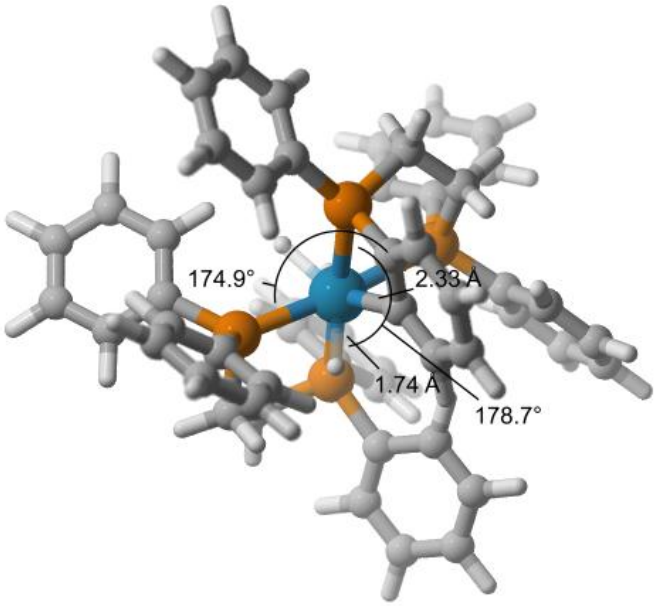

Figure 4.19: Detailed representation of the interconversion transition state $W(H)_3(dppe\text{-}\kappa^2P)(Ph_2PCH_2CH_2PPh(C_6H_4))\text{-}\kappa^2P)$ (**8b'**) between **8a** and **8b**

In transition state **8b'**, the four phosphorus centres lie almost in the same plane, with the P-W-P (*trans*) bond angles opening out to 174.9° and 178.7°. This difference is accompanied by the rotation of the H-W-H plane relative to the H-W-C plane. The initial hydride ligands from **5a** have a separation of 1.85 Å in **8a** and a separation of 1.91 Å in **8b**; this distance reduces to only 1.64 Å in 8b' and so there is no prediction for the formation of a dihydrogen ligand. The barrier created by this transition state is 31.2 kJ mol^{-1} and the pathway is favourable by -22.5 kJ mol^{-1} to form **8a**.

These findings suggest that $W(H)_3(dppe\text{-}\kappa^2P)(Ph_2PCH_2CH_2PPh(C_6H_4))\text{-}\kappa^2P$ can be formed from either initial dihydrogen addition and then by *ortho*-metallation, or by initial *ortho*-metallation and then dihydrogen addition. This second pathway (starting with the *ortho*-metallation step) is more likely, as it starts with an intramolecular reaction rather than the diffusion controlled addition of dihydrogen. This second pathway importantly has low barriers for the rearrangement of **10a** and **10b** to **7a**, which can then react in a barrierless addition of dihydrogen to form **8a**.

The formation of $W(H)_4(dppe\text{-}\kappa^2P)_2$ (**6a**) from $W(H)_3(dppe\text{-}\kappa^2P)(Ph_2PCH_2CH_2PPh(C_6H_4))\text{-}\kappa^2P$ (**8a**) must occur by reversing the *ortho*-metallation step. This reverse reaction can proceed through two pathways; directly through transition state **5aA'** to **5a** which has a barrier of +100.0 kJ mol^{-1}, or by conversion to **8b** through transition state **8b'** and then to **5a** through transition state **5aB'**. This second route is more favourable, with the intermediate **8b** unfavourably formed by 22.5 kJ mol^{-1}, with a barrier of 53.7 kJ mol^{-1} (from transition states **8c'**). Conversion of **5a** to **8b** then has a barrier of 24.2 kJ mol^{-1} (from transition state **5aB'**). These high energy pathways account for the kinetic stability of **8a**.

The reaction product energies and geometries are illustrated in Figure 4.20. The pathway involving **8b** will dominate over the direct route via **5aB'**.

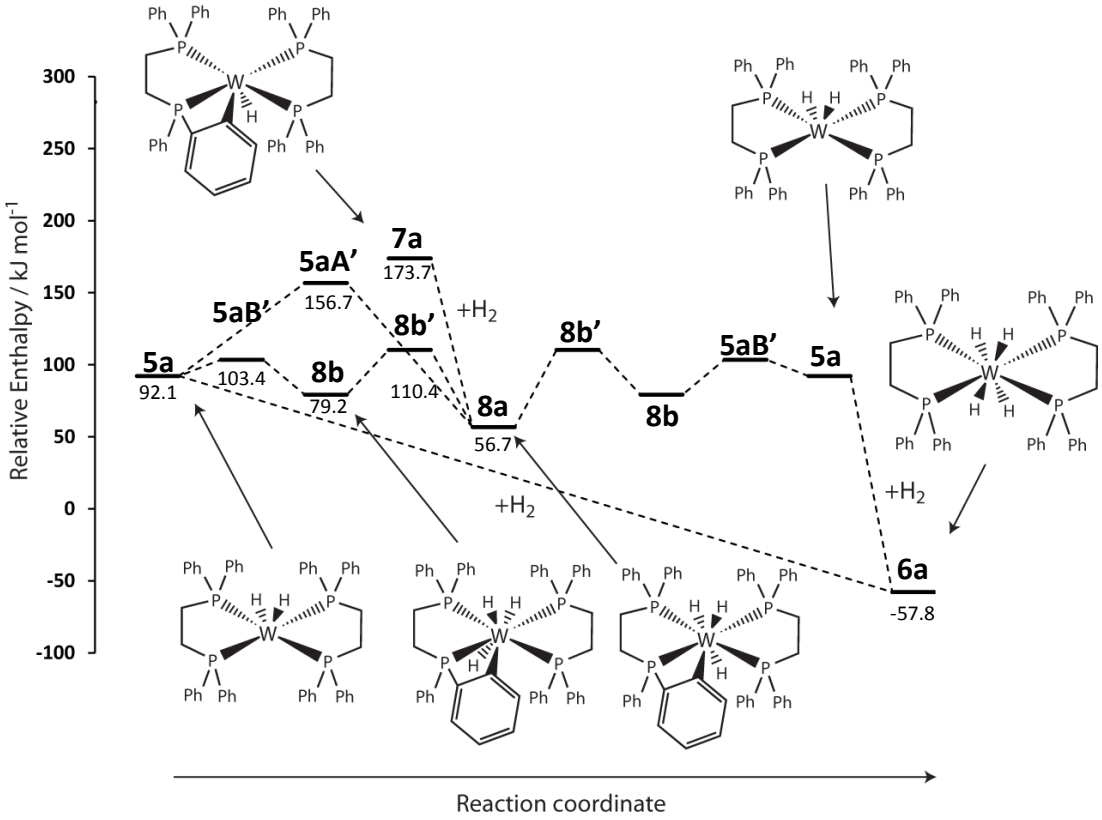

Figure 4.20: Relative enthalpy profile for the formation of **6a**. The observation of intermediate 8a is hereby rationalised. The starting intermediates **7a** and **5a** are formed as per **Figure 4.10**

The activation parameters for the conversion of **8a** to **6a** were determined experimentally to be 79 ± 3 kJ mol^{-1} ($\Delta H^{\ddagger}$) and -54 ± 11 J mol^{-1} K^{-1} ($\Delta S^{\ddagger}$). Two pathways for the conversion of **8a** to **6a** were located, with the lower pathway involving intermediate **8b**. Whilst the experimental enthalpy of activation was higher than the theoretical value of +53.7 kJ mol^{-1} for this pathway (**8a** to TS **8b'**), the free energies of activation match well, with the experimental value being +62.9 kJ mol^{-1} (at 298.15 K) and the theoretical value being +70.7 kJ mol^{-1}. The entropy of activation in this pathway and experiment were negative, with the theoretical value of -56.9 J mol^{-1} K^{-1} matching the experimental value well. The pathway via **5aB'** had a positive value of 21.2 J mol^{-1} K^{-1} in contrast, which indicates this pathway is not involved in the formation of **6a**.

4.3 Effect of explicit solvation of reaction pathways

The solvent used in the experimental investigation was THF which is capable of specific coordination to the tungsten centre. The calculations presented so far have utilised the PCM model to account for implicit solvation; the behaviour of THF explicitly bound to the metal centre was also examined. The explicit coordination of THF to W(dppe-κ^2P)$_2$ as **4b**[1] leads to two potential complexes; W(dppe-κ^2P)$_2$(THF)$_2$ (**12**) and W(dppe-κ^2P)$_2$(THF) (**13**). These geometries and selected structural parameters are illustrated in Figure 4.21.

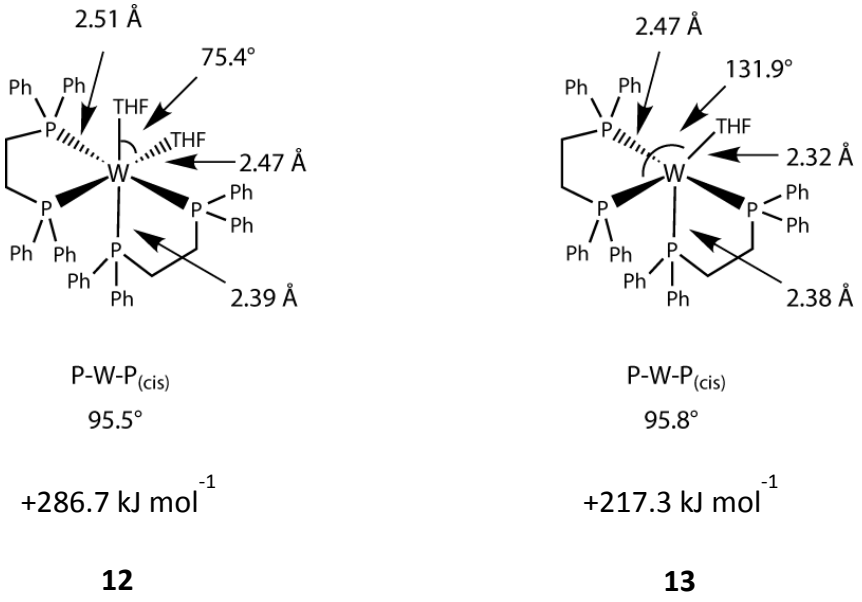

Figure 4.21: Comparison of the singlet and triplet geometries of W(dppe-κ^2P)$_2$(THF)$_2$

The enthalpy difference between **12** and **4b**[1] (at +248.6 kJ mol^{-1}) is +38.1 kJ mol^{-1} and so the formation of W(dppe-κ^2P)$_2$(THF)$_2$ is unfavourable. The enthalpy difference between **13** and **4b**[1] is -31.3 kJ mol^{-1} and so the formation of W(dppe-κ^2P)$_2$(THF) is favourable. Interestingly, the single THF ligand occupies an equatorial position in the trigonal bipyramid that results. This structure is highly distorted as the P-W-P($_{cis}$) bond angle for the two phosphorus centres in the equatorial plane is 95.8° rather than being close to 120°. Additionally, the P-W-P($_{cis}$) bond angle in both **12** and **13** remains close to the 14-electron **4b**[1] (with an angle of 98.8°). It should be noted that significant BSSE corrections were applied for the coordination of THF; this correction for two THF ligands in **12** is 48.3 kJ mol^{-1} and for one THF ligand **13** in is 28.6 kJ mol^{-1}. The potential reaction products formed from W(dppe-

$\kappa^2P)_2$(THF) were modelled to examine the role that **13** plays in the pathways identified previously.

The addition of dihydrogen to **13** results in the formation of $W(H)_2$(dppe-$\kappa^2P)_2$(THF) as **14a**, which has an enthalpy of 150.4 kJ mol^{-1} relative to **1**. This enthalpy is higher (by 22.1 kJ mol^{-1}) than that of the equivalent complex without THF (**5b**) and so THF loss from **14a** is favourable.

For *ortho*-metallation from **13**, the reaction with a phenyl ring on a phosphorus centre in the equatorial plane results in complex W(H)(dppe-κ^2P)($Ph_2PCH_2CH_2PPh(C_6H_4)$-κ^2P)(THF) as **14bA**, which has an enthalpy of 280.5 kJ mol^{-1} relative to **1**. This enthalpy is higher (by 83.1 kJ mol^{-1}) than that of the equivalent complex without THF (**10a**) and so THF loss from **14bA** is again favourable. The *ortho*-metallation reaction with a phenyl ring on a phosphorus centre in an axial position results in a second isomer of W(H)(dppe-κ^2P)($Ph_2PCH_2CH_2PPh(C_6H_4)$-κ^2P)(THF) as **14bB**, which has an enthalpy of 215.5 kJ mol^{-1}. Whilst this reaction is slightly favourable, with the difference in enthalpy between **13** and the **14bB** as -1.8 kJ mol^{-1}, this difference is essentially negligible and the difference too small to conclude if the reaction is favourable. The loss of the bound THF molecule forms **10b** described earlier with an enthalpy change of -24.4 kJ mol^{-1}. If THF plays a role in the reaction pathways, the role is limited and the dominant pathways will be those described in Section 4.2.4. These enthalpies and structures are illustrated in Figure 4.22, where the pathways shown in red represent transition states that have not been located here. This is because the reaction thermodynamics have revealed these pathways have little influence on the main pathways. For these barriers, a similar barrier of 15 kJ mol^{-1} encountered with $W(H)_2$(dppe-$\kappa^2P)_2$ (from transition state **5b'**) is used.

The conversion of **13** to the equivalent complex with a square-planar based W(dppe-$\kappa^2P)_2$ core was also examined. This conversion had a significant barrier of 78.5 kJ mol^{-1} arising from transition state **13'** and resulted in **13a**; this reaction was found to be unfavourable, with an enthalpy change of 49.3 kJ mol^{-1}. It is worth noting that the square-planar geometry of 14-electron W(dppe-$\kappa^2P)_2$ (**4a^1**) was calculated to be 33.6 kJ mol^{-1} less stable than the equivalent butterfly geometry (**4b^1**). This contrasts the trend of the 16-electron complexes as illustrated in Figure 4.10. This indicates that whilst the coordination of THF is calculated

to be favourable to **4b**[1] (forming **13**), the electron donation from oxygen in THF does not truly form a stable 16-electron complex.

It is also worth noting that it is possible for 16-electron complexes $W(H)_2(dppe\text{-}\kappa^2P)_2(THF)$ (**14**) and $W(H)(dppe\text{-}\kappa^2P)(Ph_2PCH_2CH_2PPh(C_6H_4)\text{-}\kappa^2P)(THF)$ (**14bA** and **14bB**) containing the butterfly core to undergo interconversion to the equivalent square-based core equivalent complexes. These pathways have not been explored as the major and barrierless pathway from these complexes is likely to be THF loss rather than the interconversion which would proceed through a barrier.

It is surprising therefore that THF plays no major role in this reaction, even though it has the potential to coordinate and hence stabilise unsaturated reaction intermediates.

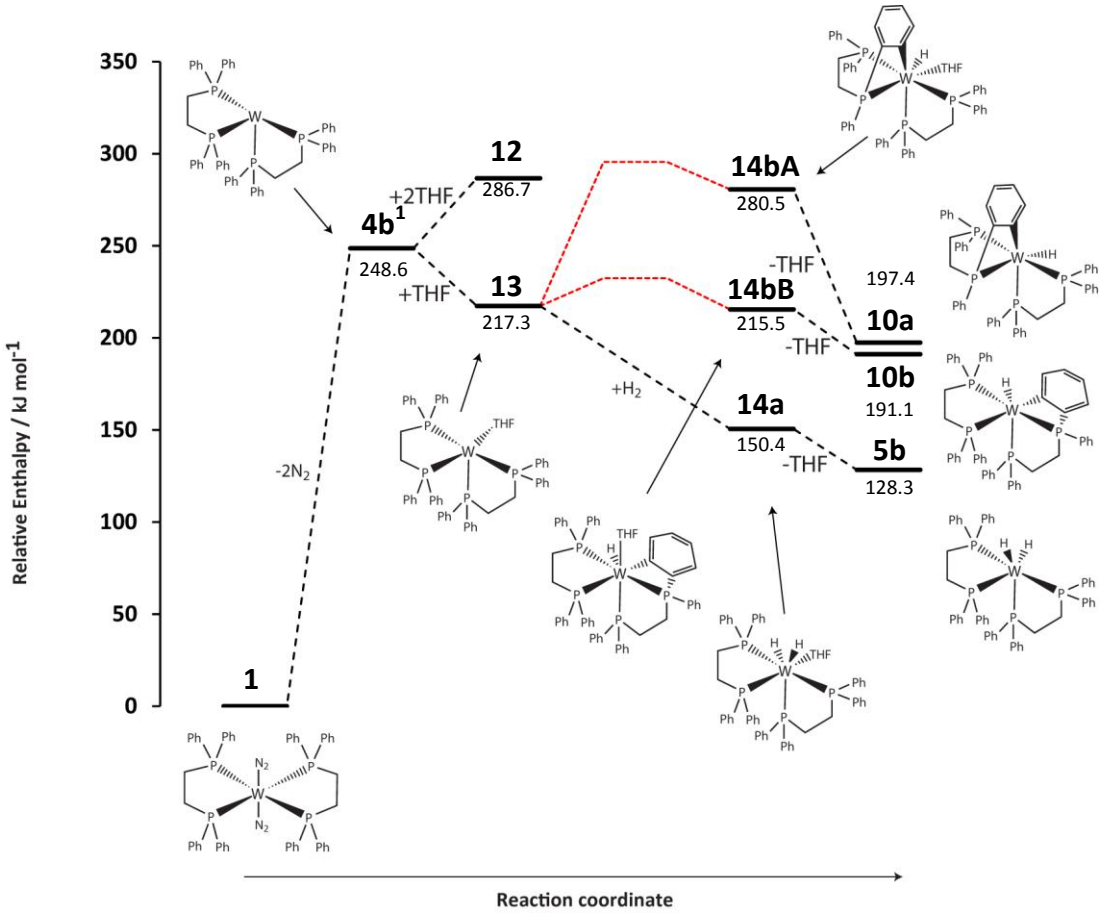

Figure 4.22: Relative enthalpy profile for reactions of **4b**[1] with H_2 to form **6a** and **8a** with explicit THF solvation. Pathways in red represent possible barriers for *ortho*-metallation

4.4 Ortho-metallation reactions with similar complexes

Ortho-metallated W(H)(dppe-κ^2P)($Ph_2PCH_2CH_2PPh(C_6H_4)$-κ^2P) (**7a**) could feasibly undergo a second *ortho*-metallation reaction, which would take place on the opposite side of the metal complex to form $W(H)_2(Ph_2PCH_2CH_2PPh(C_6H_4)$-$\kappa^2P)_2$. The double *ortho*-metallation pathway was found to be unfavourable by +10.2 kJ mol^{-1}. However, the reaction was found to have a barrier of +44.8 kJ mol^{-1}, which means that the formation of $W(H)_2(Ph_2PCH_2CH_2PPh(C_6H_4)$-$\kappa^2P)_2$ is predicted to be unlikely. This is in agreement with the experimental failure to detect this product.

Previous studies with $W(N_2)_2$(dppe-$\kappa^2P)_2$ investigated the effect that saturation of the solution with a reactive gas had on the photolysis products.[235] These reactions involved N_2 and CO. They resulted in the formation of $W(N_2)_2$(dppe-$\kappa^2P)_2$ and $W(CO)_2$(dppe-$\kappa^2P)_2$ respectively. No *ortho*-metallated complexes were detected or detected in these pieces of work.

For the potential *ortho*-metallation reactions from these 16-electron complexes of the type W(L)(dppe-$\kappa^2P)_2$, the square-based W(dppe-$\kappa^2P)_2$ core geometry will be used. This type of geometry was shown to be more stable upon the formation previous 16-electron complexes.

The formation of W(H)(N_2)(dppe-κ^2P)($Ph_2PCH_2CH_2PPh(C_6H_4)$-κ^2P) (**2b**) is unfavourable by +107.7 kJ mol^{-1} relative to $W(N_2)_2$(dppe-$\kappa^2P)_2$ (**1**). In contrast, the addition of CO to W(dppe-$\kappa^2P)_2$ as **4a**[1] and **4b**[1] was also found to be barrierless and favourable and forms W(CO)(dppe-$\kappa^2P)_2$ (**13**). This species is based on the square-planar dppe-κ^2P core, in keeping with the other 16-electron species calculated as more stable. This formation was more favourable relative to **1**, despite it being 16-electron, in keeping with the ligand donor strength of CO compared to N_2. The *ortho*-metallation reaction of W(CO)(dppe-$\kappa^2P)_2$ (**15**) was found to occur through transition state **15'** with a barrier of +72.5 kJ mol^{-1}. This pathway results in W(H)(CO)(dppe)($Ph_2PCH_2CH_2PPh(C_6H_4)$-κ^2P) (**15b**) but is unfavourable by + 69.8 kJ mol^{-1}. It is also +240.9 kJ mol^{-1} relative to $W(CO)_2$(dppe-$\kappa^2P)_2$. The presence of N_2 or CO in solution does not therefore result in the generation of any *ortho*-metallated

complexes, consistent with experiment. These pathways and thermodynamics are illustrated in Figure 4.23; note that all enthalpies shown are relative to $W(N_2)_2(dppe\text{-}\kappa^2P)_2$ (**1**). Selected structural parameters of the transition states for *ortho*-metallation (**2'**, **5aB'** and **15'**) are listed in Table 4.3.

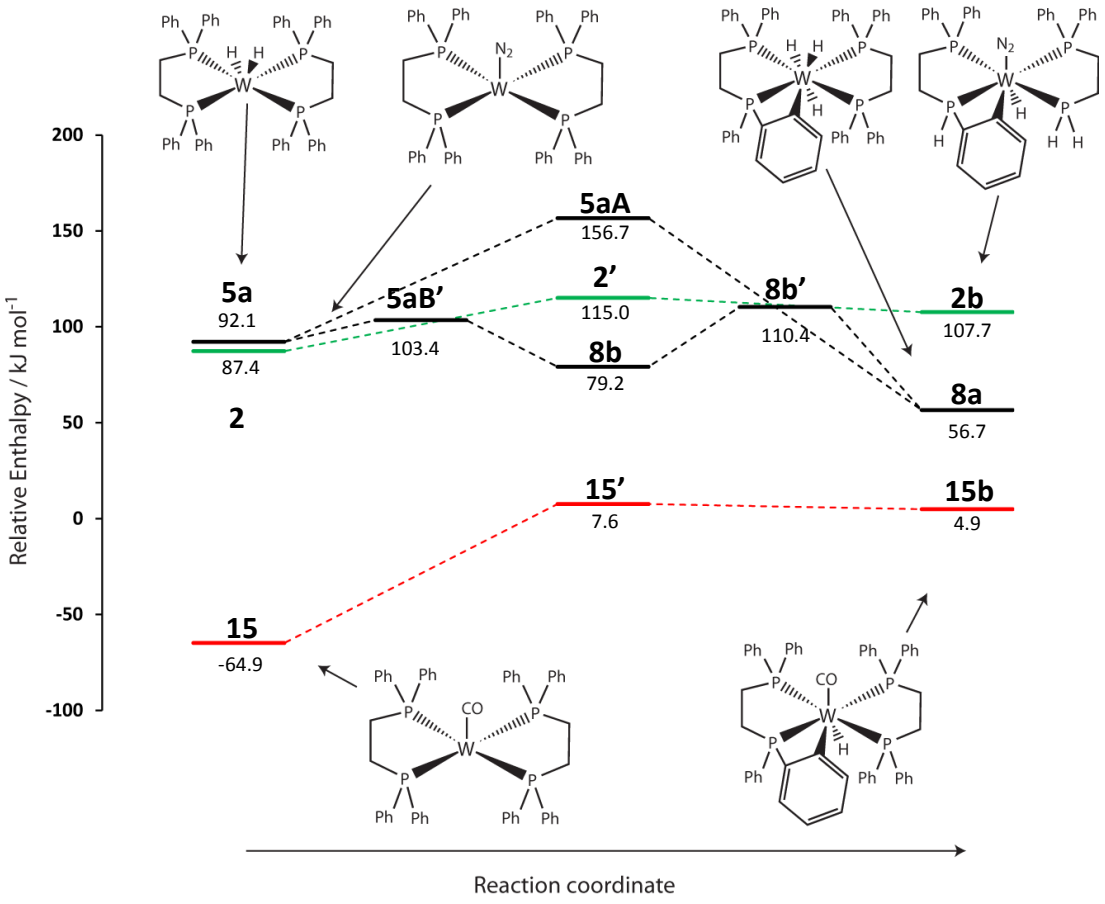

Figure 4.23: Potential energy profiles for the *ortho*-metallation pathways of $W(L)(dppe\text{-}\kappa^2P)_2$ where L = $(H)_2$, N_2 or CO

Table 4.3: Selected structural parameters for the *ortho*-metallation transition states of $W(L)(dppe\text{-}\kappa^2P)_2$ (where L=$(H)_2$, N_2 or CO)

	W-C / Å	W-H / Å	C-H / Å
5aB' (L=$(H)_2$)	2.34	1.82	1.35
2' (L=N_2)	2.29	1.74	1.65
13' (L=CO)	2.34	1.74	1.68

The bond distances listed show that the cleavage of the *ortho*-C-H bond occurs at a similar W-C distance in all three transition states, but the C-H bond length is significantly shorter in **5'** (when L=$(H)_2$). This means that bond cleavage occurs at an earlier stage in the reaction and is consistent with the poorer electron donation of a hydride ligand. Only transition states for the direct formation of **2b** and **15b** were located (**2'** and **13'**) as the formation of intermediates with similar geometries to **8b** are not possible when L=N_2 or CO.

4.5 Formation of $W(H)_6(dppe\text{-}\kappa^2P)(dppe\text{-}\kappa^1P)$

When the photochemical behaviour of $W(H)_3(dppe\text{-}\kappa^2P)(PPh_2CH_2CH_2P(C_6H_4)Ph\text{-}\kappa^2P)$ and $W(H)_4(dppe\text{-}\kappa^2P)_2$ were experimentally investigated, the formation of the hexahydride complex $W(H)_6(dppe\text{-}\kappa^2P)(dppe\text{-}\kappa^2P)$ was observed. This complex can be formed when $W(N_2)_2(dppe\text{-}\kappa^2P)_2$ is the precursor, but at a much lower level. The structures of these complexes are illustrated in Figure 4.24.

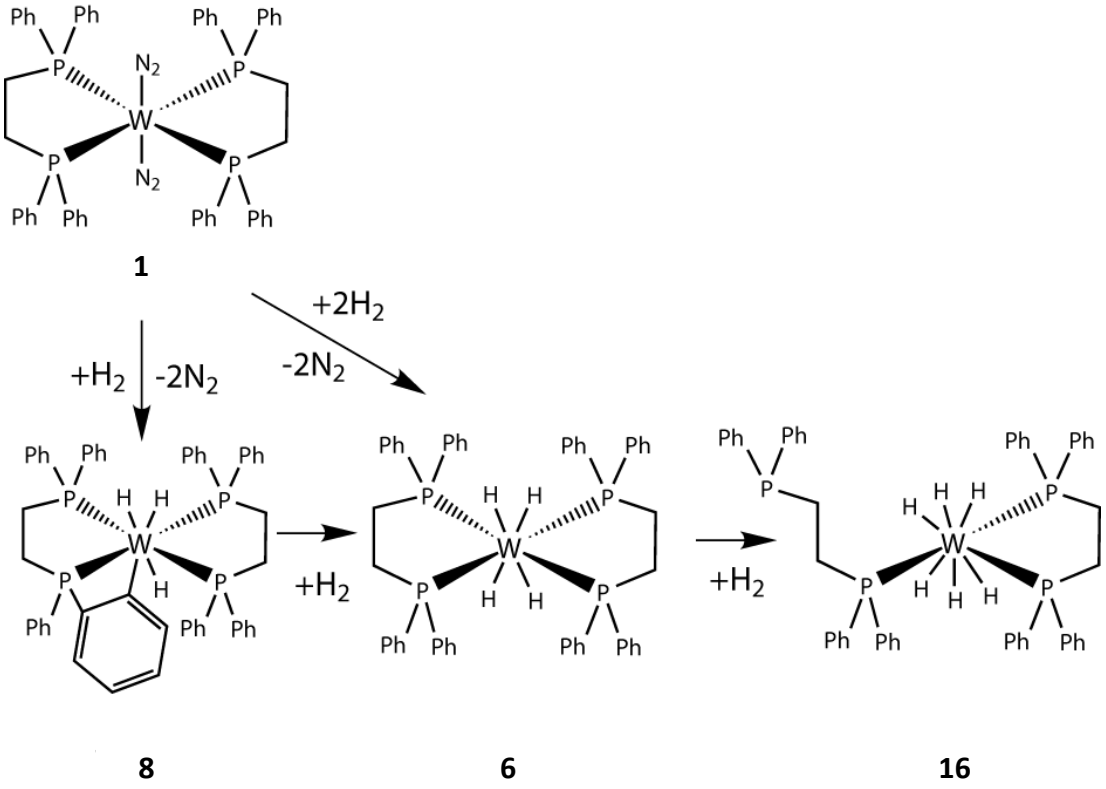

Figure 4.24: Structures of the photoproducts formed from **1**, **6** and **8**

The formation of $W(H)_6(dppe\text{-}\kappa^2P)(dppe\text{-}\kappa^1P)$ was modelled theoretically. The simplest pathway for its formation is via $W(H)_4(dppe\text{-}\kappa^2P)_2$ where the photolysis leads to initial phosphine arm dissociation. This pathway, which corresponds to the formation of $W(H)_4(dppe\text{-}\kappa^2P)(Ph_2PCH_2CH_2PPh_2\text{-}\kappa^1P)$ (**6c**) was found to be unfavourable by +160.3 kJ mol^{-1}. Whilst this barrier for phosphine dissociation is high, it was observed under photolysis; the reverse reaction was observed by heating the solution. The reaction of dihydrogen to **6c** by oxidative addition is favourable with $W(H)_6(dppe\text{-}\kappa^2P)(Ph_2PCH_2CH_2PPh_2\text{-}\kappa^1P)$ (**16**) being -97.3 kJ mol^{-1} relative to **6c** even though it is 69.5 kJ mol^{-1} above **6a**. These thermodynamics are also consistent with the experimental observations; the loss of dihydrogen is unfavourable by +97.3 kJ mol^{-1} (**16** to **6a**) but the overall reaction from **16** to **6a** is favourable by -63.0 kJ mo^{l-1}, which is observed experimentally. These energetics are illustrated in Figure 4.25.

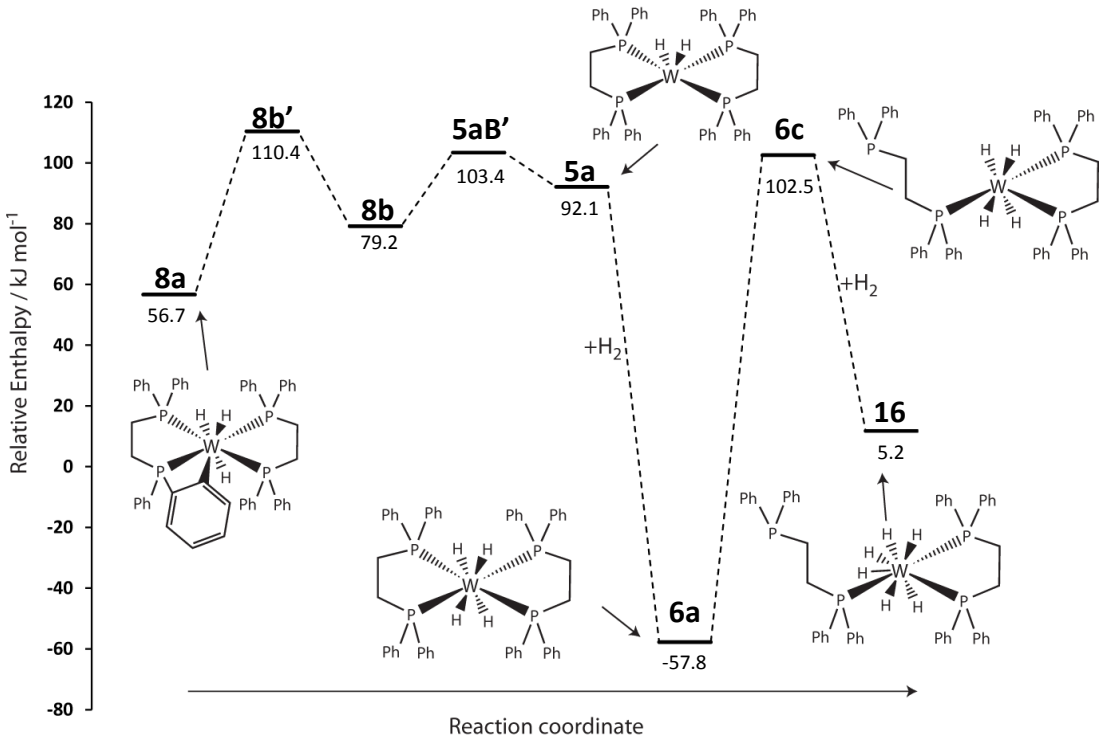

Figure 4.25: Potential energy profile for the conversion of **8a** or **6a** into **16** via phosphine dechelation

Whilst the formation of **16** from **6a** is significantly unfavourable, experimentally it is formed upon the photolysis of **1**, **8a** and **6a**. The photolysis of **6a** in the absence of H_2 prevented the detection of any new products, and the heating of a sample of **16** with *p*-H_2 did not lead to any PHIP being observed. This is consistent with the loss of dihydrogen and coordination of

the free phosphorus centre in dppe-κ^1P leading to **6a**. The ability to form **16** in sufficient amounts to allow characterisation arises from the high barrier for the loss of dihydrogen (97.3 kJ mol^{-1}); this means its lifetime is sufficient for detection. The reaction does ultimately lead to the formation of **6a**, consistent with this being the most stable product calculated for this system.

The structure of $W(H)_6$(dppe-κ^2P)($Ph_2PCH_2CH_2PPh_2$-κ^1P) (**16**) is akin to the well-known dianon of ReH_9^{2-}, whose discovery was described by R. B. King.[246] This dianion was modelled by Schaefer et al.in 2014 with various levels of theory and the geometries obtained compared to experimental data.[247] The structure was in agreement with a faced-tricapped trigonal prism, where 6 hydride ligands form the prism shape, with the remaining three hydride ligands being cap hydrides located in the centre of each face of the prism (when modelled with d_{3h} symmetry). **16** is also analogous to the hexahydride complexes and $WH_6(PMe_2Ph)_3$[248] and $WH_6(PMe_3)_3$.[249] The structure of this latter complex was obtained by Parkin *et al*. in 2014 by low temperature x-ray diffraction.[250] Until this work, two geometries had been proposed; one with D_{3h} symmetry where the hydride ligands form the prism and the PMe_3 groups cap the faces, and a second with C_{2v} symmetry where two PMe_3 ligands are part of the prism shape. The experimental and DFT data undertaken showed that the structure adopted was the C_{2v} geometry with the two PMe_3 ligands forming the prism and the third caps a triangular face. The W-P bond lengths for the two prism ligands were found to be 2.4706(6) Å and the capping ligand had a shorter bond length of 2.4156(8) Å. The P-W-P bond angle for the prism phosphorus centres was found to be 102.49°(2) and the P-W-P bond angle for the capping centre to each prism centre was 128.57(2)°.

A similar geometry is also adopted by $W(H)_6$(dppe-κ^2P)($Ph_2PCH_2CH_2PPh_2$-κ^1P) (**16**) but it is altered due to the chelating nature of the bidentate dppe ligand and the steric bulk of the phosphines. In **16**, the monodentate phosphorus centre occupies a capping position, and both phosphorus centres in dppe-κ^2P occupy an eclipsed position in a triangular face of the prism. The D_{2h} geometry proposed for $WH_6(PMe_3)_3$ would likely place the bidentate dppe ligand at too large a P-W-P angle for coordination (120° instead of the ideal 90° bite angle for dppe). The distortion from the bidentate dppe ligand on **16** is illustrated in Figure 4.26.

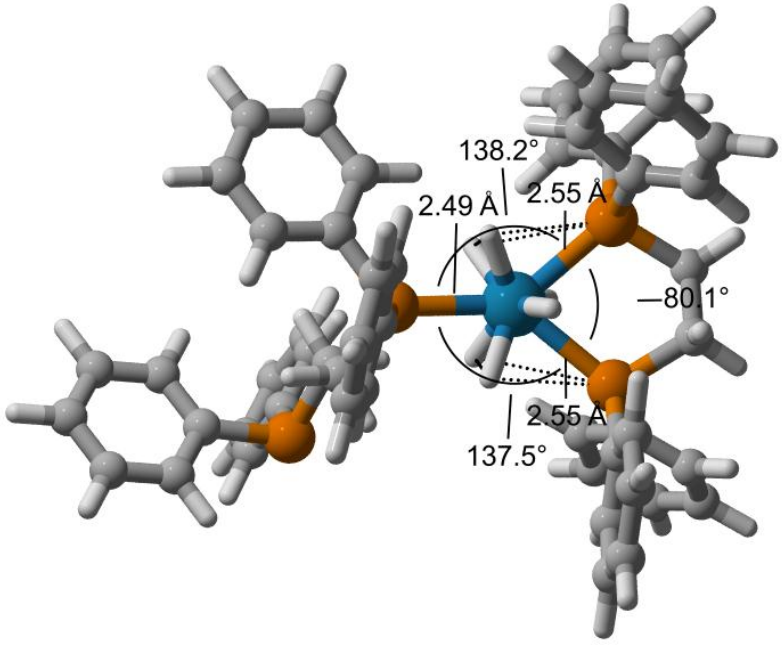

Figure 4.26: Detailed illustration of the tungsten-ligand core in **16**. The trigonal prism faces are indicated by the dotted lines

In **16**, the P-W-P bond angle for the prism phosphorus centres is 80.1° (compared to 102° in $WH_6(PMe_3)_3$); this is imposed by the bite angle of dppe and is almost identical to the angle found for $W(N_2)_2(dppe\text{-}\kappa^2P)_2$ (**1**) shown in Table 4.1. The equivalent angle[247] found in ReH_9^{2-} is around 90° and so it is likely that the angle found in $WH_6(PMe_3)_3$ arises from steric repulsion of the methyl groups; in **16** this repulsion will be supressed by the chelating nature of the dppe ligand. The P-W-P bond angles for these prism phosphorus centres to the capping phosphorus centre are around 138° (compared to 129° in $WH_6(PMe_3)_3$), the difference arising from the different bond angle of the prism phosphorus centres. The W-P bonds are also all longer in **16** than $WH_6(PMe_3)_3$; bond elongation for the capping centre is to 2.49 Å from 2.42 Å, the prism centre bonds are elongated from 2.47 Å to 2.55 Å. The longer bond lengths in **16** are consistent with the increased steric bulk on the phosphine compared to methyl groups in $WH_6(PMe_3)_3$ (PMe_3 and PPh_2Me have similar electronic properties).

Phosphine dissociation from *ortho*-metallated **8a** was calculated to be unfavourable by +147.0 kJ mol^{-1}. **8c** formed in this step adds dihydrogen via a barrierless approach to form $W(H)_5(dppe\text{-}\kappa^1P)(Ph_2PCH_2CH_2PPh(C_6H_4)\text{-}\kappa^2P)$ (**17a**) with a favourable change in enthalpy of

-90.2 kJ mol^{-1}. The subsequent conversion to **16** requires reductive CH bond formation (barrier +67.0 kJ mol^{-1} arising from transition state **17a'**) and the formation of W(H)$_4$(dhpe-κ^1P)(H$_2$PCH$_2$CH$_2$PHPh-κ^2P) (**6c**) which is favourable by 11.1 kJ mol^{-1}. An alternative pathway was located of lower enthalpy, where **17a** converts to the alternative isomer where the ortho-metallated phenyl ring and corresponding hydrogen sit in a plane which is perpendicular to the hydride ligands present from complex **8a**. This is the same type of rearrangement detailed for **5a** to **8b** via **5aB'**, and then to **8a** via **8b'** in Section4.2.2. Here, **17a** forms **17c** which is unfavourable by 12.7 kJ mol^{-1} (via a barrier of 25.1 kJ mol^{-1} arising from transition state **17b'**). This alternative geometry of **17a** can then form **6c** via a barrier of 23.5 kJ mol^{-1} from transition state **17d'** in a process which is favourable by -23.8 kJ mol^{-1}. The addition of dihydrogen to **6c** then finishes the reaction by forming **16**. The alternative CH reductive elimination routes from **8c** prior to dihydrogen addition are illustrated (via transition state **18a'** or **18b'**, **18c** and then **18d'**), together with this lower energy pathway, in Figure 4.27.

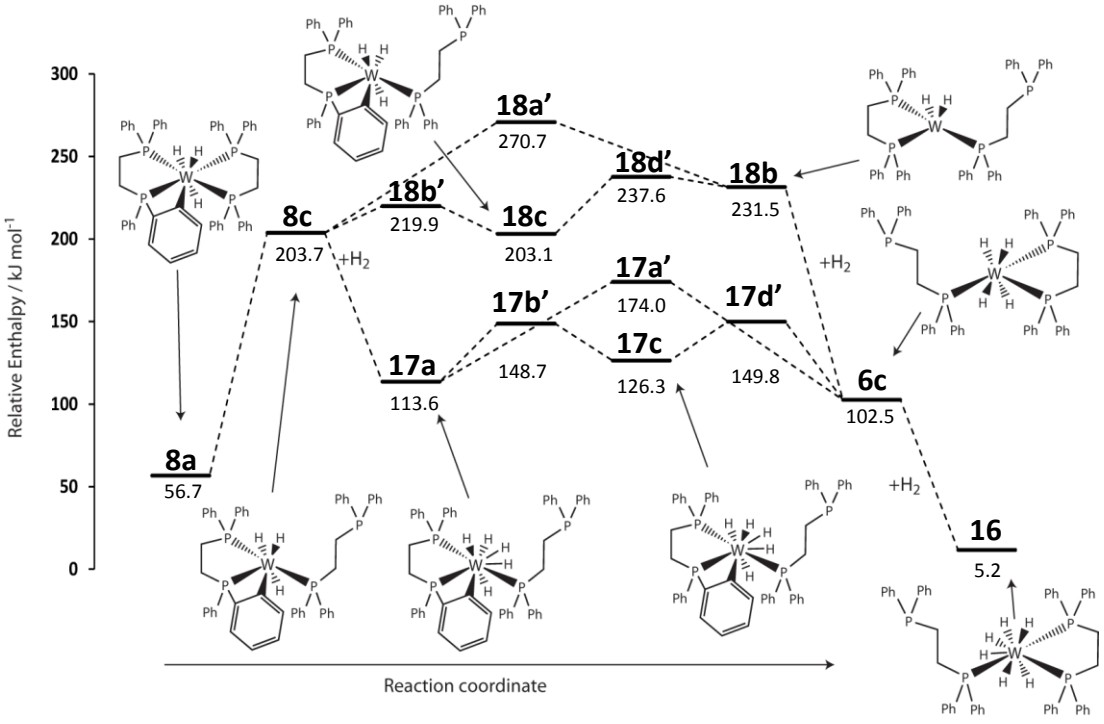

Figure 4.27: Potential energy profile for the formation of **16** via phosphine dechelation from **8**

Based on these results, the lower energy route to **16** is via tetrahydride **6a**. However, this is a photochemical reaction and hence the exact pathway will depend on the quantum yields of **6** and **8** rather than these thermodynamic parameters.

4.6 Discussion of the reactions of $W(N_2)_2(dppe\text{-}\kappa^2P)$ with *p*-H_2

The theoretical investigations into the behaviour of $W(N_2)_2(dppe\text{-}\kappa^2P)_2$ (**1**) with dihydrogen have revealed insights into its conversion to $W(H)_4(dppe\text{-}\kappa^2P)_2$ (**6**). They have also helped rationalise a number of *p*-H_2 based experimental observations.

$W(H)_4(dppe\text{-}\kappa^2P)_2$ (**6**) is predicted to be the most stable species of all those investigated, with the next most stable species the starting complex $W(N_2)_2(dppe\text{-}\kappa^2P)_2$ (**1**). The reactions of **1** have been experimentally shown to proceed through the 14-electon complex $W(dppe\text{-}\kappa^2P)_2$ (**4**) which is calculated to be the lowest energy intermediate in this study in a butterfly geometry (**4b**[1]). This 14-electron complex was modelled in both the singlet and triplet electronic states and in the square-planar and butterfly geometries. In both geometries, the singlet state is the more stable, with the butterfly geometry more stable than the square-planar geometry by -33.6 kJ mol^{-1}. No significant dihydrogen complexes were identified theoretically, in good agreement with the experimental evidence. This is also consistent with the presence of primarily σ-donating phosphine groups in the complex. The inter-conversion of these different geometries was also found to occur via low barriers and so the conversion will be facile.

The *ortho*-metallated complexes were also modelled to form via direct C-H bond activation rather than via the formation of any η^2 complex with the metal centre and a phenyl ring. The barriers for *ortho*-metallation were shown to be low enough to allow the formation of $W(H)_3(dppe\text{-}\kappa^2P)(Ph_2PCH_2CH_2PPh(C_6H_4)\text{-}\kappa^2P)$ (**8a**) to be feasible and a likely route on the pathway from **4b**[1] to form the tetrahydride **6a**.

The most significant observation was that a full model was required to most closely match the experimental data. This approach allowed for the accurate assessment of the steric impact of the dppe ligand. As expected, stable minima were observed for the three products **6a**, **8a** and **16**. A complex reaction pathway was shown to connect them involving various CH and H_2 oxidative addition reactions in conjunction with phosphine loss. The lowest energy pathway via **4b**[1] is shown in Figure 4.7, where products formed can change geometry via pathways shown in Figure 4.10, ending with the pathways shown in Figure

4.20. It features barrierless dihydrogen addition to W(dppe-κ^2P)$_2$ (**4b^1**) and a singlet landscape which accounts for the observation of PHIP. This pathway competes however with the low barrier intramolecular *ortho*-metallation reaction which is not diffusion controlled, unlike that of dihydrogen addition. This pathway accounts for the observation of W(H)$_3$(dppe-κ^2P)(Ph$_2$PCH$_2$CH$_2$PPh(C$_6$H$_4$)-κ^2P) (**8a**), and the pathway determined from this complex to the tetrahydride **6a** is also consistent with the experimental observation of **6**.

The theoretical predictions reveal that W(H)$_4$(dppe-κ^2P)$_2$ (**6a**) is the most stable complex formed from W(N$_2$)$_2$(dppe-κ^2P)$_2$ (**1**) after reaction with dihydrogen; the barriers from this complex for the loss of dihydrogen or the phosphine dechelation are 149.9 kJ mol^{-1} and 160.3 kJ mol^{-1} respectively. The barrier for dihydrogen loss from W(H)$_6$(dppe-κ^1P) (dppe-κ^2P) (**16**) is also sizable, at 97.3 kJ mol^{-1} and is consistent with the requirement of heating needed to convert W(H)$_6$(dppe-κ^1P)(dppe-κ^2P) back to W(H)$_4$(dppe-κ^2P)$_2$ (**6a**) after being formed through photolysis. The two routes for reaction from W(H)$_3$(dppe-κ^2P)(Ph$_2$PCH$_2$CH$_2$PPh(C$_6$H$_4$)-κ^2P) (**8a**) are lower in energy however, with enthalpy barriers for the loss of dihydrogen and CH reductive elimination of 117.0 and 46.7 kJ mol^{-1} respectively. It is this low barrier for CH reductive elimination which allows reactions from W(H)$_3$(dppe-κ^2P)(Ph$_2$PCH$_2$CH$_2$PPh(C$_6$H$_4$)-κ^2P) (**8a)** and hence why its observation was not reported in previous experiments without the signal enhancement provided by PHIP.

The geometry of hexahydride W(H)$_6$(dppe-κ^1P) (dppe-κ^2P) (**16**) was also found to be similar to related species of ReH_9^{2-} and WH$_6$(PMe$_3$)$_3$ forming a tricapped trigonal prism. The chelating dppe ligand distorted the geometry away from both of these known forms of this geometry, with the steric bulk of the phosphines in dppe also lengthening the tungsten-phosphorus bonds compared to WH$_6$(PMe$_3$)$_3$.

The calculations also revealed that the *ortho*-metallation reactions are unfavourable when different ligands are coordinated to the tungsten centre. When CO or N$_2$ ligands are coordinated, the barriers for *ortho*-metallation are low enough to allow the reaction to proceed, but importantly the *ortho*-metallated complexes are unfavourable compared to the starting complex where the ligand is *trans* to a vacant site (which can potentially be solvated to some extent). This finding is also consistent with the experimental data for such complexes, where no *ortho*-metallated complex was observed.

No evidence was found in the experimental data for any fluxional behaviour of the detected complexes. This is consistent with the presence of two bidentate ligands which require positions that are *cis* in the complex. These bidentate ligands prefer to occupy positions in the complex *trans* to each other which means that transition states involving the reformation and rotation of an η^2-H_2 unit do not exist. Additionally, the presence of complexes which adopt dodecahedron geometries limits the available free space for rearrangements.

The reaction of $W(N_2)_2$(dppe-κ^2P) was ultimately predicted to be different with N_2 or CO compared to that of H_2, where the presence of these two ligands in the complex results in the *ortho*-metallation pathway becoming unfavourable. The theoretical predictions therefore mean that no *ortho*-metallated products would be formed for CO or N_2, a hypothesis that has been experimentally tested. However, a mixture of these ligands with *p*-H_2 could be required to provide the enhancements at low temperature to enable the detection of any such complexes.

Chapter 5: Conclusion

The work described in this thesis, has focussed on theoretical investigations into reactions that involve hydrogen with transition metal complexes. The use of *para*-hydrogen in these reactions has allowed polarised signals NMR to be obtained, which give can be interpreted to give detailed mechanistic information that helps inform the theoretical work. Conversely, the theoretical models have yielded results which have then been used to suggest new experimental investigations. The various aspects of the work reported in this thesis have a common theme, where side reactions involving different isomers of metal complexes are carefully considered, along with the reactions that underpin them. The order of these reactions can also affect the ultimate pathway followed. The complex geometries of the products complicate the reaction landscape and can lead to the further formation of different products. The bidentate ligand dpae, and model ligand dhae, limit this freedom with their coordination requiring a *cis* arrangement. In trigonal bipyramids, there is an additional requirement for this ligand to occupy an axial and equatorial position. The allowed bite angle of this ligand is approximately 85°; the occupation of two equatorial sites would hence either strain the ligand or create an unfavourable geometry by deviation from the 120° idealised angle. The chelate effect also limits the further reactions that are possible by limiting the creation of a vacant coordination site from de-chelation. This significantly alters the reactivity of $Ru(CO)_3(dppe)$ when compared to that of the related monodentate complex $Ru(CO)_3(PMe_2Ph)_2$, along with the complexes based around dpae described and with their monodentate counterparts. Additionally, the steric bulk of the phenyl rings in dpae are directed away from the metal centre, to reduce the interaction with the other ligands in the equatorial plane. This steric bulk is noted to be important in many reactions, whether controlling reactivity or controlling the stereochemistry of a product. The direct evidence seen for dppe participation in the reactions of $W(N_2)_2(dppe\text{-}\kappa^2P)_2$ means that the full model may need to be utilised to reliably map the experimental reactions in such cases.

5.1 Summary of work presented in this thesis

5.1.1 Reactions of *p*-H_2 and substrates with the complexes $Ru(CO)_3$(dpae) and $Ru(CO)_2$(dpae)(PPh_3)

The reactions of the two complexes, $Ru(CO)_3$(dpae) and $Ru(CO)_2$(dpae)(PPh_3), were investigated in detail with hydrogen and solvent, with initiation by thermal or photochemical methods.

The 16-electron intermediates identified were more stable as electronic singlets, consistent with the observation of PHIP when studied with *p*-H_2. In contrast, the 14-electron intermediates, Ru(CO)(dhae) and Ru(dhae)(PH_3) of the simple model, were found to be slightly more stable as electronic triplets. The difference between the singlet and triplet states was found to be low, however, at *ca*. 20 kJ mol^{-1}. The 14-electron intermediates were calculated to only be accessible via photolysis and so is it possible that either singlet or triplet states could arise. The requirement for a spin-flip transition to form the triplet states could reduce their propensity of formation.

The use of the full model for Ru(CO)(dpae), found that the singlet state had the same stability as the lowest energy triplet state, and was hence more stable than the second identified triplet state. For the potential 14-electron species Ru(dhae)(PH_3), the singlet state was calculated to be the least stable, relative to the two triplet states. However, utilising the full model allowed an interaction of a phenyl ring in the PPh_3 group to provide a stabilisation, resulting in this singlet state becoming the most stable intermediate by over 20 kJ mol^{-1}. The observation of PHIP in the products confirms that singlet states are involved in the detected pathway. They also revealed a need for the full model.

The difference in reactivity of $Ru(CO)_2$(dpae)(PPh_3) to $Ru(CO)_3$(dpae) could be assigned to the strength of the metal-carbonyl bond relative to that of the metal phosphine bond. Thermal initiation is likely to liberate free phosphine, creating the 16-electron intermediate $Ru(CO)_2$(dpae) in a lower energy pathway than for CO loss from $Ru(CO)_3$(dpae). The loss of CO from $Ru(CO)_2$(dpae)(PPh_3) was calculated here to be inaccessible with thermal initiation, but photochemical initiation could allow its formation. The dominance of $Ru(H)_2$(CO)(dpae)(PPh_3), as isomer **A7a**, with photochemical initiation was validated with

the models here, its formation will dominate from the addition of dihydrogen across the more favoured CO-Ru-dpae axis in 16-electron $Ru(CO)(dpae)(PPh_3)$.

Different geometries of the 16-electron intermediate $Ru(CO)_2(dpae)$ and $Ru(CO)(dpae)(PPh_3)$ were identified here, in keeping with the work carried out into the phosphine analogues. These different geometries were calculated to have different stabilities, consistent with the ability of the π-acceptors to stabilise the metal centre by interaction with the z^2 and xy orbitals. The use of the simple model replacing the phenyl rings in these complexes by hydrogen allows the identification of low barriers which would allow the near spontaneous conversion of the less stable geometries to the more stable ones, thus accounting for the experimental products observed.

The starting geometries of $Ru(CO)_3(dpae)$ and $Ru(CO)_2(dpae)(PPh_3)$ (when modelled with the phenyl ring approximation) were found to exhibit fluxional behaviour. These rearrangements were calculated to have low barriers, and so are consistent with the experimental evidence. For $Ru(CO)_3(dpae)(PPh_3)$, only one ^{13}C signal for the CO ligands was observed, indicating rapid exchange. For $Ru(CO)_2(dpae)(PPh_3)$, the experimental evidence indicated the preference for a geometry with the phosphine occupying the axial position of the trigonal bipyramid. This preference was not reflected in the simple model which predicted a preference for the occupation of an equatorial site. The full model did predict this preference, with the difference identified to arise from the difference in π-acceptor properties of PH_3 compared to PPh_3. The low barriers predicted for rearrangement could increase with the use of the full model; the difference in stability of the two geometries also accounts for the experimental preference. The free energy difference of 7.8 kJ mol^{-1} obtained with the full model creates a ratio of the two isomers of 19:1 (at 298 K) with the phosphine in the axial position being dominant.

The dihydride complexes of $Ru(H)_2(CO)_2(dhae)$ and $Ru(H)_2(CO)(dhae)(PH_3)$ were determined to undergo fluxional behaviour. The barriers for these complexes were calculated to be significant, all above 80 kJ mol^{-1}. Several rearrangement pathways were identified, with the trigonal twist and pseudorotation being the most likely. These pathways all involved a change in position of the hydride ligands, consistent with the presence of a bidentate dhae ligand. The use of the simple model predicted both complexes to be fluxional, whereas the

experimental evidence only found $Ru(H)_2(CO)_2$(dpae) to be fluxional, with $Ru(H)_2(CO)$(dpae)(PPh_3) exhibiting reductive elimination of H_2. The modelling of the most feasible transition states identified with the full model, allowed thermodynamic values for the process to be obtained which were more consistent with the experimental observations. The barriers for $Ru(H)_2(CO)_2$(dpae) rose in enthalpy terms, with a more substantial rise in free energy terms. For $Ru(H)_2(CO)$(dpae)(PPh_3), both terms rose substantially, with the free energy terms nearing that calculated for the reductive elimination of H_2. A significant discrepancy between the experimental and calculated values was encountered; the entropy term was predicted here to be negative, indicative of a reduction in the degrees of freedom in the transition state, whereas the experimental term was positive. This means that the pathways for rearrangement may indeed be more complicated than modelled here or in previous theoretical work on these forms of ruthenium complex, or that solvation changes are dominant.

The difference in the reactions and stability of the complexes here were compared to the equivalent complexes utilising dppe rather than dpae. The simple model also predicts the formation of $Ru(H)_2(CO)_2$(dppe) to be unfavourable in keeping with $Ru(H)_2(CO)_2$(dhae) modelled here. This phosphine complex allows unambiguous experimental assignment from the phosphorus-hydride couplings and so its formation is known. This means that the models used in this work may not correctly predict the thermodynamic values of reaction, or the experimental conditions that allow the formation of these dihydride complexes to occur. The change in atom from phosphorus to arsenic in the modelled complexes of the type $Ru(H)_2(CO)_2(LMe_2Ph)_2$ (where L = P or As) found the dominant isomer to indeed change, as observed experimentally. The simple model did not predict the correct isomer distribution, whereas the full model was more consistent.

The theoretical investigations into the behaviour of the complexes of $Ru(CO)_3$(dpae) and $Ru(CO)_2$(dpae)(PPh_3) found that the approximation of the simple mode (replacing the phenyl rings in the ligands) had a role in determining the initial reaction. When the phosphine, PPh_3, is retained in the complex, the simple model yields geometry stabilities and reaction thermodynamic values that are inconsistent with experiment. These values and stabilities improve with the use of the full model. The values and stabilities obtained for the various pathways for the reactions of the complexes following the loss of the

phosphine group, are more consistent with experiment with the simple model. This can be attributed to the chelating nature of the dhae ligand, which limits possible geometries accessible. The orientation of the phenyl rings in dpae away from the metal centre, and more importantly the equatorial plane in trigonal bipyramids is likely to limit the impact of this approximation in dhae. It is fully noted that this approximation will change values calculated for reactions of the complexes presented here, and that care has been taken to consider this when discussing key points.

5.1.1.1 Catalytic reactions with diphenylacetylene

The two complexes $Ru(CO)_3$(dpae) and $Ru(CO)_2$(dpae)(PPh_3) were found experimentally to hydrogenate diphenylacetylene to *cis*- and *trans*-stilbene, 1,2-diphenylethane and the dimer 1,2,3,4-tetraphenylbutadine. Additional assignments were made for the postulated reaction intermediates which yielded signals enhanced by the use of *para*-hydrogen in an experimental study. The theoretical mapping of these reactions was found to be complex and interconversion between the identified pathways predicted to be possible.

The simple model approximation in Chapter 2 to had an impact when compared to that of the full model utilising the dpae ligand. This impact was more exaggerated when the phosphine PPh_3 was approximated to PH_3, and is discussed in detail. The internal rearrangements and transfers of the hydride migration reactions will be affected by the simple model approximation to dhae, but can be used to examine possible pathways. The pathways identified in Chapter 3 primarily involved the loss of the phosphine group from the complex and so this failure of the simple model is reduced. It is fully noted that certain conformations of diphenylacetylene, and *cis*- and *trans*-stilbene will be possible in the work presented here that are not possible with the full system. This inadequacy has been limited by the careful choice of hydride undergoing transfer, along with the alignment of the organic ligands. It is likely that certain key barriers and reactions will change with the utilisation of the full model. The verification of the formation of *trans*-stilbene in Cycle 2 with the full model showed that for this geometry, the inclusion of the phenyl rings does not prevent this reactions pathway. It is also noted that a significant number of reactions with diphenylacetylene occur at the face of the metal centre which is opposite to that of the dhae/dpae ligand, thereby limiting the impact of the approximation. If a ligand such as BINAP were used experimentally, it is likely that the theoretical results would fail to

corroborate any observations without the use of the full model including the bulky phosphine and napthyl groups in this ligand. The side reactions of dppe in Chapter 4 also exemplify this interaction of the ligand with the metal centre, where dppe becomes more than an innocent spectator ligand.

Three catalytic cycles were identified in the work; two cycles were formed by loss of two ligands and subsequent coordination of dihydrogen via oxidative addition and diphenylacetylene ligands (Cycles 1 and 2 involving **11a** and **11b** respectively). The third cycle was formed by the de-chelation of one end of the dhae ligand in $Ru(H)_2(CO)_2$(dhae) and subsequent reaction with diphenylacetylene (Cycle 3 involving **12a**). This cycle, along with that formed by the reaction of diphenylacetylene with $Ru(CO)_2$(dhae) prior to the reaction with dihydrogen (Cycle 2, **11b**) were identified as likely to involve minor pathways. The most likely catalytic cycle identified was Cycle 1, starting with **11a**, formed by the loss of CO from $Ru(H)_2(CO)_2$(dhae) and subsequent reaction with diphenylacetylene. Interestingly, the second hydride transfer to diphenylacetylene leads to rearrangement of the complex and likely crossover of the geometry to subsequently form Cycle 2 upon dissociation of *cis*-stilbene.

The complex used as the precursor and method of initiation was determined to be important in the determination of possible pathways. Thermal initiation with $Ru(CO)_3$(dhae) is likely to primarily involve the loss of CO from $Ru(H)_2(CO)_2$(dhae) and hydrogenate through Cycle 1. As the temperatures used in the reaction will be high, the lifetime of intermediates formed will be reduced, so limiting the possible dimerisation. The use of photochemical initiation can lead to the formation of reactive 14-electron Ru(CO)(dpae), which can react with dihydrogen and diphenylacetylene in different ways; the formation of this high energy 14-electon species can ultimately then allow access to both Cycles 1 and 2, depending upon the sequence of additions of CO, diphenylacetylene and CO. Thermal initiation with $Ru(CO)_2$(dhae)(PH_3) was determined to give rise to the same hydrogenation cycles as for thermal initiation with $Ru(CO)_3$(dpae), identified as Cycles 1 and 2. Photochemical initiation with this complex was experimentally determined not lead to enhanced catalysis. The differences observed with $Ru(CO)_2$(dpae)(PPh_3) were likely to arise from the lower energy requirements to initiate the loss of the phosphine group and so the increased lifetimes of intermediates in the cycles.

The formation of **12b** and subsequent catalysis through Cycle 3 was calculated here to be possible, but as a minor pathway; it significantly depends upon the coordination of diphenylacetylene to the complex, before re-coordination of the free end of dhae can occur, which is preferentially favoured by the chelate effect. If **12b** is successfully formed, the likely catalysis is limited to the formation of *cis*-stilbene; the creation of a vacant site on the metal centre is most likely to allow the recoordination of the dhae ligand. Once this is recoordination has occurred, the stable complex $Ru(CO)_2$(dhae)(*cis*-stilbene) is likely to result, for which the dominant pathway is then the dissociation of *cis*-stilbene.

The hydride transfer reactions in the three cycles were all predicted to allow the catalytic hydrogenation of diphenylacetylene to occur. The lowest barrier identified in this work was in Cycle 2, where a significant stabilisation from the metal allowed a barrier of around 16 kJ mol^{-1} to exist. This transition state leads to the formation of *trans*-stilbene. This geometry was also modelled to be possible and likely when the full model was utilised. This provides a possible pathway for the formation of *trans*-stilbene, in keeping with its detection in both NMR and via CG-MS. The barriers predicted here for the hydrogenation of *cis*-and *trans*-stilbene were notably higher than for diphenylacetylene. This is in keeping with the reduced electron density on the metal from donation from the organic species, and the steric demands placed on this ligand to be able to coordinate. Diphenylacetylene can coordinate to the metal relatively easily, but upon hydrogenation to *cis*-stilbene, this becomes more demanding, arising from the geometry of *cis*-stilbene. The coordination of *trans*-stilbene was calculated to be more favourable, with its hydrogenation calculated here to occur via slightly lower barriers than with *cis*-stilbene.

The formation of an agostic interaction with the β-hydrogen of the η^1-CHPh-$CPhH_2$ group to the metal centre was shown to hinder further hydride transfer in Cycle 1; this interaction prevents the remaining hydride ligand moving to the required *cis* position for transfer. This agostic interaction was verified via the AIM method, which identified a Critical Bonding Point between this hydrogen and the metal centre, along with a Ring Critical Point inside the resulting 5-membered ring. A rearrangement of the ligands, or the approach of another ligand was required to allow the final transfer to form 1,2-diphenyethane. These final barriers possibly account for the additional pathways that lead to the experimentally

observed complexes and species. This interaction was also seen in for Cycle 2, and while more favourable, there were smaller barriers for the further reactions.

The formation of *trans*-stilbene along with *cis*-stilbene was validated, with pathways in the two more likely cycles (Cycles 1 and 2) accounting for this isomerisation. The hydrogenation of *cis*-and *trans*-stilbene in Cycle 2 was found to share a common isomerisation transition state; this is likely to convert *cis*-stilbene to *trans*-stilbene due to the greater stability of *trans*-stilbene versus *cis*-stilbene. This difference is also mirrored when coordinated to the metal complex investigated here. The proposed complex $Ru(CO)_2$(dpae)(*trans*-stilbene) was additionally determined to be most likely to form through Cycle 2, with the lowest barriers identified for its formation.

The formation of 1,2,3,4-tetraphenylbutadiene was predicted to be possible through two key pathways; these started either in Cycle 2, from the addition of diphenylacetylene to Ru(H)(CO)(dhae)(η^1-CPh=CHPh), or to addition of diphenylacetylene to Ru(CO)(dhae)(η^2-diphenylacetylene) formed from substrate addition to 14-electron Ru(CO)(dhae). For the reaction and subsequent dimerisation pathway from Cycle 2, alternative pathways were identified, with the coordination of CO resulting in dimerisation at **27b**, consistent with the experimentally identified complex. If the dimer was formed from a ruthenium complex containing 5 ligands, the subsequent dimer formation led to the coordination of both alkene bonds of 1,2,3,4-tetraphenylbutadiene, to co-ordinately saturate the metal. If coordination of CO occurred prior to this dimerisation, only one alkene bond was coordinated. The addition of CO is possible to displace one alkene interaction, but this will occur through a barrier. The experimentally proposed complex of $Ru(CO)_2$(dpae)(1,2,3,4-tetraphenylbutadiene) was determined to lie as a minimum on the potential energy profile, consistent with experimental observation.

The experimentally proposed complexes described were also found to be stable complexes in the theoretical calculations, with reactions to and from these involving significant barriers. This provides additional theoretical evidence to validate their formation. Further experimental work could also be carried out to provide additional evidence. This could involve the use of labelled CO or dpae ligands. The use of the mixed ligand arphos (1-

diphenylphosphino-2-diphenylarsinoethane) could also allow catalysis to be probed with the presence of phosphorus-hydride coupling which would potentially aid characterisation.

5.1.2 Reaction of hydrogen with $W(N_2)_2(dppe)_2$

The tungsten complex $W(N_2)_2(dppe)_2$ was shown via the use of *p*-H_2 to undergo an unusual *ortho*-metallation reaction upon the loss of the dinitrogen ligands. This reaction was shown to be reversible, with the tetrahydride complex $W(H)_4(dppe\text{-}\kappa^2P)_2$ ultimately found to be formed. The use of theoretical models indicates that the complex formed by the *ortho*-metallation reaction was stable and that its formation was via a pathway with no barrier from 14-electron $W(dppe\text{-}\kappa^2P)_2$. This 14-electron intermediate was modelled to be most stable as a butterfly type geometry, rather than a square-planar geometry. Upon any reaction to make the complex 16-electron, the $W(dppe\text{-}\kappa^2P)_2$ core was found be more stable in a square planar arrangement. Low barriers were determined from this geometry change, with subsequent reactions retaining this ligand arrangement.

The *ortho*-metallation reaction from 16-electron $W(H)_2(dppe\text{-}\kappa^2P)_2$ showed two feasible pathways arising from creation of two different phenyl groups imposed by the coordination of dihydrogen. One pathway had a higher barrier than the other, with the lower barrier requiring a low enthalpy rearrangement of the resulting complex to form the observed product $W(H)_3(dppe\text{-}\kappa^2P)(PPh(C_6H_4CH_2CH_2Ph_2P)\text{-}\kappa^2P)$. The *ortho*-metallation reaction also occurs as an intramolecular reaction and so is more likely to occur than the reaction with a separate molecule of dihydrogen. However, the tetrahydride complex $W(H)_4(dppe\text{-}\kappa^2P)_2$ was shown to be more stable than the *ortho*-metallated complex $W(H)_3(dppe\text{-}\kappa^2P)(PPh(C_6H_4CH_2CH_2Ph_2P)\text{-}\kappa^2P)$, in agreement with experimental evidence. Importantly, this *ortho*-metallated complex had not been previously observed and it was through the use of *p*-H_2 that allowed its detection. The related reactions of $W(N_2)_2(dppe)_2$ with CO or N_2 had also not been previously observed; theoretical calculation revealed that the *ortho*-metallated reactions with these ligands were actually unfavourable.

Interestingly, this investigation also revealed that the use of a simplified model where all of the phenyl rings were replaced by hydrogen atoms would not have allowed this unexpected set of reactions to be modelled correctly. The singlet/triplet energies of the 14-electron

intermediate W(dppe-κ^2P)$_2$ were also found to be different with the full ligand model compared to the simpler model system employed in the original work.

The coordinating nature of the THF solvent was shown to have an effect of stabilising the reactive intermediates, but its interaction did not ultimately change the identified pathways of reaction, consistent with experimental evidence. This arose from the favourable dissociation of the explicit solvent molecule upon reaction of the 14-electron intermediate W(dppe-κ^2P)$_2$(THF) when the complex undergoes reactions to become 16-electron. The coordination of two solvent molecules was calculated here to be less stable than the 14-electron intermediate with no THF coordination.

The formation of the hexahydride complex W(H)$_6$(dppe-κ^1P)(dppe-κ^2P) was calculated here to form unfavourably, consistent with the lack of detection in previous work. Here it was formed photochemically, with the reverse reaction to form W(H)$_4$(dppe-κ^2P)$_2$ occurring with heating. The geometry of this hexahydride was determined to be a tricapped trigonal prism, similar to that of the known species ReH_9^{2-} and $WH_6(PMe_3)_3$. With the structure modelled in this work, a distortion was identified with the geometry arising from the steric bulk of the dppe ligands. This strain in the geometry could explain the failure to form this hexahydride complex without photochemical means.

5.2 Future work

An outer sphere pathway for the hydrogenation of quinoline was reported in 2011 by Eisenstein *et al.*[251] In this work, the approach of quinolone and reaction with a coordinated dihydrogen ligand on the iridium centre was identified. This utilised a complex of the type $[Ir(cod)(NHC)(PPh_3)]^+$ (NHC = 1,3-Benzimidazolylidene, cod = cyclooctadiene). This complex was able to hydrogenate quinolones in mild conditions, with some reactions possible at 298 K with 1 atm. of H_2. This work is relevant to the investigation using the SABRE catalyst precursor [IrCl(IMes)(cod)] (IMes = 1,3-bis(2,4,6-trimethylphenyl)imidazol-2-ylidene) with quinazoline (benzo-1,3-diazine), where hydrogenation to form 3,4-dihydroiquinazoline was determined in similar mild conditions. Initial calculations have found this hydrogenation via an inner-sphere mechanism to be unfavourable; the hydrogenation via an outer-sphere mechanism using the model carbene 1,3-Dimethylimidazol-2-ylidene has been identified

and found to be facile. Due to the importance of the steric demands imposed by the IMes ligand, this work will be repeated with the full ligand and reported shortly.

I aim to communicate results from the hydrogenation of diphenylacetylene with $Ru(CO)_3$(dpae) and $Ru(CO)_2$(dpae)(PPh_3) in due course. The work into the SABRE process is on-going in current research and investigations with different solvents and substrates are an active area of research.

Appendix 1: Published paper on the reactions of $W(N_2)_2$(dppe-κ^2P) with p-H_2

A copy of the paper prior to publishing which details the experimental work outlined in Chapter 4 along with the original published DFT results is presented in this Appendix[45].

Detection of unusual reaction intermediates during the conversion of $W(N_2)_2(dppe)_2$ to $W(H)_4(dppe)_2$ and of H_2O into H_2.

Beatriz Eguillor[a], Patrick J. Caldwell[a], Martin C. R. Cockett[a], Simon B. Duckett,[a]* Richard O. John[a], Jason M. Lynam[a], Christopher J. Sleigh[a] and Ian Wilson.[b]

[a]Department of Chemistry, University of York, Heslington, York, YO10 5DD, UK. YO10 5DD. Tel: +44 1904 432564; E-mail:sbd3@york.ac.uk

[b]Department of Safety of Medicines, AstraZeneca, Alderley Park, UK. Macclesfield, Cheshire, UK SK10.

RECEIVED DATE (automatically inserted by publisher); E-mail: *simon.duckett@york.ac.uk*

Supporting Information Placeholder

$W(N_2)_2(dppe\text{-}\kappa^2P)_2$ reacts with H_2 to form $[WH_3\{Ph(C_6H_4)PCH_2CH_2PPh_2\text{-}\kappa^2P\}(dppe\text{-}\kappa^2P)]$ and then $W(H)_4(dppe\text{-}\kappa^2P)_2$. When *para*hydrogen is used in this study, polarized hydride signals are seen for these two species. The reaction is complicated by the fact that trace amounts of water lead to the formation of H_2, $PPh_2CH_2CH_2Ph_2P(O)$ and $W(H)_3(OH)(dppe\text{-}\kappa^2P)_2$, the latter of which reacts further via H_2O elimination to form $W(H)_4(dppe\text{-}\kappa^2P)_2$ and $[WH_3\{Ph(C_6H_4)PCH_2CH_2PPh_2\text{-}\kappa^2P\}(dppe\text{-}\kappa^2P)]$. These studies demonstrate a role for the 14-electron intermediate $W(dppe\text{-}\kappa^2P)_2$ in the CH activation reaction pathway leading to $[WH_3\{Ph(C_6H_4)PCH_2CH_2PPh_2\text{-}k^2P\}(dppe\text{-}k^2P)]$. UV irradiation of $W(H)_4(dppe\text{-}\kappa^2P)_2$ under H_2 led to phosphine dechelation and the formation of $W(H)_5(dppe\text{-}k^2P)(dppe\text{-}k^1P)$ rather than H_2 loss and $W(H)_2(dppe\text{-}\kappa^2P)_2$ as expected. Parallel DFT studies using the simplified model system $W(N_2)_2((Ph)HPCH_2CH_2PH_2\text{-}\kappa^2P)(H_2PCH_2CH_2PH_2\text{-}\kappa^2P)$ confirm that *ortho*metallation is viable via both $W(dppe\text{-}\kappa^2P)_2$ and $W(H)_2(dppe\text{-}\kappa^2P)_2$ with explicit THF solvation being necessary to produce the electronic singlet-based reaction pathway that matches with the observation of *para*hydrogen induced polarization in the hydride signals of $[WH_3\{Ph(C_6H_4)PCH_2CH_2PPh_2\text{-}\kappa^2P\}(dppe\text{-}\kappa^2P)]$, $W(H)_3(OH)(dppe\text{-}\kappa^2P)_2$ and $W(H)_4(dppe\text{-}\kappa^2P)_2$ during this study. These studies therefore reveal the existence of differentiated and previously unsuspected thermal and photochemical reaction pathways in the chemistry of both $W(N_2)_2(dppe\text{-}\kappa^2P)_2$ and $W(H)_4(dppe\text{-}\kappa^2P)_2$ which have implications for their reported role in N_2 fixation.

Systems such as $W(N_2)_2(dppe\text{-}\kappa^2P)_2$ (**1**) and $W(CO)_3(PCy_3)_2$ provide important examples of complexes where the activation of small molecules by inorganic compounds can be seen in action.[1] In the case of $W(N_2)_2(dppe\text{-}\kappa^2P)_2$ the binding of dinitrogen and the resulting sensitivity to electrophilic attack has particular relevance to nitrogen fixation.[2] $W(CO)_3(PCy_3)_2$ on the other hand has provided a model system to enable the subsequent rationalization of dihydrogen activation in terms of both classical dihydride and dihydrogen interactions that are now ubiquitous to inorganic chemistry.[3-5,6]

Reactivity studies involving $W(N_2)_2(dppe\text{-}\kappa^2P)_2$[7] suggest the generation of coordinatively unsaturated $W(dppe\text{-}\kappa^2P)_2$ which has led to a range of novel reactions. These include the removal of CO from dimethylformide[8], and the conversion of benzaldehydeiminines into isocyanides.[9] Studies have also demonstrated that the dppe ligand can be converted by this complex into the *tetra*dentate phosphine *meso*-o-$C_6H_4(PPhCH_2CH_2PPh_2)_2$.[10] Furthermore, unusual reactivity has also been observed in other tungsten phosphine systems.[11] Others have demonstrated that protonation of $W(N_2)_2(dppe\text{-}\kappa^2P)_2$ leads to a hydrazido complex, with ammonia subsequently formed under mild conditions.[12,13] The involvement of a second metal has also been shown to facilitate proton transfer.[14,15]

The chemistry of tungsten polyhydride complexes containing mono and bidentate phosphine ligands has also been the subject of significant investigation,[16] with many dihydride, tetrahydride and hexahydride complexes reported. However, as in the case of related polyhydride iridium systems,[17] the mixing of η^2-H_2 and $M(H)_2$ coordination modes adds significantly to the complexity of ligand binding. This results in an array of W(0) - W(VI) complexes and difficulties in their unambiguous characterization. Utilization of $T_{1(min)}$ values as a route to achieve this differentiation is well established.[18,19]For example, NMR data for $WH_6(PPh(CH_2CH_2PPh_2)_2$ has produced T_1 values of 103 and 126 ms at 223 K which suggests classical hexahydride formulation.[20] The protonated form of this complex, $[W(H)_{7-2x}(\eta^2\text{-}H_2)_x(PPh(CH_2CH_2PPh_2)2]BF4$ (x = 1 or 2) was, however, found to yield a T_1 value of 21 ms at 223 K which is consistent with the involvement of exchanging η^2-H_2 ligands. Related protonation studies on the classical tetrahydride $W(H)_4(PMePh_2)_4$ lead to initial attack on the hydrido ligand to generate $[WH_3(\eta^2\text{-}H_2)(PMePh_2)_4]^+$ which subsequently rearranges to give the pentahydride.[21,15]

Factors that control the binding of small molecules to $W(CO)_3(PCy_3)_2$ and its agostic bonding within the cyclohexyl moiety have been explored by density functional theory (DFT).[22] The use of DFT to probe aromatic C-H bond activation at tungsten[23] and to examine polyhydride systems has also

been shown to enable rationalization of the reactivity of such systems.[24] Others have modeled the complex functionalization of N_2 by H_2 in such organometallic systems.[25] Furthermore, the interaction of hydride ligands with water has been shown to result in the generation of a metal-hydroxide complex and dihydrogen.[26] Such DFT methods are particularly useful in predicting the reactivity of reaction intermediates that are normally experimentally undetectable.

NMR spectroscopy, in conjunction with UV photolysis of samples within the NMR probe has enabled the characterization of very unstable materials and the monitoring of their reactivity. This approach has been used successfully to detect unstable alkyl hydride[27,28] complexes, a xenon complex[29] and a number of hydride complexes.[30] More recently, the approach has been used to generate unstable tungsten dihydrogen complexes.[31] The related technique of photo-Chemically Induced Dynamic Nuclear Polarization (photo-CIDNP) has been used to determine kinetic parameters for protein folding.[32]

The in situ photochemical method has been extended to enable the successful detection of materials that are unstable even at 213 K through the signal enhancement resulting from the *para*-hydrogen (*para*-H_2) induced polarization effect (PHIP[33,34,33,34,33,34,34], [33,34,35,37] an approach which has been reviewed recently.[38,39] In the present paper, we report first on a study of $W(H)_2(CO)_3(PCy_3)_2$ using the *in situ* photolysis method whose objective was to establish whether equilibration between a metal η^2-H_2 complex and its dihydride counterpart could be followed using PHIP. The reactivity of the complex $W(N_2)_2$(dppe-κ^2P)$_2$ (**1**) towards H_2 is then followed using PHIP and a number of interesting observations are described. The resulting complexes are characterized by full NMR analysis including ^{183}W NMR data.[40,41] These studies are rationalized through model DFT calculations based on $W(N_2)_2$((Ph)$HPCH_2CH_2PH_2$-κ^2P)($H_2PCH_2CH_2PH_2$-κ^2P) (**1m**) where the dppe ligand is replaced by the simplified phosphine.

Experimental

General Conditions and Materials. All manipulations were carried out under inert atmosphere conditions, using standard Schlenk techniques (with N_2 or Ar as the inert atmosphere) or high vacuum techniques. Solvents were obtained as Analytical Grade from Fisher. The WCl_6 used was obtained from Acros Organics and the *bis*-(1,2-diphenyl-phosphine)ethane (dppe) was obtained from Sigma-Aldrich and used without further purification. $W(N_2)_2$(dppe-κ^2P)$_2$ (**1**) was prepared by known literature methods[7] and characterized by NMR. NMR spectra were collected on Bruker DRX 400, Avance 600 and Avance II 700 spectrometers.

Preparation and characterization of W(H)$_4$(dppe-κ^2P)$_2$ (2) An NMR sample of **1** was prepared by charging a 5 mm NMR tube fitted with a Young's tap with ca. 1 mg of **1** and then adding toluene-d_8 via vacuum transfer. Hydrogen (3 atm.) was then added to this sample at room temperature. After 2 hours of heating at 328 K, the $^{31}P\{^1H\}$ NMR spectrum of the resultant solutions showed only a singlet at 61.0 ppm due to the known complex **2**. The room temperature NMR data for **2** agree with that in the literature.[42] We note an increase in the T_1 value to 585 ms when recorded with ^{31}P decoupling at 258 K, in accordance with a classical *tetra*hydride configuration for **2**.

^{1}H NMR (700 MHz, THF-d_8, 283 K): δ 7.90 (bs, J_{HH} = 7.3 Hz, 8H, Ph-*ortho*), 7.21 (t, J_{HH} = 7.3 Hz, 8H, Ph-*meta*), 7.17 (m, J_{HH} = 7.0 Hz, 8H, Ph-*ortho*), 7.15 (m, J_{HH} = 7.3 Hz, 4H, Ph-*para*), 6.76 (m, J_{HH} = 7.0 Hz, 8H, Ph-*meta*), 6.79 (t, J_{HH} = 7.0 Hz, 4H, Ph-*para*), 2.68 (dd, J_{HP} = 28.6 Hz, J_{HH} = 9 Hz, 4H, -CH_2-), 1.70 (m, J_{HH} = 9 Hz, 4H, -CH_2-), −3.68 (binomial quintet, J_{HP} = 26 Hz, J_{WH} = 38 Hz, 4H). $^{13}C\{^1H\}$ NMR (176.008 MHz, THF-d_8, 283K): δ 143.81 (d, J_{CP} = 39.7 Hz C_{ipso}), 139.26 (d, J_{CP} = 32.5 Hz C_{ipso}), 137.19 (Ph-*ortho*), 134.44 (Ph-*ortho*), 128.8 (Ph-*para*), 127.35 (Ph-*meta*), 127.14 (Ph-*para*), 127.03 (Ph-*meta*) 34.76 (d, J_{CP} = 32.5 Hz -CH_2-). $^{31}P\{^1H\}$ NMR (283.4 MHz, THF-d_8, 283 K): 61.5 s (J_{WP} = 169 Hz). T_1(min) (WH, 400 MHz, C_7D_8): 79 ± 1.1 ms (signal at δ -3.63, temperature 273 K). $^{183}W\{^1H\}$ NMR (16.6 MHz, C_7D_8, 298 K): δ -3354.5 (m, J_{WP} = 167.3 Hz).

NMR scale preparation of [W(H)$_3${Ph(C_6H_4)$PCH_2CH_2PPh_2$-κ^2P}(dppe-κ^2P)] (3). A sample of **1** was dissolved in toluene-d_8 and placed in a dry ice/isopropanol bath at *ca.* 230 K. The tube was then pressurized to 3 atm. with hydrogen and the resulting sample irradiated at 223 K using a broadband 180 W Oriel UV lamp for 40 min. At this point NMR spectroscopy revealed that the sample contained **3** (see below) at >90 % conversion. This process enabled the characterization of **3** to be completed at low temperature by COSY, nOe and HMQC methods where its lifetime was sufficiently extended. Full NMR data for **3** are presented in Tables 1 and s1. $^{183}W\{^1H\}$ NMR (16.6 MHz, C_7D_8, 298 K): δ −2917.

Table 1: Partial NMR data for **3** in toluene-d_8, 298 K.

Group, chemical shift δ, J (/Hz),T_1	Coupling to P_a (J/Hz)	Coupling to P_b (J/Hz)	Coupling to P_c (J/Hz)	Coupling to P_d (J/Hz)
H_a, −0.14 J_{HaHe} = 2, J_{HaHb} = 4 (T_1 773 ms at 248 K),	24	68	34	8
H_b, −2.69 J_{HbHe} = 8, (T_1 724 ms at 248 K)	62	26	12	22
H_e, −2.93 J_{HH} as above, (T_1 510 ms at 248 K)	6	24	64	38
P_b, 59.3, J_{WP} = 138	8	~	15	8
P_c, 47.4, J_{WP} = 170	76	15	~	8
P_a, 55.4, J_{WP} = 180	~	8	76	22
P_d, −13.2, J_{WP} = 122	22	8	8	~

NMR scale preparation of W(H)$_6$(dppe-κ^2P)(dppe-κ^1P) (4). A sample of **2** in toluene-d_8 was cooled to 260 K, and then pres-

surized to 3 atm. by hydrogen gas. The cooled sample was then exposed to UV irradiation (Oriel lamp) for 120 min. At this point NMR spectroscopy revealed the sample to contain both **4** (see below) and **2** with no evidence for **3** even though it had already been demonstrated to be sufficiently thermally and photochemically stable under these conditions. The ratio of **4** to **2** was found to be 1 : 1 at this point and remained unchanged at this level after 30 mins of further irradiation. This route enabled the subsequent characterization of **4** at 273 K by COSY, nOe and HMQC methods. ^{1}H NMR (700 MHz, toluene-d_8 , 273 K): δ 2.24 (m, J_{PH} = 18, H_b) δ 7.92 (ortho), δ 7.04 (meta), δ 7.00 (para), δ 2.67 (H_c) δ 7.82 (ortho), δ 6.98 (meta), δ 7.00 (para), δ 2.79 (m, H_d) δ 7.38 (ortho), δ 7.00 (meta), δ 7.03 (para); δ −2.41 (dq, J_{WH} = 38.1, $J_{HP(a)}$ = 36.3 Hz, $J_{HP(b)}$ = 26.5 Hz, H_a); ^{13}C{^{1}H} NMR (176.008 MHz, toluene-d_8, 273K), attached to P_a, δ 31.85 (d) J_{CP} = 47, δ 139.52 (*ipso*), δ 133.12 (*ortho*), δ 128.04 (*meta*), δ 129.04 (*para*), attached to P_b , δ 34.60 (d) J_{CP} = 18 δ 139.41(*ipso*), δ 132.96 (*ortho*), δ 127.23 (*meta*), δ 128.27 (*para*), attached to P_c, δ 34.80 (d) J_{CP} = 33, δ 132.93 (*ortho*), δ 129.09 (*meta*), δ 128.02 (*para*); ^{31}P{^{1}H} NMR (283.4 MHz, toluene-d_8, 273K), P_A, δ 54.7, J_{WH} = 95 Hz, $J_{P(a)P(b)}$ = 7.4 Hz, P_B, δ 42.3, J_{WH} = 62 Hz, $J_{P(a)P(b)}$ = 7.4 Hz, $J_{P(b)P(c)}$ = 38 Hz, P_C, δ -12.4, $J_{P(b)P(c)}$ = 38 Hz; (16.6 MHz, C_7D_8, 298 K), T_1(min) (WH, C_7D_8): 890 ms (signal at δ -2.41, temperature 228 K); ^{183}W{^{1}H} NMR (16.6 MHz, C_7D_8, 298 K), δ −4000 (m).


(labelled as in text, ortho proton chemical shift indicated /δ)

NMR scale preparation of W(H)$_3$(OH)(dppe-κ^2*P*)$_2$ (5). A sample of **1** was dissolved in undried toluene-d_8 and left to stand overnight at room temperature. 3 atm. of hydrogen was then added and left to react for a further 24 hours. During this period NMR signals due to **5** (see below) became evident. The ratio of **5** to **1** typically reached 1 : 5 after 24 hrs. Over a longer time period, the slow thermal conversion of **5** into both **4** and **2** (ratio ca. 1:20) occurred. Signals for compound **3** were also observed, in addition to those of free $PPh_2CH_2CH_2PPh_2$(O). This method allowed the production of sufficient **5** for its full NMR characterization at 283 K by COSY, nOe and HMQC methods. A sample where **5** is the dominant product can be obtained from a similar reaction in THF when it is doped with H_2O. Full NMR data for **5** are presented in Tables 2 and s2

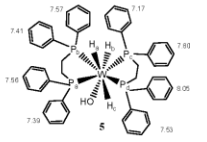
(labelled as in the text, with ortho proton chemical shift indicated /δ)

Table 2: Partial NMR data for **5.**

Group, Chemical, Shift / δ (J/Hz) and T_1 at 268 K	Coupling to P_a (J/Hz)	Coupling to P_b (J/Hz)	Coupling to P_c (J/Hz)	Coupling to P_d (J/Hz)
H_a, −2.26 (t); 284 ms	18	38	62	30
H_b , −2.37 (dd); 282 ms	62	44	18	24
H_c, 1.59 (ddd)	30	114	30	86
OH,−3.00(bs); 744 ms				
P_b, 64.0 (bs)	16	~	16	21.6
P_c, 45.7 (AB spin system J_{AB} 152, Δν 496.5 Hz)	152	14	~	14
P_a, 47.6 (AB spin system)	~	14	152	14
P_d, 36.9 (bt)	9	21.6	9	~

Results and Discussion

Photochemical Reactions of W(CO)$_3$(PCy$_3$)$_2$ with *para*hydrogen. A sample of W(CO)$_3$(PCy$_3$)$_2$ was prepared and then reacted with *para*-H_2, with the ensuing thermal reaction monitored by ^{1}H NMR spectroscopy. While hydride signals for the dihydride isomer, W(H)$_2$(CO)$_3$(PCy$_3$)$_2$, were observed at 298 K, they failed to exhibit any PHIP. We then employed the *in-situ* UV photolysis method to monitor this reaction directly at 213 K using 325 nm radiation. However, while the hydride signals for W(H)$_2$(CO)$_3$(PCy$_3$)$_2$ were detected, no PHIP was seen in the two hydride resonances. We conclude therefore that the rapid relaxation associated with the η^2-H_2 isomer quenches the PHIP effect in this system during tautomerization between the W(H$_2$)(CO)$_3$(PCy$_3$)$_2$ and W(H)$_2$(CO)$_3$(PCy$_3$)$_2$ forms. This result contrasts with that previously reported Bargon *et al.* who showed that an organic hydrogenation product can show PHIP even though it is formed via a metal-based intermediate that exists in an η^2-H_2 form.[43] In both cases, the lifetime of the M-η^2-H_2 intermediate must play a pivotal role in determining the extent of polarization in any newly formed hydrogenation product. Consequently, we decided to extend the study to target W(H)$_4$(dppe-κ^2*P*)$_2$ (**2**).

Reactions of W(N$_2$)$_2$(dppe-κ^2*P*)$_2$ (1) with *para*hydrogen. W(N$_2$)$_2$(dppe-κ^2*P*)$_2$ (**1**) reacts with H_2 to form W(H)$_4$(dppe-κ^2*P*)$_2$ (**2**)[44] and when this reaction is followed in THF-d_8 with *para*-H_2 at 333 K the resulting ^{1}H NMR spectrum contains a polarized hydride signal at δ −3.66 as shown in Figure 1a. This hydride signal appears as a quintet with J_{PH} = 28 Hz and is flanked by ^{183}W satellites with J_{HW} = 38 Hz. A 2D ^{1}H-^{183}W HMQC[40] spectrum was then recorded and showed a ^{31}P coupled multiplet at δ −3363 when referenced to TMS at 100 MHz.[45]

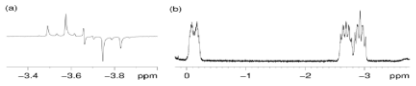

Figure 1: Selected ^{1}H NMR signals observed during reactions of W(N$_2$)$_2$(dppe-κ^2*P*)$_2$ (**1**) and H_2. (a) PHIP polarized hydride signal for W(H)$_4$(dppe-κ^2*P*)$_2$ (**2**), (b) hydride signals, H_a, H_b and H_c of [WH$_3$[Ph(C_6H_4)PCH$_2$CH$_2$PPh$_2$-κ^2*P*](dppe-κ^2*P*)] (**3**).

The origin of the PHIP enhancement seen in the NMR signal observed for the hydride ligands of **2** results from the second

order $[AX]_4$ spin system which provides the magnetic inequivalence necessary to achieve PHIP activity.[46] Interestingly, weak PHIP polarization is also seen in one of the two sets of *ortho*-phenyl proton resonances of **2** that appears at δ 7.42 where J_{PH} = 8 Hz; the anti-phase coupling reflected in the PHIP enhancement is −3 Hz. This observation provides insight into the *intra*molecular activation of the dppe-ligand (*q.v.*). The corresponding ^{1}H COSY NMR spectrum of **2** contained a weak connection between the hydride resonance and the dppe backbone ^{1}H signals at δ 2.64 in addition to the *ortho*-phenyl proton signal at δ 7.42 thereby confirming that they are all weakly scalar coupled.

Previous studies have shown that PHIP can be used to examine successfully a range of mono-, di- and tri- hydride complexes.[47] The hydride ligand polarization observed in **2** and reported here represents the first time that PHIP has been seen in such a mononuclear *tetra*-hydride complex. The $T_{1(min)}$ value of the hydride signal of **2** was determined as 0.58 s at 258 K and is fully consistent with the observation of PHIP in this species. We conclude therefore that any W-η^2-H_2 based reaction intermediate which might exist on the reaction pathway to **2** has a very short lifetime (see DFT discussion later).[20,48]

We expected this reaction to proceed *via* the intermediate $W(H)_2(N_2)(dppe\text{-}\kappa^2P)_2$ but this was not detected at 333 K. We therefore re-examined the reaction at the lower temperature of 295 K where we observed two further sets of polarized hydride signals in the corresponding ^{1}H NMR spectrum at δ −2.69 and δ −2.93 (see Figure 1b). These resonances are due to the new complex, **3**, and proved to couple to a third hydride resonance at δ −0.14 according to COSY methods. These data therefore preclude the detection of $W(H)_2(N_2)(dppe\text{-}\kappa^2P)_2$ and suggest that an unexpected reaction has taken place.

Photochemical reactions of $W(N_2)_2(dppe\text{-}\kappa^2P)_2$ (1) with para-hydrogen. We describe now how the identity of **3**, an *intra*molecular CH bond activation product, was confirmed through its formation in a series of low temperature irradiation studies. The formation of 2 and 3 from 1 is illustrated in Scheme 1.

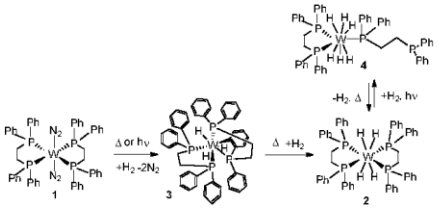

Scheme 1: Reaction products and pathways involved in the reactions of $W(N_2)_2(dppe\text{-}\kappa^2P)_2$ (1) with H_2.

297 nm irradiation of $W(N_2)_2(dppe\text{-}\kappa^2P)_2$ has previously been suggested to produce $W(dppe\text{-}\kappa^2P)_2$ as the sole photoproduct.[44] It subsequently forms $W(N_2)(dppe\text{-}\kappa^2P)_2$ and then $W(N_2)_2(dppe\text{-}\kappa^2P)_2$ upon back-reaction with N_2, although ^{15}N labeling suggests a similar sequential pathway for the original ligand loss process.[49] The first of the studies reported here was completed using *in-situ* irradiation of a sample of **1** under an atmosphere of H_2 within the NMR system at 233 K using a 325 nm HeCd laser.

One dominant photoproduct, **3** was evident in the resulting NMR spectra, and with *para*-H_2, the associated ^{1}H NMR spectra contain the same three hydride resonances all of which exhibited a strong PHIP effect. Based on the intensities of the PHIP enhanced signals we conclude that H_2 addition to the sites giving rise to the δ −2.69 and δ −2.93 signals is dominant. Under these conditions, a weakly polarized hydride signal for **2** was also seen (Figure 2).

Characterization of $WH_3\{Ph(C_6H_4)PCH_2CH_2Ph_2\text{-}\kappa^2P\}(dppe\text{-}\kappa^2P)$] (3). External UV irradiation of a similar sample at 223 K using a 180 W Oriel UV lamp was then used to produce an NMR sample that was found to contain essentially **3** (Figure 1b illustrates the hydride region of the resulting ^{1}H NMR spectrum). This enabled the complete low temperature NMR characterization of **3** via COSY, nOe and HMQC methods. Notably, the three hydride signals of **3** now clearly possess 1:1:1 integrals with 8 further distinct ethane bridge protons also evident. Examination of a series of NMR spectra revealed 39 aromatic proton resonances for **3** which arise from seven sets of five coupled signals due to a phenyl ring and one set of four coupled signals due to a CH bond activated phenyl ring. In addition to this, **3** yields four ^{31}P NMR signals that are located at δ −13.2, 47.4, 55.4 and 59.3.

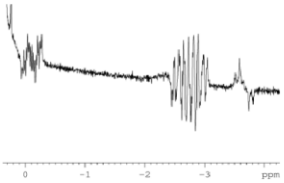

Figure 2: PHIP enhanced NMR signals observed during the generation of $W(H)_4(dppe\text{-}\kappa^2P)_2$ (**2**) and [$WH_3\{Ph(C_6H_4)PCH_2CH_2PPh_2\text{-}\kappa^2P\}(dppe\text{-}\kappa^2P)$] (**3**) under *in situ* photolysis at 298 K.

The ^{31}P NMR signal for free dppe appears at δ −12.8, close to one of the resonances of **3** at δ −13.2. This suggests that **3** may contain a phosphorus center that is no longer coordinated to the metal. However, the resonance at δ −13.2 couples strongly (64 Hz) to the hydride ligand that resonates at δ −2.63 in the ^{1}H NMR spectrum of **3**. It is therefore clear that the phosphorus center giving rise to this signal is bound to the metal. Such a high-field signal for a metal-bound phosphorus atom has precedence as similar shifts are observed for metallo-phosphorus 4-membered rings.[50] A ^{13}C resonance at δ 122.33 in **3** corresponds to a quaternary carbon directly attached to the tungsten center and supports this *ortho*metallation concept.

We conclude therefore that **3** is the trihydride complex $WH_3\{Ph(C_6H_4)PCH_2CH_2PPh_2\text{-}\kappa^2P\}(dppe\text{-}\kappa^2P)$] where one of the phosphine ligands is *ortho*metallated. This species is shown in Scheme 1 and exhibits T_{1min} values for its three hydride resonances of 0.77 s, 0.77 s and 0.51 s, respectively, at 248 K. These values serve to confirm that **3** is a classical W(IV) *tri*-hydride which explains why PHIP enhancement can be observed in its

hydride signals.[20] The ^{183}W signal of **3** appears as a ^{31}P-coupled multiplet at δ −2913 which proves to be close to that of **2** thereby supporting their similar oxidation state and 18 electron counts.

Conversion of $WH_3\{Ph(C_6H_4)PCH_2CH_2PPh_2\text{-}\kappa^2P\}(dppe\text{-}\kappa^2P)$] (3) to $W(H)_4(dppe\text{-}\kappa^2P)_2$ (2). The slow conversion of **3** into the tetrahydride complex **2** was found to occur upon warming a solution of **2** in toluene-d_8 in the presence of 3 atm. H_2. However, a new hydride resonance due to a further species, **4**, was also detected at δ −2.4 (Fig. 3c) in these experiments, although at a level of less than 5% conversion. The conversion of **3** to **2** requires the reformation of the activated CH bond which in turn offers an explanation for the observation of PHIP in the *ortho*-phenyl proton resonance of **2** at δ 7.42 as described earlier; a *para*-H_2 derived proton is placed in this site through this exchange process.

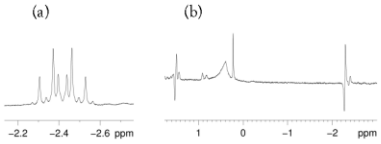

Figure 3: (a) ^{1}H hydride ligand NMR signal for $W(H)_5(dppe\text{-}\kappa^2P)(dppe\text{-}\kappa^1P)$ (**4**) and (b) Three ^{31}P decoupled PHIP polarized hydride signals seen for $W(H)_3(OH)(dppe\text{-}\kappa^2P)$ (**5**).

Kinetic studies on the conversion of 3 to 2. When this conversion was monitored in THF-d_8 under 3 atm. of H_2 only **2** is formed with a rate constant for conversion at 293 K of 4.2 x 10^{-5} s^{-1}. This reaction was then monitored over the temperature range 283-323 K and $\Delta H^{\ddagger}$ and $\Delta S^{\ddagger}$ values of 79 ± 3 kJ mol^{-1} and −54 ± 11 J K^{-1} mol^{-1}, respectively, were determined from the associated rate data. These values are consistent with a transition state that involves a reduction in the number of species present and hence a contribution from H_2 binding in the rate limiting step. Furthermore, when this reaction is completed with D_2 rather than H_2 at 293 K, while there is no evidence for D incorporation into **3**, k_H/k_D is 1.09 which supports the involvement of H_2 in this pathway The corresponding values of $\Delta H^{\ddagger}$ and $\Delta S^{\ddagger}$ for the reaction of **3** with D_2 are 70.6 ± 10 kJ mol^{-1} and −85 ± 32 J K^{-1} mol^{-1}, respectively. The value of $\Delta G^{\ddagger}$(300) for the reaction with D_2 was determined as 96.2 kJ mol^{-1} compared with that of 95.0 kJ mol^{-1} for reaction with H_2 which confirms that an interaction with the incoming ligand helps lower the barrier to this reaction. The rate data used to determine these values is presented in Table 3. The associated Eyring plot, and a typical kinetic trace are presented in Figure 4. The kinetic data that is presented in Figure 4 was recorded at 293 K and corresponds to monitoring the conversion of complex **3** into **2**.

Table 3: Rate date for the conversion of **3** into **2** through reaction with H_2 and D_2 respectively.

Temperature /K	k_H / s	k_D/s
283	9.75×10^{-6}	9.29×10^{-6}
293	4.19×10^{-5}	3.84×10^{-5}
303	1.27×10^{-4}	5.08×10^{-5}
313	2.98×10^{-4}	2.4×10^{-4}
323	9.73×10^{-4}	4.39×10^{-4}

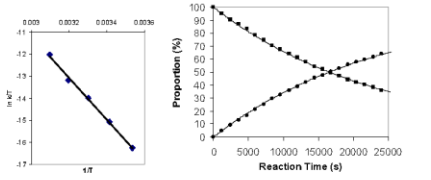

Figure 4: (a) Eyring plot for the conversion of **3** into **2**; (b) kinetic trace showing how the proportions of **3** (♦) and **2** (♦) change with reaction time (**s**) at 298 K

It should be noted that in the absence of H_2, **3** decomposes, while also forming a new hydride-containing species. This complex is highly fluxional but decomposes on exposure to H_2 rather than forming **2** or **3**. At 263 K, two mutually-coupled hydride resonances are visible at δ −0.82 and −1.03. The corresponding ^{183}W signal of this species appears at δ −2245. Despite our best efforts we have not been able to identify it conclusively, and while a $W(H)_2(dppe\text{-}\kappa^2P)_2$ formulation would match with the spectroscopic data, the DFT study now described suggests that this is not the case.

Mapping of the reaction pathway of $W(N_2)_2(dppe\text{-}\kappa^2P)_2$ (1) with hydrogen. In order to rationalize these reactions further, a series of DFT calculations was performed on the model system $W(N_2)_2((Ph)HPCH_2CH_2PH_2\text{-}\kappa^2P)(H_2PCH_2CH_2PH_2\text{-}\kappa^2P)$ (**1m**) for which the dppe ligands has been replaced by the simplified phosphine ligands indicated. An optimized DFT structure for **1m** was computed using implicit solvation for THF. The structural features of **1m** correspond well with those of **1** as detailed in the supporting information. This structure was used as a starting point in a subsequent geometry optimization calculation of the *bis*-N_2 loss-product $W((Ph)HPCH_2CH_2PH_2\text{-}\kappa^2P)(H_2PCH_2CH_2PH_2\text{-}\kappa^2P)$ (**6m**). The most stable geometry exists as a triplet ground state **6m^3**, which lies 210 kJ mol^{-1} above **1m** in Gibbs Free Energy terms (Scheme 2, further reactivity, however, is via 6m^1, the singlet). Oxidative addition of H_2 then proceeds to form the classical dihydride complex **7m** in a barrierless reaction involving the end-on approach of H_2. Similar behavior has been reported in other systems.[51]

The addition of a second molecule of H_2 to **7m** then forms the expected *tetra*hydride product $W(H)_4((Ph)HPCH_2CH_2PH_2\text{-}\kappa^2P)(H_2PCH_2CH_2PH_2\text{-}\kappa^2P)$ (**2m**) which lies 25 kJ mol^{-1} below **1m** in a barrierless reaction. Significantly, the formation of $W(H)_3\{(C_6H_4)HPCH_2CH_2PH_2\text{-}\kappa^2P\})(H_2PCH_2CH_2P(H)_2\text{-}\kappa^2P)$ (**3m**) occurs via *ortho*metallation of **7m** via a 26 kJ mol^{-1} transition state. **3m** is, however, 33 kJ mol^{-1} lower in energy than **7m** and therefore corresponds to a thermodynamically viable product in accordance with the experimental observation of **3**. **3m** can also be formed in a reaction sequence that involves CH activation (to form **8m**) from 6m^1 where the barrier to *ortho*metallation is now 20 kJ mol^{-1} followed by H_2 addition.

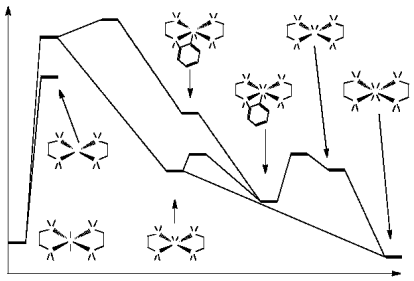

Scheme 2: DFT reaction coordinate profile for the conversion of **1m** into **2m** without specific THF involvement.

However, the explicit solvation of $\mathbf{6m}^3$ with THF yields the complex $W((Ph)HPCH_2CH_2PH_2\text{-}\kappa^2P)(H_2PCH_2CH_2PH_2\text{-}\kappa^2P)(THF)_2$ which exists in its most stable form as a singlet ($\mathbf{6s}^1$), 88 kJ mol^{-1} more stable than the triplet, $\mathbf{6s}^3$, and just 3 kJ mol^{-1} less stable than $\mathbf{6m}^3$ (Scheme 3). Given that the experimental reaction is carried out in THF, it is reasonable to assume that $\mathbf{6s}^1$ exists in solution. Following loss of a single THF ligand from $\mathbf{6s}^1$, oxidative addition of H_2 proceeds to form the classical dihydride complex **7s** in a barrierless reaction involving the end-on approach of H_2. In this scenario, THF clearly plays an important role in stabilizing the dihydride complex $W(H)_2((Ph)HPCH_2CH_2PH_2\text{-}\kappa^2P)(H_2PCH_2CH_2PH_2\text{-}\kappa^2P)(THF)$ (**7s**) over its unsolvated 16-electron counterpart **7m**.

These DFT results are consistent with the experimental observation of PHIP in the hydride resonances of both **2** and **3** when explicit THF solvation is included, and confirm that there is little contribution from any W-η^2-H_2 type species on the reaction coordinate which connects **1** with **2**. We note that, in support of this deduction, $Ru(dppe\text{-}\kappa^2P)(CO)_2$ does indeed add H_2 via the electronic singlet intermediate, with PHIP being detected in the resulting hydride NMR signals.[52] In contrast, the analogous intermediate $Fe(dppe\text{-}\kappa^2P)(CO)_2$ has been shown by DFT to exist as a triplet which is consistent with the failure to observe PHIP for $Fe(H)_2(dppe\text{-}k^2P)(CO)_2$.[52]

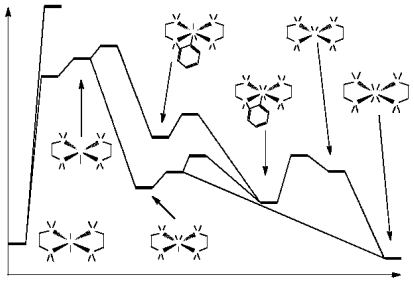

Scheme 3: DFT reaction coordinate profile for the conversion of **1m** into **2m** with specific THF involvement.

An alternative mechanism involving loss of a single N_2 from **1m**, yields the 16-electron complex $W(N_2)((Ph)HPCH_2CH_2PH_2\text{-}\kappa^2P)(H_2PCH_2CH_2PH_2\text{-}\kappa^2P)$ for which a similar barrier exists to *ortho*metallation as that determined for the equivalent THF complex, $W((Ph)HPCH_2CH_2PH_2\text{-}\kappa^2P)(H_2PCH_2CH_2PH_2\text{-}\kappa^2P)(THF)$. However, formation of the N_2 *ortho*metallation product is thermodynamically unfavorable with respect to $W(N_2)((Ph)HPCH_2CH_2PH_2\text{-}\kappa^2P)(H_2PCH_2CH_2PH_2\text{-}\kappa^2P)(THF)$. Computed binding enthalpies for the first and second N_2 ligands of **1m** are 214 kJ mol^{-1} and 129 kJ mol^{-1}, respectively. This is consistent with the experimental observation that the rate of binding of the second N_2 ligand occurs much slower than that of the first.[53] Furthermore, when coupled with the relative thermodynamic instability of the N_2 *ortho*metallation product, an explanation emerges for why no net photochemistry is observed for **1** in the absence of H_2.

Formation of $W(H)_6(dppe\text{-}\kappa^2P)(dppe\text{-}\kappa^1P)$ (4) by UV irradiation of $W(H)_4(dppe\text{-}\kappa^2P)_2$ (2). The chemistry discussed so far is further complicated by the fact that UV irradiation of a preformed sample containing **3** under H_2 at 295 K leads to the detection of both **2** and **4**. In contrast, irradiation of **1** with H_2 at 295 K results in the dominant photoproduct **2** with much lower levels of **3** and **4**. All four of these species are therefore photochemically active under these conditions.

When **2** is irradiated under an H_2 atmosphere at 263 K the dominant product is **4**. Notably, the single hydride signal seen for **4** appears at $\delta -2.4$ and couples to only three ^{31}P nuclei with J_{PH} = 26 Hz (triplet) and 36 Hz (doublet), respectively, as shown in Figure 3a. This hydride resonance also possesses ^{183}W satellites with J_{HW} = 28 Hz. The three ^{31}P nuclei which couple to the hydride, produced signals at δ 54.7 (d) and 42.3 (td), while a third signal for an uncoordinated moiety is evident as a doublet with J_{pp} = 38 Hz at $\delta -12.4$; this resonance showed no coupling to the hydride ligands. The T_1 value of 0.89 s for the hydride ligands in **4**, at 228 K, is consistent with a high oxidation state and therefore classical hydride binding.[20] **4** must therefore be the 18 electron complex $W(H)_6(dppe\text{-}\kappa^2P)(dppe\text{-}\kappa^1P)$.

These conclusions are supported by the fact that the known nine coordinate hexahydride complex $W(H)_6(PMe_2Ph)_3$ has similar J_{PH} (36 Hz) and J_{WH} (27 Hz) to those observed for **4**.[54] These data are therefore fully consistent with the proposed W(VI) *hexa*-hydride formulation of **4** and we note the diagnostically low value of J_{WH} of 28 Hz compared with that of **2** (38 Hz).[54]

The photochemical procedure described above reached a photostationary state with **2** and **4** present in a 1 : 1 ratio and with no evidence for **3** found in the associated NMR spectra. Furthermore, there was no evidence of any net reaction when **2** was irradiated in the absence of H_2. Repetition of the reaction of **2** with *para*-H_2, failed to produce PHIP in the hydride signals observed for either **2** or **4**. These results therefore suggest that UV irradiation of **2** under these conditions leads to phosphine dissociation rather than the H_2 loss suggested by others previously.[55]

Additionally, when a sample of **4** is warmed with *para*-H_2 no PHIP is evident in the detected hydride signals of **2**. This observation confirms that the displacement of H_2 and conversion of

the dppe-κ^1P ligand to its κ^2 form is *intra*molecular with respect to four of the six hydride ligands of **4**.

Formation of W(H)$_3$(OH)(dppe-κ^2P)$_2$ (5). In a number of these reactions a further product was often observed but only if NMR solvents were used without drying.

When a wet toluene-d_8 solution of **1** was left overnight, slow decomposition occurs such that ^{31}P NMR signals for **2**, free dppe, the mono phosphine oxide of dppe and a new complex **5** can be detected. In the ^{1}H NMR spectrum, three new high-field signals for **5** dominate at δ −2.26, δ −2.37 and δ −3.00. These signals, which occur in the hydride region, appear even though no H_2 has been explicitly added to the sample.

However, upon addition of *para*-H_2 to the same sample, the hydride signals at δ −2.26, δ −2.37, as well as a previously masked peak at δ 1.59 (with a peak envelope of ca. 200 Hz which indicates the presence of several strong couplings to ^{31}P) all show PHIP polarization (Fig. 3b). The signal at δ −3.00 which possesses much smaller ^{1}H-^{31}P splittings is apparently unaffected by the addition of *para*-H_2 and when D_2O and *para*-H_2 were used as reagents, only the two signals at δ −2.26, δ −2.37 were polarized.

In an H_2O-containing sample, the same ^{1}H NMR integral values were obtained for the three high field signals, the eight ethane bridge protons, and the resonance at δ 1.59. Significantly, COSY spectroscopy revealed that the δ 1.59 signal of **5** couples to the two hydride signals δ −2.26 and δ −2.37 while EXSY measurements confirm that the hydrogen atoms in these three sites undergo positional interchange. The resonance at δ −3.00 is not involved in this process. In the corresponding ^{1}H-^{31}P HMQC measurement, values of J_{PH} = 100, 30 and 60 Hz produce strong connections to the δ 1.59 ^{1}H NMR signal which is therefore confirmed as a W-hydride resonance. The three high field resonances have T_1 values of 0.28 s, 0.28 s and 0.74 s respectively at 268 K. Complex **5** yields a further 40 aromatic proton resonances that arise from eight distinct and intact phenyl rings. It also gives four ^{31}P NMR signals for tungsten coordinated phosphorus centers that appear at δ 36.6, 45.5, 47.3 and 64.0.

The identity of **5** was secured through a combination of EXSY measurements that probed the behavior of the site yielding the δ −3.00 signal together with H_2O doping studies that were conducted in toluene-d_8 solution. For the doping studies, a sample of **1** was prepared and a 20 fold excess of dppe added prior to the addition of 5 μl of H_2O. Over a period of several days at room temperature, the conversion of **1** into **5** was observed. Based on ^{31}P signal integrations, 50% of **1** converted into **5** and a similar amount of $PPh_2CH_2CH_2Ph_2P(O)$. At this stage no H_2 was evident in solution. Concurrent UV irradiation increased the rate of reaction while generating mainly **2** and **4** and free H_2; the addition of H_2O to a solution of **3** produced a mixture of **2** and **5**.

EXSY measurements revealed that magnetization transfer occurs from the protons giving rise to the δ −3.00 signal of **5** to those associated with the peak at δ 0.47, due to H_2O. This process was enhanced by increasing the water concentration. Collectively, these observations allow **5** to be identified as W(H)$_3$(OH)(dppe-κ^2P)$_2$ where the rate data associated with the proton transfer step yield $\Delta H^{\ddagger}$ = 42 ± 5 kJ mol^{-1} and $\Delta S^{\ddagger}$ = −90.5 ± 18 J K^{-1} mol^{-1}. The protons giving rise to the δ 1.59 hydride signal also show exchange with H_2O in the EXSY data. In addition, the three hydride signals show evidence for positional exchange.

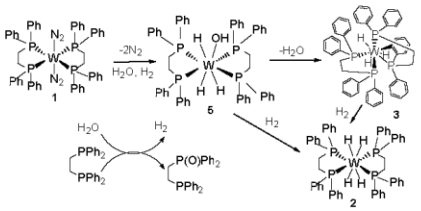

Scheme 4: Conversion of **1** to **2** where H_2O can act as the source of H_2. These transformations can be initiated thermally and photochemically.

In support of the assignment of **5** as a tungsten hydroxide complex, it should be noted that the hydroxyl proton resonance of the related complex Cp*(PMe$_3$)Ir(Ph)OH appears as a broad singlet at δ −3.1 whilst that of Ru(IMes)$_2$(CO)$_2$(OH)H appears at δ −3.75.[56,57] In contrast, the aquo complex W(CO)$_3$(P^{i}Pr$_3$)(H$_2$O) yields a signal for the coordinated H_2O at δ 3.03.[58] Consequently, the δ −3.00 signal of **5** is consistent with that of a metal hydroxyl. This is further supported by the fact that the addition of D_2O results in the rapid loss of the W(OH) resonance of **5** with subsequent reaction with *para*-H_2, yielding only the PHIP enhanced δ −2.26 and δ −2.37 signals.

On a slower timescale, **5** converts thermally into **2** although ultimately in the presence of an excess of water only phosphine oxides of dppe remain according to ^{31}P NMR spectroscopy. This is consistent with the slow reductive elimination of H_2O from the metal center in **5** and subsequent reaction to form **2** or **3** as shown in Scheme 4. These observations also reveal that the 16 electron fragment W(H)$_2$(dppe-κ^2P)$_2$ is capable of *intra*molecular CH bond activation, in agreement with the DFT study discussed earlier.

Diffusion Ordered Spectroscopy. In order to confirm that these signals all originate from molecules with similar masses a series of DOSY measurements were undertaken. These resulted in similar diffusion coefficients for **2**, **3**, **4** and **5**, thereby confirming our mono-nuclear hypothesis, as illustrated in Table 4.

Table 4: Diffusion data for 2, 3, 4 and 5.

Complex, solvent and temperature	Resonance /δ	Diffusion coefficient (cm^2/s)
2, THF, 293 K	-3.94	1.27
3, THF, 293 K	-0.25	1.50
	-2.98	1.50
	-3.12	1.50
4, THF, 293 K	-2.85	2.42
5, Toluene, 273 K	-2.29	0.57
	-2.40	0.57
	-3.00	0.57

Conclusions

The conversion of $W(N_2)_2(dppe\text{-}\kappa^2P)_2$ (**1**) into $W(H)_4(dppe\text{-}\kappa^2P)_2$ (**2**) has been shown to involve the initial formation of the *ortho*metallated CH activation product $[WH_3(Ph(C_6H_4)PCH_2CH_2PPh_2\text{-}\kappa^2P)(dppe\text{-}\kappa^2P)]$ (**3**). Caulton *et al.* prepared the related complex $W(H)_3(\eta^2\text{-}C_6H_4PMe_2)(PMe_2Ph)_3$ from $WH_2Cl_2(PMe_2Ph)_4$ *via* reaction with ^{t}BuLi.[59] Furthermore, Hidai *et al.* have speculated that warming benzene solutions of **1** to reflux leads to the formation of meso-$C_6H_4(PPhCH_2CH_2PPh_2)_2$ via the proposed reaction intermediate $[WH\{Ph(C_6H_4)PCH_2CH_2PPh_2\text{-}\kappa^2P\}(dppe\text{-}\kappa^2P)]$; we note that some of their reported NMR data[10] appear to match that presented here for **3**. The observation of a CH bond activation pathway during the formation of **2** is therefore entirely consistent with the known chemistry of related systems.

The theoretical studies used $W(N_2)_2((Ph)HPCH_2CH_2PH_2\text{-}\kappa^2P)(H_2PCH_2CH_2PH_2\text{-}\kappa^2P)$ (**1m**) as a starting point from which to explore these reactions. They revealed that N_2 loss leads to $W(N_2)_2((Ph)HPCH_2CH_2PH_2\text{-}\kappa^2P)(H_2PCH_2CH_2PH_2\text{-}\kappa^2P)$ (**6m^3**) which exists as a triplet unless explicitly solvated by two molecules of THF. *Ortho*metallation and H_2 addition were both shown to be feasible reaction steps prior to the formation of **3** and **2** respectively. These results therefore rationalized the observation of both **3** and **2** in the reaction chemistry of **1**. They also help explain the detection of PHIP in the corresponding reaction products.

The trapping of hydrogen by organometallic complexes and the reverse process have proven important in energy storage applications.[60] It has been demonstrated in this work that $W(N_2)_2(dppe\text{-}\kappa^2P)_2$ (**2**) is capable of releasing H_2 from H_2O in conjunction with the formation of a phosphine oxide and ultimately $W(H)_4(dppe\text{-}\kappa^2P)_2$ (**2**). This transformation involves the metal hydroxyl-hydride complex $W(H)_3(OH)(dppe\text{-}\kappa^2P)_2$ (**5**) via the reaction sequence illustrated in Scheme 4. Such species have been shown to play a role in organic oxidations.[61] This reaction therefore illustrates a route to H_2 production from H_2O facilitated, in this case by phosphorus acting as a suitable oxygen acceptor.

When these reactions are conducted with *para*-H_2, PHIP is evident in the hydride signals of **2**, **3** and **5**. This confirms the utility of PHIP as a powerful method for examining the reactivity of polyhydride complexes of this type. Furthermore, the experimental and computation results also suggest that non-classical dihydride complexes do not play a significant role in the oxidative addition process. In contrast, H_2 addition to $W(CO)_3(PCy_3)_2$ was shown not to produce detectable PHIP in the $W(H)_2(CO)_3(PCy_3)_2$ product. In this latter case, a role for a non-classical dihydrogen complex in the addition process has been well established.[3,5] The postulation here that **3** and **4** exist as classical W(IV) and W(VI) species was further supported by the long $T_{1(min)}$ values of the hydride ligands (>0.3 s), the observation of appropriate J_{HW} couplings and the detection of ^{183}W signals for **2**, **3** and **4**. The ^{183}W resonance for W(VI) **4** appears at the high field value of δ –4000, in accordance with its high oxidation state. This compares with values of δ –3363 for **2** and δ –2913 for **3** both of which complexes exists as W(IV) species. Attempts to locate the corresponding signal in **5** failed, presumably as a consequence of its dynamic behavior leading to signal broadening.

It has previously been reported that UV irradiation of $W(H)_4(dppe\text{-}\kappa^2P)_2$ under N_2 leads to low yields of ammonia[62] and alkene hydrogenation. It has also been reported that H_2 loss corresponds to the main photochemical process in such systems.[53,55] Here we have demonstrated that $W(H)_6(dppe\text{-}\kappa^2P)(dppe\text{-}\kappa^1P)$ (**4**) is formed under UV irradiation which suggests that 16-electron $W(H)_4(dppe\text{-}\kappa^2P)(dppe\text{-}\kappa^1P)$ and not $W(H)_2(dppe\text{-}\kappa^2P)_2$ is responsible for these conversions.

Thus, the results presented here demonstrate that CH bond activation, phosphine dechelation and the oxidative addition of OH bonds are all important in the chemistry of $W(N_2)_2(dppe\text{-}\kappa^2P)_2$ (**1**).

ACKNOWLEDGMENT We are grateful for financial support from the BBSRC (PJC), AstraZeneca and the Spanish MEC Consolider Ingenio 2010-ORFEO-CSD2007-00006 (BE) research programme. We also thank Professor Robin Perutz for helpful discussions.

"Supporting Information Available:"

Supporting Information Available Material is available relating to the characterization of **3** and **5**, and the DFT derived energetics and coordinates for all the species discussed This material is available free of charge via the Internet at http://pubs.acs.org

References

(1) Bell, B.; Chatt, J.; Leigh, G. J. *J. Chem. Soc.-Dalton Trans.* **1972**, 2492.
(2) Hidai, M.; Mizobe, Y. *Chem. Rev.* **1995**, *95*, 1115.
(3) Kubas, G. J.; Unkefer, C. J.; Swanson, B. I.; Fukushima, E. *J. Am. Chem. Soc.* **1986**, *108*, 7000.
(4) Khalsa, G. R. K.; Kubas, G. J.; Unkefer, C. J.; Vandersluys, L. S.; Kubatmartin, K. A. *J. Am. Chem. Soc.* **1990**, *112*, 3855.
(5) Kubas, G. J.; Ryan, R. R.; Swanson, B. I.; Vergamini, P. J.; Wasserman, H. J. *J. Am. Chem. Soc.* **1984**, *106*, 451.
(6) Heinekey, D. M.; Oldham, W. J. *Chem. Rev.* **1993**, *93*, 913.
(7) Bell, B.; Chatt, J.; Leigh, G. J. *Journal of the Chemical Society D-Chemical Communications* **1970**, 842.
(8) Ishida, T.; Mizobe, Y.; Tanase, T.; Hidai, M. *J. Organomet. Chem.* **1991**, *409*, 355.
(9) Seino, H.; Arita, C.; Nonokawa, D.; Nakamura, G.; Harada, Y.; Mizobe, Y.; Hidai, M. *Organometallics* **1999**, *18*, 4165.
(10) Arita, C.; Seino, H.; Mizobe, Y.; Hidai, M. *Bulletin of the Chemical Society of Japan* **2001**, *74*, 561.
(11) Sattler, A.; Parkin, G. *Nature* **2010**, *463*, 523.
(12) Chatt, J.; Pearman, A. J.; Richards, R. L. *J. Chem. Soc.-Dalton Trans.* **1977**, 2139.
(13) Jia, G.; Morris, R. H.; Schweitzer, C. T. *Inorg. Chem.* **1991**, *30*, 593.
(14) Nishibayashi, Y.; Iwai, S.; Hidai, M. *Science* **1998**, *279*, 540.
(15) Nishibayashi, Y.; Takemoto, S.; Iwai, S.; Hidai, M. *Inorg. Chem.* **2000**, *39*, 5946.
(16) Hlatky, G. G.; Crabtree, R. H. *Coordination Chemistry Reviews* **1985**, *65*, 1.

(17) Crabtree, R. H.; Lavin, M. *J. Chem. Soc.-Chem. Commun.* **1985**, 1661.
(18) Hamilton, D. G.; Crabtree, R. H. *J. Am. Chem. Soc.* **1988**, *110*, 4126.
(19) Ammann, C.; Isaia, F.; Pregosin, P. S. *Magn. Reson. Chem.* **1988**, *26*, 236.
(20) Michos, D.; Luo, X. L.; Faller, J. W.; Crabtree, R. H. *Inorg. Chem.* **1993**, *32*, 1370.
(21) Oglieve, K. E.; Henderson, R. A. *J. Chem. Soc.-Chem. Commun.* **1992**, 441.
(22) Muckerman, J. T.; Fujita, E.; Hoff, C. D.; Kubas, G. J. *J. Phys. Chem. B* **2007**, *111*, 6815.
(23) Li, J.; Yoshizawa, K. *Chem-Eur J* **2012**, *18*, 783.
(24) Maseras, F.; Lledos, A.; Clot, E.; Eisenstein, O. *Chem. Rev.* **2000**, *100*, 601.
(25) Balu, P.; Baskaran, S.; Kannappan, V.; Sivasankar, C. *Polyhedron* **2012**, *31*, 676.
(26) Suresh, C. H.; Sandhya, K. S. *Dalton T* **2012**.
(27) Ball, G. E.; Brookes, C. M.; Cowan, A. J.; Darwish, T. A.; George, M. W.; Kawanami, H. K.; Portius, P.; Rourke, J. P. *Proc. Natl. Acad. Sci. U. S. A.* **2007**, *104*, 6927.
(28) Geftakis, S.; Ball, G. E. *J. Am. Chem. Soc.* **1999**, *121*, 6336.
(29) Ball, G. E.; Darwish, T. A.; Geftakis, S.; George, M. W.; Lawes, D. J.; Portius, P.; Rourke, J. P. *Proc. Natl. Acad. Sci. U. S. A.* **2005**, *102*, 1853.
(30) Cunningham, J. L.; Duckett, S. B. *Dalt. Trans.* **2005**, 744.
(31) Matthews, S. L.; Heinekey, D. M. *J. Am. Chem. Soc.* **2006**, *128*, 2615.
(32) Lyon, C. E.; Suh, E. S.; Dobson, C. M.; Hore, P. J. *J. Am. Chem. Soc.* **2002**, *124*, 13018.
(33) Bowers, C. R.; Weitekamp, D. P. *J. Am. Chem. Soc.* **1987**, *109*, 5541.
(34) Eisenberg, R.; Eisenschmid, T. C.; Chinn, M. S.; Kirss, R. U. *Advances In Chemistry Series* **1992**, 47.
(35) Blazina, D.; Dunne, J. P.; Aiken, S.; Duckett, S. B.; Elkington, C.; McGrady, J. E.; Poli, R.; Walton, S. J.; Anwar, M. S.; Jones, J. A.; Carteret, H. A. *Dalt. Trans.* **2006**, 2072.
(36) Dunne, J. P.; Blazina, D.; Aiken, S.; Carteret, H. A.; Duckett, S. B.; Jones, J. A.; Poli, R.; Whitwood, A. C. *Dalt. Trans.* **2004**, 3616.
(37) Anwar, M. S.; Blazina, D.; Carteret, H. A.; Duckett, S. B.; Halstead, T. K.; Jones, J. A.; Kozak, C. M.; Taylor, R. J. K. *Phys. Rev. Lett.* **2004**, *93*.
(38) Duckett, S. B.; Mewis, R. E. *Accounts of Chemical Research* **2012**.
(39) Duecker, E. B.; Kuhn, L. T.; Muennemann, K.; Griesinger, C. *Journal of Magnetic Resonance* **2012**, *214*, 159.
(40) Benn, R.; Brenneke, H.; Heck, J.; Rufinska, A. *Inorg. Chem.* **1987**, *26*, 2826.
(41) Carlton, L.; Emdin, A.; Lemmerer, A.; Fernandes, M. A. *Magn. Reson. Chem.* **2008**, *46*, S56.
(42) Crabtree, R. H.; Hlatky, G. G. *Inorg. Chem.* **1982**, *21*, 1273.
(43) Thomas, A.; Haake, M.; Grevels, F. W.; Bargon, J. *Angew. Chem.-Int. Edit. Engl.* **1994**, *33*, 755.
(44) Thomas, R. J. W.; Laurence, G. S.; Diamantis, A. A. *Inorganica Chimica Acta* **1978**, *30*, L353.
(45) Carlton, L.; Emdin, A.; Lemmerer, A.; Fernandes, M. A. *Magn. Reson. Chem.* **2008**, *46*, S56.
(46) Schott, D.; Sleigh, C. J.; Lowe, J. P.; Duckett, S. B.; Mawby, R. J.; Partridge, M. G. *Inorg. Chem.* **2002**, *41*, 2960.
(47) Duckett, S. B.; Wood, N. J. *Coordination Chemistry Reviews* **2008**, *252*, 2278.
(48) Desrosiers, P. J.; Cai, L. H.; Lin, Z. R.; Richards, R.; Halpern, J. *J. Am. Chem. Soc.* **1991**, *113*, 4173.
(49) Archer, L. J.; George, T. A. *Inorganica Chimica Acta-Letters* **1980**, *44*, L129.
(50) Mohr, F.; Priver, S. H.; Bhargava, S. K.; Bennett, M. A. *Coordination Chemistry Reviews* **2006**, *250*, 1851.
(51) Macgregor, S. A.; Eisenstein, O.; Whittlesey, M. K.; Perutz, R. N. *J. Chem. Soc.-Dalton Trans.* **1998**, 291.
(52) Schott, D.; Callaghan, P.; Dunne, J.; Duckett, S. B.; Godard, C.; Goicoechea, J. M.; Harvey, J. N.; Lowe, J. P.; Mawby, R. J.; Muller, G.; Perutz, R. N.; Poli, R.; Whittlesey, M. K. *Dalton Trans.* **2004**, 3218.
(53) Pivovarov, A. P. *Russ. Chem. Bull.* **2008**, *57*, 289.
(54) Crabtree, R. H.; Hlatky, G. G. *Inorg. Chem.* **1984**, *23*, 2388.
(55) Graff, J. L.; Sobieralski, T. J.; Wrighton, M. S.; Geoffroy, G. L. *J. Am. Chem. Soc.* **1982**, *104*, 7526.
(56) Woerpel, K. A.; Bergman, R. G. *J. Am. Chem. Soc.* **1993**, *115*, 7888.
(57) Jazzar, R. F. R.; Bhatia, P. H.; Mahon, M. F.; Whittlesey, M. K. *Organometallics* **2003**, *22*, 670.
(58) Kubas, G. J.; Burns, C. J.; Khalsa, G. R. K.; Vandersluys, L. S.; Kiss, G.; Hoff, C. D. *Organometallics* **1992**, *11*, 3390.
(59) Rothfuss, H.; Huffman, J. C.; Caulton, K. G. *Inorg. Chem.* **1994**, *33*, 2946.
(60) Kubas, G. J. *J. Organomet. Chem.* **2009**, *694*, 2648.
(61) Bryndza, H. E.; Tam, W. *Chem. Rev.* **1988**, *88*, 1163.
(62) Dziegielewski, J. O.; Gilbortnowska, R.; Mrzigod, J.; Malecki, J. G. *Polyhedron* **1995**, *14*, 1375.

Appendix 2: Summary of complexes and isomers

Complexes in Chapter 2 and 3

Real complexes are assigned a prefix, such as A or P. All other complexes are theoretical models.

The suffix ‘ is used to define a transition state. A triplet state is indicated by a superscript 3 as a suffix. If two transition states are possible from a single geometry, the suffix H or C is used to indicate the migrations of H or C for the creation of a C-C bond.

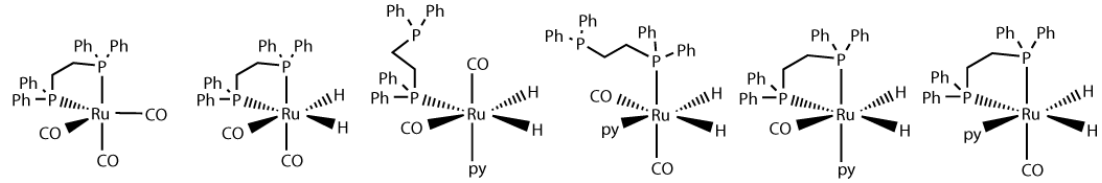

P1 **P2** **P2a** **P2b** **P2c** **P2d**

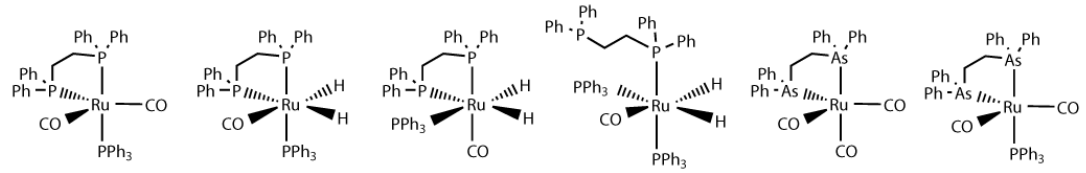

P3 **P4a** **P4b** **P5** **A1** **A2**

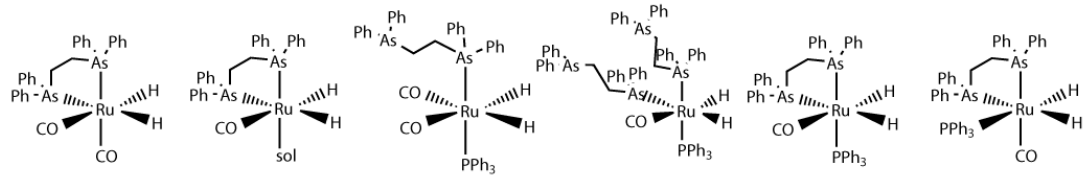

A3 **A4** **A5** **A6** **A7a** **A7b**

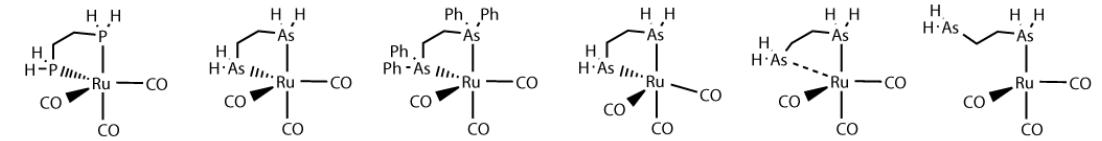

P1m **1** **A1a** **1a’** **1b’** **1b**

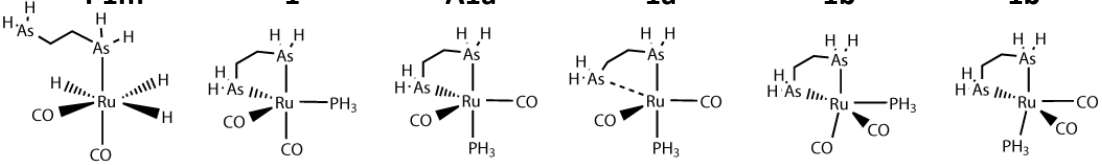

1c **2a** **2b** **2b’** **2c’** **2d’**

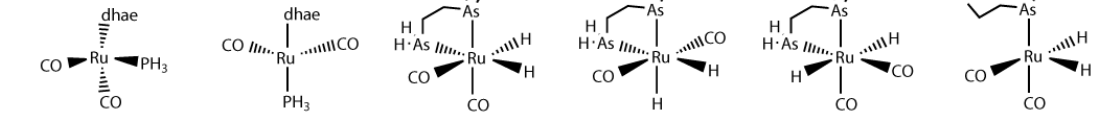

2e **2f** **3a** **3b** **3c** **3d**

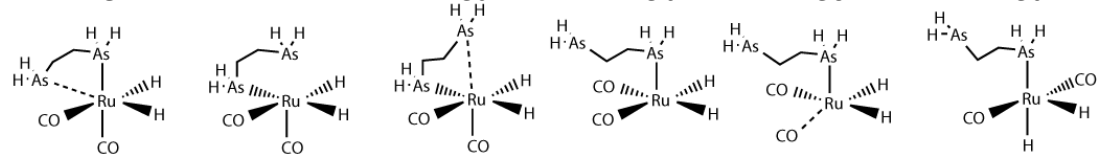

3d’ **3e** **3e’** **3f** **3f’** **3g**

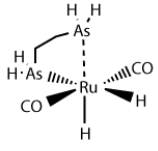

3g’

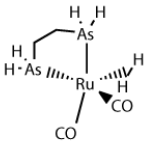

3xA’

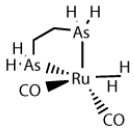

3xB’

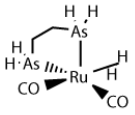

3xC’

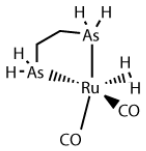

3xD’

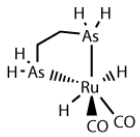

3xE’

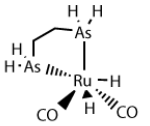

3xF’

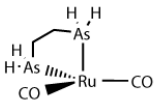

4a

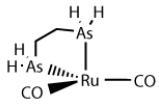

4a^3

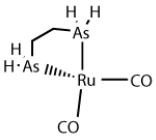

4b

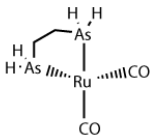

4b^3

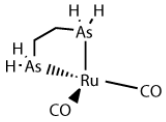

4c’

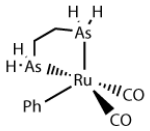

4b^s

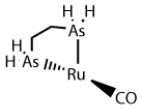

5a

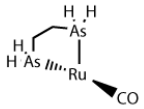

5a^3

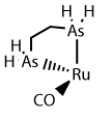

5b^3

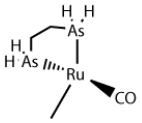

5a^s

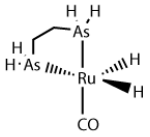

6a

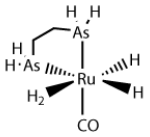

6b

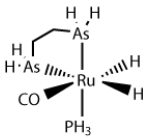

7a

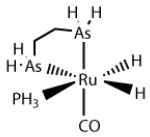

7b

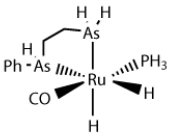

7c

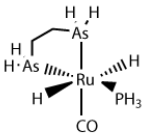

7d

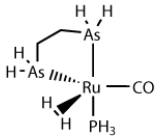

7xA’

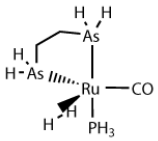

7xB’

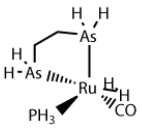

7xC’

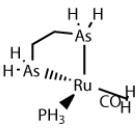

7xD’

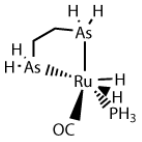

7xE’

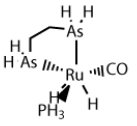

7xF’

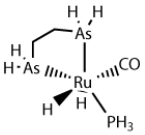

7xG’

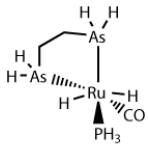

7xH’

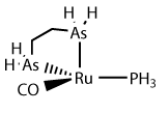

8a

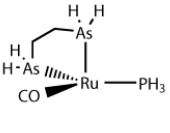

8a^3

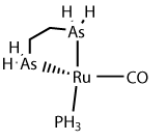

8b

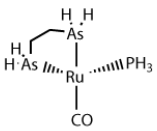

8c^3

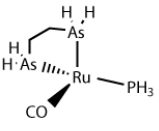

8d’

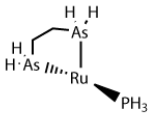

9a

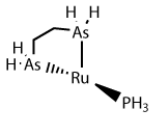

9a^3

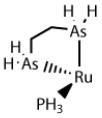

9b^3

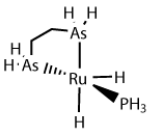

10a

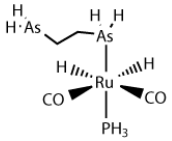

10b

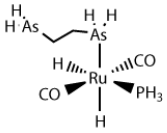

10c

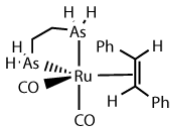

A8

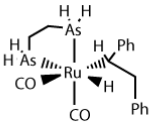

A9a

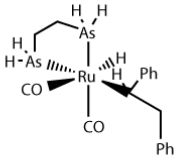

A9b

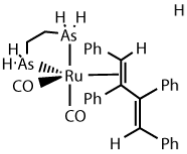

A10

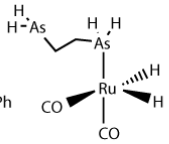

3d

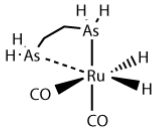

3d’

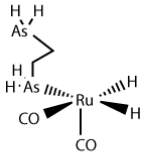

3d’

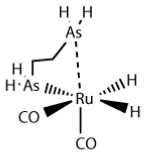

3e’

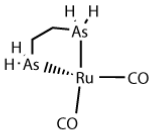

4b

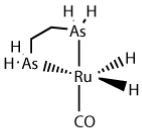

6a

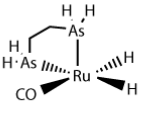

6c

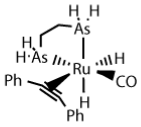

11a

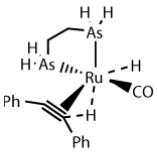

11a’

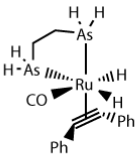

11b

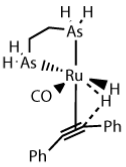

11b’

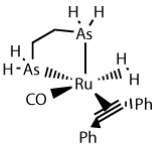

11c

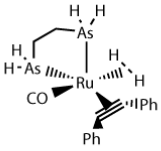

11c’

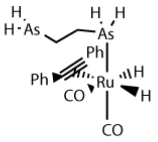

12a

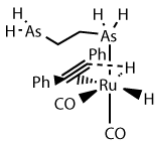

12a’

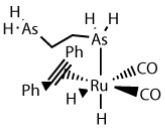

12b

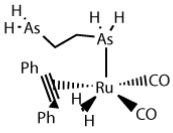

12c

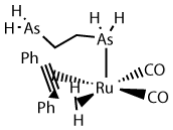

12c’

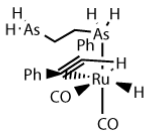

12d

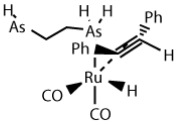

12d’

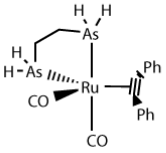

13

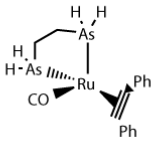

13a

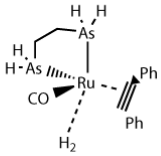

13a’

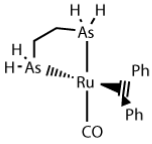

13b

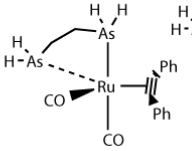

13’

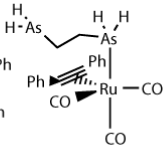

14

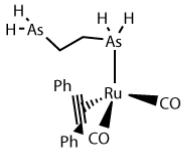

14a

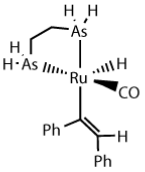

15a

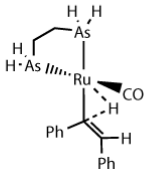

15a’

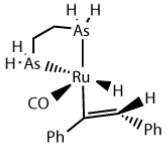

15b

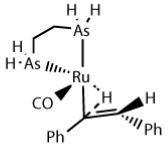

15b’

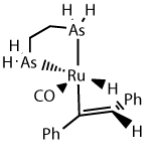

15c

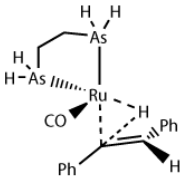

15d’

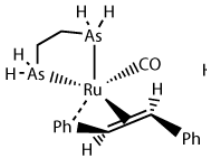

16a

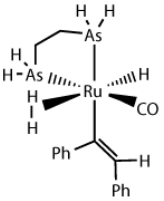

16b

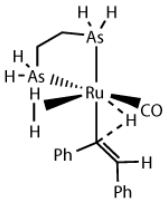

16b’

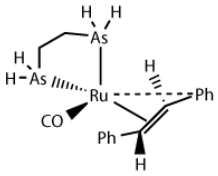

16c

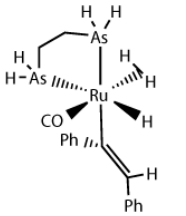

16d

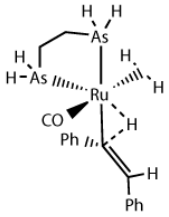

16d’

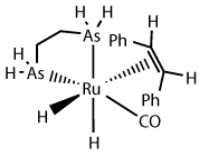

17a

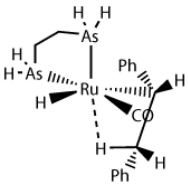

17a’

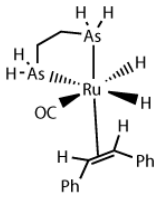

17b

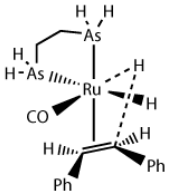

17b’

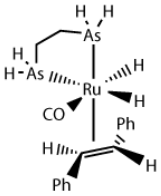

17c

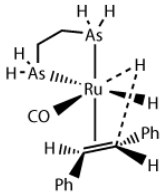

17c’

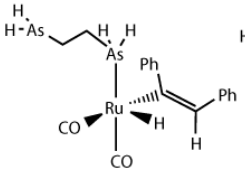

18a

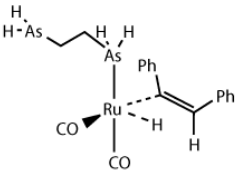

18a’

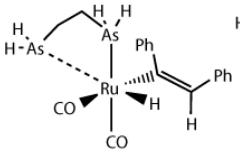

18aR’

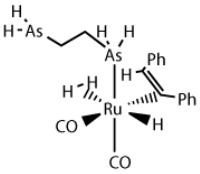

19a

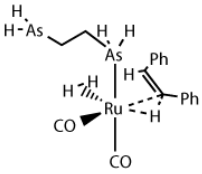

19a’

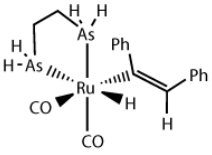

20a

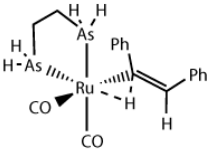

20a’

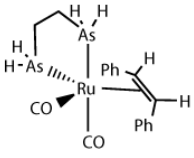

20b

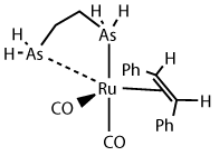

20b’

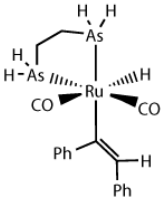

20c

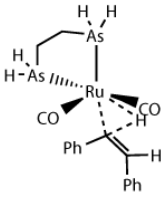

20c’

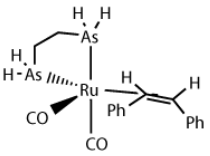

20d

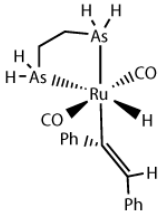

20e

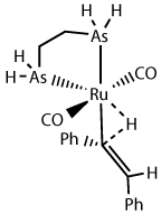

20e’

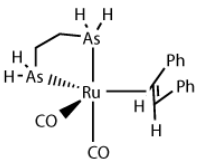

20f

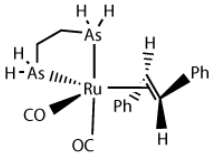

20g

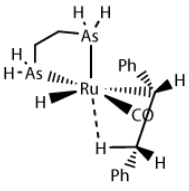

22a

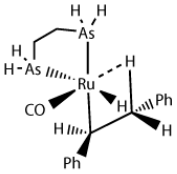

22b

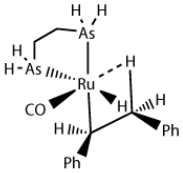

22c

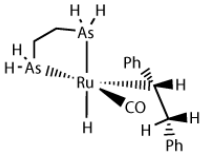

23a

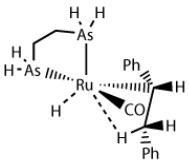

23a’

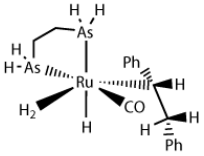

23b

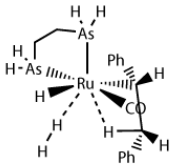

23b’

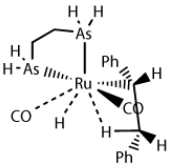

23c’

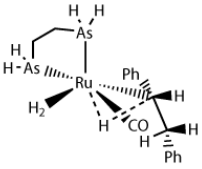

23d’

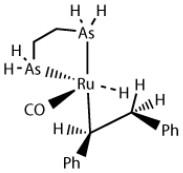

23e’

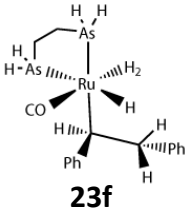

23f

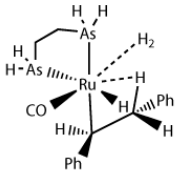

23f’

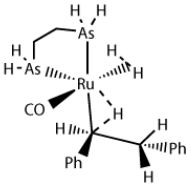

23g’

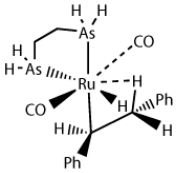

23h

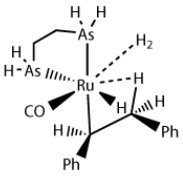

23i’

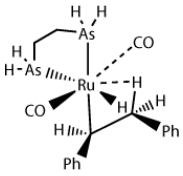

23j’

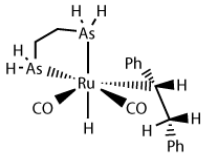

24

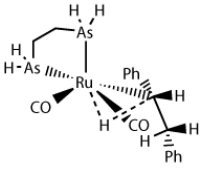

24a’

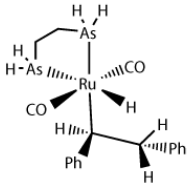

24b

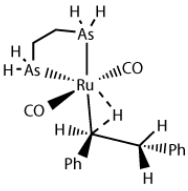

24b’

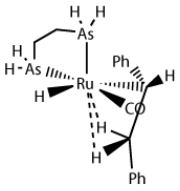

22aT’

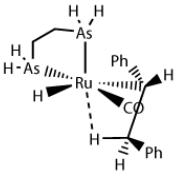

22aT

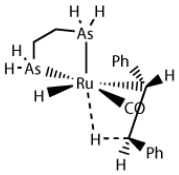

17aT’

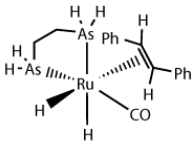

17aT

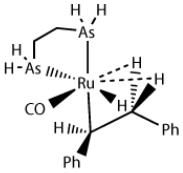

22bT’

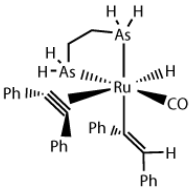

25a

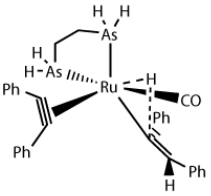

25a’

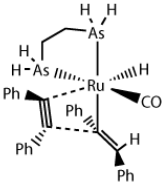

25aC’

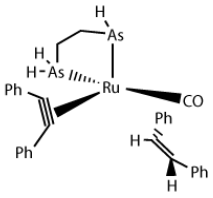

25b

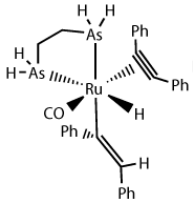

25c

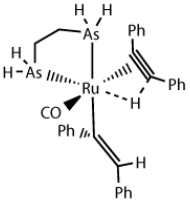

25c’

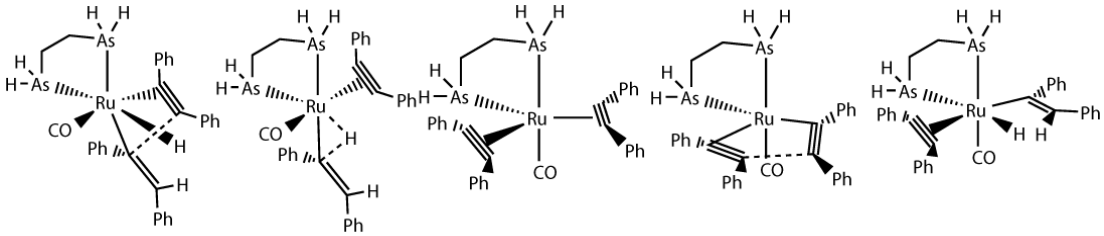

25cC’ **25cV’** **25d** **25d’** **25e**

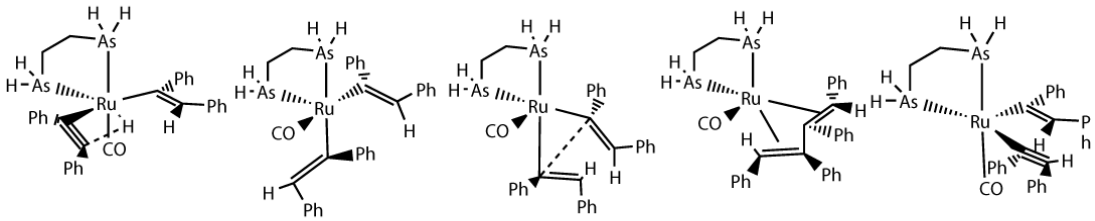

25e’ **26a** **26a’** **26b** **26c**

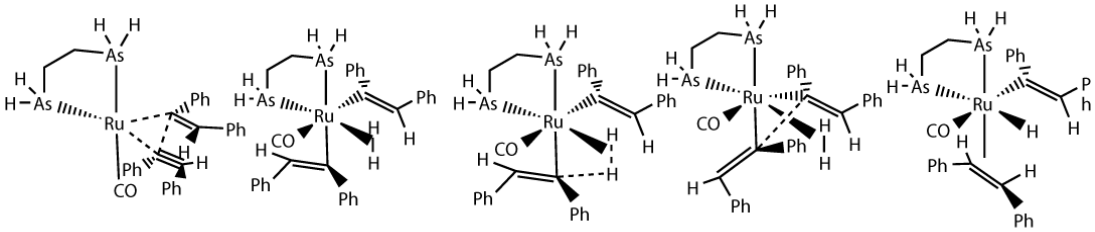

26c’ **27a** **27a’** **27aC’** **27b**

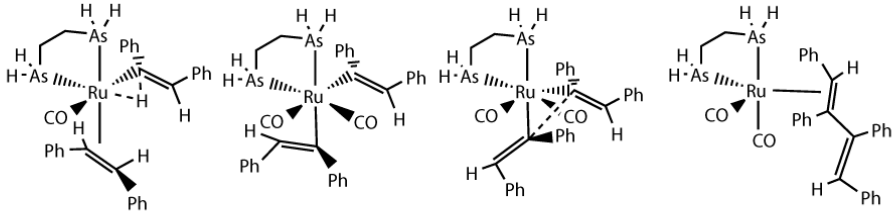

27b’ **28a** **28a’** **28b**

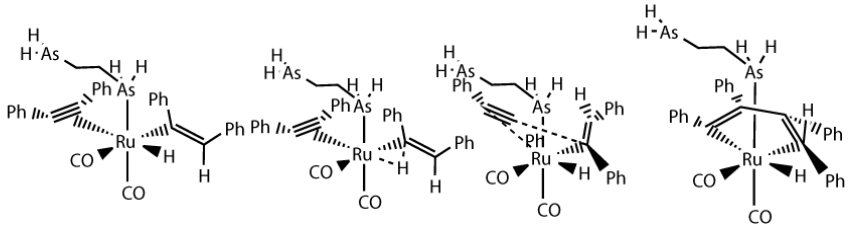

29a **29a’** **29aC’** **29b**

Complexes in Chapter 4

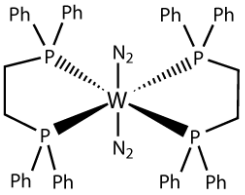

1

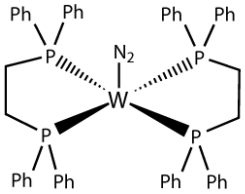

2

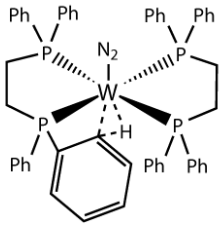

2’

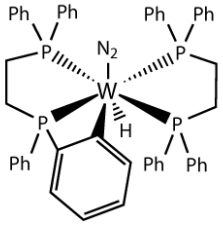

2b

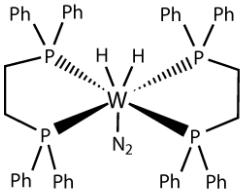

3

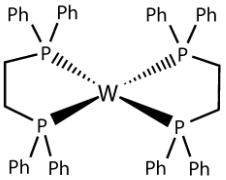

4a[1]

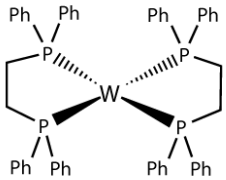

4a[3]

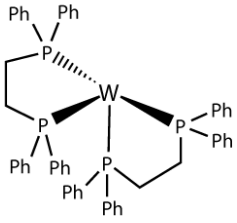

4b[1]

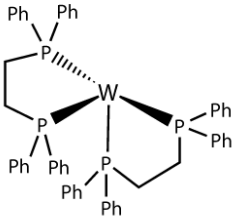

4b[3]

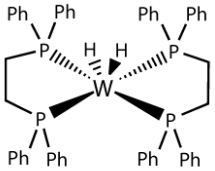

5a

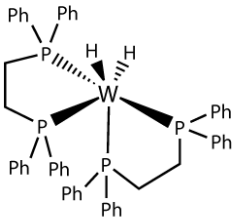

5b

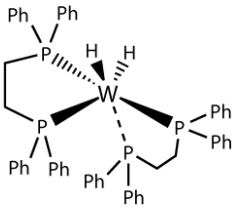

5a’

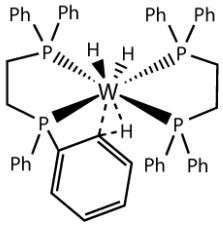

5aA’

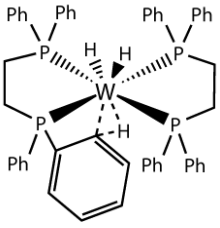

5aB’

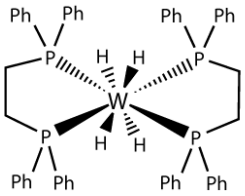

6a

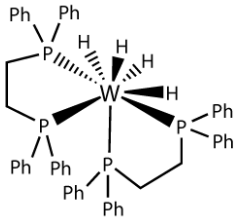

6b

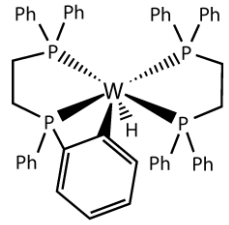

7a

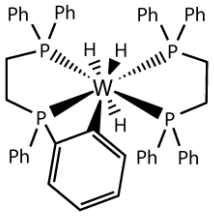

8a

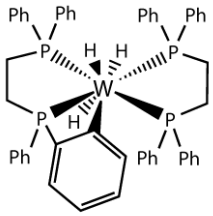

8b

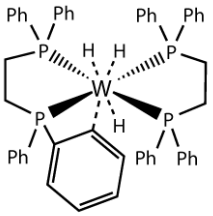

8b'

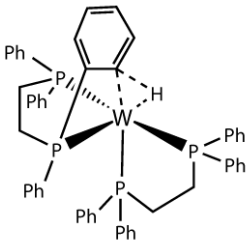

9a'

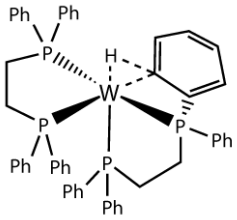

9b'

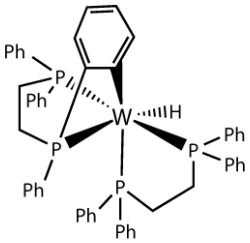

10a

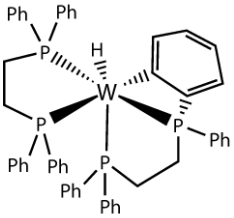

10b

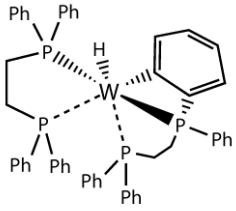

10a'

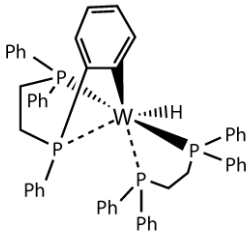

10b'

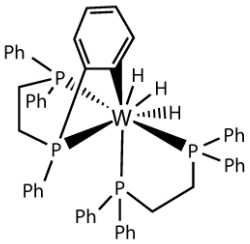

11a

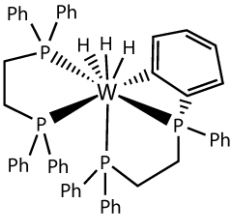

11b

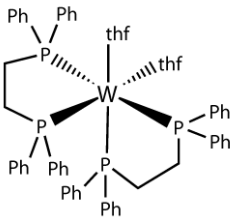

12

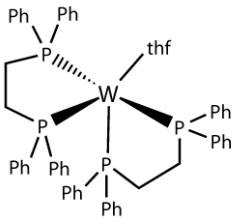

13

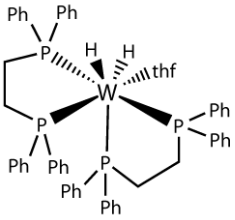

14a

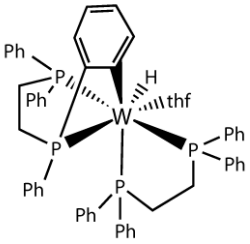

14bA

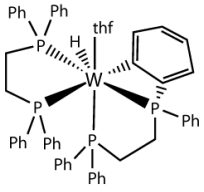

14bB

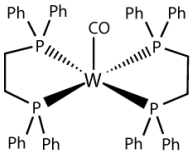

15

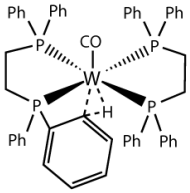

15’

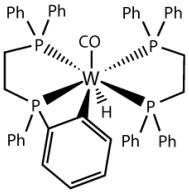

15b

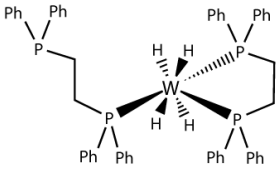

6c

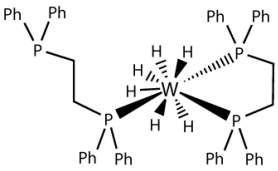

16

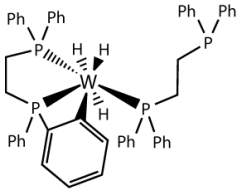

8c

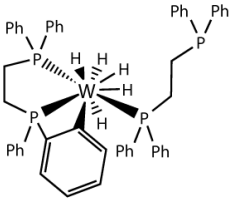

17a

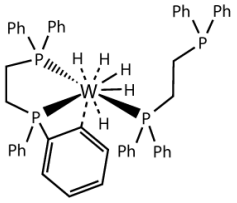

17b’

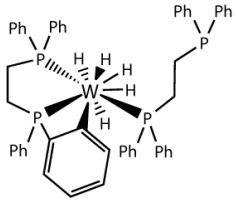

17c

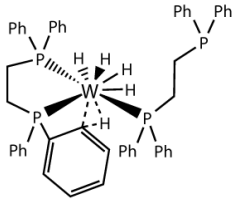

17d’

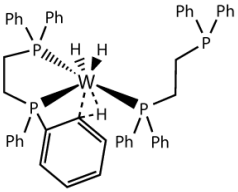

18a’

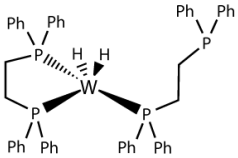

18b

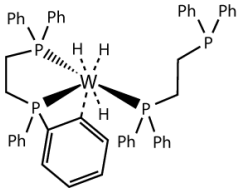

18b’

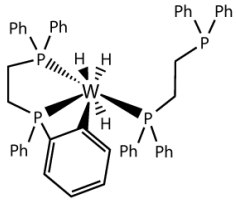

18c

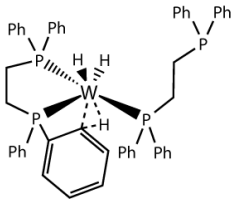

18d’

Definitions

This section contains Definitions of any terms specific to the thesis, including abbreviations and codes used in illustrations.

General Chemistry

dppe = diphenylphosphinoethane, $Ph_2PCH_2CH_2PPh_2$-κ_2P

dpae = diphenylarsinoethane, $Ph_2AsCH_2CH_2AsPh_2$-κ^2P

dhae = dihydroarsinoethane, $Ph_2AsCH_2CH_2AsPh_2$-κ^2P

BINAP = 2,2'-Bis(diphenylphosphino)-1,1'-binaphthyl

dmpe = dimethylphosphinoethane

THF = tetrahydrofuran

Ph = phenyl C_6H_5

COD = Cyclooctadiene

cy = cyclohexyl C_6H_{11}

η^2– = eta^2 bound ligand

TBP = Trigonal Bipyramidal geometry

SBP = Square based Bipyramidal geometry

p-H_2 = *para*-hydrogen

py = pyridine C_5H_5N

^{t}Bu = tertiary-Butyl $C(CH_3)_3$

Å = Angstrom (1 x 10^{-10} m)

GC-MS = Gas Chromatography- Mass Spectrometry

NMR terms

NMR = Nuclear Magnetic Resonance

PHIP = Para-Hydrogen Induced Polarisation

EXSY = Exchange Spectroscopy

SABRE = Signal Enhancement by Reversible Exchange

PASADENA = *Para*-hydrogen and Synthesis Allow Dramatically Enhanced Nuclear Alignment

ALTADENA = Adiabatic Longitudinal Transport After Dissociation Engenders Net Alignment

HSQC = Heteronuclear Single Quantum Coherence

HMBC = Heteronuclear Multiple Bond Coherence

NOE = 2D Nuclear Overhauser Effect

OPSY = Only *Para*-hydrogen Spectroscopy

COSY = Homonuclear Correlation Spectroscopy

Computational Chemistry terms

DFT = Density Functional Theory

BSSE = Basis Set Superposition Error

A.U. = Hartree Atomic Units with 1 A.U. = 2625.4996 kJ mol^{-1}

SCF = Self Consistent Field

IEFPCM = Integral Equation Formalism Polarisable Continuum Model

COSMO = Conductor-like Screening Model

SMD = Solvation Model using Density from Truhlar and co. workers

def2-SVP = double-zeta basis set family from Ahlrichs, with polarisation functions on all atoms

def2-TZVP = triple-zeta basis set family from Ahlrichs, with polarisation functions on all atoms

lanl2dz = Basis set family using the D97V from Dunning and the Los Alamos ECP with associated DZ functions

ECP = Effective Core Potential MP2 = Second order Möller-Plesset theory

LSDA = Local Spin Density Approximation

GGA = Generalised Gradient Approximation

PBE0 = Hybrid functional by Adamo based on the GGA functional PBE

bp86 = GGA functional using the B88 exchange functional and VWN and P86 correlation functionals

xDH-PBE0 = Double hybrid functional based upon the PBE0 hybrid functional

STQN = Synchronous Transit and Quasi Newton methods from Peng for locating transition states

QM:MM = Quantum Mechanical: Molecular Mechanics Hybrid method

ONIOM = Our own N-layered Integrated molecular Orbital and molecular Mechanics

QM:MM method used in Gaussian software

RI = Resolution of Identity approximation RIJCOSX = Resolution of Identity approximation with the Chain of Spheres method

ZORA = 0th Order Regular Approximations, a method for representing relativistic effect on heavy nuclei.

GIAO = Gauge Including Atomic Orbitals

IGLO = Individual Gauge for Local Orbitals

FC = Fermi Contact

SD = Spin Dipolar

PSO = Paramagnetic Spin-Orbit

DSO = Diamagnetic Spin-Orbit

AIM = Atoms in Molecules

NCP = Nuclear Critical Point

BCP = Bond Critical Point

RCP = Ring Critical Point

List of References

1. Rabi, I.I. *Physical Review*. 1938; 53: 318-327.
2. Bloch, F. *Phys. Rev.* 1946; 70: 460-474.
3. Levitt, M.H., *Spin Dynamics: Basics of Nuclear Magnetic Resonance, 2nd Edition*. 2008: Wiley.
4. Kubas, G.J. *Journal of Organometallic Chemistry*. 2014; 751(0): 33-49.
5. Vaska, L. and J.W. DiLuzio. *Journal of the American Chemical Society*. 1962; 84(4): 679-680.
6. Kubas, G.J., et al. *Journal of the American Chemical Society*. 1986; 108(22): 7000-7009.
7. Kubas, G.J., R.R. Ryan, and D.A. Wrobleski. *Journal of the American Chemical Society*. 1986; 108(6): 1339-1341.
8. Osborn, J.A., et al. *Journal of the Chemical Society A - Inorganic Physical Theoretical*. 1966(12): 1711.
9. Halpern, J. *Inorganica Chimica Acta-Articles*. 1981; 50(1): 11-19.
10. *Bond Energies - Chemwiki*. 2015 15/09/2015]; Available from: http://chemwiki.ucdavis.edu/Theoretical_Chemistry/Chemical_Bonding/General_Principles_of_Chemical_Bonding/Bond_Energies.
11. Noyori, R., et al. *Journal of the American Chemical Society*. 1987; 109(19): 5856-5858.
12. Kitamura, M., M. Tokunaga, and R. Noyori. *Journal of the American Chemical Society*. 1993; 115(1): 144-152.
13. Clapham, S.E., A. Hadzovic, and R.H. Morris. *Coordination Chemistry Reviews*. 2004; 248: 2201-2237.
14. Eisenschmid, T.C., et al. *Journal of the American Chemical Society*. 1987; 109(26): 8089-8091.
15. Bowers, C.R. and D.P. Weitekamp. *Physical Review Letters*. 1986; 57(21): 2645-2648.
16. Pravica, M.G. and D.P. Weitekamp. *Chemical Physics Letters*. 1988; 145(4): 255-258.
17. Bowers, C.R. and D.P. Weitekamp. *Journal of the American Chemical Society*. 1987; 109(18): 5541-5542.
18. Hausser, K.H. and D. Stehlik, *Dynamic Nuclear Polarization in Liquids*, in *Advances in Magnetic Resonance*, J.S. Waugh, Editor. 1968, Academic Press. p. 79-139.
19. Borghini, M., W. Deboer, and K. Morimoto. *Physics Letters A*. 1974; A 48(4): 244-246.
20. Abragam, A. and M. Goldman. *Reports on Progress in Physics*. 1978; 41(3): 395-467.
21. Ardenkjaer-Larsen, J.H., et al. *Proceedings of the National Academy of Sciences of the United States of America*. 2003; 100(18): 10158-10163.
22. Prisner, T. and W. Koeckenberger. *Applied Magnetic Resonance*. 2008; 34(3-4): 213-218.
23. Colpa, J.P., D. Stehlik, and H.M. Vieth. *Chemical Physics*. 1980; 47(1): 73-85.
24. Bargon, J. *Helvetica Chimica Acta*. 2006; 89(10): 2082-2102.
25. Bargon, J., H. Fischer, and U. Johnsen. *Zeitschrift fur Naturforschung Part A - Astrophysik Physik und Physikalische Chemie*. 1967; A 22(10): 1551.
26. Lawler, R.G. *Journal of the American Chemical Society*. 1967; 89(21): 5519-&.

27. Bargon, J. and H. Fischer. *Zeitschrift fur Naturforschung Part A - Astrophysik Physik und Physikalische Chemie*. 1967; A 22(10): 1556.
28. Bhaskar, N.D., W. Happer, and T. McClelland. *Physical Review Letters*. 1982; 49(1): 25-28.
29. Albert, M.S., et al. *Nature*. 1994; 370(6486): 199-201.
30. Walker, T.G. and W. Happer. *Reviews of Modern Physics*. 1997; 69(2): 629-642.
31. Vieth, H.M., V. Macho, and D. Stehlik. *Chemical Physics Letters*. 1979; 60(3): 368-371.
32. Hartmann, S.R. and E.L. Hahn. *Physical Review*. 1962; 128(5): 2042.
33. Pelupessy, P. and E. Chiarparin. *Concepts in Magnetic Resonance*. 2000; 12(3): 103-124.
34. Brewer, W.D. *Journal of Low Temperature Physics*. 1977; 27(5-6): 651-682.
35. http://history.nasa.gov, S.P.a.a.h., *(retrieved 16.09.2014)*.
36. Green, R.A., et al. *Progress in Nuclear Magnetic Resonance Spectroscopy*. 2012; 67(0): 1-48.
37. Dennison, D.M. *Proceedings of the Royal Society of London Series A-Containing Papers of a Mathematical and Physical Character*. 1927; 115(771): 483-486.
38. Bonhoeffer, K.F. and P. Harteck. *Zeitschrift Fur Physikalische Chemie-Abteilung B-Chemie Der Elementarprozesse Aufbau Der Materie*. 1929; 4(1/2): 113-141.
39. Bonhoeffer, K.F. and P. Harteck. *Naturwissenschaften*. 1929; 17: 182-182.
40. Duckett, S.B., C.L. Newell, and R. Eisenberg. *Journal of the American Chemical Society*. 1994; 116(23): 10548-10556.
41. Burk, M.J., et al. *Journal of the American Chemical Society*. 1988; 110(15): 5034-5039.
42. Sargent, A.L. and M.B. Hall. *Inorganic Chemistry*. 1992; 31(2): 317-321.
43. Hasnip, S.K., et al. *Chem. Commun.* 1999: 1717-1718.
44. Adams, R.W., et al. *Science*. 2009; 323(5922): 1708-1711.
45. Eguillor, B., et al. *Journal of the American Chemical Society*. 2012; 134(44): 18257-18265.
46. Schott, D., et al. *Dalton Transactions*. 2004(20): 3218-3224.
47. Wang, W.H., et al. *Journal of the American Chemical Society*. 1996; 118(36): 8654-8657.
48. Poliakoff, M. and E. Weitz. *Accounts of Chemical Research*. 1987; 20(11): 408-414.
49. Aguilar, J.A., et al. *Chemical Communications*. 2007(11): 1183-1185.
50. Heitler, W. and F. London. *Zeitschrift fur Physik*. 1927; 44(6-7): 455-472.
51. Schrödinger, E. *Phys. Rev.* 1926; 28: 1049-1070.
52. Atkins, P.W., *Physical Chemistry*. 1999: Oxford university Press.
53. Hartree, D.R. *Proceeding of the Cambridge Philosophical Society*. 1928; 24: 89-110.
54. Hartree, D.R. *Proceeding of the Cambridge Philosophical Society*. 1928; 24: 111-132.
55. Hartree, D.R. *Proceeding of the Cambridge Philosophical Society*. 1928; 24: 426-437.
56. Fock, V. *Zeitschrift fur Physik*. 1930; 61(1-2): 126-148.
57. Headgordon, M., et al. *Chemical Physics Letters*. 1994; 219(1-2): 21-29.
58. Maurice, D. and M. Headgordon. *Molecular Physics*. 1999; 96(10): 1533-1541.
59. Purvis, G.D. and R.J. Bartlett. *The Journal of Chemical Physics*. 1982; 76(4): 1910-1918.
60. Van Voorhis, T. and M. Head-Gordon. *The Journal of Chemical Physics*. 2001; 115(11): 5033-5040.
61. Raghavachari, K., et al. *Chemical Physics Letters*. 1989; 157(6): 479-483.
62. Moller, C. and M.S. Plesset. *Physical Review*. 1934; 46(7): 0618-0622.

63. Coletti, C. and N. Re. *Performance of DFT and MP2 Approaches for Geometry of Rhenium Allenylidenes Complexes and the Thermodynamics of Phosphines Addition*. in *Computational Science and its Applications - ICCSA 2012, PT I*. SPRINGER-VERLAG BERLIN.
64. Hohenberg, P. and W. Kohn. *Physical Review B*. 1964; 136(3B): B864.
65. Kohn, W. and L.J. Sham. *Physical Review*. 1965; 140(4A): 1133.
66. Becke, A.D. *Journal of Chemical Physics*. 2014; 140(18): 18A301-18A318.
67. Jensen, F., *Introduction to Computational Chemistry*. 2004: John Wiley & Sons, Inc.
68. Sousa, S.F., P.A. Fernandes, and M.J. Ramos. *The Journal of Physical Chemistry A*. 2007; 111(42): 10439-10452.
69. Dirac, P.A.M. *Proceeding of the Cambridge Philosophical Society*. 1930; 26: 376-385.
70. Slater, J.C. *Physical Review*. 1951; 81(3): 385-390.
71. Ceperley, D. *Physical Review B*. 1978; 18(7): 3126-3138.
72. Ceperley, D.M. and B.J. Alder. *Physical Review Letters*. 1980; 45(7): 566-569.
73. Vosko, S.H., L. Wilk, and M. Nusair. *Canadian Journal of Physics*. 1980; 58(8): 1200-1211.
74. Perdew, J.P. and A. Zunger. *Physical Review B*. 1981; 23(10): 5048-5079.
75. Perdew, J.P. and Y. Wang. *Physical Review B*. 1992; 45(23): 13244-13249.
76. Ahlrichs, R., F. Furche, and S. Grimme. *Chemical Physics Letters*. 2000; 325(1â€“3): 317-321.
77. Becke, A.D. *The Journal of Chemical Physics*. 1997; 107(20): 8554-8560.
78. Becke, A.D. *Journal of Chemical Physics*. 1986; 84(8): 4524-4529.
79. Becke, A.D. *Journal of Chemical Physics*. 1992; 96(3): 2155-2160.
80. Becke, A.D. *Journal of Chemical Physics*. 1992; 97(12): 9173-9177.
81. Becke, A.D. *Journal of Chemical Physics*. 1993; 98(7): 5648-5652.
82. Becke, A.D. *Journal of Chemical Physics*. 1996; 104(3): 1040-1046.
83. Perdew, J.P. and W. Yue. *Physical Review B*. 1986; 33(12, 2): 8800-8802.
84. Becke, A.D. *Physical Review A*. 1988; 38(6): 3098-3100.
85. Langreth, D.C. and J.P. Perdew. *Physical Review B*. 1980; 21(12): 5469-5493.
86. Perdew, J.P. *Physical Review Letters*. 1985; 55(16): 1665-1668.
87. Perdew, J.P. *Physical Review B*. 1986; 33(12): 8822-8824.
88. Wang, Y. and J.P. Perdew. *Phys. Rev. B*. 1991; 43: 8911-8916.
89. Perdew, J.P., K. Burke, and M. Ernzerhof. *Physical Review Letters*. 1996; 77(18): 3865-3868.
90. Kurth, S., J.P. Perdew, and P. Blaha. *International Journal of Quantum Chemistry*. 1999; 75(4-5): 889-909.
91. Perdew, J., *Electronic Structure of Solids '91*. 1991: John Wiley & Sons, Inc.
92. Lee, C.T., W.T. Yang, and R.G. Parr. *Physical Review B*. 1988; 37(2): 785-789.
93. Colle, R. and O. Salvetti. *Theoretica Chimica Acta*. 1975; 37(4): 329-334.
94. *TURBOMOLE V6.4 2012, a development of University of Karlsruhe and Forschungszentrum Karlsruhe GmbH, 1989-2007, TURBOMOLE GmbH, since 2007; available from* http://www.turbomole.com.
95. Becke, A.D. *Journal of Chemical Physics*. 1993; 98(2): 1372-1377.
96. Pople, J.A., et al. *Journal of Chemical Physics*. 1989; 90(10): 5622-5629.
97. Curtiss, L.A., et al. *Journal of Chemical Physics*. 1990; 93(4): 2537-2545.
98. Perdew, J.P., M. Emzerhof, and K. Burke. *Journal of Chemical Physics*. 1996; 105(22): 9982-9985.
99. Vetere, V., C. Adamo, and P. Maldivi. *Chemical Physics Letters*. 2000; 325(1-3): 99-105.

100. Nie, D., et al. *Journal of Molecular Structure-Theochem*. 2008; 861(1-3): 97-102.
101. Kulkarni, A.D. and D.G. Truhlar. *Journal of Chemical Theory and Computation*. 2011; 7(7): 2325-2332.
102. Grimme, S. *Journal of Computational Chemistry*. 2006; 27(15): 1787-1799.
103. Grimme, S., et al. *Journal of Chemical Physics*. 2010; 132(15): 154104-154104.
104. Grimme, S. *The Journal of Chemical Physics*. 2006; 124(3): 034108-1.
105. Schwabe, T. and S. Grimme. *Physical Chemistry Chemical Physics*. 2006; 8(38): 4398-4401.
106. Bremond, E. and C. Adamo. *The Journal of Chemical Physics*. 2011; 135(2): 024106-024106.
107. Perdew, J.P. and K. Schmidt, *Density Functional Theory and Its Application to Materials*. 2001: AIP Press.
108. Zhang, I.Y., et al. *The Journal of Chemical Physics*. 2012; 136(17): 174103-1 - 174103-8.
109. Slater, J.C. *Phys. Rev.* 1930; 36: 57-64.
110. Kendall, R.A., T.H. Dunning, and R.J. Harrison. *Journal of Chemical Physics*. 1992; 96(9): 6796-6806.
111. Jr, T.H.D. and P.J. Hay, *Modern Theoretical Chemistry*. 1976: Plenum, New York.
112. Xu, X. and D.G. Truhlar. *Journal of Chemical Theory and Computation*. 2011; 7(9): 2766-2779.
113. Ramsey, N.F. *Physical Review*. 1950; 77(4): 567-567.
114. Ramsey, N.F. *Physical Review*. 1950; 78(6): 699-703.
115. Hornig, J.F. and J.O. Hirschfelder. *Journal of Chemical Physics*. 1955; 23(3): 474-476.
116. Guy, J. and J. Tillieu. *Journal of Chemical Physics*. 1956; 24(5): 1117-1117.
117. Das, T.P. and R. Bersohn. *Physical Review*. 1956; 104(3): 849-849.
118. McGarver, B.R. *Journal of Chemical Physics*. 1957; 27(1): 68-74.
119. Ziegler, T. and J. Autschbach. *Chemical Reviews*. 2005; 105(6): 2695-2722.
120. Cheeseman, J.R., et al. *Journal of Chemical Physics*. 1996; 104(14): 5497-5509.
121. Schindler, M. and W. Kutzelnigg. *Journal of Chemical Physics*. 1982; 76(4): 1919-1933.
122. Frisch, M.J. and others, *Gaussian 09, Revision B.01*. 2010.
123. Lenthe, E.v., E.J. Baerends, and J.G. Snijders. *The Journal of Chemical Physics*. 1993; 99(6): 4597-4610.
124. Deng, W., J.R. Cheeseman, and M.J. Frisch. *Journal of Chemical Theory and Computation*. 2006; 2(4): 1028-1037.
125. Helgaker, T., M. Watson, and N.C. Handy. *Journal of Chemical Physics*. 2000; 113(21): 9402-9409.
126. Rablen, P.R., S.A. Pearlman, and J. Finkbiner. *Journal of Physical Chemistry A*. 1999; 103(36): 7357-7363.
127. Kutzelnigg, W., U. Fleischer, and M. Schindler, *The IGLO-Method: Ab-initio Calculation and Interpretation of NMR Chemical Shifts and Magnetic Susceptibilities*, in *Deuterium and Shift Calculation*. 1991, Springer Berlin Heidelberg. p. 165-262.
128. Miertus, S., E. Scrocco, and J. Tomasi. *Chemical Physics*. 1981; 55(1): 117-129.
129. Mennucci, B. *Wiley Interdisciplinary Reviews: Computational Molecular Science*. 2012; 2(3): 386-404.
130. Barone, V. and M. Cossi. *Journal of Physical Chemistry A*. 1998; 102(11): 1995-2001.
131. Cossi, M., et al. *Journal of Computational Chemistry*. 2003; 24(6): 669-681.
132. Scalmani, G. and M.J. Frisch. *Journal of Chemical Physics*. 2010; 132(11): 15-15.
133. Klamt, A. and G. Schuurmann. *J. Chem. Soc. Perkin Trans. 2*. 1993: 799-805.

134. Neese, F. *Journal of Computational Chemistry*. 2003; 24(14): 1740-1747.
135. Neese, F., T. Schwabe, and S. Grimme. *Journal of Chemical Physics*. 2007; 126(12): 124115-124115.
136. Kossmann, S. and F. Neese. *Chemical Physics Letters*. 2009; 481(4-6): 240-243.
137. Neese, F. *Wiley Interdisciplinary Reviews: Computational Molecular Science*. 2012; 2(1): 73-78.
138. Eichkorn, K., et al. *Chemical Physics Letters*. 1995; 242(6): 652-660.
139. Billings, F.P. and J.E. Bloor. *Journal of Chemical Physics*. 1971; 55(11): 5178-5190.
140. Whitten, J.L. *Journal of Chemical Physics*. 1973; 58(10): 4496-4501.
141. Neese, F., et al. *Chemical Physics*. 2009; 356(1-3, SI): 98-109.
142. Dunne, J.P., et al. *Dalton Transactions*. 2004(21): 3616-3628.
143. Blazina, D., et al. *Dalton Transactions*. 2006(17): 2072-2080.
144. Lopez-Serrano, J., A. Lledos, and S.B. Duckett. *Organometallics*. 2008; 27(1): 43-52.
145. Kozinets, E.M., et al. *Dalton Transactions*. 2013; 42(32): 11720-11730.
146. Evans, D., et al. *Nature*. 1965; 208(5016): 1203-1203.
147. Evans, D., J.A. Osborn, and G. Wilkinson. *Journal of the Chemical Society A - Inorganic Physical Theoretical*. 1968(12): 3133-3133.
148. Matteoli, U., et al. *Journal of Molecular Catalysis*. 1981; 12(3): 265-319.
149. Bielawski, C.W., J. Louie, and R.H. Grubbs. *Journal of the American Chemical Society*. 2000; 122(51): 12872-12873.
150. Macgregor, S.A., et al. *Journal of the Chemical Society-Dalton Transactions*. 1998(2): 291-300.
151. Harvey, J.N. and M. Aschi. *Faraday Discussions*. 2003; 124: 129-143.
152. Harvey, J.N. and R. Poli. *Dalton Transactions*. 2003(21): 4100-4106.
153. Duckett, S.B., R.J. Mawby, and M.G. Partridge. *Chem. Commun.* 1996: 383-384.
154. Schott, D., et al. *Inorganic Chemistry*. 2002; 41(11): 2960-2970.
155. Kim, J.Y., M.J. Jun, and W.Y. Lee. *Polyhedron*. 1996; 15(21): 3787-3793.
156. Jung, C.W. and P.E. Garrou. *Organometallics*. 1982; 1(4): 658-666.
157. Kawano, H., et al. *Chemistry Letters*. 1999; 28(5): 401-402.
158. Ball, G.E. and B.E. Mann. *Journal of the Chemical Society-Chemical Communications*. 1992(7): 561-563.
159. Said, R.B., B. Tangour, and J.-C. Barthelat. *Journal of Molecular Structure-Theochem*. 2008; 857: 115-122.
160. Bailar, J.C. *Journal of Inorganic; Nuclear Chemistry*. 1958; 8: 165-175.
161. Heinekey, D.M. and W.J. Oldham. *Chemical Reviews*. 1993; 93(3): 913-926.
162. Soubra, C., et al. *Inorganic Chemistry*. 2001; 40(4): 620-627.
163. Al-Ibadi, M.A.M., S.B. Duckett, and J.E. McGrady. *Dalton Trans.* 2012; 41: 4618-4625.
164. Frisch, M.J. and others, *Gaussian 03, Revision C.02*. 2004.
165. Hay, P.J. and W. Wadt. *Journal of Chemical Physics*. 1985; 82(1): 270-283.
166. Wadt, W.R. and P.J. Hay. *Journal of Chemical Physics*. 1985; 82(1): 284-298.
167. Hay, P.J. and W. Wadt. *Journal of Chemical Physics*. 1985; 82(1): 299-310.
168. Check, C.E., et al. *The Journal of Physical Chemistry A*. 2001; 105(34): 8111-8116.
169. Raghavachari, K., et al. *Journal of Chemical Physics*. 1980; 72(1): 650-654.
170. McLean, A.D. and G.S. Chandler. *Journal of Chemical Physics*. 1980; 72(10): 5639-5648.
171. Peng, C.Y. and H.B. Schlegel. *Israel Journal of Chemistry*. 1993; 33(4): 449-454.
172. Peng, C.Y., et al. *Journal of Computational Chemistry*. 1996; 17(1): 49-56.
173. Adamo, C. and V. Barone. *Journal of Chemical Physics*. 1999; 110(13): 6158-6170.
174. Andrae, D., et al. *Theoretica Chimica Acta*. 1991; 78(4): 247-266.

175. Weigend, F. and R. Ahlrichs. *Physical Chemistry Chemical Physics*. 2005; 7(18): 3297-3305.
176. Hirva, P., et al. *Journal of Molecular Modeling*. 2008; 14(3): 171-181.
177. Fomine, S. and M.A. Tlenkopatchev. *Organometallics*. 2010; 29(7): 1580-1587.
178. Boys, S.F. and F. Bernadi. *Molecular Physics*. 1970; 19(4): 553-553.
179. Simon, S., M. Duran, and J.J. Dannenberg. *Journal of Chemical Physics*. 1996; 105(24): 11024-11031.
180. Bunten, K.A., et al. *Organometallics*. 2000; 19(18): 3674-3682.
181. Frisch, M.J. and others, *Gaussian 98*. 1998.
182. Gottschalk-Gaudig, T., et al. *Inorganic Chemistry*. 2000; 39(18): 3957-3962.
183. Elian, M. and R. Hoffmann. *Inorganic Chemistry*. 1975; 14(5): 1058-1076.
184. Ogasawara, M., et al. *Journal of the American Chemical Society*. 1995; 117(34): 8869-8870.
185. Albright, T.A., J.K. Burdett, and M.H. Whangbo, *Orbital Interactions in Chemistry*. 1985: Wiley, New York.
186. Tamura, H., et al. *Journal of the American Chemical Society*. 2003; 125(51): 16114-16126.
187. Sakaki, S., et al. *Journal of the American Chemical Society*. 2004; 126(10): 3332-3348.
188. Sumimoto, M., et al. *Journal of the American Chemical Society*. 2004; 126(33): 10457-10471.
189. Buhl, M., et al. *Journal of Chemical Theory and Computation*. 2008; 4(9): 1449-1459.
190. Fomine, S., S. Gutierrez, and M.A. Tlenkopatchev. *Journal of Organometallic Chemistry*. 2009; 694(20): 3287-3296.
191. Cances, E., B. Mennucci, and J. Tomasi. *Journal of Chemical Physics*. 1997; 107(8): 3032-3041.
192. Mennucci, B., E. Cances, and J. Tomasi. *Journal of Physical Chemistry B*. 1997; 101(49): 10506-10517.
193. Cances, E. and B. Mennucci. *Journal of Mathematical Chemistry*. 1998; 23(3-4): 309-326.
194. Devarajan, D. and D.H. Ess. *Inorganic Chemistry*. 2012; 51(11): 6367-6375.
195. Schwarzenbach, G. *Helvetica Chimica Acta*. 1952; 35(7): 2344-2359.
196. Gargulak, J.D., et al. *Journal of the American Chemical Society*. 1992; 114(23): 8933-8945.
197. Sanchez-Delgado, R.A., J.S. Bradley, and G. Wilkinson. *J. Chem. Soc., Dalton Trans.* 1976: 399-404.
198. Gordon, E.M. and R. Eisenberg. *Journal of Organometallic Chemistry*. 1986; 306(2): C53-C57.
199. J. Sleigh, C., et al. *Chem. Commun.* 1999: 1223-1224.
200. Li, C., et al. *Organometallics*. 1997; 16(19): 4223-4225.
201. L'Eplattenier, F. and F. Calderazzo. *Inorganic Chemistry*. 1968; 7(7): 1290-1293.
202. Bray, J.M. and R.J. Mawby. *J. Chem. Soc., Dalton Trans.* 1987: 2989-2993.
203. Field, L.R., E. Wilhelm, and R. Battino. *The Journal of Chemical Thermodynamics*. 1974; 6(3): 237-243.
204. Schwab, P., et al. *Angewandte Chemie International Edition in English*. 1995; 34(18): 2039-2041.
205. Tsipis, A.C., A.G. Orpen, and J.N. Harvey. *Dalton Transactions*. 2005(17): 2849-2858.
206. Tolman, C.A. *Journal of the American Chemical Society*. 1970; 92(10): 2953-2956.
207. Tolman, C.A. *Chemical Reviews*. 1977; 77(3): 313-348.
208. Setiawan, D., et al. *Inorganic Chemistry*. 2016; 55(5): 2332-2344.

209. Ogasawara, M., et al. *Journal of the American Chemical Society*. 1996; 118(42): 10189-10199.
210. Bray, J.M. and R.J. Mawby. *Journal of the Chemical Society, Dalton Transactions*. 1989(4): 589-594.
211. Bader, R.F.W. *Chemical Reviews*. 1991; 91(5): 893-928.
212. Lu, T. and F. Chen. *Journal of Computational Chemistry*. 2012; 33(5): 580-592.
213. Martins, L.S.C., et al. *Computational and Theoretical Chemistry*. 2013; 1013: 62-69.
214. Rossi, A.R. and R. Hoffmann. *Inorganic Chemistry*. 1975; 14(2): 365-374.
215. Brookhart, M., M.L.H. Green, and G. Parkin. *Proceedings of the National Academy of Sciences of the United States of America*. 2007; 104(17): 6908-6914.
216. Tsipis, A.C. *Coordination Chemistry Reviews*. 2014; 272: 1-29.
217. Lein, M. *Coordination Chemistry Reviews*. 2009; 253(5–6): 625-634.
218. Tognetti, V., et al. *The Journal of Physical Chemistry A*. 2012; 116(22): 5472-5479.
219. Lopez-Serrano, J., S.B. Duckett, and A. Lledos. *Journal of the American Chemical Society*. 2006; 128(30): 9596-9597.
220. Noyori, R. *Advanced Synthesis & Catalysis*. 2003; 345(1-2): 15-32.
221. Halpern, J. *The Journal of Physical Chemistry*. 1959; 63(3): 398-403.
222. Syrkin, Y.K. *Uspekhi Khimii*. 1959; 28(8): 903-920.
223. Mohr, F., et al. *Coordination Chemistry Reviews*. 2006; 250: 1851-1888.
224. Kubas, G.J., et al. *Journal of the American Chemical Society*. 1984; 106(2): 451-452.
225. Khalsa, G.R.K., et al. *Journal of the American Chemical Society*. 1990; 112(10): 3855-3860.
226. Tomas, J.J., A. Lledos, and Y. Jean. *Organometallics*. 1998; 17(2): 190-195.
227. Muckerman, J.T., et al. *Journal of Physical Chemistry B*. 2007; 111(24): 6815-6821.
228. Arita, C., et al. *Bulletin of the Chemical Society of Japan*. 2001; 74(3): 561-567.
229. Rothfuss, H., J.C. Huffman, and K.G. Caulton. *Inorganic Chemistry*. 1994; 33(13): 2946-2953.
230. Bennett, M.A. and D.L. Milner. *Chemical Communications*. 1967(12): 581.
231. Keim, W. *Journal of Organometallic Chemistry*. 1969; 19(1): 161-161.
232. Bruce, M.I. *Angewandte Chemie International Edition in English*. 1977; 16(2): 73-86.
233. Geoffroy, G.L. and R. Pierantozzi. *Journal of the American Chemical Society*. 1976; 98(25): 8054-8059.
234. Thomas, A., et al. *Angewandte Chemie International Edition in English*. 1994; 33(7): 755-757.
235. Thomas, R.J.W., G.S. Laurence, and A.A. Diamantis. *Inorganica Chimica Acta*. 1978; 30(2): L353-L355.
236. Archer, L.J. and T.A. George. *Inorganica Chimica Acta*. 1980; 44(0): L129-L132.
237. Feller, D. *Journal of Computational Chemistry*. 1996; 17(13): 1571-1586.
238. Schuchardt, K.L., et al. *Journal of Chemical Information and Modeling*. 2007; 47(3): 1045-1052.
239. Andrae, D., et al. *Theoretica Chimica Acta*. 1990; 77(2): 123-141.
240. Weigend, F. *Phys. Chem. Chem. Phys.* 2006; 8: 1057-1065.
241. Dunlap, B. *Journal of Chemical Physics*. 1983; 78(6): 3140-3142.
242. Dunlap, B.I. *Journal of Molecular Structure-Theochem*. 2000; 529(SI): 37-40.
243. Coquet, R., M. Tada, and Y. Iwasawa. *Physical Chemistry Chemical Physics*. 2007; 9(45): 6040-6046.
244. Zyder, M., et al. *Organometallics*. 2009; 28(20): 5857-5865.
245. Wagner, T. and U. Englert. *Structural Chemistry*. 1997; 8(5): 357-365.
246. King, R.B. *Coordination Chemistry Reviews*. 2000; 200–202: 813-829.

247. Li, C., J. Agarwal, and H.F. Schaefer. *The Journal of Physical Chemistry B*. 2014; 118(24): 6482-6490.
248. Moss, J.R. and B.L. Shaw. *Journal of the Chemical Society, Dalton Transactions*. 1972(17): 1910-1911.
249. Hursthouse, M.B., et al. *Journal of the Chemical Society, Chemical Communications*. 1983(8): 476-477.
250. Sattler, A., A.A. Zuzek, and G. Parkin. *Inorganica Chimica Acta*. 2014; 422: 102-108.
251. Dobereiner, G.E., et al. *Journal of the American Chemical Society*. 2011; 133(19): 7547-7562.